FINAL SCIENTIFIC/TECHNICAL REPORT
Prepared for
THE U.S. DEPARTMENT OF ENERGY

Formation of Imploding Plasma Liners for HEDP and MIF Applications - Diagnostics

April 27, 2015

DoE Award No. **DE-SC0003585**
Project Duration: **December 15, 2009 – May 31, 2014**

Principal Investigator: Mark Gilmore, Associate Professor
Electrical & Computer Engineering and
Physics and Astronomy Departments
University of New Mexico
Albuquerque, NM 87131
Phone: 505-277-2579
gilmore@ece.unm.edu

Collaborators:

1. Scott Hsu (PI of overall PLX project), Los Alamos National Laboratory, 505-667-3386, scotthsu@lanl.gov
2. F. Douglas Witherspoon (co-PI), HyperV Tech., 703-378-4882, witherspoon@hyperv.com
3. Jason Cassibry (co-PI), Univ. Alabama Huntsville, 256-824-5107, cassibj@eng.uah.edu
4. Bruno S. Bauer (co-PI), Univ. Nevada Reno, (775) 784-1363, bruno.s.bauer@gmail.com

1. Executive Summary

The goal of the plasma liner experiment (PLX) was to explore and demonstrate the feasibility of forming imploding spherical plasma liners that can reach High Energy Density (HED)-relevant (~ 0.1 Mbar) pressures upon stagnation. The plasma liners were to be formed by a spherical array of 30 – 36 railgun-driven hypervelocity plasma jets (Mach 10 – 50). Due to funding and project scope reductions in year two of the project, this initial goal was revised to focus on studies of individual jet propagation, and on two jet merging physics. PLX was a collaboration between a number of partners including Los Alamos National Laboratory, HyperV Technologies, University of New Mexico (UNM), University of Alabama, Huntsville, and University of Nevada, Reno. UNM's part in the collaboration was primary responsibility for plasma diagnostics. Though full plasma liner experiments could not be performed, the results of single and two jet experiments nevertheless laid important groundwork for future plasma liner investigations. Though challenges were encountered, the results obtained with one and two jets were overwhelmingly positive from a liner formation point of view, and were largely in agreement with predictions of hydrodynamic models.

2. Research Objectives and Revised Scope after Funding Changes

The original goal of the plasma liner experiment (PLX) was to explore and demonstrate the feasibility of forming imploding spherical plasma liners that could reach High Energy Density (HED)-relevant (~ 0.1 Mbar) pressures upon stagnation [1]. The liners were to be formed via the merging of 30 - 36 dense, high Mach number plasma jets ($n \sim 10^{16} - 10^{17}$ cm^{-3}, M ~ 10–35, v ~ 50–70 km/s, r_{jet} ~ 5 cm) in a spherically convergent geometry. The plasma jets were to have been generated and launched by pulsed power-driven plasma guns that were being developed by HyperV Technologies for this purpose. The liners were to implode onto vacuum as well as solid and gaseous targets. This was to have been a staged, exploratory project, where scientific issues were to have been studied first at modest energy levels (150–300 kJ stored energy), before attempting to reach HED relevant pressures (requiring ~ 1.5 MJ).

The PLX project was a collaboration between five principle parties, with additional theory, modeling and other support from a number of other collaborators. The PLX experiment was partially constructed at Los Alamos National Laboratory (LANL). The University of New Mexico (UNM) team was primarily responsible for diagnostic development and implementation on PLX, with help from other collaborators – the University of Nevada, Reno (UNR) in particular. Table 1 shows a list of important physics measurements for PLX, and the planned diagnostics that were to have been implemented by the final phase of the project, in which full liner implosions (without a target plasma) utilizing 30 – 36 jets were to have been conducted.

In FY 2011, the original five year PLX project was reduced to three years (ending in May 2012) due to budget constraints within the DOE Office of Science. At that point, the PLX experiment was largely on track. The vacuum and data acquisition systems were fully operational, two plasma guns and the associated pulsed power systems were in place and

operating, and the associated theory and modeling efforts were well underway. UNM's contribution to the project – plasma diagnostics – were mostly operating routinely. UNM was given a small amount of additional funding for student support from June 2012 – June 2013, and a one year no cost extension was granted, through May 31, 2014.

Due to the reduced project scope and funding, results were limited to studies of the propagation of single hypervelocity jets, and the oblique merging of two jets. Despite not being able to study a liner formation by a more full spherical array of jets, the single and two jet merging studies that were performed laid important groundwork for future plasma liner development. The UNM team played an important role in this work through the development, deployment, and operation of the plasma diagnostics that provided the experimental measurements. UNM, especially Ph.D. student Elizabeth Merritt, also played a key role in the detailed physics studies performed with one and two plasma jets.

3. Research Methods and Results

Results in two areas are described below: 1) plasma diagnostics and 2) PLX physics. While results from both of these areas were described in a number of publications (listed in section 6), much more detail was published on the physics that the diagnostic systems. Thus, this report will focus primarily on diagnostics (1), and the reader is referred to publications included in the appendix for a more complete description of physics results.

3.1 Plasma Diagnostic Development and Deployment

To meet the needs of the first phase of operation, the UNM effort focused on implementing "Day 1" diagnostics to provide the needed measurements to meet the physics goals of the first phase of the PLX experiment (i.e. single jet propagation, merging of two jets). These diagnostic systems are listed in the first four rows of Table 1. In particular, we concentrated on implementation of multi-chord visible interferometry and visible spectroscopy, both of which became the PLX "workhorse" diagnostics on which physics results were based. Other diagnostics were also fielded, including fast cameras and photodiodes and magnetic probes. Each of these systems is discussed below.

A. Multi-Channel Interferometer

Significant effort went into development of an 8 channel visible interferometer system. The system utilized a fiber optic-coupled front end, whose viewing chords are relatively easily reconfigured. In particular, the launched and received light was brought to the launch and receiver ports on the vacuum chamber via fiber optics, with only fiber-lens couplers, turning mirrors, and final focusing lenses mounted on the chamber on small (~ 24 inch by 12 inch) optical breadboards. Thus, chords could be moved relatively easily.

Table 1. PLX physics measurements and diagnostics.

Physics Measurement	Diagnostic
Jet Mach number and transverse expansion prior to merging	Multichord interferometry (561 nm), Visible frame imaging, Fast diode array imaging, Schlieren imaging
Merging Physics (shock structure, liner thickness, shock heating, instabilities)	Schlieren imaging, Visible frame imaging, Multichord interferometry (561 nm), Visible spectroscopy, Pressure probe
Plasma Gun Operation	dB/dt probe, Rogowski coil, photodiode, voltage monitor (each gun)
Jet trapped B-field	dB/dt probes
Liner implosion/compression dynamics (liner thickness vs. R)	Multichord interferometry (561 nm), Schlieren imaging, Visible frame imaging, VUV spectroscopy, Pressure probe
Parameters at stagnation and after liner collapse, especially pressure, stagnation radius, and (equation of state) on axis	XRD array, Bolometry, VUV spectroscopy, Visibleframe imaging, "Crush ball" pressure sensor

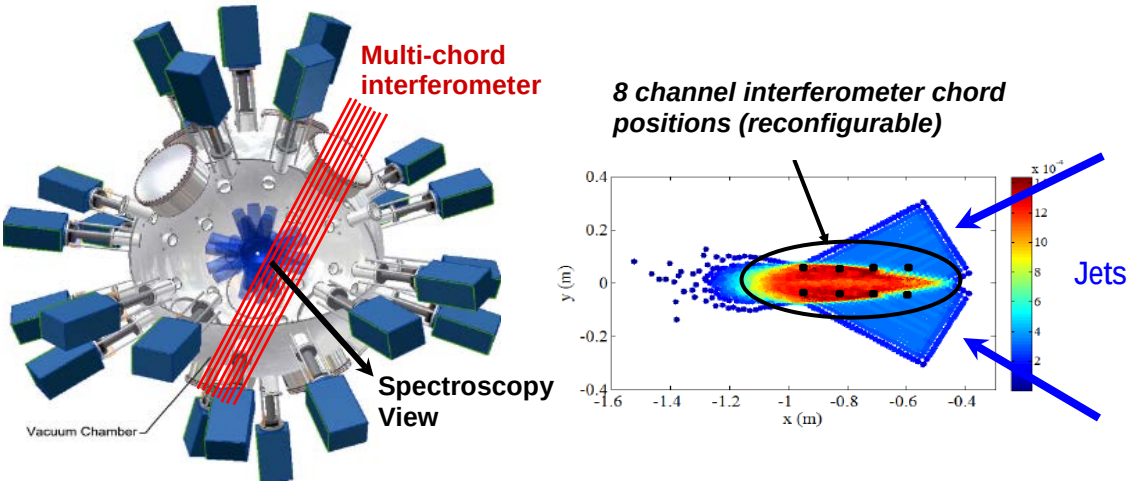

Fig. 1. Left: Chordal views of diagnostics across the plasma merging radius. Right, merging of two jets [excerpted from "Modeling of Formation and Implosion of Plasma Liners by Discrete Jets ," Seth Thompson, Jason Cassibry, AIAA 2008-3890, 39th Plasmadynamics and Lasers Conference, Seattle, Washington, June 23-26, 2008] showing one possible positioning of 8 interferometer chords. Chords could also be arranged in many other configurations, such as in a linear array along a jet.

The interferometer layout is shown in Fig. 2, and photos are shown in Fig. 3. The system design was relatively unique, in that reference legs have significantly different path lengths. This path difference was enabled by use of a high power diode laser (Oxxis DPSS), with sufficient

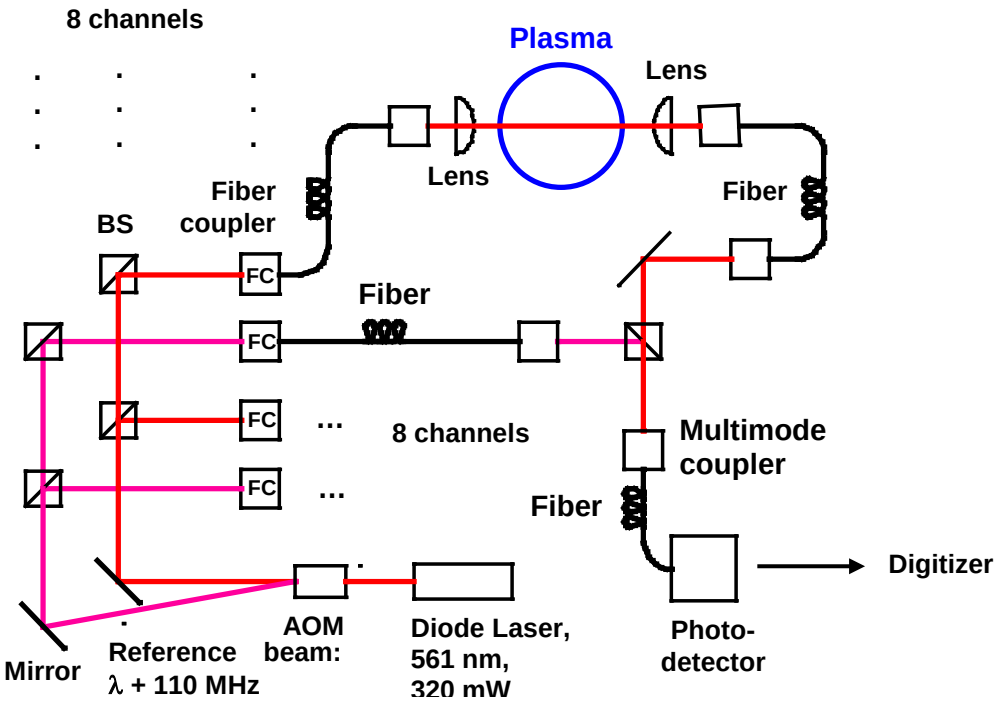

Fig. 2. PLX 8 channel interferometer.

power for 8 channels. Additionally, this laser has an extremely long coherence length (> 100 m), so that the interfering reference and signal beams remain coherent, even with a path length difference > tens of meters.

It turned out that due to the high Z (Ar), relatively low temperature, and high density of the plasma jets, the interferometer phase shift was sensitive to bound electrons (ions and neutrals) as well as free electrons. Thus, the analysis of interferometry data was nontrivial, and required estimates of ionization fraction and charge state from visible spectroscopy. A full description is given in ref. [2]. In addition to density, the mutichord interferometer gave information on jet velocity and acceleration/deceleration (via time delay between channels), jet expansion, and oblique shock structures.

B. Visible Spectroscopy

Two spectroscopy systems were fielded for initial PLX operations – a high resolution, fast time response, system (shown in Fig. 4), and a wide spectrum survey system – both operating at visible wavelengths. Mainly, the survey system was utilized. Since jets were cold (electrons and ions ~ few eV or less), UV or VUV systems were not required. The survey spectrometer was an 0.275 m Acton Research Corp. SpectraPro 275 with a gated 1024-pixel multi-channel-plate array (EG&G Parc 1420). A 600 line/mm grating giving a resolution of 0.152 nm/pixel. The high resolution instrument was a 1 meter SPEX 1802 spectograph that operates over 400 – 15,000 Å,

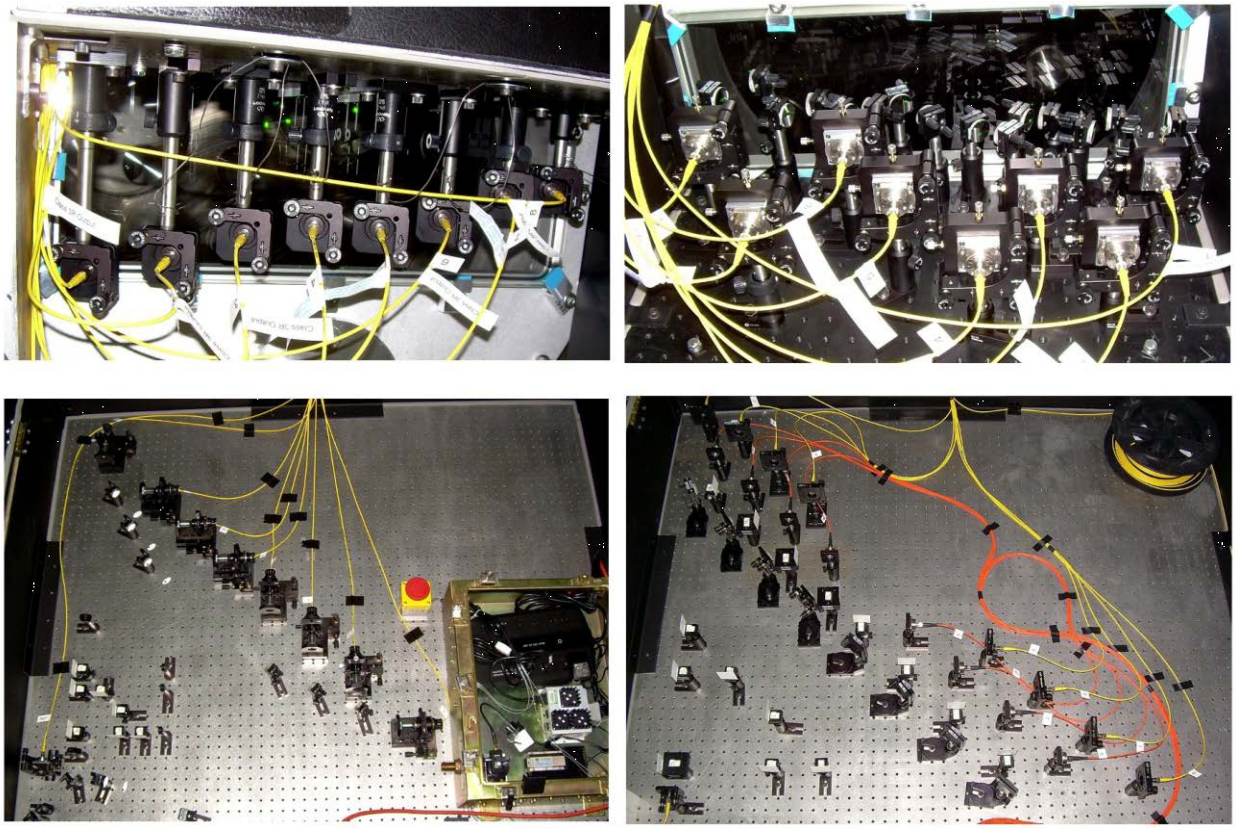

Figure 3. Photos of the optical components of all stages of the interferometer. Single mode fiber is yellow and multi-mode fiber is orange. Lower Left: Initial establishment of the chords. Upper Left: Laser beam collimators mounted on the chamber. Upper Right: Beam-to-fiber couplers mounted on the chamber. Lower Right: Recombination of the probe and reference beams.

Fig. 4. High resolution sprectrometer equipment. Left: 1 m SPEX spectograph, right: detectors – 4QuickE fast camera (upper) and 1024 x x1024 CCD detector (lower).

with a 1200 groove/mm grating, and a resolution of 0.008 nm. Visible spectroscopy provided information on jet velocity, plasma density, T_e, and impurity content (including entrained neutrals).

Estimates of the electron temperature were based on the presence of ionization lines in the spectra in comparison to non-local-thermodynamic-equilibrium (non-LTE) spectra calculated by the PrismSPECT code [3]. Electron density was also estimated via Stark broadening of the impurity hydrogen H_β line (486.1 nm). The analysis and results are further described in ref. [4].

C. Fast Imaging

Several cameras were used for fast imaging of plasma jets and merging, including an intensified Stanford Computer Optics 4 Quick E, 1024 x 1024 pixels, ≥ 1.2 ns exposure instrument, two comparable PIMax cameras, and a 24 frame, t > 15 ns, 1024 x 1024, Hadley Ultra 24 camera.

D. B-dot Probes

B-dot probes were deployed for operation with a single jet in order to quantify jet-trapped magnetic fields. Minimal B-field, B < 5 Gauss, was measured in all experiments (as was the goal for PLX).

E. Schlieren Imaging

A Schlieren imaging was also developed and deployed in order to complement multi-chord interferometry and visible imaging to view the merging dynamics of two jets. The system, shown in Fig. 5, was based on a fast pulsed (3 ns), 2 Joule Nd:YAG laser (Coherent Infinity 40-100), and imaged via slow CCD camera. Though the system functioned as designed, it was

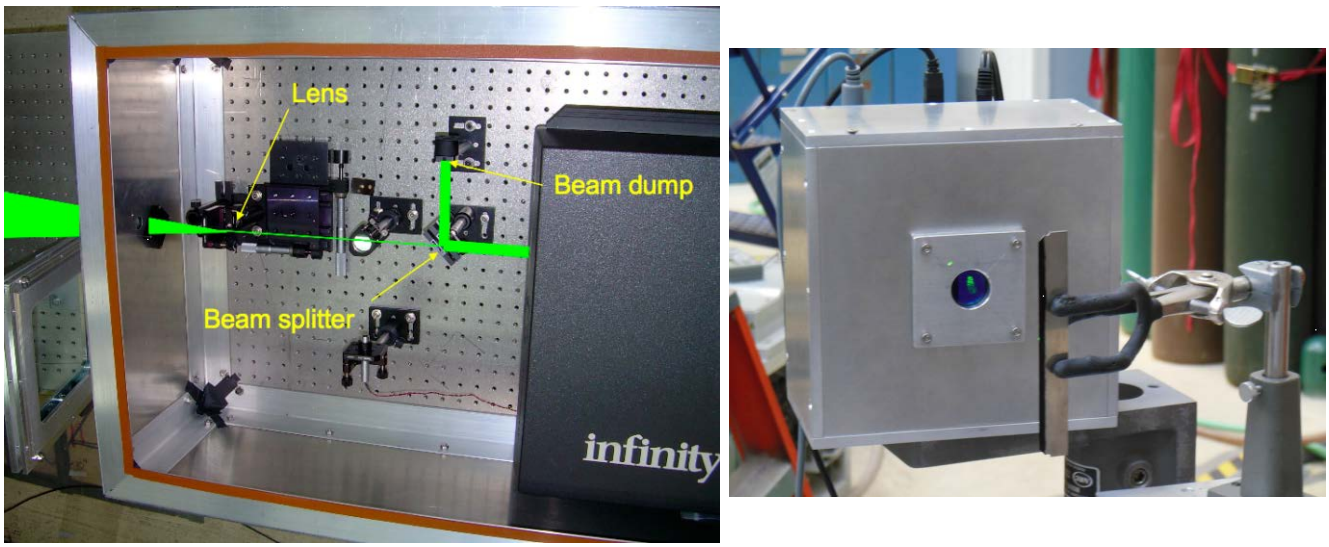

Fig. 5. Left: Pulsed Nd:YAG-based Schlieren imaging system on PLX. Right: source and source optics. Right: knife edge (foreground) and CCD detector inside aluminum screen box.

found that density gradients were shallower than predicted by numerical models, and were not

resolvable in the Schlieren imaging data. A detailed description is given in ref. [5].

3.2 Physics Results

As mentioned above, only a very brief summary of physics results are given here. The reader is referred to publications attached in the appendix for details.

A. One Jet Propagation

The project characterized in detail, for the first time, the propagation and expansion of hypervelocity argon and hydrogen plasma jets produced by plasma "mini-railguns" built by HyperV Technologies. Additionally, basic parameters such as density, ionization state, impurity concentration, and trapped magnetic field were characterized. In order to extend the lifetime of the plasma guns, they were operated at reduced currents, I < 300 kA. Nevertheless, the gun performance was very promising for future plasma liner formation.

Plasma jets were found to have initial densities, $n \sim 10^{16}$ cm^{-3}, $T_e \sim 1.4$ eV, and velocities v ~ 30 km/s, which correspond to Mach numbers ~ 15. Jet density was peaked axially and radially, showing that most of the mass was confined to the jet center. Jets were found to remain cohesive, with only sonic expansion, as they propagated to $R \approx 60$ cm (the radius where jets would merge to begin liner formation in a full PLX liner experiment). At the merging radius (60 cm) density dropped by a factor of ~ 10, which is within an acceptable range for liner formation.

Plasma impurities, especially C, O, H, and Al, were a challenge, but significant improvements were made over the course of the project. Impurities, primarily from the railgun insulators were introduced when the guns were fired. However, improvements in gun insulator materials and design over the course of the project reduced impurity content significantly. This is further discussed in the DOE Final Report by F. Douglas Witherspoon of HyperV Technologies.

B. Two Jet Merging Physics

Experiments to study the oblique (24°) merging of two plasma jets revealed fundamental behavior consistent with 2D collisional hydrodynamic models. It was found that a double reflected oblique shock forms at the merging plane, which transitions to a detached shock at later times. Each shock structure was of the order of λ_{ii}, the directed ion-ion collision mean free path, as expected from collisional shock theory. Density, n, increases at the shock greater than simply a superposition of the two jet densities were also clearly observed, indicating that shock ionization occurs. The density jumps were found to be consistent with collisional shock jump conditions from hydrodynamics. Additionally, no evidence of large scale instability was observed in the merging. (In the worst case scenario, instabilities might be expected due to streaming or Rayleigh-Taylor effects.) These observations are all very positive with respect to the formation of plasma liners.

4. Relevance, Impact, and Technology Transfer

Though the scope of the PLX project did not allow for an investigation of full 30 – 36 gun spherical plasma liners, important results relevant to the formation of such liners were obtained nevertheless. The plasma diagnostics fielded by UNM under this grant played a key role in obtaining these experimental results. Overall, single jet and two jet merging results were very positive from the point of view of formation of spherical plasma liners, and were largely consistent with hydrodynamic modeling of hypervelocity gun-driven plasma liner formation. No fundamental physics that could significantly impact plasma liners were uncovered in the course of this work. The challenges that were encountered were, in particular, reliable pulsed power/railgun operation, and high impurity content in the plasma jets. These are topics that will require continued research if such guns will be used for liner formation in the future.

Since the PLX project was focused on basic research, no technology ready for transfer resulted from this work.

5. Personnel Supported and Students Graduated

The following personnel were supported by funds on this project.

1. Dr. Alan Lynn, Assistant Research Professor, University of New Mexico
2. Dr. Elizabeth Merritt, Ph.D. student, University of New Mexico. Dr. Merritt completed her Ph.D. in August 2013. Her dissertation research was performed on this project.
3. Mr. Jaksa Osinski, Undergraduate Laboratory Assistant, University of New Mexico.

6. Publications and Presentations

6.1 Journal Publications

1. A.G. Lynn, *et al* (2010). *Diagnostics for the Plasma Liner Experiment.* Rev. Sci. Instrumen. **81**, 10E115.
2. Elizabeth C. Merritt, Alan G. Lynn, Mark A. Gilmore, and Scott C. Hsu (2012). "Multi-chord fiber-coupled interferometer with a long coherence length laser", *Rev. Sci. Instrum.* **83**, 033506
3. Elizabeth C. Merritt, Alan G. Lynn, Mark A. Gilmore, Carston Thoma, John Loverich, and Scott C. Hsu (2012). "Multi-chord fiber-coupled interferometry of supersonic plasma jets (invited)", *Rev. Sci. Instrum.* **83**, 10D523
4. E. C. Merritt, A. L. Moser, S. C. Hsu, J. Loverich, and M. Gilmore (2013). "Experimental Characterization of the Stagnation Layer between Two Obliquely Merging Supersonic Plasma Jets", *Phys Rev Lett* **111**, 085003.
5. Elizabeth C. Merritt, Auna L. Moser, Scott C. Hsu, Colin S. Adams, John P. Dunn, A. Miguel Holgado and Mark A. Gilmore (2014). "Experimental evidence for collisional shock formation via two obliquely merging supersonic plasma jets", *Phys. Plasmas* **21**, 055703

6.2 Ph.D. Dissertations

1. Elizabeth C. Merritt, *Measurements of Railgun Generated Supersonic Plasma Jet Propagation and Two Jet Oblique Merging*, Ph.D. Dissertation in Physics, University of New Mexico, 2013.

6.3 Invited Conference Presentations

1. E.C. Merritt, "Multi-chord fiber-coupled interferometry of supersonic plasma jets", invited talk presented at the *19th Topical Conference High-Temperature Plasma Diagnostics*, Monterey, CA, May 6-10, 2012.
2. E.C. Merritt, "Experimental Characterization of the Stagnation Layer between Two Obliquely Merging Supersonic Plasma Jets ", invited presentation at the *55th Annual Meeting of the American Physical Society Division of Plasma Physics*, Denver, CO November 11-15, 2013.

6.4 Conference Publications

1. M. Gilmore, *et al* (2010). *Diagnostics for the Plasma Liner Experiment.* Proc. 2010 International Conference on Plasma Diagnostics, April 12 – 16, 2010, Nancy, France.

7. Patents and Copyrights

No patents or copyrights were applied for in the course of this work.

8. Literature Cited

[1] S. C. Hsu, T. J. Awe, S. Brockington, A. Case, J. T. Cassibry, G. Kagan, S. J. Messer, M. Stanic, X. Tang, D. R. Welch, and F. D. Witherspoon (2012). "Spherically imploding plasma liners as a standoff driver for magnetoinertial fusion," *IEEE Trans. Plasma Sci.* **40**, 1287.

[2] Elizabeth C. Merritt, Alan G. Lynn, Mark A. Gilmore, Carston Thoma, John Loverich, and Scott C. Hsu (2012). "Multi-chord fiber-coupled interferometry of supersonic plasma jets (invited)", *Rev. Sci. Instrum.* **83**, 10D523

[3] J. J. MacFarlane et al., Simulation of the ionization dynamics of aluminum irradiated by intense short-pulse lasers, Inertial Fusion Sciences and Applications 2003 (B. A. Hammel, D. D. Meyerhofer, and J. Meyer-ter-Vehn, eds.), American Nuclear Society, 2004, p. 457.

[4] S. C. Hsu, E. C. Merritt, A. L. Moser, T. J. Awe, S. J. E. Brockington, and *et al* (2012). "Experimental characterization of railgun-driven supersonic plasma jets motivated by high energy density physics applications," *Phys. Plasmas* **19**, 123514.

[5] Colin S. Adams, “Rayleigh-Taylor-Instability Evolution in Colliding-Plasma-Jet Experiments with Magnetic and Viscous Stabilization”, Ph.D. Dissertation, University of New Mexico, 2015.

9. Appendices – Copies of Journal Publications and Dissertations

Measurements of railgun generated supersonic plasma jet propagation and two jet oblique merging

by

Elizabeth C. Merritt

B.A., Physics, Mathematics, Mount Holyoke College, 2007

DISSERTATION

Submitted in Partial Fulfillment of the
Requirements for the Degree of

Doctorate of Philosophy
Physics

The University of New Mexico

Albuquerque, New Mexico

June, 2013

Dedication

To my parents, Maggie and Bernie, for inspiring me to pursue a life in science and encouraging me along the journey so far. I hope I make you proud.

Acknowledgments

I would first like to thank my advisor, Mark Gilmore, for being the kind of professor that is not just an advisor, but a mentor. Thank you for all your support, your encouragement made a world of difference to me. Next I would like to thank our PI, Scott Hsu, for all the effort he dedicated to helping my succeed. Thank you, I know it can't have been easy. And I would like to thank Alan Lynn, for his advice, friendship and comedy relief over the last few years. I would also like to thank Jason Cassibry and David Dunlap for taking the time and effort to serve on my dissertation committee.

I would like to acknowledge my lab-mates at the PLX facility at LANL: John Dunn, Auna Moser, Josh Davis (now a student at U. of Michigan), Colin Adams and Tom Awe (now at Sandia Labs). I would also like to acknowledge our extensive network of collaborators for the PLX project: F. Doug Witherspoon, Sam Brockington, Andrew Case and Sarah Messer at HyperV Technologies for advice and experimental support on the railgun operation, and John Thompson at Fartech Inc. John Loverich at Tech-X Corp. Carsten Thoma at Voss Scientific, and again Jason Cassibry at U. of Alabama in Hunstville for discussions and contributions of their simulation results.

And I would like to thank the other graduate students in my program, Tiffany Hayes, Ralph Kelly, Yue Zhang, and Tyler Wynkoop, for support and companionship throughout this process. And I would like to thank my friends Jenn and Bryan Krohn-Bourgeois helping me with stress relief and dissertation edits.

Finally, I would like to thank my family. Thank you mom and dad for the lifetime of encouragement. And thank you to my brother and sister-in-law, Sam and Lisa, and my Aunt Helen for coming out to see and support me. And last but not least, thank you to my partner, David Culter, for sticking with me through all of this. I love you.

Measurements of railgun generated supersonic plasma jet propagation and two jet oblique merging

by

Elizabeth C. Merritt

B.A., Physics, Mathematics, Mount Holyoke College, 2007

PhD, Physics, University of New Mexico, 2013

Abstract

Imploding spherical plasma liners have been proposed as a possible method for creating high-energy-density (HED) laboratory plasmas and as a standoff driver for magneto-inertial fusion (MIF). The Plasma Liner Experiment (PLX) planned a three-phase experimental program to study the feasibility of using railgun-driven supersonic jets to form imploding spherical plasma liners. The three phases are to investigate single-jet evolution during propagation, to merge 2–5 jets to assess the suitability of merging for liner formation, and to merge 30 jets in spherical symmetry to form a complete liner. We present here details of single-jet propagation and two-jet oblique merging experiments completed on PLX.

A key component of this dissertation was the design, implementation, and operation of a novel 8 chord, fiber-coupled interferometer based on a long coherence length ($>$ 100 m) 561 nm diode-pumped solid state laser. This interferometer was a critical diagnostic in both single-jet propagation and two-jet merging studies. The long laser coherence length and fiber-optic design allowed signal and reference path lengths in

the interferometer to be mismatched by many meters without signal degradation, greatly simplified interferometer optical layout, and added flexibility in interferometer positioning for both propagation and merging experiments. The interferometer sensitivity to ions, neutral atoms, and electrons required development of a phase shift analysis that incorporated the presence of neutrals, impurities, and multiply ionized species. Interferometry, coupled with spectroscopic ionization fraction estimates, was used to assess time resolved density profile measurements. Survey spectroscopy inferred both T_e and ionization fraction f via non-local-thermodynamic-equilibrium (non-LTE) atomic/equation-of-state (EOS) modeling. A fast CCD camera and photo-diode array allowed for assessment of plasma emission for velocity and jet profile measurements.

Initial jet parameters were $n_e \sim 10^{16}$ cm^{-3}, $T_e \approx 1.4$ eV, velocity $v \approx 30$ km/s, sonic Mach number $M \approx 14$, diameter≈ 5 cm, and length≈ 20 cm. Interferometry in conjunction with CCD line-out data showed that the average jet density decreases by a factor of ten after propagating 40 cm, which is at the very low end of the 8–160 times drop predicted by ideal hydrodynamic theory. In oblique merge experiments, interferometry identified a density increase consistent with shock formation as opposed to simple plasma interpenetration, and the consistent formation of a density structure (with scale length $\lambda_{ii'}$) near the merge plane. Imaging showed formation of a multi-peaked emission structure transverse to the jet-merging plane with widths similar to the density structure. Since the merging regime was semi-collisional and the counter-streaming ion collisionality was comparable to the merged-structure size, we interpreted the observations using both hydrodynamic oblique shock and multi-fluid plasma theory and simulations. We find that our observations were consistent with oblique shock theory and a collisional, one-dimensional, multi-fluid plasma simulation.

Contents

List of Figures

List of Tables

Chapter 1

Introduction

The Plasma Liner Experiment (PLX) is intended as a proof-of-concept experiment for forming spherical plasma liners for possible use in both basic science investigations of high-energy-density (HED) plasmas and energy research applications like magneto-inertial fusion (MIF).[25, 59] In this system, a plasma liner is a spherical shell of plasma with an inward momentum that converges on either vacuum or a target located at its center. The goal of PLX is to form a plasma liner from discrete plasma jets (shown in Fig 1.1), where the combined kinetic energy of the jets is high enough that the plasma liner can reach peak pressures of 0.1–1 Mbar during liner implosion. If initial experiments are successful, then it would motivate experiment upgrades to the MIF-relevant higher peak pressure range of > 10 Mbar.[25]

High-energy density (HED) physics begins when matter has an internal energy high enough, $\sim 10^{11}$ J/m^3 , or is compressed enough, ~ 1 Mbar of pressure.[51, 21] At these energies and pressures even simple solid matter, such as metals, begin to exhibit ionized or plasma characteristics. More broadly, HED regimes encompass phenomena from low-density plasmas traveling near the speed of light to the high-density plasmas found in the hearts of stars, as shown in Fig. 1.2. HED plasmas tend

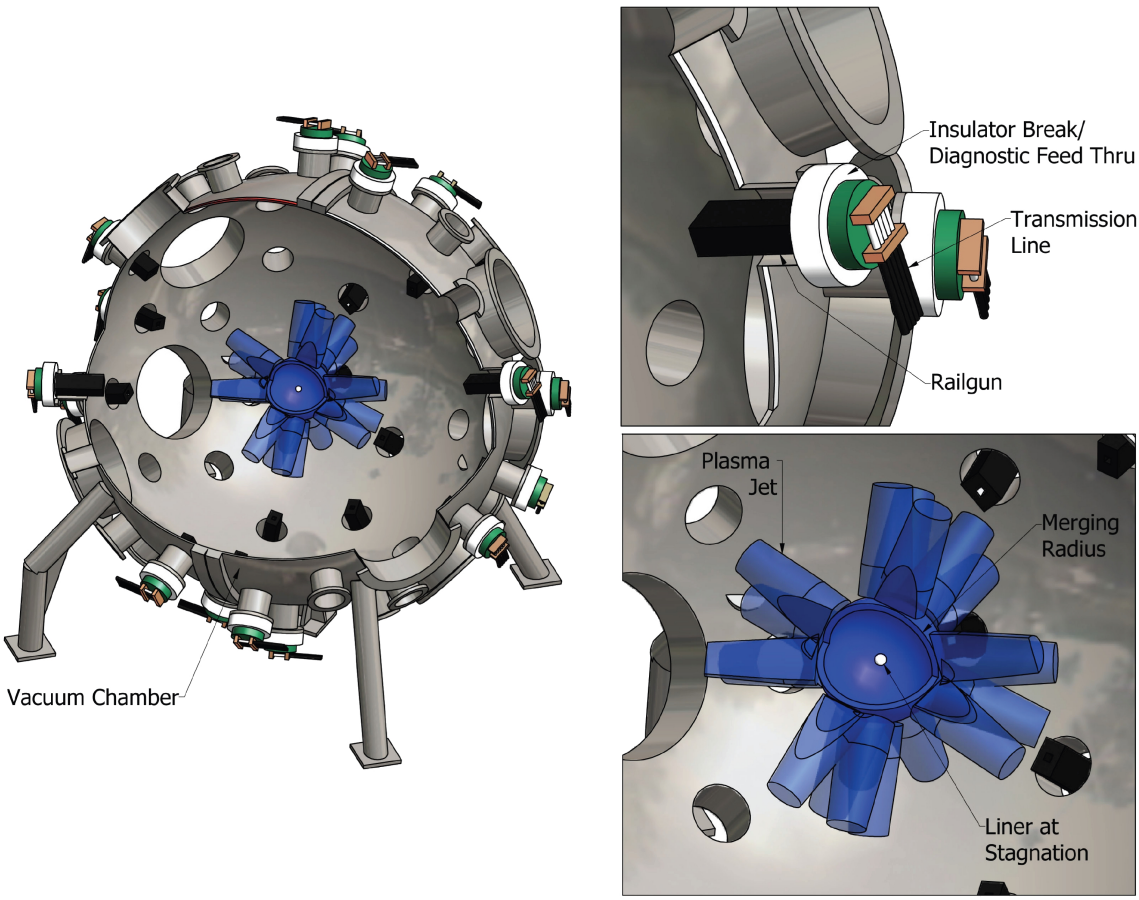

Figure 1.1: Early illustration of the PLX concept with 30 plasma railguns on a 9 ft (2.7 m) spherical vacuum chamber. The plasma jets are created and accelerated by the railguns (not shown) and then propagate until they merge near the center of the chamber to form a plasma liner (shown). Figure provided by HyperV Technologies.

to bridge the gap between traditional plasma physics and condensed-matter physics. They display collective behavior but, unlike traditional plasmas they display higher correlated behavior or relativistic effects and, unlike condensed matter, they are highly dependent on ionization and Coulomb collisions. Overall, HED investigations may be able to address fundamental physics questions such as the potential existence of plasma phase transitions, the structure of neutron star interiors, and the possibility of creating thermonuclear fusion in the lab.[51]

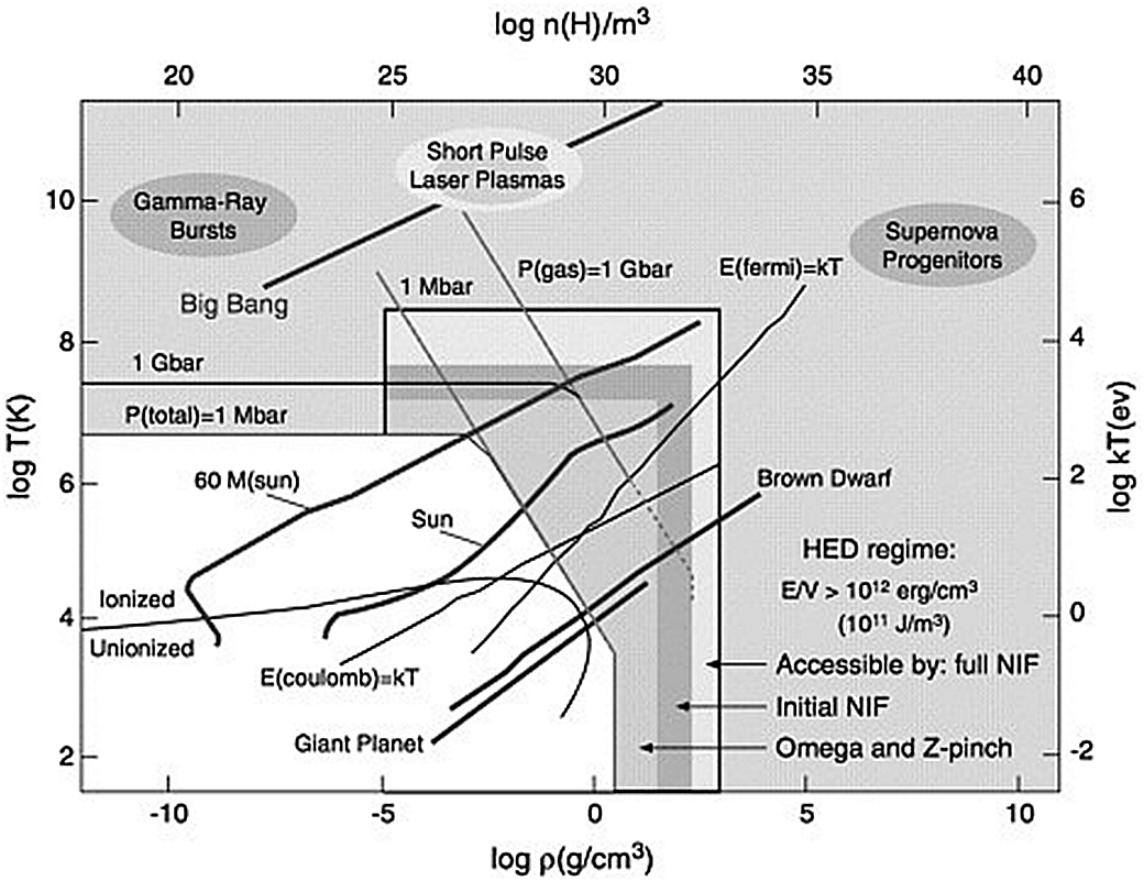

Figure 1.2: HEDP regimes. Excerpted from [51, 21].

Historically, HED physics has been the purview of astro- and theoretical-physics, due to an inability to reproduce the proper conditions in a laboratory for systematic study. However, over the last few decades a variety of potential HED facilities have been constructed. Particle accelerators such as the Stanford Linear Accelerator and the Large Hadron Collider are capable of producing near-relativistic charged particles. Laser facilities such as OMEGA at the Laboratory for Laser Energetics and the National Ignition Facility (NIF) at Lawrence Livermore National Laboratory are pursuing fusion experiments. The primary focus of the laser-based fusion studies has been inertial confinement fusion (ICF). Simply put, the lasers deliver energy

to the surface of a solid target containing fusible material, generally deuterium (D) and tritium (T), which causes the surface of the target to ablate and expand very quickly. The expansion of the ablated material causes the remaining target material to compress to high pressures. In these systems, since the lasers provide energy to the target they are referred to as the driver.

Traditionally the ICF targets have consisted of unmagnetized material. However, the addition of an embedded strong magnetic field in the target is postulated to reduce energy losses by decreasing the thermal conductivity and increasing alpha particle deposition in the target. Reduced energy loss expands the possible ignition parameter space, as shown in Fig. 1.3(a), and the size and power required for a fusion system.[9, 39] This parameter-space expansion consequently reduces the size and power required for a fusion-viable experimental facility (Fig 1.3(b) for example).[39] Fusion schemes using inertial compression of a magnetic fuel target are known as magneto-inertial fusion (MIF) approaches. Expanded parameter space and reduced cost have led to the proposal and construction of a variety of new fusion oriented experiments.

Along the lines of laser-driven ICF, experiments are currently being conducted using the OMEGA laser facility to study the effects of magnetic-flux compression on target implosion performance. Recent results show that with seed magnetic fields of $\sim$ kG, it is possible to generate peak magnetic fields of $\sim$ MG in the target as required for MIF schemes in the laser driven regime. Addition of an embedded magnetic field did produce an enhancement of 15% in the observed ion temperature (decreased thermal conduction) and 30% in the neutron yield compared to unmagnetized target experiments.[23] Experiments in magnetized liner inertial fusion (MagLIF) are scheduled to begin this year (2013) at the Z pulsed-power facility at Sandia National Laboratory. MagLIF experiments propose a system with a cylindrical metal liner around a cold fusible material gas, such as D_2 or D-T, with an axial embedded mag-

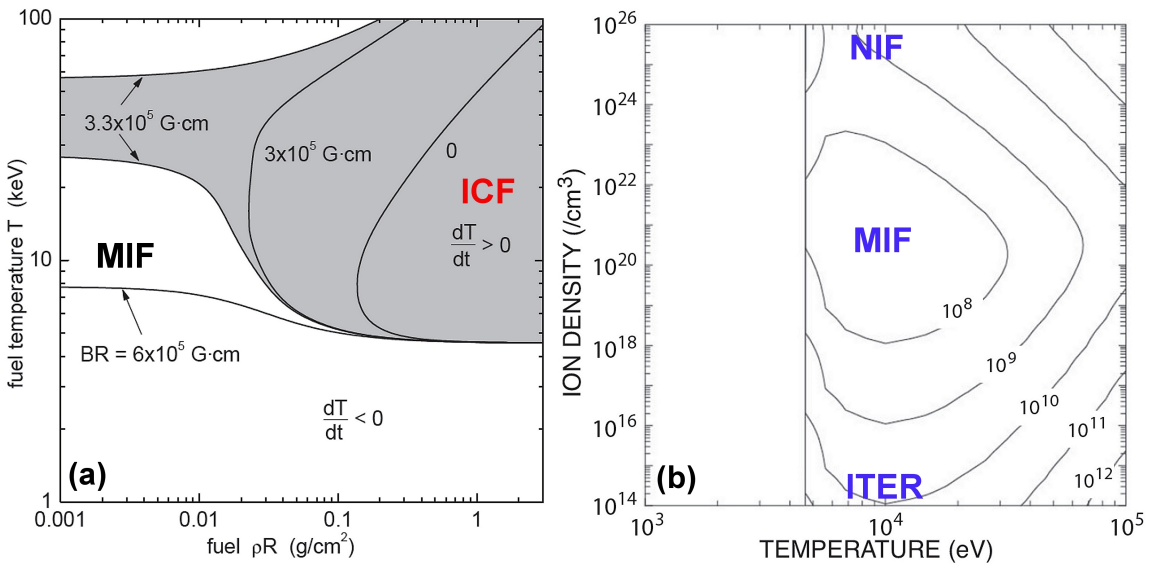

Figure 1.3: (a) Lindl-Widner diagram of ignition parameter space, using the BR instead of ρR form, with MIF and ICF portions of the parameter space indicated. Excerpted from [9, 27]. (b) The parameter space for the minimum MIF facility cost, in US $, vs. ion density and temperature for magnetized fuel in a cylindrical system with magnetic field $B = 5$ MG. Excerpted from [39, 27]. Approximate costs vs. ignition parameters for both the NIF and ITER facilities are also shown.

netic field. A laser preheats the cold target gas, and then an azimuthal magnetic field implodes the cylindrical liner (drives the system) and compresses the target gas.[18] Similar to MagLIF, the Field Reversed Compression and Heating Experiment (FRCHX), a collaborative effort between Los Alamos and Sandia National Laboratories, uses a cylindrical metal liner imploded with a magnetic field to compress its target. However, the target for FRCHX is a field reversed configuration plasma (FRC), which is a plasma with embedded closed magnetic field lines.[31]

For each of the previous MIF systems, either the target (OMEGA experiments) or the liner (FRX-L/Shiva) or both (MagLIF) are solid manufactured components and are destroyed during the course of a single shot. Since part of the equipment must be replaced between shots, this severely limits the repetition rate of the experiments

and poses a hurdle for improving the experiments to the high shot rate needed for the continuous energy output of a fusion reactor. The PLX concept is an effort to create an MIF scheme that would not require the manufacture and destruction of either the liner or the target. PLX proposes to use both a plasma target and a plasma liner, where both target and liner are created by equipment at some standoff distance from the liner/target implosion. The standoff distance of the equipment will theoretically allow it to avoid damage over the course not just one but many shots.

1.1 PLX Background

In 2001, Thio *et al.* [59] proposed a two-stage proof-of-concept experiment for using plasma jets to form unmagnetized plasma liners capable of achieving MIF relevant conditions. The first stage would attempt to study the simpler 2D dynamics of jet merging by using 12 plasma guns in circular symmetry to create a cylindrical liner. The second stage would expand to up to 60 plasma guns in spherical symmetry for 3D studies. The spherical liner is designed to reach peak compression densities of $n \sim 10^{19}$ cm^{-3} and confinement (dwell) times of > 60 ns to create energy conditions within three orders of magnitude of breakeven. Breakeven here is defined as producing the same amount of energy from fusion as was originally contained in the plasma, which is dominantly the liner kinetic energy, for a gain of $G = E_{\text{fusion}}/E_{\text{plasma}} = 1$. To create these peak conditions would require a total liner energy of 0.4 MJ, corresponding to 60 jets with $v = 200$ km/s and a mass of 0.33 mg each. Smooth-particle hydrodynamics simulations for the 3D liner, using Los Alamos National Laboratory's SPHINX code, showed promising results for the formation of both cylindrical and spherical shells from discrete jets.

In 2008, Parks [53] proposed a new self-similarity model to study the heating of the surrounding cold unmagnetized liner by alpha particles emitted by the hot

target. This model predicted similar scale liner dwell times to those of Thio *et al.*, on the order of $\sim$ 100 ns assuming a target radius of $R = 0.5$ cm, jet velocity of $v_j = 100$ km/s, and $t_{\text{dwell}} \sim 2R/v_j$. This significantly limited the projected gain of the system by limiting the fraction of the target fuel that burns. Parks also showed that a low liner adiabatic index ($\gamma < 5/3$) improves the achievable peak target pressures for a given initial liner Mach number. Later studies by Cassibry *et al.* [13] using the self-similar converging shock model predict much longer dwell times, on the order of μs. This dwell times takes into account outgoing shock and rarefaction times through the plasma liner at peak compression, instead of just using estimates from the initial jet velocity. The liner dwell time was found to be insensitive to the target radius R but was found to be linearly dependent on the liner thickness ΔR. Cassibry *et al.*'s model also showed stagnation pressures of 1 Mbar for a spherical liner with density $n \sim 10^{18}$ cm^{-3}, velocity $v = 20$ km/s, and $\gamma = 1.1$.[24]

Awe *et al.* [8] found a similar form for the dwell time for the liner imploding on vacuum instead of a target during a numerical scaling study in 2011: $t_{\text{dwell}} \sim \Delta R/v_0$ where v_0 is the initial liner velocity. Awe *et al.*'s scaling study used two separate 1D radiation hydrodynamic simulations, RAVEN and HELIOS, which allowed for the inclusion of radiation- and thermal-energy transport in the liner parameter study. Both codes included ideal gas equation-of-state (EOS) tables for argon (Ar) from Prism Computational Sciences, Inc.[1] The scaling study also found that the peak liner pressure during stagnation ,P_{stag}, scales as $P_{\text{stag}} \sim v_0^{15/4}$ with initial liner velocity. The pressure scaling is lower than that expected for an ideal system ($P_{\text{stag}} \sim v_0^5$) in which the liner kinetic energy (KE) is perfectly converted into the thermal energy (TE) of the stagnated plasma with no thermal or radiative losses. The peak pressure also scales as $P_{\text{stag}} \sim n_0^{1/2}$ with initial liner density and $P_{\text{stag}} \sim M^{3/2}$ with initial liner Mach number for PLX relevant parameters. Since the Mach number scales with electron temperature as $M \propto T_e^{-1/2}$, this means that the *ideal plasma jets for PLX should have high velocity and high density but low temperature.* The relevant

parameters for the PLX proof-of-concept tests assumed 30 jets and were designed to reflect current peak performance of HyperV Technologies Minirailguns, which can create argon plasma jets of ion density $n_i \sim 10^{17}$ cm^{-3}, $v_j \approx 50$ km/s and injected mass ≈ 8 mg at the gun nozzle.[8, 62, 25] For these parameters, and assuming the jet density decreases from $n_i \sim 10^{17}$ cm^{-3} to $n_i \sim 10^{15}$–10^{16} cm^{-3} during jet propagation and merging, the simulations show that PLX 30-jet liner experiments should be able to reach HED-relevant peak pressures of 0.66–4.63 Mbar.[8] *These parameters and predictions formed the basis of the current PLX experimental plans and specifications.*

The simulations in Awe *et al.* [8] also only considered high-Z (high atomic number) noble gases argon and HyperV has focused on improving plasma gun performance with high-Z gases.[65, 25] High-Z liner materials are preferable since they provide higher mass, and thus kinetic energy, for a given (gun-limited) number density. High-Z materials also have a lower adiabatic index γ than the ideal-gas value of $\gamma = 5/3$,[21] which Parks showed increased target peak-pressure performance, and they undergo more radiative cooling than lower-Z materials which helps enhance the jet/liner Mach number.[25, 38] Finally, high-Z materials may not experience as much shock heating during liner formation (jet merging) since energy can go into excitation of the bound electrons instead.[21] This reduction in shock heating decreases damping of the liner Mach number. All PLX experiments presented in this dissertation use argon jets and an assumed adiabatic index of $\gamma = 1.4$.

In 2012, Kim *et al.* [34] applied the FronTier code and a plasma EOS model including ionization and dissociation effects to several simulation cases from Awe *et al.*, to study the impact of these processes on liner performance. Kim *et al.*'s model was also 1D and included thermal conduction like Awe *et al.*'s model, but did not include radiation transport which Awe *et al.*'s study showed was essential. Kim *et al.* found that with these conditions the same linear parameters yielded

liner stagnation pressures approximately three orders of magnitude smaller than those reported in Awe *et al.*. However, when neither radiation nor thermal energy transport are included then Kim *et al.*'s and Awe *et al.*'s models agree reasonably well.

Davis *et al.* 2012 [19] expanded upon Awe *et al.*'s [8] simulations of an imploding liner by using the HELIOS code but adding plasma ionization/excitation effects to the simulations in addition to both the previously studied radiative and thermal effects. Davis *et al.* did this through use of a detailed tabular EOS model instead of the polytropic EOS model used in Awe *et al.*. For the same liner parameters used in Awe *et al.*, Davis *et al.* found similar scaling of liner peak pressure with initial density $P_{\text{stag}} \sim n_0^{1/2}$, specifically $P_{\text{stag}} \sim n_0^{0.64\pm0.14}$, to Awe *et al.*'s $P_{\text{stag}} \sim n_0^{0.54\pm0.02}$. The additional of thermal and radiative effects already showed depression of the pressure with scaling with liner velocity, from an ideal $P_{\text{stag}} \sim v_0^5$ to $P_{\text{stag}} \sim v_0^{15/4}$ ($P_{\text{stag}} \sim v_0^{3.71\pm0.08}$). Ionization/excitation effects further depress the scaling to $P_{\text{stag}} \sim v_0^{2.91\pm0.30}$. This does result in lowering of liner stagnation pressures by a factor of $\approx$ 4–9, but for jet parameters of $n_i = 10^{17}$ cm^{-3}, $v_j = 50$ km/s and an injected mass of 8 mg, peak pressures of 0.1–1 Mbar should still be possible. Davis *et al.* also did an atomic species study and found that the highest simulation stagnation pressures occurred for the highest-Z liner materials.

All the previously cited theoretical studies assumed a pre-formed plasma liner so they did not contain residual effects from the jet-merging/liner-formation process. The models were also all 0D or 1D and thus neglected 3D effects present in the actual PLX experiment. Cassibry *et al.* [14] conducted some 3D smooth-particle hydrodynamic (SPH) simulations using both pre-formed symmetric liners and 30 discrete jets. The goal of the simulations was to benchmark the 3D results against the 1D results, and to study the effects of jet merging on liner performance. Both the symmetric liner and 30-jet cases showed consistent P_{stag} results with Awe *et al.*'s 1D

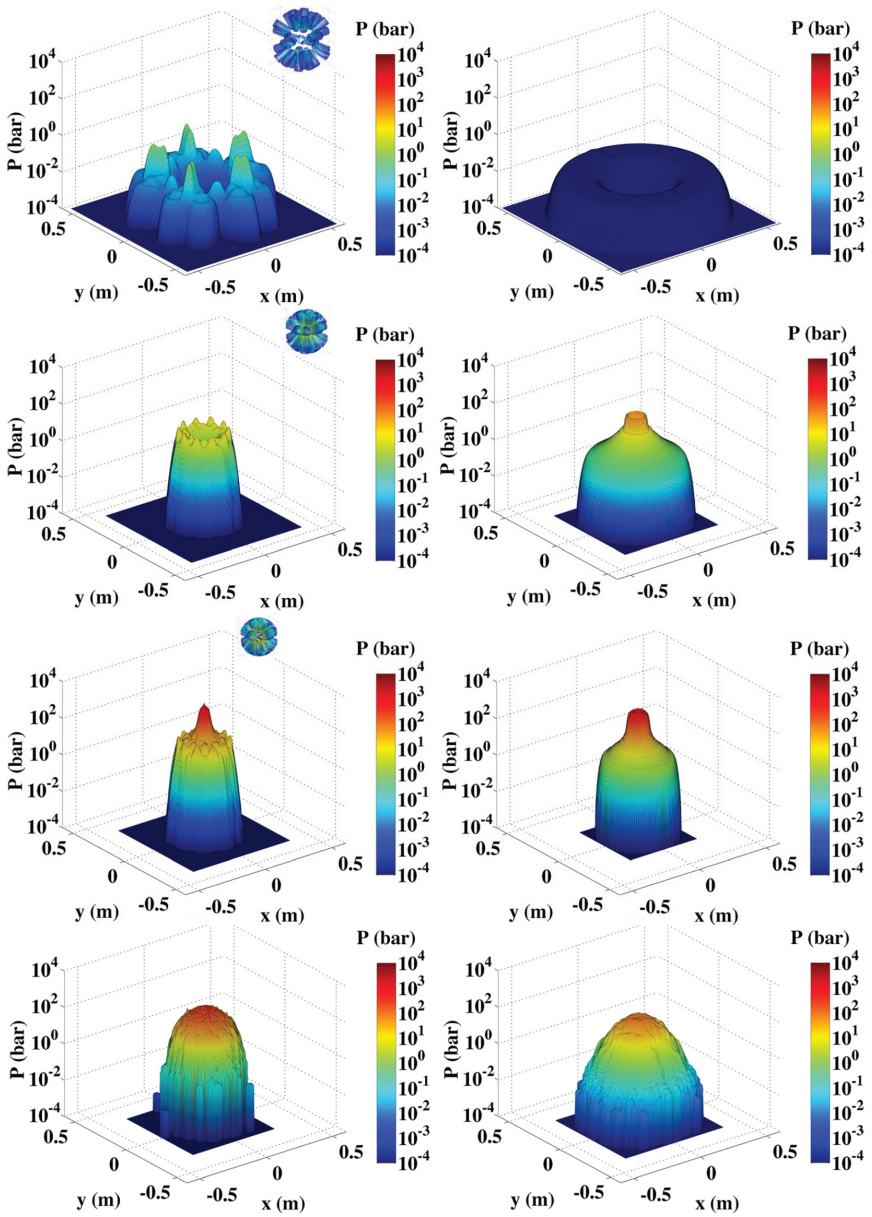

Figure 1.4: SPH model results excerpted from Cassibry *et al.* 2012 [14]. Pressure contours in the x-y plane for the 30-jet case (left column) and symmetric liner (right column). Results taken at different times and z-plane positions. Values for each row beginning at the top are $t = 0$ μs and $z = 0.2$ m, $t = 3.6$ μs and $z = 0.0$ m, $t = 4.8$ μs and $z = 0.0$ m, and $t = 8.0$ μs and $z = 0.0$ m.

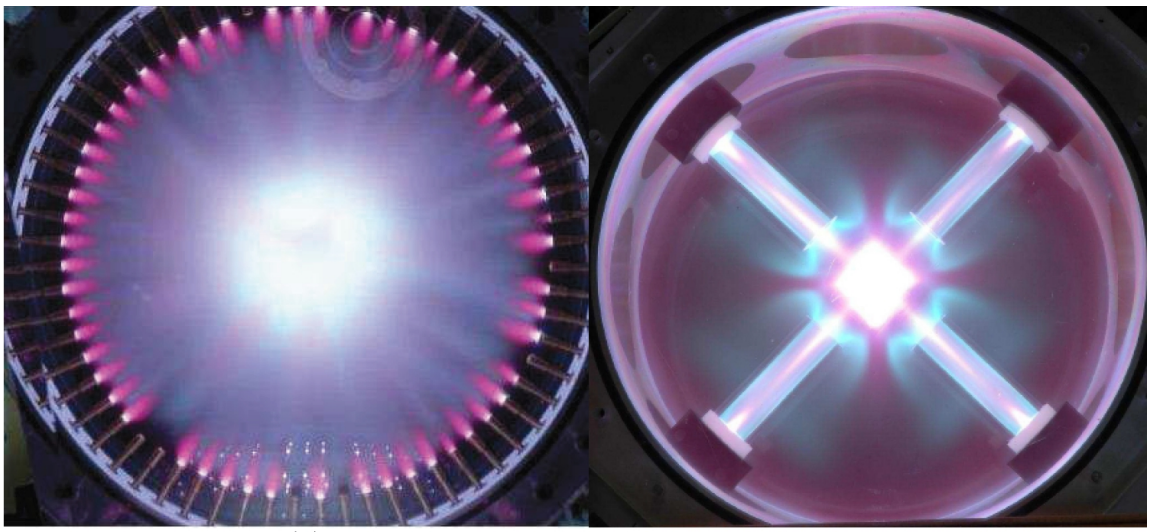

Figure 1.5: HyperV Technologies merging experiments. (a) TwoPi experiments using 64 jets from low-energy capillary discharges. Figure excerpted from [38]. (b) QuadJet experiment using four higher-energy Minirailguns. Figure excerpted from [63].

RAVEN and HELIOS results for the 30-jet, $n_i = 10^{16}$ cm^{-3} and $v_0 = 50$ km/s case. A comparison of the pressure evolution with time for the 30-jet and symmetric liner cases, as shown in Fig. 1.4 [14], shows good agreement between the evolutions and suggests that jet merging does not necessarily compromise liner performance. The simulations also suggested that liner formation was robust to the Rayleigh-Taylor instabilities that may develop during liner formation and implosion on vacuum.

Several previous cylindrical geometry jet-merging experiments also show good results for the formation of symmetric, cylindrically-converging plasma from arrays of discrete jets. In 1999 a group at Kirtland Air Force Research Laboratory (ARFL) did cylindrical-merging experiments with 12- and 24-gun arrays.[20] More recently HyperV Technologies has done cylindrical-merging experiments with an array of 64 capillary guns on their TwoPi test fixture (Fig. 1.5(a)),[65] as well as four-jet merging experiments using higher-energy Minirailguns on their QuadJet experiment

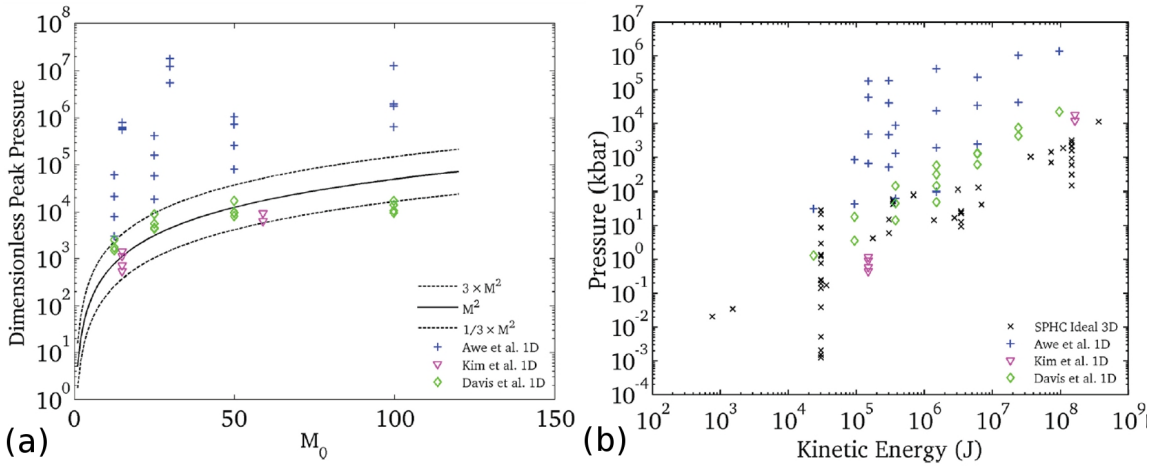

Figure 1.6: Comparisons of simulation results from Awe *et al.* [8], Davis *et al.* [19], Kim *et al.* [34] and Cassibry *et al.* [15]. Plots of pressure scaling with (a) Mach number and (b) kinetic energy are excerpted from Cassibry *et al.*.

(Fig. 1.5(b)).[38, 63] The capillary guns are supersonic with a performance of $M \sim 1$ while the Minirailguns are highly-supersonic with performances of $M \approx 30$. Wu *et al.* [38] at HyperV recently performed merging-jet simulations using the 3D hybrid particle-in-cell (PIC) code LSP for the cases of four and 16 cylindrically merging jets with Minirailgun parameters. The jets were assumed to have QuadJet and PLX relevant initial conditions of $n_i = 10^{17}$ cm^{-3} and $v_0 = 80$ km/s for a number of high- and low-Z gases. Wu *et al.* also predicts that high-Z gases will lead to higher liner pressures and performance. Though Wu *et al.*'s simulations used off-axes instead of on-axis jet injection, the results still show a strong tendency of the jets to merge into a cylindrical plasma.

Cassibry *et al.* [15] later extended their SPH simulations to systematic 3D scaling study of liner parameters. These SPH simulations do not include non-ideal effects such as ionization and radiative/thermal energy transport, but there are plans to include them in future simulations. The 3D results found that peak thermal pressure P scales linearly with initial jet density $P \sim n_i$, linearly with jet Mach number

$P \sim M$, and quadratically with initial jet velocity $P \sim v_0^2$ as well as finding that P scales linearly with the number of jets and inversely with initial jet length. Cassibry *et al.* predicts that to design liners for high peak pressures, the jets should again have high Mach number and high total initial kinetic energy but also small initial liner thickness. Figure 1.6 shows a comparison of simulation results from Awe *et al.* [8], Davis *et al.* [19], Kim *et al.* [34] and Cassibry *et al.* [15].

Overall, the variety of models and predictions cover a wide range of potential outcomes for achievable liner peak pressures depending on the different physical processes they include, such as ionization/excitation and radiation/thermal energy transport. This indicates that in addition to having the potential to form HED- and MIF-relevant plasma liners, the PLX experiments should be rich in a variety of physics and can serve to help establish the importance of different processes and benchmark simulations in this plasma regime.

		radiative & thermal transport	ionization & excitation effects	$P_{\text{stag}} \sim$		
RAVEN [8]	1D	X		$v_0^{15/4}$	$n_0^{1/2}$	$M^{3/2}$
HELIOS [19]	1D	X	X	$v_0^{2.91\pm0.30}$	$n_0^{1/2}$	
SPH [15]	3D			v_0^2	n_0	M

Table 1.1: Summary of simulation results for scaling studies of liner peak pressures.

1.1.1 Jet Propagation and Merging

Simulations show that plasma liner performance is dependant on liner density, velocity, temperature and Mach number. Thus, to design a HED- or MIF-relevant liner experiment it is imperative that we first investigate how the initial plasma jet parameters evolve during the propagation interval between jet injection and jet merging/liner formation. For example, if a jet density of $n \sim 10^{16}$ cm^{-3} at jet merging is

required for achieving ~ 1 Mbar peak liner pressures, then we must know how the jet density decreases during jet propagation to determine the appropriate initial jet density at the railgun nozzle. Hydrodynamic theory predicts a factor of $\sim 10^1$–10^2 (detailed in Sec. 4.6) drop in density during jet propagation from the railgun nozzle to the merging radius, where the merging radius is defined as the distance from the railgun nozzle that the jets are expected to merge for liner formation. So to meet the example jet density of $n \sim 10^{16}$ cm^{-3} at the merging radius, the railguns would have to be capable of producing jets with an initial density of either $n \sim 10^{17}$ cm^{-3} or $n \sim 10^{18}$ cm^{-3} depending on the expansion. In addition to setting the railgun performance, determining the initial jet density also sets the required jet injection energy (KE) and thus system power requirements. A similar argument can be made about the importance of understanding the jet cooling and jet acceleration/deceleration dynamics to determine the initial requirements on jet temperature and velocity.

As is suggested by the large uncertainty in the theoretical hydrodynamic density decrease, predicting the jet parameter evolution is not a simple problem. While pulsed plasma guns are a well established field, the bulk of plasma gun research has been focused on either the development of the gun design itself and the thrust and efficiency performance of the gun,[44, 2] with little research focused on the plasma dynamics after jet ejection. Thus, we focus the first stage of our experiments on measurements of a single railgun-generated jet during propagation away from the gun.

In addition to depending on the jet conditions before merging, initial liner parameters also depend on the plasma evolution during jet merging. Since the jets for liner formation are supersonic, hydrodynamic theory [37, 21] and simulation [14, 40, 61, 38] predict oblique shock formation when the jets merge, as shown in Fig. 1.7. In the case of shock formation, hydrodynamic theory predicts increases in density and temperature across the shock boundary and a decrease in jet velocity. Thus, the liner

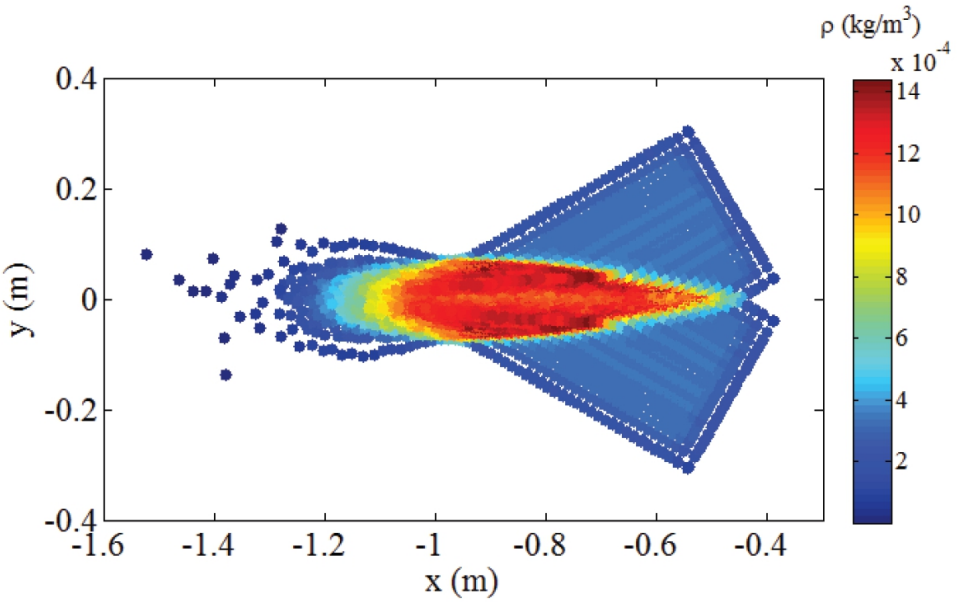

Figure 1.7: Excerpted from [61]. A two-dimensional density slice of a three-dimensional SPH simulation of two jets merging at 30°. Density jumps coinciding to oblique shock boundaries are visible.

should be denser but with a lower Mach number than the individual jets. The exact balance of the density increase to Mach number decrease, and thus liner peak pressure performance, is complicated to predict. Plasma shock formation, as compared to hydrodynamic shock formation, has the added complications of potential kinetic effects, such as interpenetration which can affect the density dynamics, and potential atomic effects, such as plasma ionization which affects the liner Mach number. Thus, whether shocks form and the physics of the potential shocks will play a large role in dictating the initial liner parameters.

Instability formation during jet merging is a potential concern for liner formation since instabilities may disrupt final liner uniformity and decrease achievable peak pressures. Since jet merging could result in density and velocity discontinuities at the merging interface, the system may be prone to Rayleigh-Taylor instabilities as well as

Kelvin-Helmholtz and other streaming instabilities. Neither two-dimensional hybrid particle-on-cell (PIC) Large Plasma Simulation (LSP) [38] nor three-dimensional SPH [61] modeling of two-jet oblique merging in the PLX plasma-jet regime seemed to predict significant instability formation. This may be because the predicted jet-merging time interval is small compared to theoretical instability growth times.[3] However, in merging experiments it is probable that asymmetries between the jets will be present and may lead to greater likelihood of instability formation at the jet-merging interface.

Thus, the second stage of our experiments will be to obliquely merge two railgun-generated plasma jets in order to examine the relationship of post-merge parameters to pre-merge parameters. Specifically, our experiments will focus on density changes in the system during jet merging as well as determining whether or not jet-merging dynamics are consistent with the predicted shock formation. Jet-merging experiments will also attempt to determine whether or not instabilities are present during merging, but that is beyond the scope of this dissertation and left for future work.

1.2 Dissertation Overview

This dissertation is organized to follow the timeline of the completed PLX experiments. Chapter 2 discusses the PLX experimental setup including the railgun equipment and some diagnostic details. Chapter 3 covers the details and development of both the equipment and the phase analysis for the PLX multi-chord visible interferometer. We then proceed to discuss the results of single-jet propagation experiments in Chap. 4. PLX did complete a series of two-jet oblique-merging experiments, the results of which are reported in Chap. 5. Finally, we will discuss potential future experiments in the interest of both basic science and liner formation on PLX.

Chapter 2

PLX Experimental Overview

The end design objective of PLX is to form imploding plasma liners, imploding on either vacuum or stationary solid targets, capable of reaching peak stagnation pressures of 0.1–1 Mbar using 30 argon plasma jets created and accelerated by HyperV Technologies Minirailguns, as shown in Fig. 1.1. As previously stated, the Minirailguns are capable of producing jets with ion density $n_i \sim 10^{17}$ cm^{-3}, $v_j \approx 50$ km/s and injected mass ≈ 8 mg at the gun nozzle.[8, 62, 25] PLX's original plan to pursue this objective involved a three-stage experimental program. The first stage would study the evolutions of a single plasma jet during propagation. The second stage would study the merging dynamics of two to five plasma jets, and the third and final stage would attempt actual liner formation using a full 30 jets.

2.1 Experimental Setup

PLX experiments take place in a 9 ft (2.7 m) diameter stainless steel spherical vacuum chamber, as shown in in Fig. 2.1. The chamber has 70 ports, 60 of which are 'small' ports with 11 in. (27.9 cm) outer diameters and 7.75 in. (19.7 cm) inner diameters.

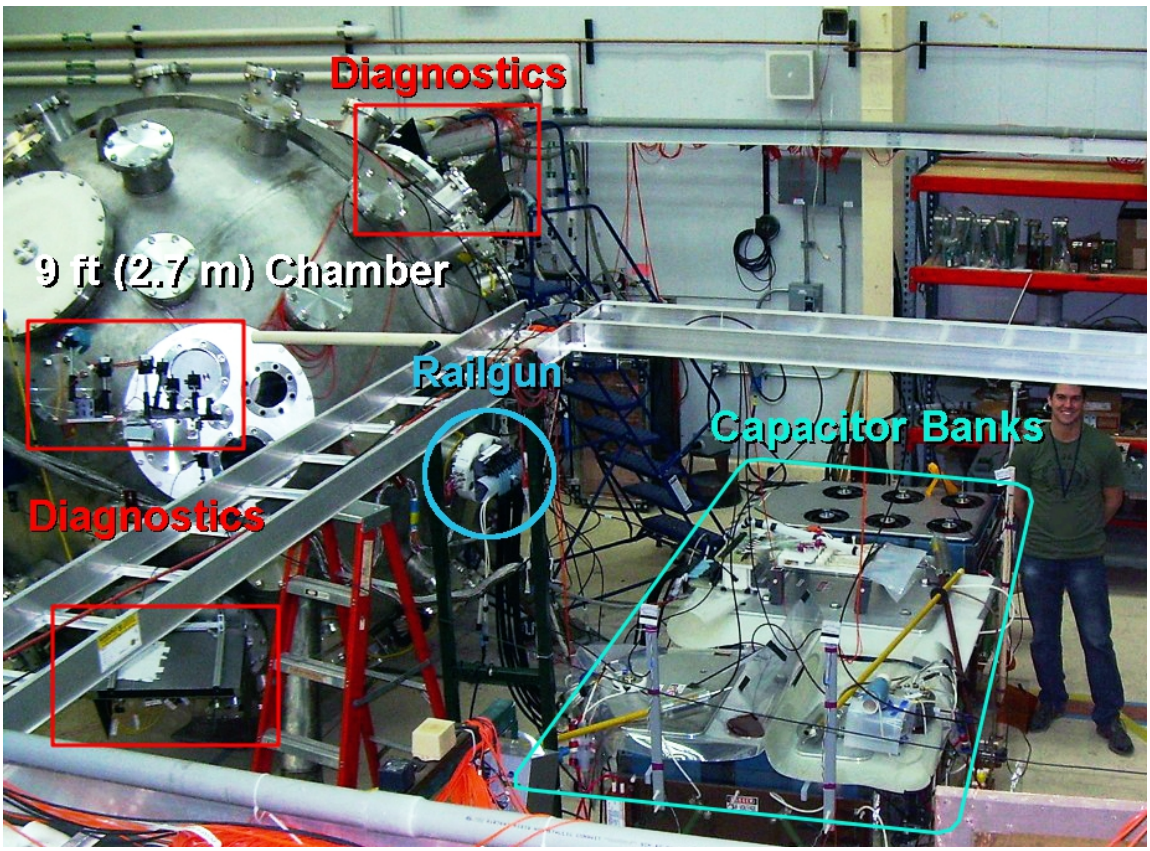

Figure 2.1: Photograph of the PLX setup with one HyperV railgun installed with railgun, capacitor banks and diagnostics positions indicated.

The small ports are situated in a Buckyball configuration and can be used either for railgun or diagnostic mounts. Ultimately 30 (half) of the small ports are intended as railgun mounts during liner-formation experiments. The remaining ten ports are 'large' ports with 29.5 in. (74.9 cm) outer diameters and 23.5 in. (59.7 cm) inner diameters and are used primarily for diagnostics. Two flange designs were developed for the PLX large ports, as shown in Fig. 2.2. One design includes a 22.45 in. (57.0 cm) by 7.80 in. (19.8 cm) port for a 1 in. (2.54 cm) thick borosilicate window intended to maximize volume of the chamber the diagnostics are capable of viewing. The other flange design includes two 7.75 in. (19.7 cm) window ports with bolt

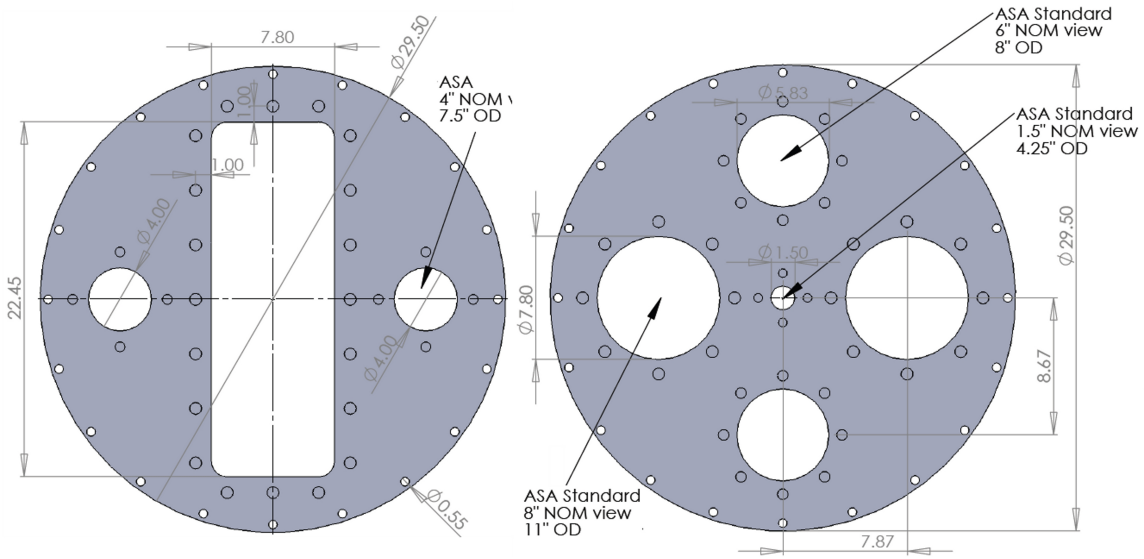

Figure 2.2: Flanges designed for the PLX experiment.

placement positions that mimic the small chamber port. This is meant to allow easy repositioning of any diagnostics from the small ports onto the large flanges or vice versa. The designs include 20 perimeter bolt-holes for securing the flanges to the chamber port; this allows the flanges to be rotated in increments of 18° to adjust the desired viewing area of the windows.

The PLX diagnostic suite was originally designed with jet-merging and liner-formation experiments in mind. As such, we placed high importance on maintaining jet/liner symmetry and choosing diagnostics that would not introduce perturbations into the jet flow. This effectively limited the diagnostics to light-based measurements instead of other methods, such as probes. The diagnostics suite was also designed to be built in several phases corresponding to the plasma parameters expected in each experiment stage. Ultimately the diagnostics suite is planned to include multi-chord visible interferometry, visible and vacuum ultraviolet spectroscopy, fast visible imaging, fast-diode array imaging, Schlieren imaging, pressure sensors and bolometry.[41]

Diagnostics currently installed on PLX are discussed in Sec. 2.3. Currently only two railguns are installed on PLX.

2.2 Railgun Operation

The HyperV Minirailguns operate in a three step process: neutral gas injection, plasma ionization, and plasma acceleration. The railgun model used for all presented PLX experiments has a corresponding three-part structure as shown in Fig. 2.3: a fast gas valve (GV), a set of ring electrodes, and the metal rails. The fast gas valve consists of a lightweight aluminum flyer plate that is electromagnetically driven by a high-voltage (HV) pulse through a double solenoid. A high-pressure gas line containing neutral argon is connected to the outside of the GV. When the GV is open for ≈ 100 μs, it can allow up to 35 mg of argon to be injected moving at an injection velocity of ~ 2 km/s.[64, 26] In the time the GV is open, the injected gas moves between the two pre-ionizer (PI) electrodes. Once the gas valve is closed, a HV is applied across the PI electrodes, which results in sub-μs current discharge between the electrodes and breaks down the neutral argon into a several eV plasma. The plasma proceeds to propagate into the space between the rails in the bore of the gun.

A HV difference, between 20–30 kV, is then applied across the gun rails. The plasma in the bore serves as a conducting path between the rails allowing 250–300 kA of current to flow from one rail to the other through the plasma. In a simple model, the current flow in the rails creates a magnetic field in the bore. The current through the plasma is transverse to the magnetic field from the rails and thus experiences a $J \times B$ force directed down the gun bore. This $J \times B$ force accelerates the plasma until the plasma jet exits the bore.

An individual railgun is ≈ 60 cm long and after mounting protrudes ≈ 23.3 cm

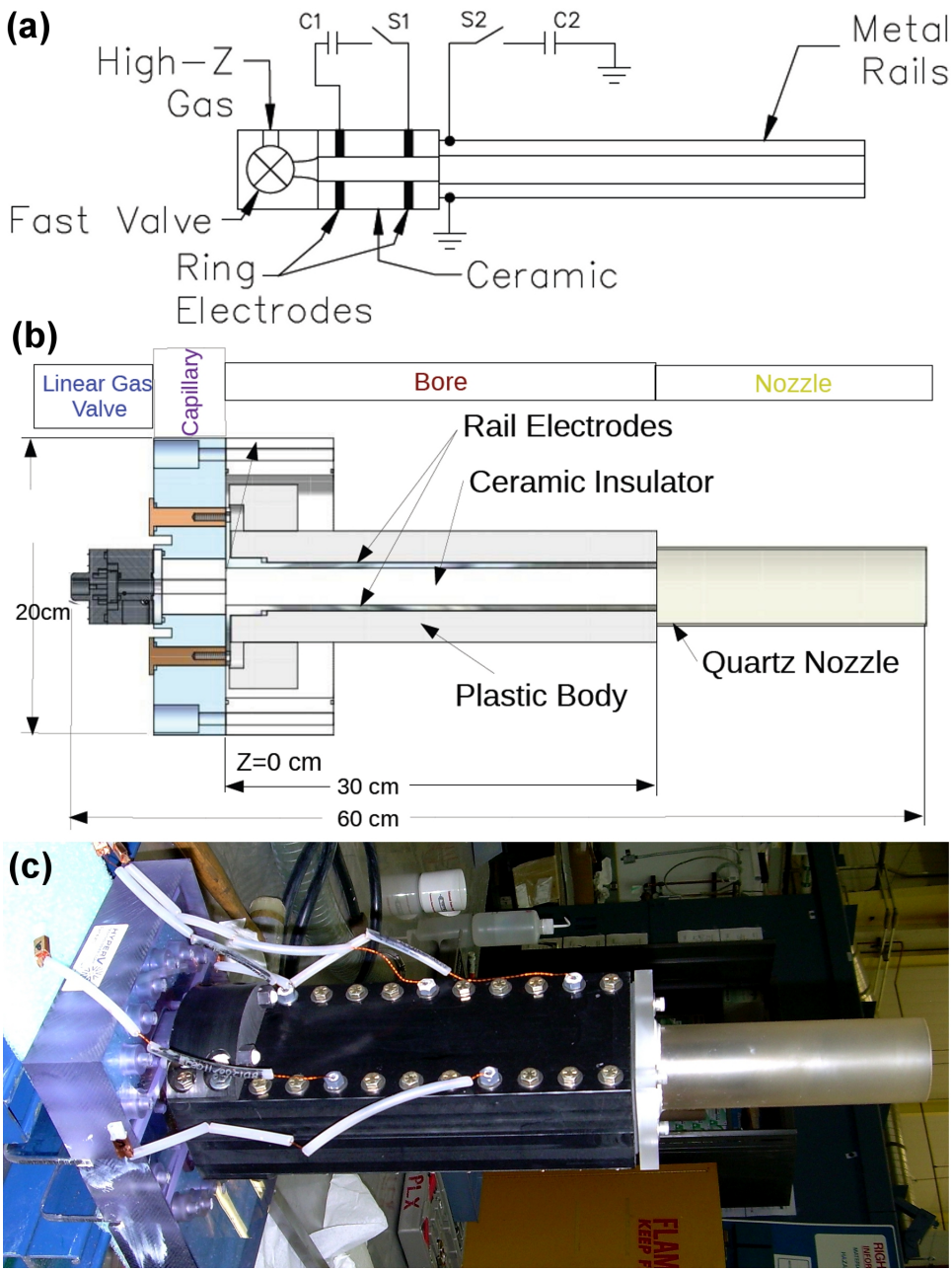

Figure 2.3: (a) Electrical diagram, excerpted from [63], (b) CAD schematic, excerpted from [64], and (c) photograph of a HyperV Minirailgun. The photograph is of the original railgun used on PLX.

into the vacuum chamber. The railgun body is composed of Noryl, a blend of polyphenylene oxide and polystyrene. The gun bore is a Noryl clamshell surrounding tungsten alloy rails and zirconium toughened alumina (ZTA) insulators between the rails. Early experiments used Delrin (polyoxymethylene) insulators, but those were found to ablate easily and introduced a high percent ($> 90\%$) of impurities into the plasma jet. All jet parameter/evolution and merging results presented here use the ZTA insulators. At the end of the railgun bore is an acrylic nozzle with a 19 cm length and 5 cm diameter.

Since the railguns require three separate HV pulses, an individual gun requires connections to three different HV capacitor banks: a 36 μF and 20–30 kV gun (rail) bank, a 6 μF and 20 kV PI bank, and a 24 μF and 8 kV GV bank.[26] The capacitor banks are fired in sequence with the GV fired $\sim$ 300 μs before the main rails and the PI fired at $\sim$ 30 μs before the rails. For the rest of the dissertation, we define $t = 0$ as the time the main rails are fired. Both the voltage of the capacitor banks and their relative trigger times can be adjusted to change jet performance, but a full investigation of those parameters is left for other studies.

	Gun	PI	GV
Bank Voltage	-24 kV	20 kV	8 kV
Trigger Time	0 μs	-30 μs	-300 μs
$I_{\text{peak}} \approx$	270 kA	7 kA	7 kA
$V_{\text{peak}} \approx$	15 kV	1 kV	7.5 kV

Table 2.1: Railgun/pulsed power system parameters for shot 744.

The railgun and pulsed-power system include a variety of diagnostics to monitor the railgun performance during an experimental shot. The diagnostics include Rogowski coils (for monitoring discharge currents) and Pearson model 2877 current monitors on parallel resistors (for monitoring bank voltages) attached to all three capacitor banks. Figure 2.4(a) & (b) show discharge current and voltage traces for

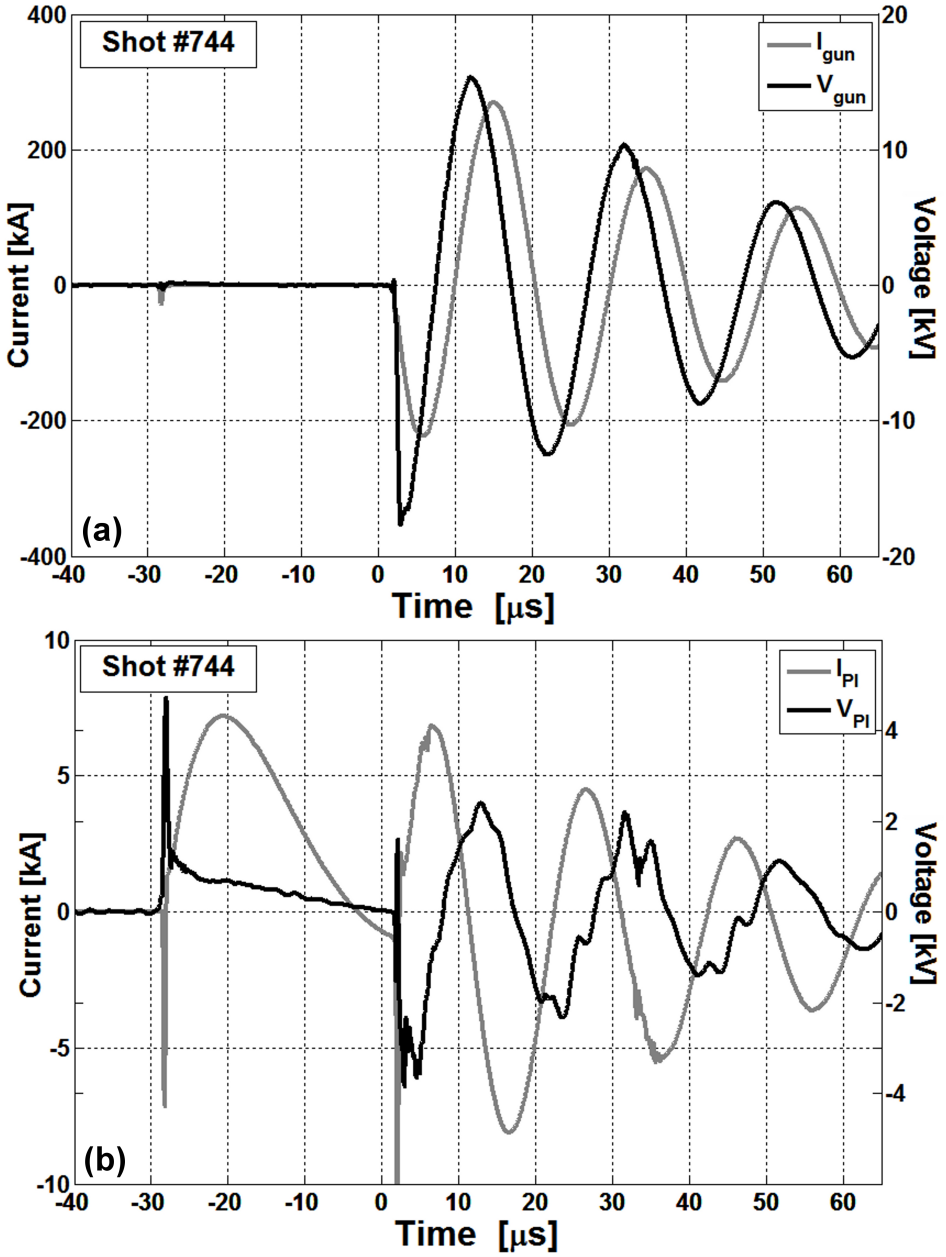

Figure 2.4: (a) I_{gun} and V_{gun} and (b) I_{PI} and V_{PI} vs. time for single-gun shot 744. The main gun bank trigger is defined as $t = 0$ μs and the PI bank is triggered at $t = -30$ μs. Both banks show current/voltage ringing for times $t > 0$ μs.

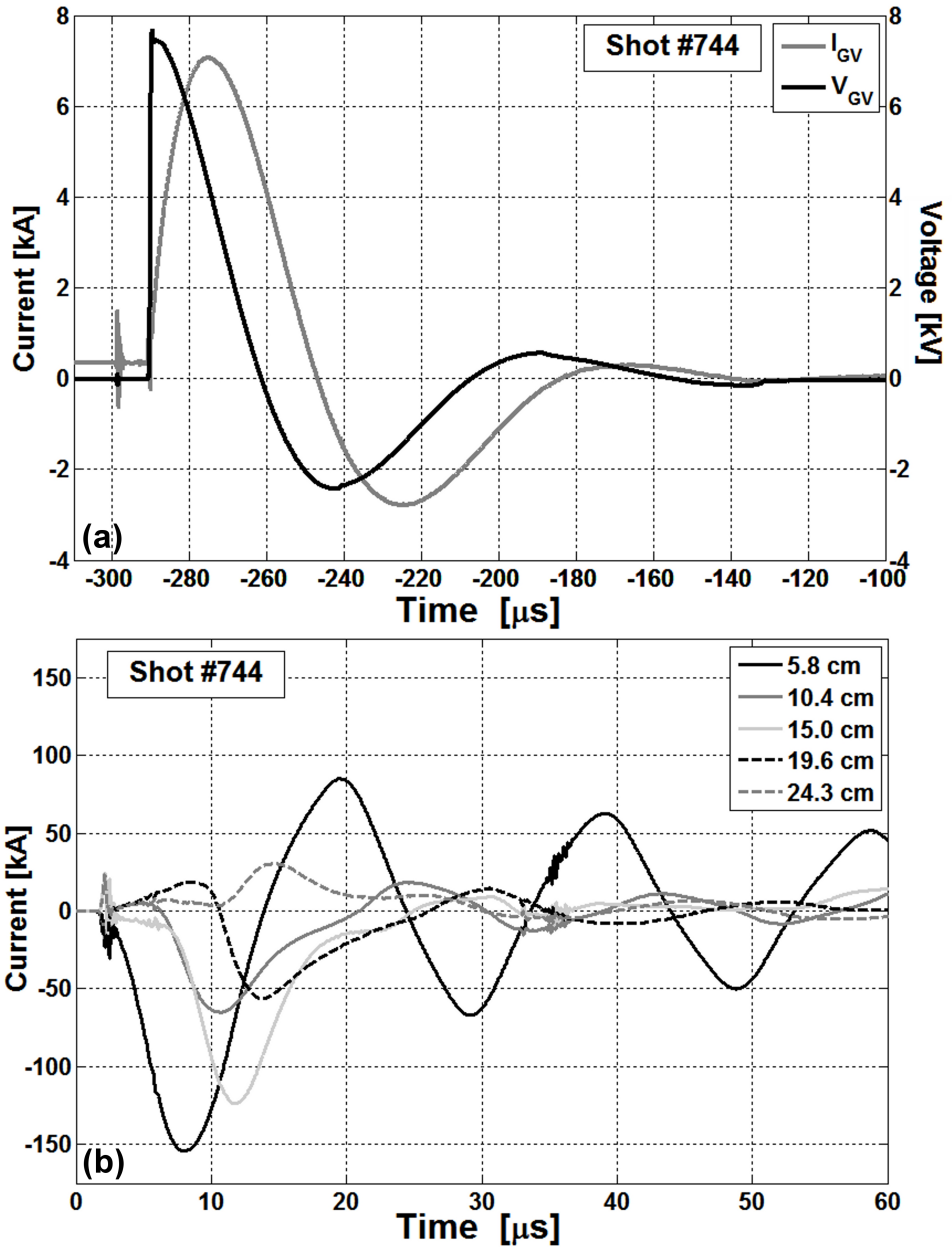

Figure 2.5: (a) I_{GV} and V_{GV} vs. time for single-gun shot 744. The GV bank is triggered at $t = -300$ μs. (b) Bdot probe current measurements vs. time for all five probe positions in the gun bore. Bdot distances are given in reference to the base of the gun bore, near the plasma injection capillary (Fig. 2.3(b)).

a typical single-gun shot (shot 744), for the gun and PI banks respectively. Figure 2.5(a) shows discharge and voltage traces for the GV bank during the same single-gun shot. The railgun diagnostics also include five magnetic probe coils along the railgun bore for monitoring electrical current propagation down the bore. Figure 2.5(b) shows measurements of the current in the bore from all five magnetic probes. Both PI and gun traces show a decaying sinusoidal current/voltage, which is referred to as ringing, for $t > 0$ μs. Modifications can be made to the HV banks to limit, or crowbar, the currents in the system so only the first current discharge occurs, as discussed in more detail in Sec. 4.2. Table 2.1 gives the railgun/pulsed-power system settings for shot 744, which is used as the example 'typical' single-gun shot for most of this dissertation.

2.3 Diagnostics

The existing diagnostic suite for PLX includes the eight-chord interferometer, a visible and near-infrared (IR) survey spectrometer, an array of three photodiode detectors, and an intensified CCD (charge-coupled device) imaging camera. The photodiode array was originally built and field by Joshua Davis. The survey spectrometer system was implemented by Thomas Awe and Jacob Schwartz, initially operated by Thomas Awe and most recently by Auna Moser. All diagnostics use line-of-sight measurements, thus all measurements are averaged quantities over their viewing chords.

The photodiode array is a velocity diagnostic for single-jet studies that is composed of three channels, where each channel is positioned to collect broadband emission from the jet at three different Z positions. Each channel consists of an adjustable aperture to limit the photodiode field-of-view (to nominally < 1 cm) and increase spatial resolution and a collimating lens to direct the light into a silica multi-mode

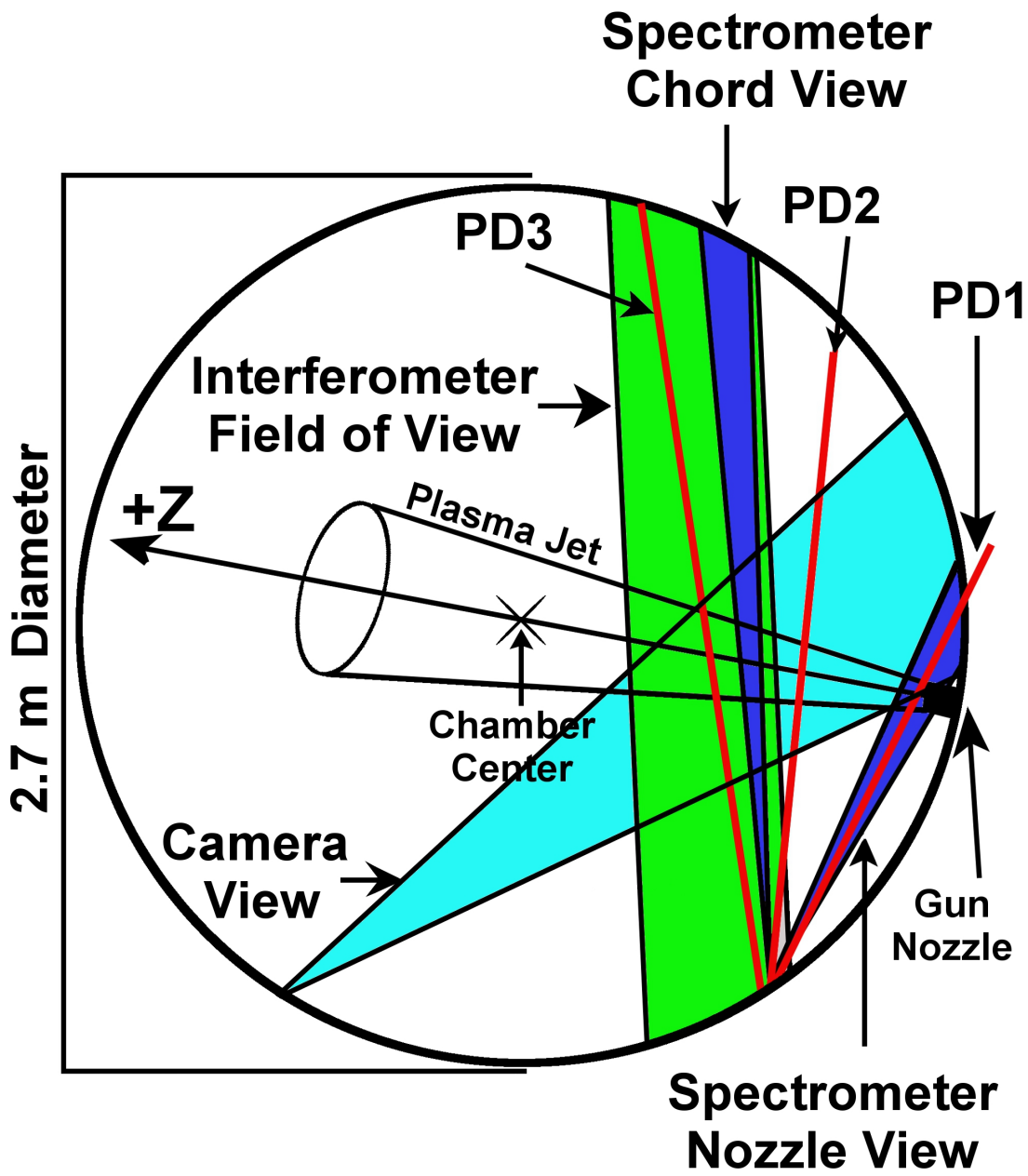

Figure 2.6: Schematic of diagnostic positions, for single-jet experiments, for the three photo-diode (PD) array (red), survey spectrometer (dark blue), interferometer chord range (green), and fast-framing CCD camera field-of-view (light blue).

fiber which transmits the light to an amplified silicon photodiode (Thorlabs PDA36A) with variable gain and a wavelength response range of approximately 300-850 nm. The peak responsivity of the photodiodes is 0.65 A/W at 970 nm but the quoted frequency response decreases with increasing gain. For the experiments in this dissertation, the channels at Z = 2.7, 27.7, and 52.7 cm (discussed in Sec. 4.1) had gain settings of 20, 50, and 50 dB, respectively, corresponding to quoted bandwidths of 2.1, 0.1, and 0.1 MHz.[26] However, we note that the observed rise times for the second and third channels are much faster than the quoted 0.1MHz bandwidth would dictate, as shown in Sec. 4.3.1.[26] The velocity is calculated by dividing the distance between the photodiode viewing positions by the difference in arrival times of the peak in the emission signal. We use the arrival time of the peak signal rather than the leading edge to obtain a more accurate estimate of the bulk jet velocity.

The CCD camera is a DiCam Pro ICCD with a sensitivity range from the UV to the near-IR; further camera specifications are given in [26]. All CCD image results are for unfiltered emission over the full sensitivity range. The CCD camera records one frame per shot with an exposure time of 20 ns. The front lens of the CCD camera can be swapped out to adjust the field-of-view of the camera for different experimental stages. We generally attempt to set the CCD field-of-view to encompass as much of the area with emitting plasma as possible, as well as to encompass as many of the other diagnostic positions for comparison purposes.

Spectroscopy supplies estimates of the electron temperature T_e based on the presence of ionization lines in the spectra in comparison to non-local-thermodynamic-equilibrium (non-LTE) PrismSPECT spectra,[42] and electron density n_e via Stark broadening of the impurity hydrogen H_β line (486.1 nm). The survey spectrometer is an 0.275 m Acton Research Corp. SpectraPro 275 with a gated 1024-pixel multi-channel-plate array (EG&G Parc 1420). For these results, we use a 600 line/mm grating giving us a resolution of 0.152 nm/pixel. All spectral results presented are

taken in the 430-520 nm spectral range. Further details of the spectrometer setup can be found in [26].

We use interferometry, in conjunction with spectroscopy, to estimate the density of the plasma. The interferometer is sensitive to ions and neutrals atoms as well as electrons, and thus the phase measurement from the interferometer requires a secondary measurement of the plasma ionization to resolve the total atomic density, n_{tot}. The phase analysis is discussed in detail in Chap. 3, as well as the equipment specifications for the interferometer. The spectrometer supplies the ionization fraction measurements for the density analysis by again comparing the experimental spectra to PrismSPECT predictions. However, to estimate the ionization fraction requires an initial n_e estimate, while n_e calculations require an estimate of the ionization fraction. Thus estimating n_e and the ionization fraction for the system is a feedback process, where estimates of n_e and ionization fraction are iterated until they begin to converge on a solution. Initial n_e estimates can be found using Stark broadening of the impurity hydrogen H_β line, while interferometer measurements are used when available in subsequent iterations to estimate n_e.

2.4 Additional Equipment Information

Chapter 3 covers a discussion of the interferometer equipment and analysis since the interferometer development and results are a primary focus of this dissertation. The specific details of the railgun and diagnostic positions used during each discussed experimental stage will be covered their respective chapters: single-jet experiments in Chap. 4 and jet-merging experiments in Chap. 5. Additional details on the PLX experimental setup are also available in [26].

Chapter 3

Theory, Design, and Implementation of the PLX Interferometer

Density measurements were paramount to achieving the objectives of characterizing single-jet propagation and two-jet merging experiments. We chose to design and build a multi-chord interferometer to obtain these important density measurements.

An interferometer is a diagnostic instrument that measures the index of refraction of a medium using the interference properties of an electromagnetic wave from a coherent source such as a laser. PLX employs a Mach-Zehnder configuration interferometer. A simple Mach-Zehnder interferometer (Fig. 3.1) takes a beam from a coherent source and splits it into two beams, which travel two different paths before being recombined. Since both beams are from the same coherent source, they have the same frequency and produce an interference or fringe pattern when recombined. The interference pattern is dependent on the phase difference between the two beams introduced by variations between their beam paths. It is this phase difference which

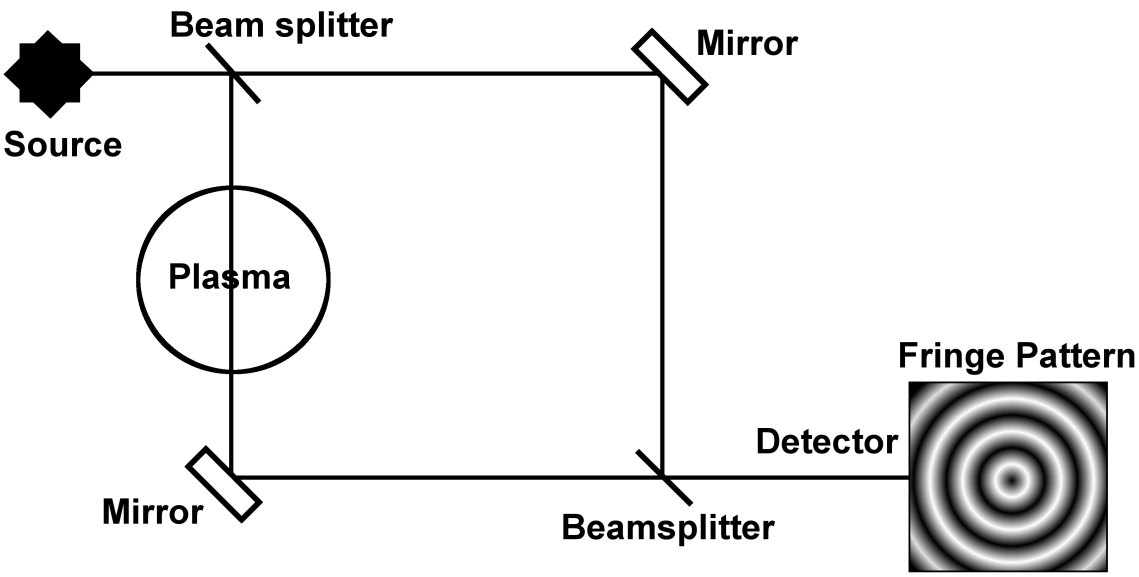

Figure 3.1: Schematic of a simple Mach-Zehnder interferometer.

can be used to measure the index of refraction of a material placed in the path of one of the beams.

3.1 Phase Shift Relation to Plasma Density and Ionization Fraction

The index of refraction of a material N is defined as the ratio of the speed of light in vacuum, c, to the phase velocity, ν_ϕ, of light in the material:

$$N = \frac{c}{\nu_\phi} = \frac{ck}{\omega} \tag{3.1}$$

where the phase velocity of an electromagnetic wave with the form $e^{i(\vec{k}\cdot\vec{r}-\omega t)}$, with frequency ω and wave vector $\vec{k}$, is defined as: [17]

$$\nu_\phi = \frac{\omega}{k}. \tag{3.2}$$

The wave traveling through a material serves as an electromagnetic perturbation, such that the refraction from the material experienced by the wave is dependent on both the frequency of the perturbing wave and the amount of material the wave propagates through. The phase change an electromagnetic wave experiences as it travels through a material is: [30]

$$\phi = \int k dl = \int N \frac{w}{c} dl. \tag{3.3}$$

Thus the phase difference generated by the presence of a plasma (gas) in the vacuum chamber is

$$\Delta\phi = \frac{\omega}{c}\int (N_{gas} - N_{vacuum}) dl = \frac{2\pi}{\lambda}\int (N_{gas} - 1) dl, \tag{3.4}$$

where λ is the wavelength of the electromagnetic wave.

In this experiment the coherent source is a visible wavelength laser. For argon plasma, electromagnetic waves in the visible light spectrum interact with both bound and free electrons. The index of refraction of a multiple-species material can be calculated as a superposition of the indices of refraction of individual species.[29] Thus, free- and bound-electrons' contribution to the index of refraction can be treated separately. Bound-electron contributions can be further separated into those bound in ions and those bound in neutral atoms, since the configuration of a species' electron shell determines the species' index of refraction.[6]

3.1.1 Free-Electron Contribution to the Phase Shift

The electron index of refraction is typically calculated by assuming visible light propagating through a fully ionized hydrogen plasma. This plasma is a two species system consisting of free electrons and protons. The perturbed system can be described by linear theory [17] such that the dependent variables of the system can be described as a superposition of an equilibrium component, denoted by the subscript "0", and a perturbed component, denoted by the subscript "1". For a plasma, the equations become:

$$\vec{v}_e = \vec{v}_{e0} + \vec{v}_{e1} \qquad \vec{E} = \vec{E}_0 + \vec{E}_1 \qquad \vec{B} = \vec{B}_0 + \vec{B}_1, \tag{3.5}$$

where $\vec{v}_e$ is the electron velocity function, $\vec{E}$ is the electric field, and $\vec{B}$ is the magnetic field. For a uniform neutral plasma at rest with no magnetic field we assume:

$$\vec{v}_{e0} = \vec{E}_0 = \vec{B}_0 = 0 \qquad \text{and} \qquad \frac{\partial \vec{v}_{e0}}{\partial t} = \frac{\partial \vec{E}_0}{\partial t} = \frac{\partial \vec{B}_0}{\partial t} = 0. \tag{3.6}$$

After linearization Maxwell's equations become:

$$\vec{\nabla} \times \vec{E}_1 = -\frac{\partial \vec{B}_1}{\partial t} \tag{3.7}$$

$$\vec{\nabla} \times \vec{B}_1 = \mu_0 \vec{J} + \epsilon_0 \mu_0 \frac{\partial \vec{E}_1}{\partial t}. \tag{3.8}$$

These equations can be combined as:

$$\begin{aligned}
\frac{\partial}{\partial t}[\vec{\nabla} \times \vec{B}_1 &= \mu_0 \vec{J} + \epsilon_0 \mu_0 \frac{\partial \vec{E}_1}{\partial t}] \\
\vec{\nabla} \times \frac{\partial \vec{B}_1}{\partial t} &= \mu_0 \frac{\partial \vec{J}}{\partial t} + \epsilon_0 \mu_0 \frac{\partial^2 \vec{E}_1}{\partial t^2} \\
-\vec{\nabla} \times (\vec{\nabla} \times \vec{E}_1) &= \mu_0 \frac{\partial \vec{J}}{\partial t} + \epsilon_0 \mu_0 \frac{\partial^2 \vec{E}_1}{\partial t^2} \\
-\vec{\nabla}(\vec{\nabla} \cdot \vec{E}_1) + \nabla^2 \vec{E}_1 &= \mu_0 \frac{\partial \vec{J}}{\partial t} + \epsilon_0 \mu_0 \frac{\partial^2 \vec{E}_1}{\partial t^2},
\end{aligned} \tag{3.9}$$

which simplifies to an expression in terms of $\vec{E}_1$ and the current $\vec{J}$. Since the plasma is assumed to be uniform, neutral and at rest, then the only currents present are a result of the perturbation. Since the perturbation is a light wave, it is of high enough frequency that only the electrons, and not the protons, respond. Thus, the current is only dependent on the electron motion:

$$\vec{J} = \vec{J}_1 = -n_e e \vec{v}_{e1}, \tag{3.10}$$

where e is the charge of an electron and n_e is the electron number density of the plasma. From the plasma fluid equation with no magnetic field and no thermal oscillations, the electron motion is related to the perturbed electric field by:

$$m_e n_e [\frac{\partial \vec{v}_{e1}}{\partial t} + (\vec{v}_{e1} \cdot \vec{\nabla})\vec{v}_{e1}] = -e n_e \vec{E}_1, \tag{3.11}$$

where m_e is the mass of an electron. Since $\vec{v}_{e1}$ is a perturbation term, it is assumed to be small enough that any $|\vec{v}_{e1}|^2$ terms are negligible. The relation between $\vec{J}$ and $\vec{E}_1$ simplifies to

$$\frac{\partial \vec{J}_1}{\partial t} = -n_e e \frac{\partial \vec{v}_{e1}}{\partial t} = \frac{n_e e^2}{m_e} \vec{E}_1. \tag{3.12}$$

Substituting this back into Maxwell's equations yields:

$$-\vec{\nabla}(\vec{\nabla} \cdot \vec{E}_1) + \nabla^2 \vec{E}_1 = \frac{\mu_0 n_e e^2}{m_e} \vec{E}_1 + \epsilon_0 \mu_0 \frac{\partial^2 \vec{E}_1}{\partial t^2}. \tag{3.13}$$

Since $\vec{E}_1$ is the electric field of a light wave, we can assume it has the planar wave form $\vec{E}_1 \propto e^{i(\vec{k} \cdot \vec{r} - \omega t)}$. Therefore, the spatial and time derivatives of $\vec{E}_1$ go as $\vec{\nabla} \rightarrow i\vec{k}$ and $\frac{\partial}{\partial t} \rightarrow -i\omega$. The differential equation then becomes:

$$\vec{k}(\vec{k} \cdot \vec{E}_1) - \vec{k}^2 \vec{E}_1 = \frac{\mu_0 n_e e^2}{m_e} \vec{E}_1 - \epsilon_0 \mu_0 \omega^2 \vec{E}_1. \tag{3.14}$$

Light is a transverse electromagnetic wave, so $\vec{k} \cdot \vec{E}_1 = 0$, and the equation becomes:

$$-k^2 \vec{E}_1 = \frac{\mu_0 n_e e^2}{m_e} \vec{E}_1 - \epsilon_0 \mu_0 \omega^2 \vec{E}_1. \tag{3.15}$$

Remembering that $c = 1/\sqrt{\mu_0 \epsilon_0}$ and that the plasma frequency is defined as $\omega_p^2 = n_e e^2 / \epsilon_0 m_e$, the expression simplifies further to:

$$\begin{aligned} -k^2 \vec{E}_1 &= (\frac{\mu_0 n_e e^2}{m_e} - \epsilon_0 \mu_0 \omega^2) \vec{E}_1 \\ \frac{c^2 k^2}{\omega^2} \vec{E}_1 &= (-\frac{n_e e^2}{\epsilon_0 m_e \omega^2} + 1) \vec{E}_1 \\ \frac{c^2 k^2}{\omega^2} \vec{E}_1 &= (1 - \frac{\omega_p^2}{\omega^2}) \vec{E}_1 \\ \frac{c^2 k^2}{\omega^2} &= (1 - \frac{\omega_p^2}{\omega^2}). \end{aligned} \tag{3.16}$$

Finally, from the definition of the index of refraction we can write:

$$N = \frac{ck}{\omega} = \sqrt{1 - \frac{n_e e^2}{\epsilon_0 m_e \omega^2}}. \tag{3.17}$$

The index of refraction of the free-electron component of a plasma is a function of both the wavelength of the laser light passing through the plasma and the electron density of the plasma. The laser wavelength is a known constant, so the index of refraction reduces to a function of the plasma electron density. From Eqn. (3.4) the electron contribution to the phase shift is:

$$\Delta\phi_e = \frac{2\pi}{\lambda} \int (\sqrt{1 - \frac{n_e e^2}{\epsilon_0 m_e \omega^2}} - 1) dl. \tag{3.18}$$

Assuming a generous experimental upper limit of $n_e < 10^{20}$ cm^{-3} and visible light, then $\frac{n_e e^2}{\epsilon_0 m_e \omega^2} << 1$. Using a Maclaurin series expansion, the phase shift reduces to:

$$\Delta\phi_e = \frac{2\pi}{\lambda} \int (1 - \frac{1}{2} \frac{n_e e^2}{\epsilon_0 m_e \omega^2} - 1) dl = \frac{-e^2 \lambda}{4\pi \epsilon_0 m_e c^2} \int n_e dl. \tag{3.19}$$

In addition to allowing us to use small number approximations, $\frac{n_e e^2}{\epsilon_0 m_e \omega^2} << 1$ also fulfills the $\omega > \omega_p$ cutoff criteria for wave propagation in a plasma. If the laser frequency is below cutoff, $\omega < \omega_p$, then the index of refraction becomes imaginary and the wave becomes evanescent, decaying exponentially with distance as it propagates through the plasma. Thus, we choose a laser frequency with $\omega \gg \omega_p$ to limit laser power attenuation due to this form of wave decay.

3.1.2 Bound-Electron Contributions to the Phase Shift

For any atomic species consisting of a nucleus surrounded by an electron cloud of bound-electrons, the index of refraction of the species is due to the interaction of the perturbative electromagnetic wave with the bound-electrons. Similar to the simple case, the nucleus of the species has enough inertia to make any interaction with the high frequency wave negligible. The index of refraction of a neutral or ionized gas species can be found using the Dale-Gladstone relation,[6]

$$K\rho = (N - 1) = \delta N, \tag{3.20}$$

where ρ is the mass density of the gas, K is the specific refractivity and $\delta N = N - 1$. The specific refractivity of the gas is determined by the element species and ionization state. For most neutral gases, the index of refraction and the density are well documented at standard temperature and pressure (STP) and can be used to calculate the specific refractivity. Thus the index of refraction of the neutral atoms in the plasma is:[6, 35]

$$\delta N_n = K m_n n_n = \frac{\delta N_n^{STP}}{n_n^{STP}} n_n. \tag{3.21}$$

The phase change due to neutral atoms in the plasma is then: [35]

$$\Delta\phi_n = \frac{2\pi}{\lambda} \frac{\delta N_n^{STP}}{n_n^{STP}} \int n_n dl. \tag{3.22}$$

Unlike neutral gases, most ionized species cannot be found at STP. Instead, their specific refractivity must either be measured directly or calculated from atomic first principles. Thus, the phase change due to ions in the plasma is simply:

$$\Delta\phi_i = \frac{2\pi}{\lambda} K_i m_i \int n_i dl. \tag{3.23}$$

3.1.3 Total Phase Shift in a Singly-Ionized Plasma

The total phase shift is a superposition of the electron, ion, and neutral atom contributions.[29] The interferometer signal analysis has been defined such that the contribution from any material with $N < 1$ will give $\Delta\phi > 0$, and materials with $N > 1$ will give $\Delta\phi < 0$. Since $N_e < 1$ and $N_i, N_n > 1$, then the total phase shift is :

$$\begin{aligned} \Delta\phi_{tot} &= |\Delta\phi_e| - |\Delta\phi_i| - |\Delta\phi_n| \\ &= \frac{\lambda e^2}{4\pi\epsilon_0 m_e c^2} \int n_e dl - \frac{2\pi}{\lambda} K_i m_i \int n_i dl - \frac{2\pi}{\lambda} \frac{\delta N_n^{STP}}{n_n^{STP}} \int n_n dl. \end{aligned} \tag{3.24}$$

Since the phase change from the ions and neutral atoms is in the opposite direction of the phase change from the electrons, using the approximation $\Delta\phi_{tot} = |\Delta\phi_e|$ can result in underestimation the actual electron density of the plasma. Also, the contribution to the phase shift from free-electrons is linearly proportional to the light wavelength, while bound-electron contributions are inversely proportional to the wavelength. This becomes important when choosing a source wavelength for a given plasma density regime.

The plasma jets are cold ($T_e \approx 1$ eV) by the time they intersect the interferometer chords, and thus the plasma is assumed to consist of only singly-ionized and neutral atoms, i.e., $n_e = n_i$. The total phase change is thus:

$$\Delta\phi_{tot} = (\frac{\lambda e^2}{4\pi\epsilon_0 m_e c^2} - \frac{2\pi}{\lambda} K_i m_i) \int n_i dl - \frac{2\pi}{\lambda} \frac{\delta N_n^{STP}}{n_n^{STP}} \int n_n dl, \tag{3.25}$$

which is a function of only the line-integrated ion and neutral densities.

3.1.4 Total Atomic Density in a Singly-Ionized Plasma

The total atomic density of the plasma is defined as the sum of the ion and neutral densities, $n_{tot} = n_i + n_n$. The interferometer is not equally sensitive to ion and neutral densities, so a second relation between n_i and n_n is required in order to determine the total phase shift in terms of total atomic density. Assuming a form for the ionization fraction,

$$f = \frac{n_i}{n_i + n_n} = \frac{n_i}{n_{tot}}, \tag{3.26}$$

fulfills this requirement. The total phase shift can now be written in terms of f and the total atomic density n_{tot}:

$$\begin{aligned} \Delta\phi_{tot} &= (\frac{\lambda e^2}{4\pi\epsilon_0 m_e c^2} - \frac{2\pi}{\lambda} K_i m_i + \frac{2\pi}{\lambda}\frac{\delta N_n^{STP}}{n_n^{STP}}) \int f n_{tot} dl \\ &\quad - \frac{2\pi}{\lambda}\frac{\delta N_n^{STP}}{n_n^{STP}} \int n_{tot} dl. \end{aligned} \tag{3.27}$$

Assuming an uniform ionization along the path of the laser through the plasma, $f \equiv f(l) =$ constant, then the phase shift simplifies to

$$\Delta\phi_{tot} = [(\frac{\lambda e^2}{4\pi\epsilon_0 m_e c^2} - \frac{2\pi}{\lambda} K_i m_i) f - \frac{2\pi}{\lambda}\frac{\delta N_n^{STP}}{n_n^{STP}}(1-f)] \int n_{tot} dl. \tag{3.28}$$

3.1.5 Adding Multiple Ionizations to Phase Shift Analysis

Previous phase analysis assumes a singly ionized plasma. Singly ionized approximations are sufficient for low temperature plasmas, $T_e \approx T_i \sim 1$ eV, as observed in our single jets experiments. In multiple jet merging experiments higher ionization states are observed and the phase analysis must be expanded. In the case that a plasma is more than singly ionized, then we can write the phase shift formula in the general

form

$$\Delta\phi_{tot} = \Delta\phi_e - \sum_j \Delta\phi_j = \int C_e n_e dl - \int \sum_j C_j n_j dl, \tag{3.29}$$

where j is the ionization state of the atom, $j = 0$ denotes a neutral particle, and C is the sensitivity of the interferometer to that atomic species. For a species with ionization state j, the electron density due to that species is $n_{e,j} = jn_j$. The total electron density is then $n_e = \sum_j n_{e,j} = \sum_j jn_j$. The average charge state of the plasma is then

$$Z_{\text{eff}} = \frac{n_e}{n_i} = \frac{\sum_j n_{e,j}}{\sum_j n_j} = \frac{\sum_j jn_j}{n_{tot}}, \tag{3.30}$$

where $n_{tot} = \sum_j n_j$ is the total atomic density of the plasma. The phase shift equation becomes

$$\begin{aligned} \Delta\phi_{tot} &= \int [C_e Z_{\text{eff}} n_{tot} - \sum_j C_j n_j] dl \\ &= \int C_e [Z_{\text{eff}} - \sum_j \frac{C_j}{C_e} \frac{n_j}{n_{tot}}] n_{tot} dl \\ &\approx C_e [Z_{\text{eff}} - Err] \int n_{tot} dl, \end{aligned} \tag{3.31}$$

assuming a uniform average charge state along the path length through the plasma, and defining and error $Err = \sum_j \frac{C_j}{C_e} \frac{n_j}{n_{tot}}$. If all the sensitivity constants for all ionization states of the plasma gas are known, then the error can be calculated explicitly. However, many indices of refraction for ionized materials, and thus their sensitivity constants, are un-measured and hard to calculate. In this case Eqn. 3.31 can limit the possible range of n_{tot} instead of calculating it explicitly. Re-writing Eqn. 3.31 gives

$$\int n_{tot} dl = \frac{\Delta\phi_{tot}}{C_e [Z_{\text{eff}} - Err]}. \tag{3.32}$$

Assuming that $Err \rightarrow 0$ maximizes the R.H.S. denominator and gives the lower bound for n_{tot}. Thus the lower bound for n_{tot} is just

$$(\int n_{tot} dl)_{min} = \frac{\Delta\phi_{tot}}{C_e Z_{\text{eff}}}. \tag{3.33}$$

To find the upper bound on n_{tot} we must find an upper bound on Err. For Argon, the higher the ionization the smaller the Slater screening constant K becomes. Since the sensitivity constant C_j is directly proportional to the Slater screen constant, $C_j = (2\pi K_j m_j)/\lambda$, the sensitivity constant also decreases with increasing ionization state. Thus, the largest sensitivity constant is for the neutral particles for Argon. This also holds true in general for other types of gases. The sensitivity constant for a given species and ionization is proportional to sum of mean square electron orbits for all bound electrons: [6]

$$C_j \propto K_j m_j = N_j - 1 \propto \sum_i (< r_i^2 >)^2, \tag{3.34}$$

where r is the electron radius. As the ionization of an atom gets higher, the number of terms contributing to the sum in Eqn. 3.34 gets smaller, and thus the sensitivity constant decreases. The upper bound on the error is then given by

$$Err = \sum_j \frac{C_j}{C_e} \frac{n_j}{n_{tot}} \leq \frac{C_0}{C_e} \sum_j \frac{n_j}{n_{tot}} = \frac{C_0}{C_e} = Err_{max}. \tag{3.35}$$

Thus the upper bound on n_{tot} is given by

$$(\int n_{tot} dl)_{max} = \frac{\Delta\phi_{tot}}{C_e[Z_{\text{eff}} - \frac{C_0}{C_e}]}. \tag{3.36}$$

3.1.6 Adding Multiple Atomic Species to Phase Shift Analysis

Merging experiments also show a large increase in impurities in the plasma. Thus, assuming a single gas species plasma is no longer sufficient. The method for accommodating multiple gas species in the phase shift analysis for the plasma is similar to the method for incorporating multiple ionizations. The total phase shift is a superposition of the phase shift contributions from each gas species, k, as well as each ionization state for a given gas species, j:

$$\begin{aligned} \Delta\phi_{tot} &= \sum_k \Delta\phi_{tot,k} = \sum_k C_e[Z_{\text{eff,k}} - Err_k] \int n_{tot,k} dl \qquad (3.37) \\ &= \int \sum_k C_e[Z_{\text{eff,k}} - \sum_j \frac{C_{j,k}}{C_e}\frac{n_{j,k}}{n_{tot,k}}] n_{tot,k} dl. \qquad (3.38) \end{aligned}$$

The average charge state of the multiple gas species plasma is defined as

$$Z_{\text{eff}} = \frac{n_e}{n_{tot}} = \frac{\sum_k n_{e,k}}{\sum_k n_{tot,k}} = \frac{\sum_k Z_{\text{eff,k}} n_{tot,k}}{\sum_k n_{tot,k}}. \qquad (3.39)$$

The phase shift is then

$$\begin{aligned} \Delta\phi_{tot} &= C_e \int [\sum_k Z_{\text{eff,k}} n_{tot,k} - (\sum_j \frac{C_{j,k}}{C_e}\frac{n_{j,k}}{n_{tot,k}}) n_{tot,k}] dl \\ &= C_e \int [Z_{\text{eff}} n_{tot} - (\sum_k \sum_j \frac{C_{j,k}}{C_e} n_{j,k})] dl \\ &\approx C_e [Z_{\text{eff}} - (\sum_k \sum_j \frac{C_{j,k}}{C_e}\frac{n_{j,k}}{n_{tot}})] \int n_{tot} dl \\ &= C_e [Z_{\text{eff}} - Err] \int n_{tot} dl, \qquad (3.40) \end{aligned}$$

where the error in this case is given by $Err = \sum_{k,j} \frac{C_{j,k}}{C_e}\frac{n_{j,k}}{n_{tot}}$. As expected, this gives the same general form for the phase shift dependence as a single gas species with

multiple ionizations only with an expanded error term. Thus, the lower bound on n_{tot} still occurs for $Err = 0$. The upper bound for n_{tot} can be found by approximating $C_j = C_{max}$, where C_{max} is the sensitivity constant largest sensitivity constant for all present gas species and ionization states. Since neutral atoms have a larger C_j than ions and $C_J \propto N_j - 1$, then $C_{max} = C_{0,k}$ for the gas species with the highest neutral particle index of refraction. Thus the upper bound on n_{tot} is given by

$$(\int n_{tot} dl)_{max} = \frac{\Delta\phi_{tot}}{C_e[Z_{\text{eff}} - \frac{C_{max}}{C_e}]}. \tag{3.41}$$

3.1.7 Comparing Densities

Since this method calculates bounds for n_{tot} rather than calculating n_{tot} explicitly, then any introduced error must be accounted for when comparing values between two data sets. If we take a ratio of the line-integrated densities between two different data sets, then we can write that as

$$\frac{\int n_{tot,2} dl}{\int n_{tot,1} dl} = \frac{\Delta\phi_2}{\Delta\phi_1} \frac{(Z_{\text{eff},1} - Err_1)}{(Z_{\text{eff},2} - Err_2)}. \tag{3.42}$$

The upper limit of this ratio occurs when $(Z_{\text{eff},1} - Err_1)$ is at maximum and $(Z_{\text{eff},2} - Err_2)$ is at minimum. Thus the upper limit is

$$(\frac{\int n_{tot,2} dl}{\int n_{tot,1} dl})_{max} = \frac{\Delta\phi_2}{\Delta\phi_1} \frac{Z_{\text{eff},1}}{(Z_{\text{eff},2} - \frac{C_{max}}{C_e})}. \tag{3.43}$$

Similarly, the ratio's lower limit occurs when $(Z_{\text{eff},1} - Err_1)$ is at minimum and $(Z_{\text{eff},2} - Err_2)$ is at maximum. Thus the lower limit is

$$(\frac{\int n_{tot,2} dl}{\int n_{tot,1} dl})_{min} = \frac{\Delta\phi_2}{\Delta\phi_1} \frac{(Z_{\text{eff},1} - \frac{C_{max}}{C_e})}{Z_{\text{eff},2}}. \tag{3.44}$$

3.2 Choosing a Laser Wavelength

PLX planned a three-stage sequence of experiments to study potential liner formation: single-jet evolution, multiple jet merging, and thirty jet liner formation. Interferometry is desired to study density dynamics over all experimental stages, thus ideally the interferometer laser wavelength should be applicable over the entire experimental density range.

Early single-jet tests of the Mark I plasma MiniRailguns, [63] performed at HyperV Technologies, indicated a plasma electron density of order $n_e \sim 10^{16}-10^{17}$ cm^{-3} and diameter of D $\approx$ 5 cm at the railgun nozzle. These parameters correspond to a line-integrated electron density of $\int n_e dl \sim 10^{17} - 10^{18}$ cm^{-2}. HyperV Technologies' used a HeNe visible interferometer with $\lambda = 632$ nm for both MiniRailgun single-jet characterization as well as coaxial plasma accelerator experiments with electron densities $n_e \sim 10^{14} - 10^{15}$cm^{-3}.[12, 63] Thus, visible light interferometry is suitable for single-jet experiments on PLX.

The interferometer wavelength for full liner formation was chosen by 2D ray-tracing simulation, which included light deflection, fringe shift, and free-free Bremsstrahlung absorption as the mechanism of attenuation. Laser chords were assumed to pass through a circularly symmetric plasma of radius 35 cm, with an exponentially-decaying radial electron density profile. This plasma is a 2D approximation of the plasma liner expected to be generated by all 30 railguns. The plasma maximum and minimum electron densities were assumed to be $n_e = 10^{19}$ cm^{-3} and $n_e = 10^{16}$ cm^{-3} respectively. An electron density only approximation is used since the simulation is only required to identify an appropriate wavelength range. The phase shift seen by the interferometer for a given wavelength λ is approximated as $\Delta\phi = |\Delta\phi_e| = \frac{e^2\lambda}{4\pi\epsilon_0 m_e c^2}\int n_e dl$.

Free-free Bremsstrahlung absorption is where a free electron in the plasma is

accelerated through the absorption of a photon as the electron is deflected by another charged particle. The photon absorption decreases the total power of the laser beam still propagating through the plasma. Since the simulation approximates the liner as an electron only plasma, photon-electron interactions are the only existing mechanism of laser attenuation, and free-free Bremsstrahlung absorption is a valid attenuation approximation.

The laser chords passed through the plasma normal to the plasma radius. The chord distance from the plasma center was varied in order to vary line-integrated density seen by the interferometer and determine the density limits for interferometer operation. The simulation found that phase shift is the limiting factor for the interferometer wavelength selection instead of attenuation of laser deflection. Line-integrated electron densities of $10^{17} - 10^{18}$ cm^{-2} (corresponding to path lengths of 10-20 cm through the plasma, for the plasma region with densities between $10^{16} - 10^{17}$ cm^{-3}) generated a phase-shift in excess of $N = 15$ fringes, where $N = 15$ is an approximate upper limit on the time-resolvable number of fringes (Fig. 3.2(a)). These values yield the same order of line integrated plasma densities as the single-jet experiments. Thus, visible interferometry should be viable for single- and several-jet density experiments as well as for the thirty-jet experiments.

PLX choose an Oxxius diode-pumped solid-state, 320 mW, $\lambda = 561$ nm laser. At the phase shift limit, a $\lambda = 561$ nm beam generated a laser deflection of $< 0.5 \times 10^{-3}$ m and a laser intensity of $> 95\%$ of the original intensity (Fig. 3.2(b)) making it suitable for full liner experiments. The laser wavelength $\lambda = 561$ is also near the HeNe wavelength of the HyperV interferometer. However, the Oxxius laser has an output power of 320 mW, which is significantly larger than the 50 mW upper limit on HeNe power. For the eight chord PLX interferometer the higher output power was desirable because it allowed higher initial power per chord and reduced concerns about plasma and equipment attenuation effects in the system.

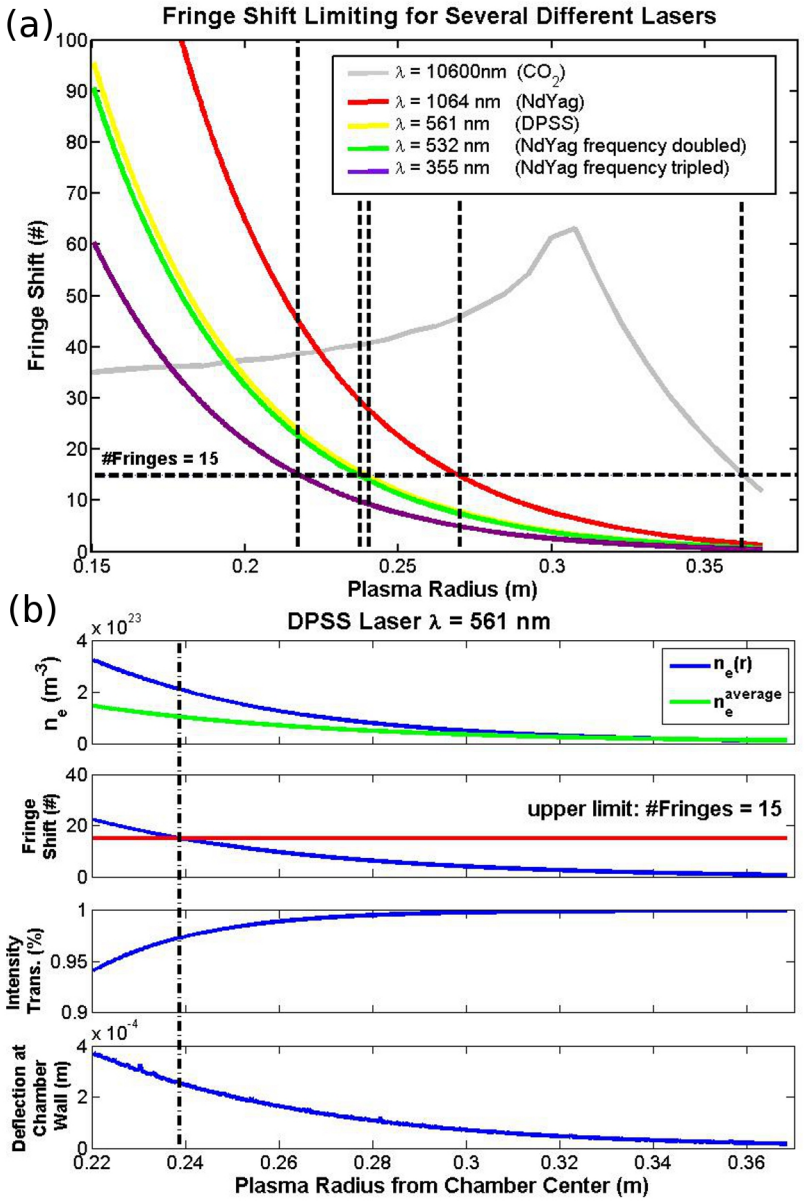

Figure 3.2: (a) A comparison of simulated fringe shift limitation results for any array of available lasers. (b) Simulated electron density, fringe shift, beam attenuation, and beam deflection vs plasma profile radius for a $\lambda = 561nm$ diode-pumped solid-state laser. Beam deflection and attenuation are minimal at the given fringe shift upper limit of 15 fringes.

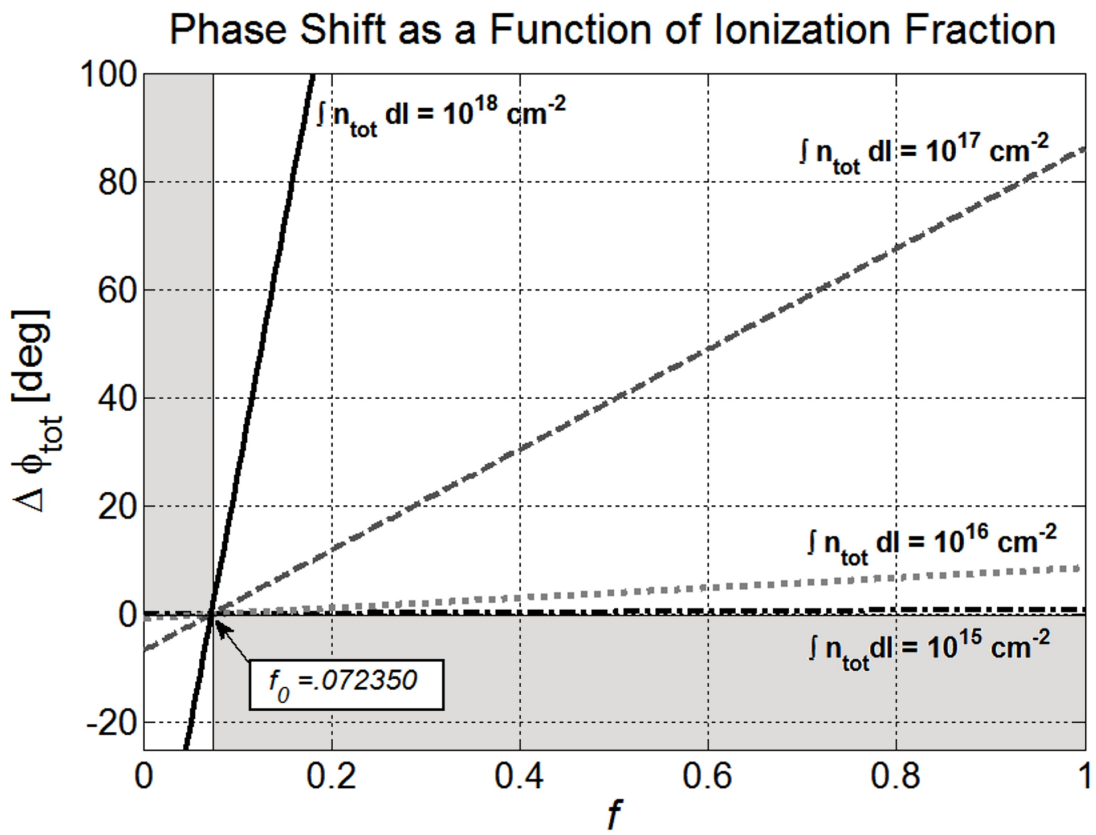

Figure 3.3: Calculated phase shift versus ionization fraction for an argon plasma at a variety of PLX-relevant atomic densities. The phase shift of $\Delta\phi_{tot} = 0$ occurs at $f_0 = 0.072350$. The gray areas are inaccessible parameters.

3.2.1 Phase Shift for a Singly-Ionized Argon Plasma and Interferometer Wavelength $\lambda = 561$ nm

Once the laser wavelength and plasma species is known, the plasma phase shift formula can be calculated. For single jet experiments, PLX uses a single-ionized argon plasma jet and a $\lambda = 561$ nm interferometer. For argon, the Slater screening constant gives a specific refractivity for singly ionized argon:[7]

$$K_{ArII} = 0.67 \times K_{ArI} = 0.67 \times \frac{\delta N_{ArI}}{m_{Ar} n_{ArI}}. \tag{3.45}$$

The phase shift from singly ionized argon is then:

$$\begin{aligned}\Delta\phi_{tot} &= [\frac{\lambda e^2}{4\pi\epsilon_0 m_e c^2} f - (1 + 0.67f - f)\frac{2\pi}{\lambda}\frac{\delta N_{ArI}^{STP}}{n_{ArI}^{STP}}] \int n_{tot} dl \\ &= 1.6204 \times 10^{-17}[f - 0.07235] \int n_{tot} dl, \end{aligned} \tag{3.46}$$

a function of only f and n_{tot}. For argon, $\Delta\phi_{tot} = 0$ occurs for $f = 0.07235$. The most general form for the phase shift is then:

$$\Delta\phi_{tot} = C[f - f_0] \int n_{tot} dl, \tag{3.47}$$

where C is a scale factor for the gas species and f_0 is the ionization fraction for which $\Delta\phi_{tot} = 0$. Figure 3.3 shows a plot of $\Delta\phi_{tot}$ versus f for a variety of $\int n_{tot} dl$ values of relevance for a single plasma jet. Since $\int n_{tot} dl$ is always positive, then $\Delta\phi > 0$ requires $f > f_0$ and $\Delta\phi < 0$ requires $f < f_0$.

3.3 Homodyne versus Heterodyne Interferometry

In homodyne interferometry the light waves from both the probe and reference paths have the same frequency ω. The electric fields for the reference- and probe-waves are written $\vec{E}_r = |\vec{E}_r| \cos \omega t$ and $\vec{E}_p = |\vec{E}_p| \cos[\omega t + \phi(t)]$, where $\phi(t)$ is the time-dependent phase difference between the probe- and reference-waves due to probe-wave propagation through the medium under investigation. The interference inten-

sity from the two waves is then:

$$\begin{aligned}
I(t) &= (\vec{E}_r + \vec{E}_p)^2 = \vec{E}_r \cdot \vec{E}_r + 2\vec{E}_r \cdot \vec{E}_p + \vec{E}_p \cdot \vec{E}_p \\
&= |E_r|^2 \cos^2 \omega t + |E_p|^2 \cos^2[\omega t + \phi(t)] + 2\vec{E}_r \cdot \vec{E}_p \cos \omega t \cos[\omega t + \phi(t)] \\
&= \frac{|E_r|^2}{2}(1 + \cos 2\omega t) + \frac{|E_p|^2}{2}(1 + \cos 2[\omega t + \phi(t)]) \\
&\quad + \vec{E}_r \cdot \vec{E}_p(\cos[2\omega t + \phi(t)] + \cos[\phi(t)]) \\
&= \underbrace{\frac{|E_r|^2}{2} \cos 2\omega t + \frac{|E_p|^2}{2} \cos 2[\omega t + \phi(t)] + \vec{E}_r \cdot \vec{E}_p \cos[2\omega t + \phi(t)]}_{\text{high frequency}} \\
&\quad + \underbrace{\frac{|E_r|^2 + |E_p|^2}{2}}_{\text{constant}} + \underbrace{\vec{E}_r \cdot \vec{E}_p \cos[\phi(t)]}_{\text{interference term}} .
\end{aligned} \tag{3.48}$$

Both the constant and high-frequency terms can be filtered out during analysis or by the electronics, leaving only the interference term. In an ideal system the wave amplitudes are constant, $E_r \neq E_r(t)$ and $E_p \neq E_p(t)$, and only $\phi(t)$ is time-varying. Thus the desired signal, $\phi(t)$, due to the experimental medium is easily distinguishable. In a physical system $E_r \equiv E_r(t)$ and $E_p \equiv E_p(t)$ are time-varying due to effects such as attenuation and vibrational noise. So $\vec{E}_r \cdot \vec{E}_p \equiv f(t)$ is also time-varying and can obscure the $\phi(t)$ signal.

I/Q detection removes wave amplitude effects from the final signal. In a heterodyne system the probe-waveform remains unchanged, but a frequency modulation ω_m is added to the reference wave, $\vec{E}_r = |\vec{E}_r| \cos(\omega + \omega_m)t$. The interference intensity

in this system is

$$\begin{aligned} I(t) &= \underbrace{\frac{|E(t)_r|^2}{2}\cos 2(\omega+\omega_m)t + \frac{|E(t)_p|^2}{2}\cos 2[\omega t+\phi(t)]}_{\text{high frequency}} \\ &+ \underbrace{\vec{E}(t)_r\cdot\vec{E}(t)_p\cos[2\omega t+\omega_m t\phi(t)]}_{\text{high frequency}} \\ &+ \underbrace{\frac{|E(t)_r|^2+|E(t)_p|^2}{2}}_{\text{constant}} + \underbrace{\vec{E}(t)_r\cdot\vec{E}(t)_p\cos[\omega_m t-\phi(t)]}_{\text{interference term}}. \end{aligned} \tag{3.49}$$

In our interferometer, the intensity signal is sent to a photodetector where it is converted into a voltage signal for processing. The signal is sent through a bandpass filter centered at ω_m to filter out both the constant (DC) and high-frequency signal components. The filtered signal is then $S_{RF} = V_{RF}(t)\cos[\omega_m t-\phi(t)]$. This experimental signal is mixed using an IQ demodulator with a signal at the original modulation frequency, $S_{LO} = V_{LO}\cos\omega_m t$, to give:

$$\begin{aligned} S(t)_I &= S_{RF}\times S_{LO} = V_{RF}(t)\cos[\omega_m t-\phi(t)]\times V_{LO}\cos\omega_m t \\ &= \frac{V_{RF}V_{LO}}{2}(\cos[\phi(t)]+\cos[2\omega_m t+\phi(t)]). \end{aligned} \tag{3.50}$$

The IQ demodulator also generates a second signal, a $\pi/2$ phase shift of $S(t)_I$, equal to $S(t)_Q = \frac{V_{RF}V_{LO}}{2}(\sin[\phi(t)]+\sin[2\omega_m t+\phi(t)])$. A final low-pass filter reduces these signals to $S(t)_I = \frac{V_{RF}V_{LO}}{2}\cos[\phi(t)]$ and $S(t)_Q = \frac{V_{RF}V_{LO}}{2}\sin[\phi(t)]$. After digitization, these signals are combined, and the phase shift is

$$\tan\phi(t) = \frac{\frac{V_{RF}V_{LO}}{2}\sin[\phi(t)]}{\frac{V_{RF}V_{LO}}{2}\cos[\phi(t)]} = \frac{S(t)_Q}{S(t)_I}. \tag{3.51}$$

Any signal variation due to changes in the wave amplitudes has been removed. The heterodyne system also has the advantage of shifting the signal to higher frequencies than the homodyne case. This has the dual noise reduction benefits of decreasing

the amount of electronic 1/f noise on the initial signal and allowing a wider range of potential low frequency mechanical noise to be removed out at the bandpass filter.

3.4 Interferometer Setup

PLX uses a fiber-optic, 561 nm, heterodyne interferometer to provide time-resolved measurements of line-integrated plasma electron density within the range of $10^{15} - 10^{17}$ cm^{-2}. A long coherence length, 320 mW laser allows for a strong, sub-fringe phase-shift signal without the need for closely-matched probe and reference path lengths. Thus only one reference path is required for all eight probe paths, and an individual probe chord can be altered without altering the reference or other probe path lengths. Fiber-optic decoupling of the probe chord optics on the vacuum chamber from the rest of the system allows the probe paths to be easily altered to focus on different spatial regions of the plasma. The interferometer is capable of sub-fringe resolution of 0.5^o even in a high EMI noise environment.

3.4.1 Optics

The fiber-optic nature of the interferometer splits the optics into three functionally-decoupled stages: the initial establishment of the probe and reference chords, the chord-positioning optics on the chamber, and the final probe/reference beam recombination. The initial establishment of the chords and the final recombination take place on a 3.05 m x 1.22 m optical table located at a distance of approximately 6.1 m from the chamber. One of the primary advantages of fiber-coupling is the ability to place the bulk of the optics at a distance from the chamber without the need to preserve direct line-of-sight paths between the optics. Figure 3.4 shows a schematic of optical and electronic components for a single chord of the fiber-coupled, hetero-

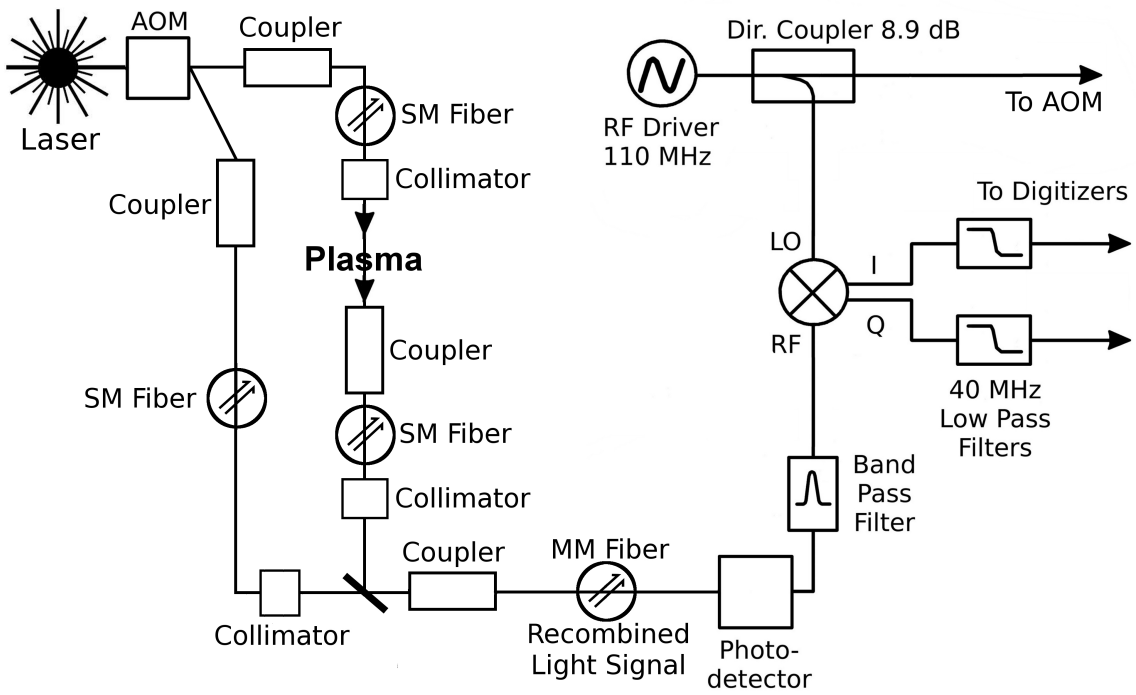

Figure 3.4: Schematic of the optics and electronics layout for a single chord of the fiber-coupled heterodyne PLX interferometer.

dyne PLX interferometer. This is expanded into the eight chord arrangement of the PLX interferometer in Figs. 3.5, 3.6, and 3.7.

An Oxxius 561-300-COL-PP-LAS-01079, diode-pumped solid-state, 320 mW, 561 nm laser [52] produces the initial beam. A 50 percent attenuation filter is attached to the aperture of the laser, bringing the transmitted laser power down to 160 mW. A beam divergence of 1.2 mrad, a path length of $\approx$ 2 m before being coupled into the fiber, and an initial beam diameter of 0.6 mm renders collimation optics in this stage unnecessary. The coherence length of the Oxxius laser is at least 10m as conservatively specified by the manufacturer, [52] but the theoretical coherence length is much higher as estimated from the laser frequency linewidth [52] of 1 MHz

as follows: [11]

$$\Delta l = c\Delta t \approx \frac{c}{\Delta\nu} = \frac{c}{1 \text{ MHz}} \approx 100 \text{ m}. \tag{3.52}$$

As long as length differences between the reference and probe paths are kept small compared to the laser coherence length, fringe visibility will still be high. [11, 57] Bench tests of one chord of the interferometer allowed at least a 2.4 m path length mismatch between the probe and reference chord without any appreciable signal degradation. This allows the use of one reference chord with respect to all eight probe chords, since the probe chord length variation due to the optics' placement on the chamber is easily kept below 2.4 m.

Thorlabs 460HP single-mode fiber is used for all fiber paths before the probe and reference beams are recombined. Single-mode fiber, while requiring greater laser power due to poorer coupling into the small fiber core, bypasses any signal degradation due to the interference effects from uneven wave-packet spreading and delay in different transverse lasing modes in multi-mode fiber. [57, 22] Thus, single-mode fiber preserves the interferometer's ability to function with chord path length differences. Thorlabs BFH48-400 multi-mode fibers is used for carrying the final signal to the electronics since the phase relationship between the light of the two chords is established in the interference pattern and coherence concerns are no longer an issue.

An IntraAction ATM-1102DA1B Bragg cell beam splitter splits the original laser beam into the reference beam, now with a frequency shift of 110 MHz, and an unaltered beam, which is then split by seven beam splitters into the eight probe beams. The Bragg cell power splitting is uneven, making the reference beam $\approx$ 20 mW and the initial unmodulated beam 140 mW, which is filtered with 50 % attuation neutral density filter. After splitting, all beams are attenuated to < 8.3 mW and then routed to the first set of fiber-couplers, as shown in Figs. 3.5 and 3.6. The reference

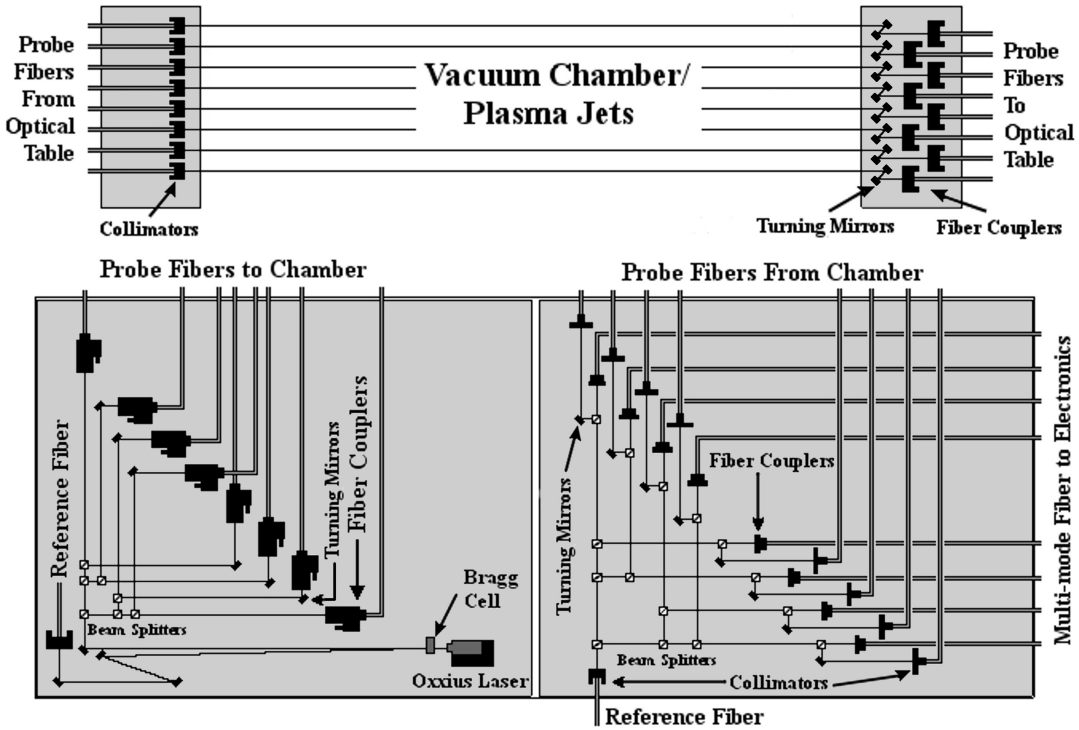

Figure 3.5: Interferometer optics layout, showing optical component layout for all three fiber-coupled stages: the establishment of the probe and reference chords, the chord-positioning optics on the chamber, and the final probe/reference beam recombination.

beam is coupled, using a Thorlabs PAF-X-18-PC-A fiber coupler in a K6X kinematic mount, into a 42 m, single-mode fiber and routed directly to the recombination optics. Each probe chord is coupled using a Newport F-91-C1 fiber coupler into a 20 m, single-mode fiber. These fibers run from the optical table containing all previous optics to a 61 cm x 30.5 cm optical breadboard mounted on a 75 cm flange on the vacuum chamber. The breadboard is mounted with the 61 cm edge of the board adjacent to the 57 cm edge of a 57 cm x 19.8 cm x 2.54 cm borosilicate window.

The probe fibers terminate at a set of eight Thorlabs CFC-11X-A adjustable focal-length collimators in Thorlabs KM100T kinematic mounts. Each collimator

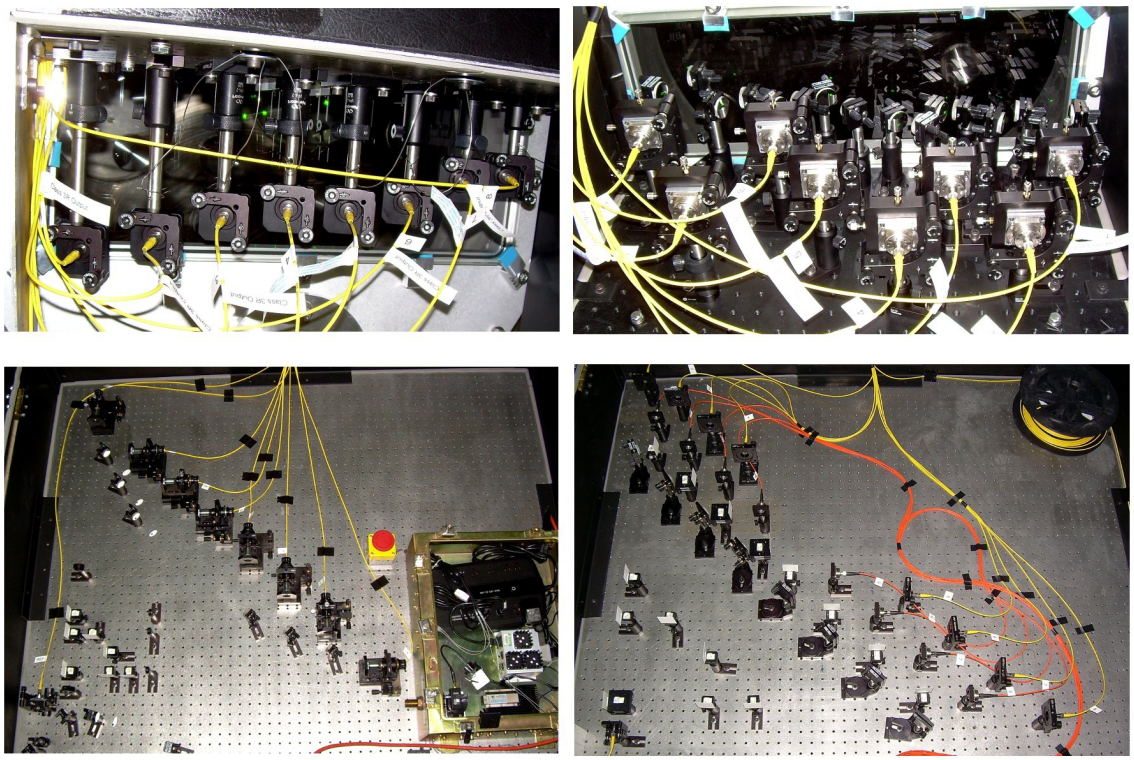

Figure 3.6: Pictures of the optical components of all stages of the interferometer. Single mode fiber is yellow and multi-mode fiber is orange. Lower Left: Initial establishment of the chords. Upper Left: Laser beam collimators mounted on the chamber. Upper Right: Beam-to-fiber couplers mounted on the chamber. Lower Right: Recombination of the probe and reference beams.

produces a collimated beam of $\approx$ 3 mm diameter over a distance of 3 m. All eight probe beams pass through the chamber to an identical rectangular window/optical breadboard setup on a port on the opposite hemisphere of the 2.74 m diameter spherical chamber. A set of eight Thorlabs fiber-couplers are mounted on the second breadboard. Turning mirrors on either or both breadboards route the probe beams from the collimators to the fiber-couplers, where the beams are coupled into a second set of 20 m single-mode fibers. The exact optics arrangement varies depending on the physics being studied. For jet axial evolution studies, the optics were positioned

through the center of a single jet at eight different points along the axis of jet propagation. The optics were also reconfigured into two additional arrangements to a single jet's radial density profile and two jet merging effects. All chord arrangements are discussed in more detail in conjunction with results in later chapters. Optics' configurations for these chord arrangements are presented in Appendix B. The other major advantage of the fiber-optic system is the decoupling of the optics that dictate chord placement in the plasma from the rest of the system. This decoupling reduces the task of altering chord arrangement to the placement of approximately 32 components (four per chord) instead of the realignment of all 110 optical components in the system.

All probe and reference fibers are routed to the recombination optics. Each fiber terminates at an adjustable focus collimator, where they are again collimated into ≈ 3 mm diameter beams. Beam splitters split the reference beam into eight beams, one for recombination with each probe chord. Each of the reference beams pass through another beam splitter, where the recombination with the probe beam occurs, and to the final Thorlabs fiber coupler, mounted in a simple CP02FP fiberport mount. Each probe beam exits the fiber and reflects off a turning mirror into the beam splitter containing the corresponding reference beam. At the final fiber couplers, the light containing the interference signal is coupled into multi-mode fibers.

Since the beams have passed through different fibers, the polarization rotating effect of the fibers must be considered. Light emitted from the fibers is plane polarized, so to maximize the interference present when the probe and reference beams overlap, the polarizations of the light in both beams must be parallel to each other.[22, 11] Each probe chord collimator is held in a rotatable mount, which allows each probe beam polarization to be independently matched to the reference beam polarization.

3.4.2 IF Electronics

The Bragg cell (acousto-optic modulator, AOM) operation requires an IntraAction ME-1002 RF generator that produces a 110 MHz, 2 W signal. This signal passes through an 8.9 dB directional coupler, transmitting a small portion of the 110 MHz signal to the processing electronics while the rest of the signal is transmitted to the Bragg cell. The processing portion of the 110 MHz signal is transmitted to a Mini-Circuits ZCS-8-13-S+ eight-way electronic splitter, creating one 110 MHz Local Oscillator (LO) signal for each chord. Each LO signal is then transmitted to a Pulsar Microwave IDO-05-412 IQ Demodulator, as shown in Fig. 3.7.

The multi-mode fibers carrying the interference signals terminate at a set of Thorlabs PDA10A photoreceivers. The output signal from the photoreceivers pass through Lark Engineering MC110-55-6AA bandpass filters of 110 ± 55 MHz to filter out high-frequency components of the heterodyne-mixing, electromagnetic interference from the pulsed-power system, and most low-frequency electrical noise. The filtered signal is transmitted to the RF channel of an IQ Demodulator, which decomposes the interference signal into two signals, I and Q, proportional to the sine and cosine of the frequency difference between the signal frequency and the LO frequency. The I and Q signals pass through a low-pass filter of maximum frequency 40 MHz, which removes any remaining high-frequency noise. Line-integrated electron densities of the plasma are extracted from the remaining frequencies contained in the I and Q signals.

3.4.3 Resolution Results

PLX single-jet studies with the HyperV Mark I plasma railgun at < 300 kA of peak current examine jet propagation at a typical phase shift range of $|\Delta\phi| \lessapprox 50°$.

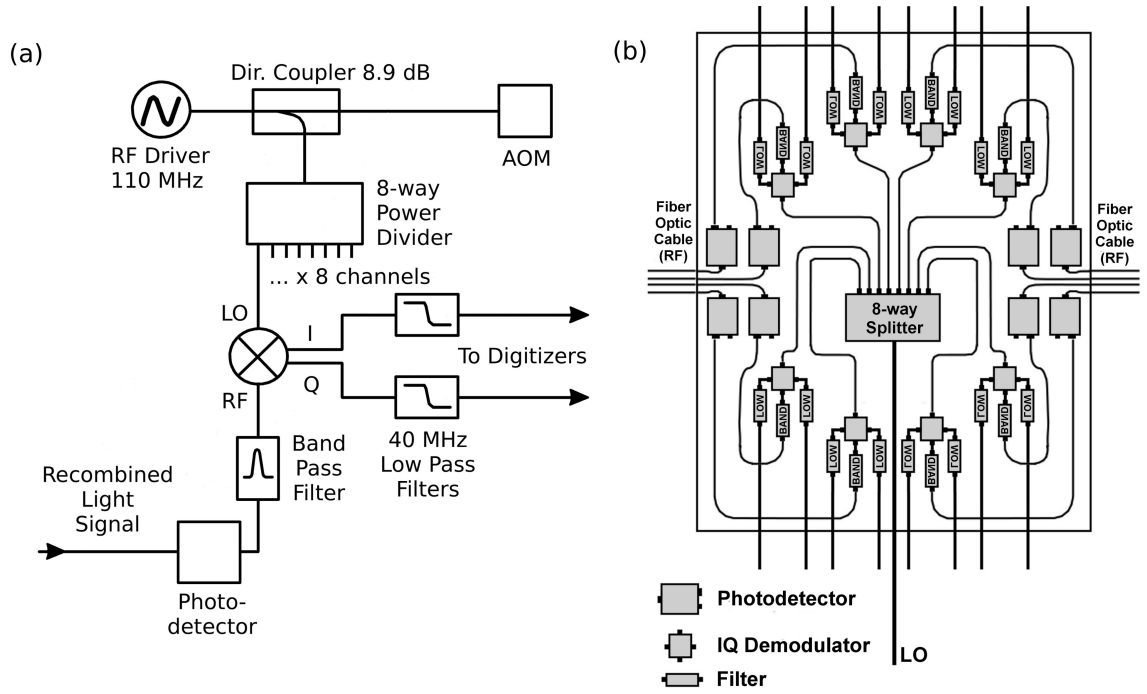

Figure 3.7: (a) An electrical schematic of RF components for all eight interferometer channels. (b) A layout of the RF electronics for all eight interferometer channels.

Figure 3.8 presents interferometry results and processing steps for Shot 744, a typical single-jet shot. As demonstrated in Fig. 3.8(a) and 3.8(b), the interferometer is capable of the sub-fringe measurements necessary for resolving phase shifts on the order of 10°. Figure 3.8(a) demonstrates the raw S_Q signal for the chord with the highest phase shift for Shot 744. The fringe amplitude of the electronic signal is approximately ±80 mV, and the plasma signal, while only a fraction of the total fringe amplitude, is distinguishable from the bit noise as well as the lower-frequency vibrational noise. The average electronic signal per chord is approximately ±100 mV with a bit-noise amplitude of ±2 mV.

In addition to bit-noise in the electronics, the PLX high-voltage pulsed-power environment generates significant electromagnetic interference (EMI) that can be

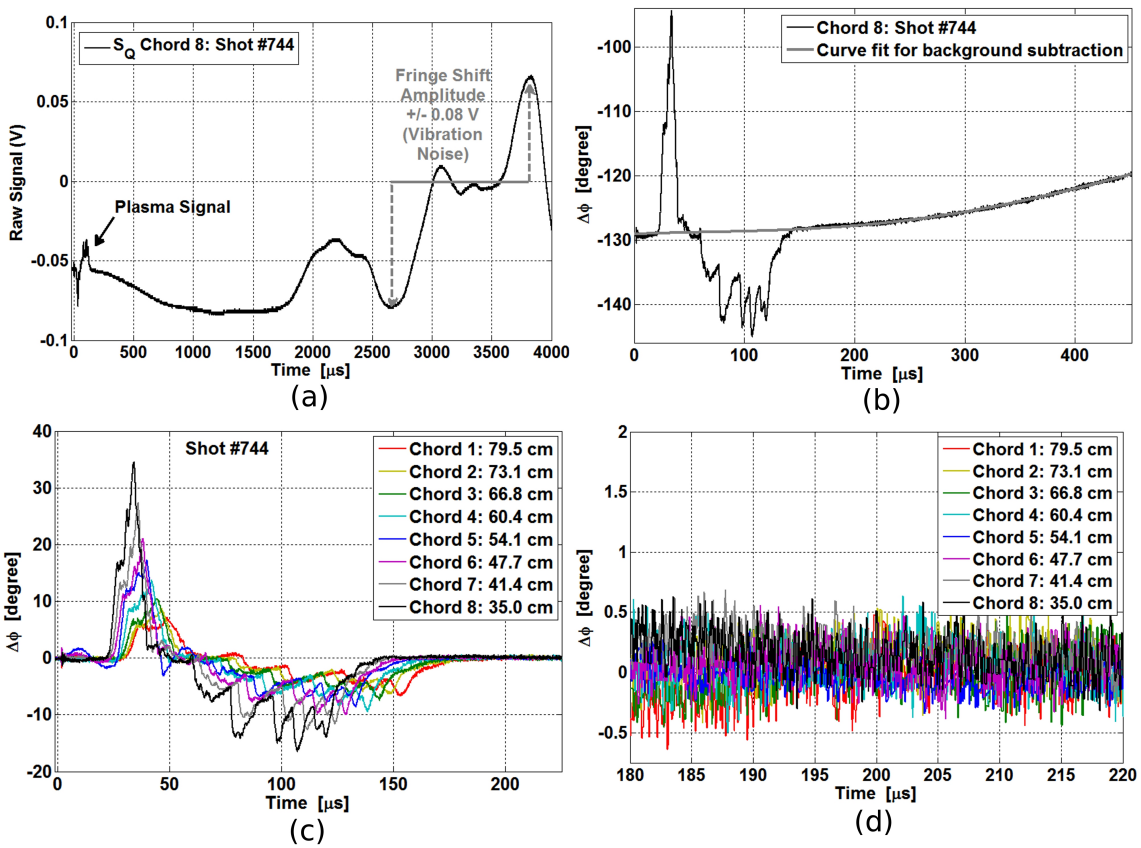

Figure 3.8: (a) Raw interferometer signal, S_Q for chord 8 and Shot 744 showing both the sub-fringe plasma signal and full fringe shift of vibration noise. (b) Phase shift signal and background signal curve fit for chord 8 and Shot 744 before background subtraction. (c) Phase shift signal for Shot 744 and all chords after background subtraction and smoothing. (d) Close up of baseline noise for Shot 744 after all signal processing.

picked up by the electronics. EMI on the time-scale of the experiment came from either the high-frequency trigger signals for the railgun switches, or from current ringing in the railgun's pre-ionization and pulse-forming capacitor banks. All interferometer electronics were enclosed in the electrically isolated Faraday cages to reduced sensitivity to EMI pickup. Trigger noise has a short duration, $\Delta t \sim 1$ μs, high frequency, $f \approx 4$ MHz, and occurs at early time $t \approx 2$ μs. Since trigger noise has

both short duration an occurs before the plasma signal times $t > 20$ μs, it is easily distinguished from the experimental signal. In addition, trigger noise is of higher frequency than structures in the plasma signal, the noise can be further reduced using signal smoothing without degrading the experimental signal.

Ringing in the capacitor bank network is responsible for both plasma jet generation and EMI production. Thus, the plasma signal and the EMI pick-up have approximately the same frequency and the noise cannot be easily removed during analysis. Instead, extensive shielding of the RF electronics was required to reduce the magnitude of bank pickup noise on the signal. The pickup noise was due to current induction in ground loop in the RF circuit. During single-jet experiments all I and Q signal cables shared common grounds at both cable ends. However, the Faraday cage reduced the EMI experienced by the RF circuit such that bank pickup noise was limited to $\Delta\phi < 5°$, and was as low as $\Delta\phi < 1°$ for many shots, for times $t < 30$ μs. For two-jet experiments the digitizers were modified to remove the common ground at one end of the I and Q cables. This modification broke the ground loops in the RF circuit and removed all bank pickup noise from the experimental signal.

If we neglect bank pickup noise, the limiting signal noise is the bit-noise from the digitizers. Thus, the interferometer can detect sub-fringe shifts of approximately 5° with a signal to noise ratio of 2:1 without signal processing. To further reduce the effects of bit-noise and potential trigger noise, all signals are smoothed with boxcar smoothing during processing; the MATLAB 'filter' function returns a data array, $Signal_{new}$, where for every point in the array, $Signal_{new}(n) = \frac{1}{N}\Sigma_{i=n-N}^{n} Signal_{old}(i)$, where $N = 5$ is the number of points the data was averaged over. The long-timescale background noise due to the lower-frequency vibrations is subtracted by using the MATLAB function 'polyfit' to fit a polynomial function to the signal, excluding the time interval for which plasma is present, and subtracting that polynomial approximation from the entire signal array. Figure 3.8(b) shows the phase shift signal

post-smoothing without background subtraction and the polynomial approximation of the background signal. All signals in Figs. 3.8(c) and 3.8(d) have had the background signal removed.

Figures 3.8(c) and 3.8(d) show the phase shift measurements over multiple chords, where Chord 8 is 35 cm from the railgun nozzle and consecutive chords are placed at 6.35 cm intervals further along the axis of jet propagation. The multiple peaks in each trace are due to electrical current ringing in the plasma gun source. Each ring produces a local density peak in the plasma jet. Negative phase shifts indicate a low-temperature late-time secondary jet due to this effect. This phenomenon will be covered in more detail in later chapters. Due to the curvature of the spherical vacuum chamber and the choice of diagnostic ports, this chord arrangement has an average path length mismatch of 2 cm between consecutive chords, a cumulative path length mismatch of $\approx$ 14 cm between Chord 8 and Chord 1, and an average path length mismatch of 20 cm between probe and reference path lengths. Limited space on the breadboards at the chamber forces optics placement that can add up to an additional 12 cm of path length discrepancy. Despite a total path length mismatch of $\sim$ 30 cm in the system, the interferometer has a resolution of $\Delta\phi < 1^\circ$ after processing, as shown in Fig. 3.8(d).

3.5 Conclusions

PLX employs an eight-chord, heterodyne, visible, fiber-optic interferometer with sub-fringe resolution for both single jet propagation and multiple jet merging experiments. The interferometer is also a viable diagnostic for full liner formation experiments. The interferometer is capable of sub-fringe resolution down to $< 1^\circ$ even with path length discrepancies on the order of tens of centimeters between each probe-chord path length and the reference path length. The ability to have

path length discrepancies in the system without signal degradation allows reduction in the complexity and cost of the interferometer by permitting the use of only one reference beam for all probe beams. The ability to have path length discrepancies also makes path length variations created by the spherical geometry of the vacuum chamber and limited space for optics a non-issue. The fiber-optic decoupling of the optics at the chamber from the rest of the interferometer greatly increases the flexibility of possible chord beam arrangements, and thus increases the range of accessible experiments. Measured interferometry phase shifts are consistent with a partially ionized plasma in which both positive and negative phase shift values are observed depending on the ionization fraction. In this case, both free electrons and bound electrons contribute to the index of refraction. We derived a general phase shift formula accounting for free-electrons, neutral atoms, and singly ionized argon ions. The formula depends only on n_{tot} and f.

Chapter 4

Single-Jet Propagation Experiments

The first stage of PLX experiments was designed to assess the evolution of a single railgun-generated plasma jet for use in liner formation experiments. The original PLX liner design called for initial plasma jet conditions of density $\approx 10^{17}$ cm^{-3}, velocity $\approx$ 50 km/s and injected mass of $\approx$ 8 mg; simultaneous achievement of these parameters has been demonstrated at HyperV Technologies with similar model railguns. A 3D ideal hydrodynamic simulation study predicted[15] that jets with these initial parameters were sufficient to achieve liner parameter of 0.1–1 Mbar pressures with a total liner kinetic energy of $\approx$ 375 kJ. As discussed in Chap. 1, liner formation and achievable stagnation pressures are sensitive to the plasma jet properties during jet merging. Understanding the single-jet parameter evolution during propagation is essential to predicting jet parameters during merging and thus the achievable liner performance.

While jet parameters at the railgun nozzle had been assessed by HyperV Technologies, the evolution of the jet temperature, density, velocity and jet profiles as the

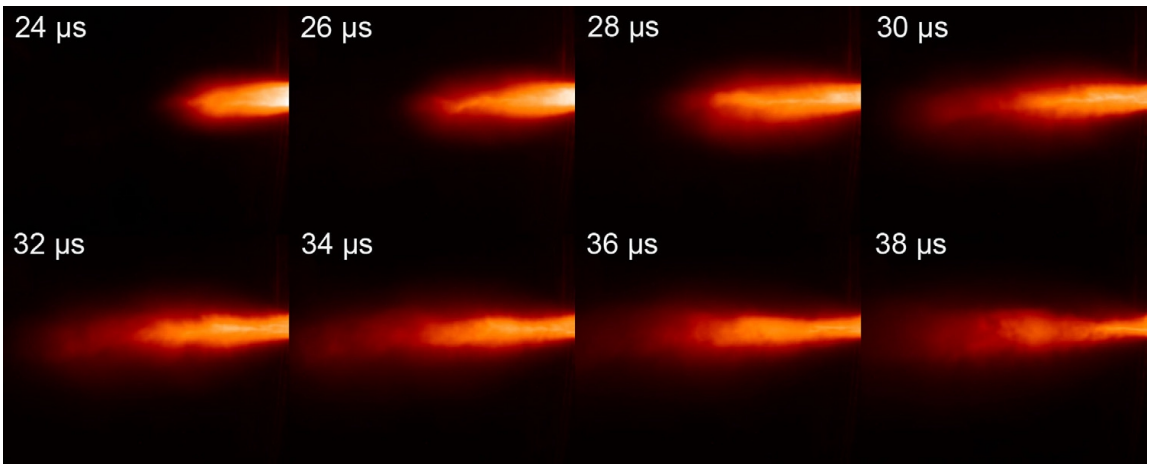

Figure 4.1: Excerpted [26]. CCD images of plasma jet evolution as recorded over eight separate shots (800 and 784-790). The railgun nozzle is slightly off the right edge of each image. The images show the logarithm of the CCD intensity in false color.

jet propagates over ~ 50 cm had not been well studied. Simulation[14] and hydrodynamic estimates[26] predict the jets will begin to merge at a radius of $R \approx 50$ cm from the chamber center corresponding to a propagation distance of ≈ 60 cm. Thus, we focused our studies on jet evolution over that propagation distance.

4.1 Diagnostic Suite Setup

Since experiments are focused on examining the evolution of jet parameters, as well as the jet axial and radial profiles, the diagnostics were placed at a variety of positions in relation to the railgun nozzle. For axial profile measurements, the diagnostics were spaced along the jet axis of propagation, where Z is the distance from the end of the gun nozzle along the propagation axis, shown in Fig. 2.6. The photodiode positions are $Z = 2.7$ cm, 27.7 cm, and 52.7 cm along the single-jet axis of propagation, where the line-of-sight of each channel is approximated in red in Fig. 2.6. In these

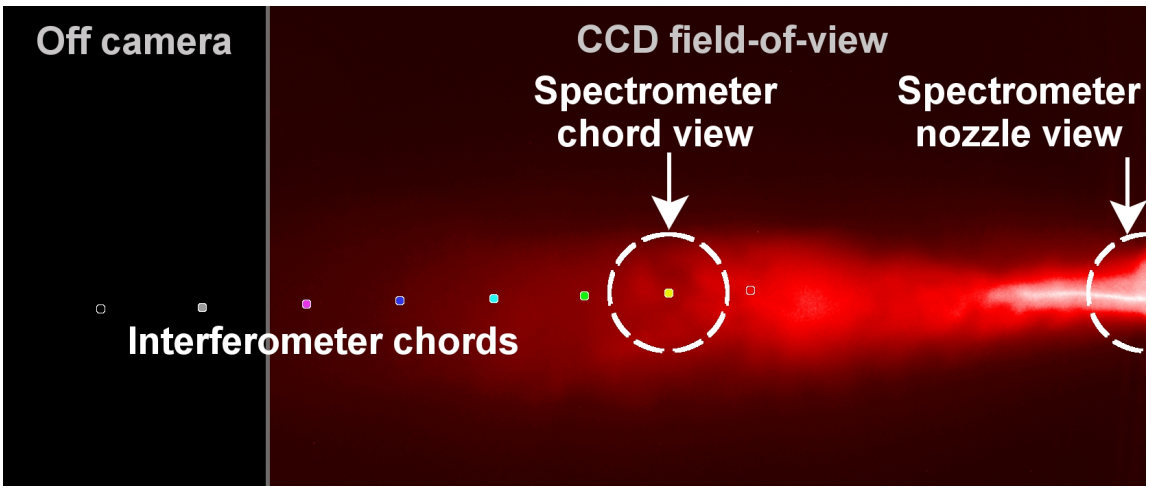

Figure 4.2: Interferometer chord and spectroscopy view positions for axial measurements configuration during single-jet experiments. The interferometer has eight chords, marked as colored dots, starting at $Z = 35$ cm and positioned at 6.35 cm intervals. The spectrometer has two different views, each with diameter ≈ 7 cm marked by dashed circles, at the gun nozzle and the $Z \approx 41$ cm interferometer chord. The limit of the CCD field of view is marked and encompasses six of the eight interferometer chords and both spectrometer views.

experiments the CCD camera primarily provides radial emission profile data for the jet. For the majority of single-jet shots, the CCD camera field-of-view covers from $Z \approx 0$–70 cm as represented by the light-blue cone in Fig. 2.6. The CCD camera field-of-view encompasses both spectrometer, all three photodiode, and six of the eight interferometer lines-of-sight used for axial jet measurements.

For the majority of single-jet experiments, the interferometer is positioned to measure the jet axial profile. The eight chords are positioned approximately transverse to the direction of jet propagation (Z axis) through the jet center, starting at $Z = 35$ cm in 6.35 cm intervals, shown in Fig. 4.2. The survey spectrometer is positioned to measure the jet self-emission at two positions, one at the gun nozzle and one at the $Z \approx 41$ cm interferometer chord (Fig. 4.2). Each spectrometer view has a diameter of ≈ 7 cm at the jet.

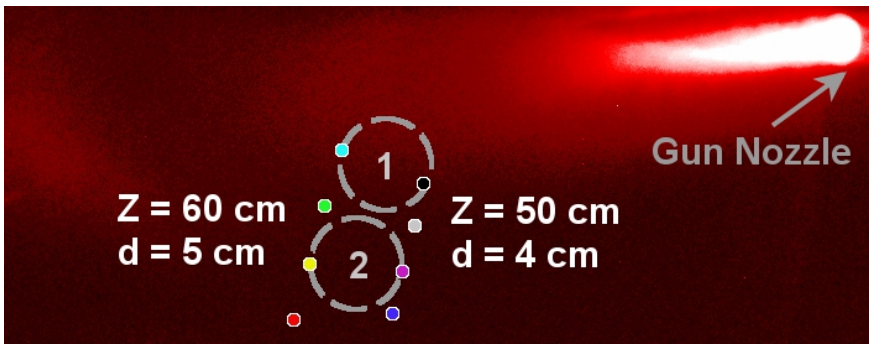

Figure 4.3: Interferometer chord and spectroscopy view positions for radial measurements configuration during single-jet experiments. The interferometer has eight chords, marked as colored dots, in two columns. One column is at $Z \approx 50$ cm with ≈ 4 cm between chords and the second column is at $Z \approx 60$ cm with ≈ 5 cm. The spectrometer has two different views, each with diameter ≈ 7 cm marked by dashed circles, marked as '1' and '2'.

The interferometer and spectrometer also have a separate set of positions used for radial profile measurements of the jet, as shown in Fig. 4.3. The details of this positioning are discussed further in Sec. 5.1.1, as this configuration is also used during the two-jet oblique merging experiments. This configuration has four interferometer chords at $Z \approx 50$ cm with inter-chord spacing of $d = 4$ cm, and four chords at $Z \approx 60$ cm with inter-chord spacing of $d = 5$ cm. Both lines of chords are approximately perpendicular to the midplane. The spectrometer has two possible views between the two chord columns at $Z \approx 55$ cm. For single-jet propagation experiments this configuration is only used for radial profiles measurements, Sec. 4.5.

4.2 Leading/Trailing Jet Structure

The time evolution of interferometer phase shifts, which also gives axial spatial profile information due to the jet's propagation along Z, show a characteristic two-

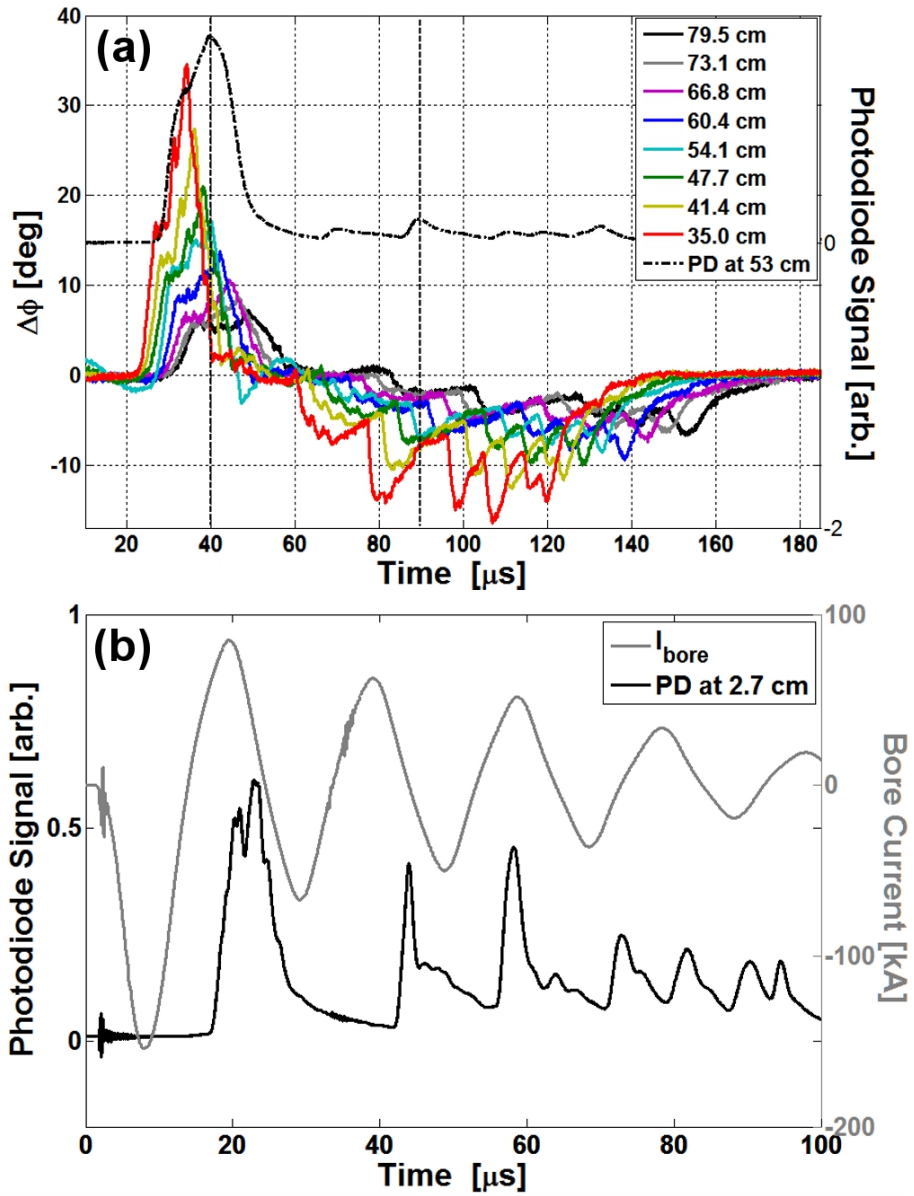

Figure 4.4: (a)Plot of $\Delta\phi$ for chord positions between Z = 35.0–79.5 cm and the photodiode signal at Z = 52.7 cm vs time for shot 744. Photodiode signal peaks closely correspond to $\Delta\phi$ peaks at Z = 54.1 cm (light blue), as demonstrated by vertical lines at two selected peaks. (b) Plot of the photodiode signal at Z = 2.7 cm (gun nozzle) and measured current in the gun bore I_{bore} vs time for shot 744.

part structure, with positive $\Delta\phi$ early in time and negative later in time (shown in Fig. 4.4(a)). Early observations of this two-part structure led to speculation that the negative phase shift was due to vibration in the system, since we've already shown that low-frequency vibrations are discernable in the interferometer signal (Section 3.4.3). The initial appearance time of both the positive and negative phase structures at various chords occurs in the same order that the jet would pass through those chords; i.e, the structures appear first on the chord at $Z = 35.0$ cm, then at $Z = 41.4$ cm and so on. The magnitude of peak $|\Delta\phi|$ of both structures also follows this order convention, with larger $|\Delta\phi|$ signals observed at chords closer to the gun nozzle. Since both the $\Delta\phi > 0$ and $\Delta\phi < 0$ signals share these ordering trends, then this suggests that both phase structures are generated by the same physical process.

Comparison of the photodiode signal at $Z = 52.7$ cm to the interferometer $\Delta\phi$ signal at $Z = 54.1$ cm, shows a large initial peak at $t \approx 40$ μs in both the emission and $\Delta\phi$ signals (Fig. 4.4(a)). At later times the photodiode signal at $Z = 52.7$ cm has a series of small emission peaks which correspond to negative $\Delta\phi$ peaks in the interferometer signal, such as the peak at $t \approx 90$ μs. The photodiodes are insensitive to both vibrations, since the photodiode field-of-view is on the order of centimeters at the jet axis, and reflections inside the chamber, since matte black foil was added to the chamber wall at positions within the photodiode field of view. These peaks in the photodiode signal indicate the presence of emitting plasma at the photodiode position at these times. Thus, both the positive and negative $\Delta\phi$ structures correspond to plasma signals. This information led to inclusion of ion and neutral phase contributions, as discussed in Chap. 3, and the conclusion that a negative phase shift corresponds to a low plasma-ionization fraction. This is consistent with the observation that the positive $\Delta\phi$ peak corresponds to the large emission signal measured by the photodiode, which is expected from a highly ionized plasma, while only small emission peaks in the photodiode signal correspond to the negative $\Delta\phi$ signal, which

is expected for a very low plasma ionization.

Observations of the photodiode signal at the railgun nozzle ($Z = 2.7$ cm) show a multi-peaked emission structure, with larger emission peaks at late times. Comparison of the $Z = 2.7$ cm photodiode signal to current measurements in the railgun bore, I_{bore}, shows a correspondence between the period of the current ringing and the appearance of emission peaks. The railguns are designed such that the initial current discharge in the railgun bore (I_{bore} peak) is the acceleration mechanism for the plasma. The plasma serves as the conductive material for allowing current to flow from one rail to the other. Multiple current peaks suggests that either plasma remains in the bore after the initially injected plasma jet leaves, or that a plasma is being formed with ablated bore material during subsequent current discharges. Thus the correspondence of the peaks in I_{bore} and the photodiode signal suggest the formation of multiple plasma jets.

The initial emission peak at $Z = 2.7$ cm persists as the large emission peak at $Z = 52.7$ cm, so the positive $\Delta\phi$ signal corresponds to the initial or leading plasma jet from the first railgun discharge. This is the only plasma jet for which we injected argon. All negative $\Delta\phi$ signals correspond to subsequent or trailing plasma jets. During single-jet experiments, the leading jet is estimated to be $\gtrsim 80\%$ argon. When we fire the gas valve alone, the observed chamber pressure rise is assumed to be due only to the injected argon. When the gas valve and railgun are both fired, we observe an approximately 25% higher chamber pressure rise compared to when only the gas valve is fired. The pressure discrepancy is most likely explained by the railgun current ablating material from the inside the gun bore. The ablated material may be present in the leading jet and is most likely the primary component of any trailing jets. Since the leading jet is $\gtrsim 80\%$ argon, for the remainder of the single-jet analysis we assume this leading jet to be functionally a pure argon plasma and use the phase analysis from Sec. 3.2.1. Since the trailing jets are most likely

composed of a higher fraction of ablated gun material, such as the tungsten rails and the zirconium-toughened alumina insulators, their composition would require further investigation to resolve.

For plasma liner experiments, only the leading jets are desirable since they are they jets that would initially form the plasma liner, and thus dictate liner performance. In an actual fusion-relevant experiment, the pulsed power system would be engineered such that only the leading capacitor bank pulse would be present. The bank ringing after the leading pulse would be crowbarred and the remaining capacitor energy somehow recovered for the next shot. So, we conducted a series of experiments where a crowbar was added to the railgun circuit to remove any current ringing in the railgun after the initial discharge. We did this in order to show that trailing jets were indeed produced as a result of the current ringing. During a shot series, we trigger the crowbar on some shots to investigate the effect on the plasma jet structure. Figure 4.5(a) shows the $\Delta\phi$ signal for the plasma jet with the railgun circuit allowed to ring. As expected, the signal shows the typical leading, $\Delta\phi > 0$, and trailing, $\Delta\phi < 0$, jet structure. When the crowbar is triggered, Fig. 4.5(b) (shot 601), only the leading jet structure remains, as predicted by our assumption that $\Delta\phi < 0$ structures were late-time jets due to ringing in the railgun current. Since the crowbar is triggered after the initial railgun discharge, the leading jet structure should remain unaltered. A comparison of the unaltered and crowbarred shots shows no qualitative difference, outside of normal shot-to-shot variation, in the width or magnitude of the $\Delta\phi > 0$ jet structure. Thus, crowbarring the railgun systems is viable for final liner experiments and allows us to limit our investigations to the dynamics of the leading jet, the jet intended for liner formation. For the remainder of our experiments we forgo use of the crowbar, since it does not change the structure of the jet of interest but does introduce complications to the railgun operation.

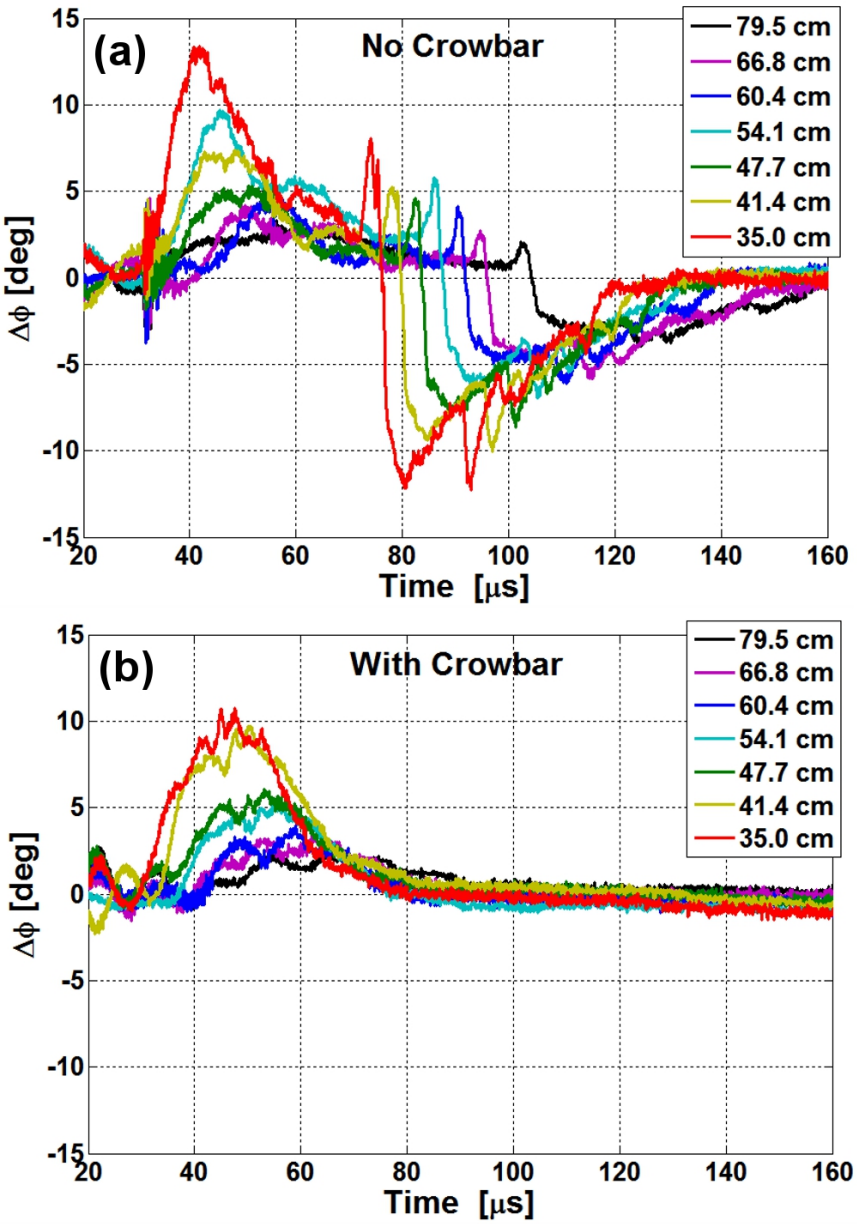

Figure 4.5: (a) Plot of $\Delta\phi$ for chord positions between $Z = 35.0$–79.5 cm vs time, for shot 609 with no crowbar on the railgun circuit. (b) Plot of $\Delta\phi$ for chord positions between $Z = 35$–79 cm vs time, for shot 601 with the railgun circuit crowbarred after the initial capacitor discharge.

4.3 Jet Velocity and Axial Profile Measurements

The axial $\Delta\phi$ profile from the interferometry data at $Z = 35.0$–79.5 cm is the first look at the experimental jet density profile. The axial profile is characterized by a steeply-sloped, approximately linear rise in $\Delta\phi$ at the jet leading edge, followed by a central phase peak, and an approximately linear decay in $\Delta\phi$ at the jet falling edge (Fig. 4.6(a)). Now we can improve the accuracy of jet-merging or full-liner simulations by using an approximation of the physical jet profile instead of assuming an arbitrary jet density profile, such as a gaussian or step function. Since the axial $\Delta\phi$ profile has well-defined structures, and the structures persist as the jet propagates past multiple chords, we can use the axial profile to measure parameters such as the jet velocity, axial length, and axial expansion.

4.3.1 Velocity Calculations

Distinct structures in the signal, such as the jet peak or edges, have distinguishable arrival times at each interferometer chord. The distance between each chord is known (6.35 cm), so the velocity of each distinguishable structure can be calculated using the time difference between the structure arrival times for different interferometer chords. The velocity measured using the profile edges is a combined function of both the jet bulk and jet expansion velocities. The jet bulk velocity, which we are more interested in, can be estimated using the time information for the largest $\Delta\phi$ peak in the profile. The bulk velocity can be found using the time delay between the peak arrival times for any two chords, 'i' and 'j', where the peak is still distinctive (Fig. 4.6(a)):

$$v = \frac{\Delta Z}{\Delta t} = \frac{(j - i) \times 6.35 \text{ cm}}{t_j - t_i}. \tag{4.1}$$

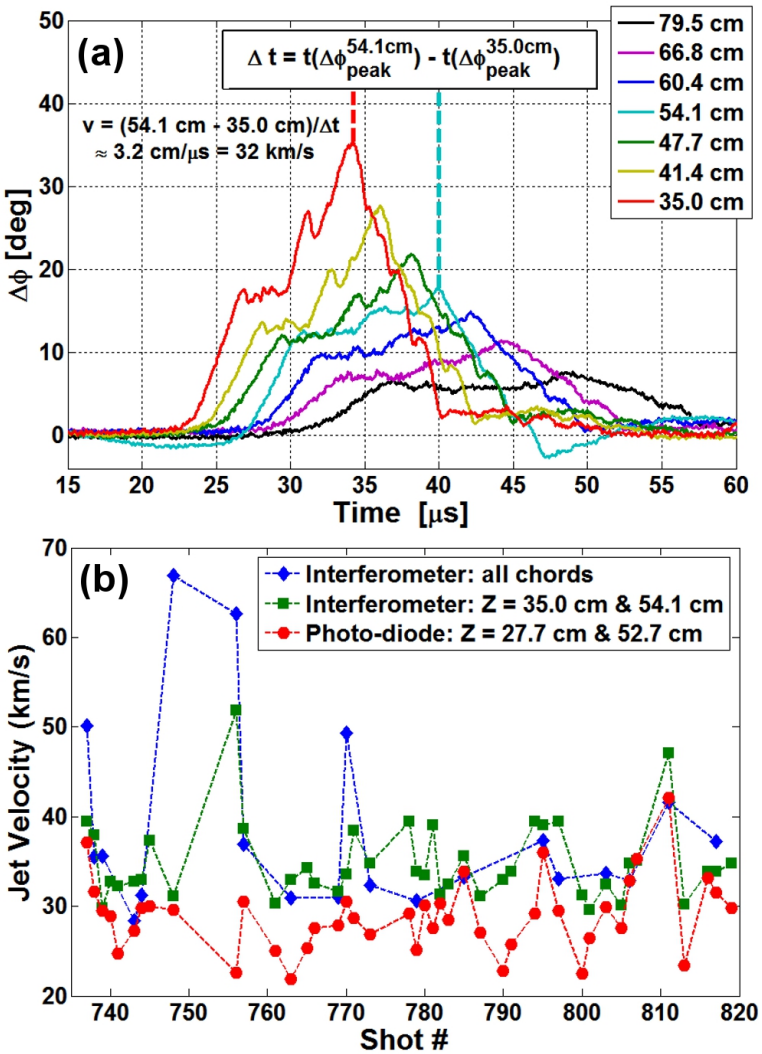

Figure 4.6: (a) Leading jet $\Delta\phi$ profile vs time for shot 744. Jet bulk velocity is calculated using the difference in arrival times of the $\Delta\phi$ peak, as shown for chords at $Z = 35.0$ cm and $Z = 54.1$ cm by dashed lines marking the peak arrival times. For shot 744, the jet velocity is ≈ 32 km/s. (b) Leading jet velocity as calculated using the average difference in $\Delta\phi$ peak arrival times at subsequent chord positions for all eight chords, the difference in $\Delta\phi$ peak arrival times for only chords $Z = 35.0$ cm and $Z = 54.1$ cm, and the jet velocity as calculated using the photodiode emission profile peak arrival times at $Z = 27.7$ cm and $Z = 52.7$ cm. Velocities are shown for applicable shots for each type of velocity calculation, in the data set shots 737–819.

Since the peak is often distinctive at many chords for a single shot, we can also calculate an average velocity using a Δt averaged over the time differences for consecutive chords:

$$v_{avg} = \frac{6.35 \text{ cm}}{\Delta t_{avg}} = \frac{6.35 \text{ cm}}{(1/(n-1)) \sum_1^{n-1} (t_{i+1} - t_i)}, \tag{4.2}$$

where n is the number of interferometer chords with usable signals. We use both of these two different methods to calculate the jet velocity: using the arrival times at several adjacent chords and calculating the average, or using measurements from just two non-consecutive chords. There is tradeoff between the two methods in terms of accuracy.

The v_{avg} measurement uses data points from a larger number of chords and so the average velocity includes effects from velocity variation, if variation is present, over the included propagation range. However, the v_{avg} calculation is susceptible noise in the phase signals. EMI noise in the system can create distortion of the $\Delta\phi$ profile significant on $\Delta t \sim \mu$s timescale between consecutive chords. Analysis algorithms, for all velocity measurements, were designed to require both normal gun operation and $t_{i+1} > t_i$ for all chords used in the calculation (i.e. the jet peak arrives at subsequent chords in order). This constraint manages to exclude shots where noise contributions make the data results non-physical. The v_{avg} calculation is also susceptible to bit-noise considerations: some shots show sets of small peaks, $\Delta\phi \sim 1°$, located atop the the primary $\Delta\phi \sim 10°$–$50°$ peaks. Since the small peaks have magnitudes near the bit-noise threshold, algorithms designed to select the correct peak for velocity calculations are often inaccurate. Manual selection can provide more accurate estimates of jet velocity from shots with multiple-peak structures, but the time required becomes prohibitive for large data sets.

Using Δt measurements from two non-consecutive chords does increase calculation precision but assumes a constant jet velocity over the applicable jet propagation

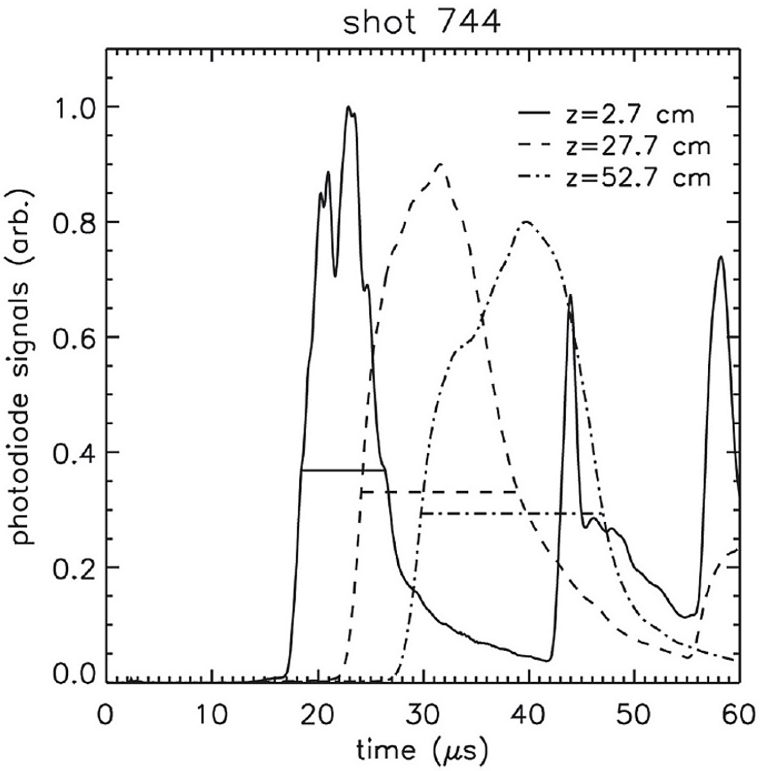

Figure 4.7: Photodiode signals for shot 744 and $Z = 2.7$ cm, 27.7 cm, and 52.7 cm. Excerpted from [26].

distance. The non-consecutive chord calculations are more robust to noise considerations since the larger the Δt (the greater the distance between chords), the smaller the percent error introduced by noise. Figure 4.6(b) shows bulk velocity calculations for applicable shots, shots that fulfill $t_{i+1} > t_i$ for applicable chords in the data set of shots 737–819, for both v_{avg}, calculated using the peak arrival times for all eight chords, and v, calculated using just chords $Z = 35.0$ cm and $Z = 54.1$ cm. As shown in Fig 4.6(b), bulk velocity estimates using v for chords $Z = 35.0$ cm and $Z = 54.1$ cm have more applicable shots as well smaller variation than v_{avg} estimates.

Photodiode axial emission profiles can also be used to estimate the jet bulk velocity. The emission profiles share a peaked structure similar to the $\Delta\phi$ profiles, as

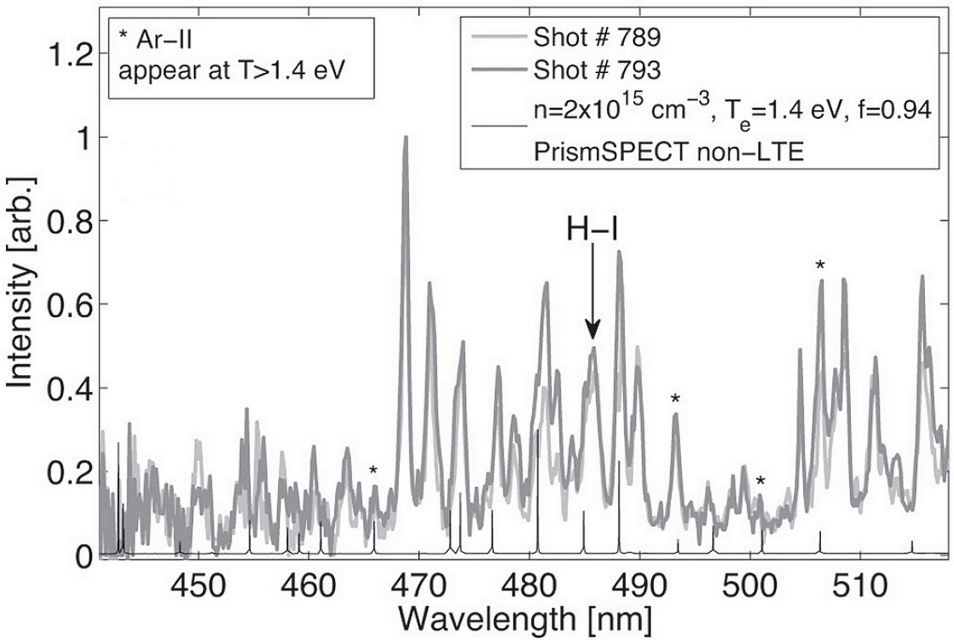

Figure 4.8: Spectra for the spectrometer at $Z \approx 41$ cm and shots 789 and 793, both at $t = 364$ μs corresponding to the jet peak arrival time at interferometer chord $Z = 41.4$ cm. Plot also includes argon spectra from PrismSPECT non-LTE calculations. Excerpted from [26].

shown in Fig. 4.7, so v is calculated in a similar way. The photodiodes are located at $Z = 2.7$ cm, 27.7 cm, and 52.7 cm. We compare interferometer and photodiode bulk velocity estimates, v_{int} and v_{pd} respectively, for similar propagation regions: $Z = 27.7$ cm and 52.7 cm for the photodiodes, $Z = 35.0$ and 54.1 cm for the interferometer chords. Figure 4.6(b) shows reasonable agreement between photodiode and interferometer velocity estimates at these positions, though for almost every shot the interferometer phase shift estimates a greater bulk velocity than the photodiodes. The average bulk velocity of a single jet for this data set is:

$$\begin{aligned} v_{int} &= 34.9 \pm 4.6 \text{ km/s} \\ v_{pd} &= 29.5 \pm 4.5 \text{ km/s}. \end{aligned} \tag{4.3}$$

Again the interferometer velocity estimate is greater than the photodiode estimate, but the estimates agree within the margins of error for each calculation. The offset between the estimates may be due to a difference in what each diagnostic measures; the interferometer measures the velocity of the mass peak of the plasma jet while the photodiodes measure the emission peak. Plasma emission is both density- and temperature-dependent, so the density and emission peaks may not always have the same spatial location within the jet depending on the jet temperature profile. However, this standard of agreement still implies a reasonable accuracy of our velocity measurements.

Velocity measurements also show we can achieve 30 km/s velocities even with the equipment operating at less-than-peak-power capabilities to reduce equipment degradation. For this data set, the PFN bank voltage is set at -24 kV, keeping the current across the PFN switch and in the gun bore to ≈ 280 kA. Railgun operation during this data set has $\approx 86\%$ of shots with $<10\%$ variation in gun current, $I = 280 \pm 28$ kA. HyperV has achieved the desired velocities of ~ 50 km/s with equivalent equipment but at higher power performance, > 300 kA.

Now that we have the plasma bulk velocity, we would like to calculate the jet Mach number. As previously discussed, a high jet Mach number is desirable for final liner formation. The plasma Mach number is given by:[4]

$$M = \frac{v}{C_s} = \frac{v}{\sqrt{\gamma Z_{\text{eff}} k T_e / m_i}}, \tag{4.4}$$

where C_s is the ion sound speed in the plasma, Z_{eff} is still the plasma mean charge, T_e is the electron temperature, m_i is the ion mass, k is the Boltzmann constant and γ is the polytropic index. Spectroscopy measurements of the jet at $Z \approx 41$ cm and $t = 36$ μs (the time the jet peak arrives at $Z = 41.4$ cm interferometer chord, Fig. 4.8) gives us estimates of both T_e and Z_{eff} for the jet bulk. Ar II lines appear in the experimental spectra only for $T_e \geq 1.4$ eV in the PrismSPECT non-LTE

calculations. Thus, $T_e = 1.4$ eV is the lower bound on estimates of peak T_e in the jet. At $T_e = 1.4$ eV PrismSPECT gives us an estimate of mean charge $Z_{\text{eff}} = f = 0.94$ for a pure argon plasma with $n_e = 2 \times 10^{15}$ cm^{-3} (discussed in Sec. 4.6) Assuming $\gamma = 1.4$, $v = 30$ km/s, and a pure argon plasma, then these parameters yield $M \approx 14$ for a single jet. Thus our single jet is strongly supersonic.

4.3.2 Axial Jet Length and Expansion

Similar to velocity measurements, the jet structure lends itself to axial jet-length measurements as well. The jet length in the time domain, ℓ, is found using the difference in arrival times of the jet leading and falling edges, calculated as the signal full-width (FW) at $\Delta\phi_{peak}/e$ and shown in Fig. 4.9(a) for the chords at $Z = 35.0$ cm. The jet length in the time domain, for a measurement at any chord is given by

$$\ell = t_f - t_i = t_{fall}(\Delta\phi_{peak}/e) - t_{rise}(\Delta\phi_{peak}/e), \tag{4.5}$$

where t_i and t_f are the arrival times of the leading and falling edges respectively. Since the slopes of the jet edges are so steep, calculating the edge arrival times measured at 0.5 or $2/e$ of $\Delta\phi_{peak}$ value gives arrival-time results within a 2% variation of results for $\Delta\phi_{peak}/e$. To convert this to a jet length in the spatial domain, L, for any chord measurement, we multiply ℓ by the velocity of the jet at that position. Photodiode velocity measurements show little variation in jet velocity over the range from $Z =$ 2.7–52.7 cm. For shot 744 photodiode measurements yield $v_{12} = 28.7$ km/s between the first and second photodiodes ($Z = 2.7$ cm and 27.7 cm) and $v_{23} = 30.5$ km/s between the second and third photodiodes ($Z = 27.7$ cm and 52.7 cm). The velocity variation between the photodiode pairs is $\approx 6\%$ for this shot. For this data set, the average velocity variation between the photodiode pairs is small ($\approx 2\%$), with $v_{12} = 28.9 \pm 3.9$ km/s and $v_{23} = 29.4 \pm 4.5$ km/s. The velocity variation is small over ~ 50 cm jet propagation distances, so we can assume the velocity at any given

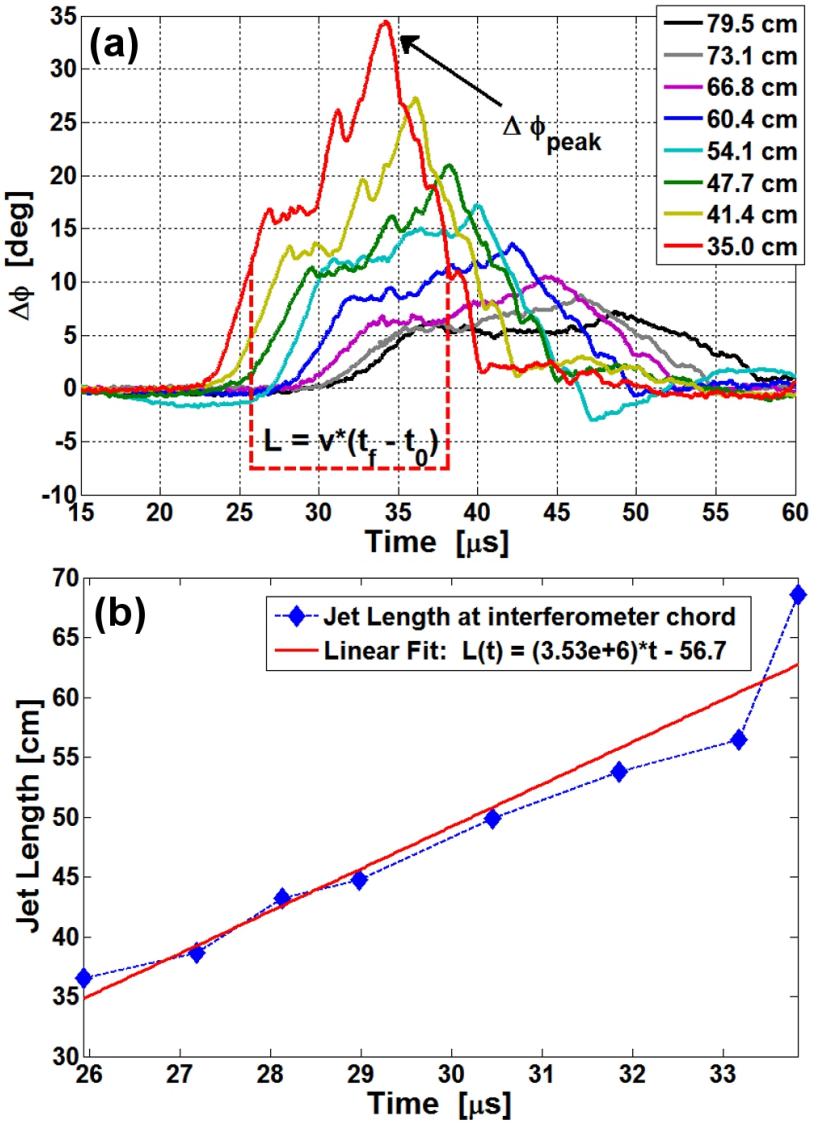

Figure 4.9: (a) Leading jet $\Delta\phi$ profile vs time for shot 744. Jet length is calculated using the time difference between the initial (leading) and final (falling) edges of the $\Delta\phi$ profile times the jet bulk velocity. The profile edge times are calculated at $\Delta\phi_{peak}/e$, as shown for chord $Z = 35.0$ cm. (b) Plot of jet length L vs time, for the experimental value L at each chord for shot 744, and a linear fit to the experimental data. The time t for any experimental length value is the corresponding measured peak arrival time, $t = t(\Delta\phi_{peak})$.

interferometer chord is approximately $v_{avg} = v_{int} \equiv v$ since the interferometer spans an ≈ 45 cm jet propagation distance. Also, since the jet is highly supersonic, $M \approx 14$, the bulk velocity of the jet is significantly greater than bulk-expansion speed of C_s, and greater by a factor ~ 3 than the edge-expansion speeds of $2C_s/(\gamma-1)$ for $\gamma = 1.4$. From this, we approximate the velocity profile of the jet as constant and equal to the bulk velocity v. Then, the jet length L at any chord j can be approximated as

$$L_j \approx v \times \ell_j = v \times (t_f - t_i)_j. \tag{4.6}$$

Figure 4.9(b) shows a plot of estimated jet length versus time for shot 744, which includes the estimated L_j for each of the eight chords. The corresponding time for each L_j is the measured peak arrival time, $t = t(\Delta\phi_{peak})$, at that chord. The axial jet length is not constant, but increases approximately linearly during the times the jet is propagating past the interferometer. We can fit a line to the data to give us an estimate for the axial length as a function of time, $L(t)$, and the axial expansion rate $\dot{L}$. Since the jet length increases linearly, then $\dot{L}$ is the slope of $L(t)$. Thus, we can approximate the expansion rate by either fitting a line to many data points or by simply finding $\dot{L} = \Delta L/\Delta t$ for just two chords.

Similar to our velocity estimates, the photodiode emission signals can also be used to estimate jet length and axial expansion of the emitting plasma. As shown in Fig. 4.7, we can find ℓ of the photodiode signals by following the same procedure as for the interferometer measurements, FW of the jet profile at $1/e$ of the peak signal. The jet length and axial expansion can then be estimated as $L = v(t_f - t_i)$ for a single photodiode and as $\dot{L} = \Delta L/\Delta t$ for any photodiode pair. Again we can compare the interferometer and photodiode estimates: jet length at chord $Z = 54.1$ cm and photodiode $Z = 52.7$ cm, and axial expansion between chords $Z = 35.0$ cm and 54.1 cm and photodiodes $Z = 27.7$ cm and 52.7 cm (to approximate the same propagation range and distance). Since the photodiode setup can only measure

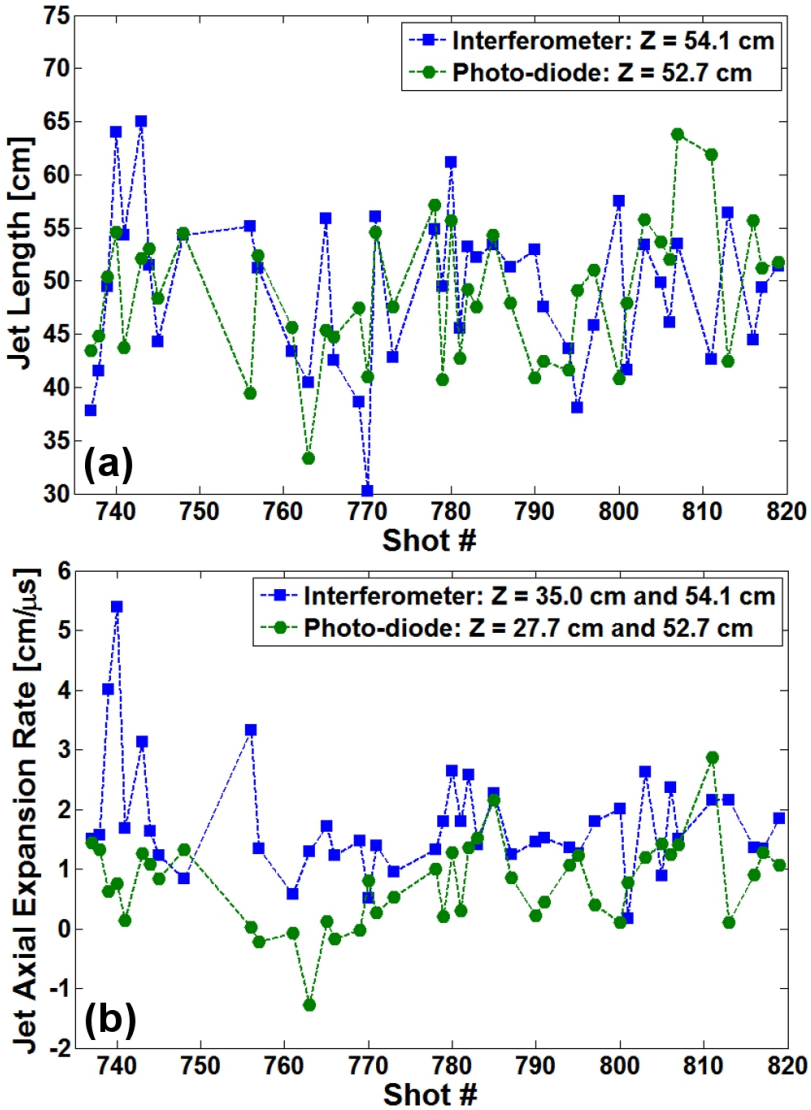

Figure 4.10: (a) Jet length as calculated using the edge arrival times for only chord $Z = 54.1$ cm, and the jet length as calculated using the photodiode emission profile edge arrival times at $Z = 52.7$ cm. Jet lengths are shown for applicable shots for each type of velocity calculation in the data set shots 737–819. (b) Jet axial expansion rate for applicable shots for the same data set as in part (a), for the change in jet length between interferometer chords at $Z = 35.0$ cm and $Z = 54.1$ cm, and between photodiodes at $Z = 27.7$ cm and $Z = 52.7$ cm.

velocity for the propagation ranges between photodiodes pairs, we approximate the jet lengths as

$$\begin{aligned} L_{27.7\text{ cm}} &= \frac{(v_{12}+v_{23})}{2}(t_f - t_i)_{27.7\text{ cm}} \\ L_{52.7\text{ cm}} &= v_{23}(t_f - t_i)_{52.7\text{ cm}}. \end{aligned} \tag{4.7}$$

Figure 4.10 shows a comparison of (a) jet length L and (b) axial expansion over the shot 737–819 data set. There is very good agreement between L estimates from the interferometer and photodiodes, with the average values being

$$\begin{aligned} L_{int} &= 49.2 \pm 7.3\text{ cm} \\ L_{pd} &= 48.9 \pm 7.5\text{ cm}. \end{aligned} \tag{4.8}$$

The axial expansion doesn't show as strong an agreement between the diagnostics, with

$$\begin{aligned} \dot{L}_{int} &= 1.76 \pm 0.93\text{ cm}/\mu\text{s} \\ \dot{L}_{pd} &= 0.90 \pm 0.73\text{ cm}/\mu\text{s}. \end{aligned} \tag{4.9}$$

Like the earlier velocity measurements, the photodiode estimates are consistently lower than the interferometer estimates even if the average $\dot{L}$ values agree within the margin of error. Again, this may be due to the discrepancy between what the diagnostics are measuring.

If we assume an edge of the jet expands at $2C_s/(\gamma-1)$ from hydrodynamics,[37] then

$$\dot{L}/2 = \frac{2C_s}{(\gamma-1)} = \frac{2\sqrt{\gamma Z_{\text{eff}} k T_e/m_i}}{(\gamma-1)}. \tag{4.10}$$

For a pure argon plasma and using $\gamma = 1.4$, $Z_{\text{eff}} = 0.94$ and $T_e = 1.4$ eV (from spectroscopy estimates) this predicts an axial expansion of $\dot{L} = 2.1$ cm/μs, which is

within the margin of error for the interferometer measurements. Thus, our measured axial expansion is consistent with hydrodynamic estimates.

4.4 Comparison to Synthetic Interferometry

Synthetic diagnostics are an effort to translate simulation results into the forms of actual diagnostic signals for direct comparison. Synthetic interferometry translates simulated density and ionization profiles into line-integrated phase-shift calculations to see what simulation parameters are required to mimic actual experimental $\Delta\phi$ measurements. To do this, the phase-shift formulas, Eqn. 3.25 (with appropriate constants for argon) and Eqn. 3.47, have been applied to single-fluid USim (formerly Nautilus) [40] and two-fluid Large Plasma Simulation (LSP)[60] simulated-jet data, provided by collaborators John Loverich and Carsten Thomas at Tech-X Corp. and Voss Scientific respectively. Line-integrated measurements are taken through the simulation at positions approximating the chord locations in the experiment; synthetic and experimental chord positions are approximately the same. Relative positive and negative $\Delta\phi$ amplitudes, jet structures such as the sharp leading-jet edge and the transition between positive and negative phase shifts, and jet arrival times at the interferometer chords are all used to calibrate simulation conditions. The simulated phase-shift calculations show an insensitivity to the assumption that the ionization fraction is constant along the chord length, $f \equiv f(l) = \text{constant}$, making equations Eq. (10) and Eq. (14) equivalent within $\leq 6\%$ error.

Figures 4.11(a) and 4.11(b) show synthetic interferometer phase-shift signals from 1D LSP[60] two-fluid simulations and 3D USim[40] single-fluid simulations, respectively. Both simulations include non-local-thermodynamic-equilibrium (non-LTE) equation-of-state (EOS) tabular models.[43] Both simulations also assume a leading and a trailing jet, as discussed in Sec. 4.2, with initial conditions as given in Fig. 4.11.

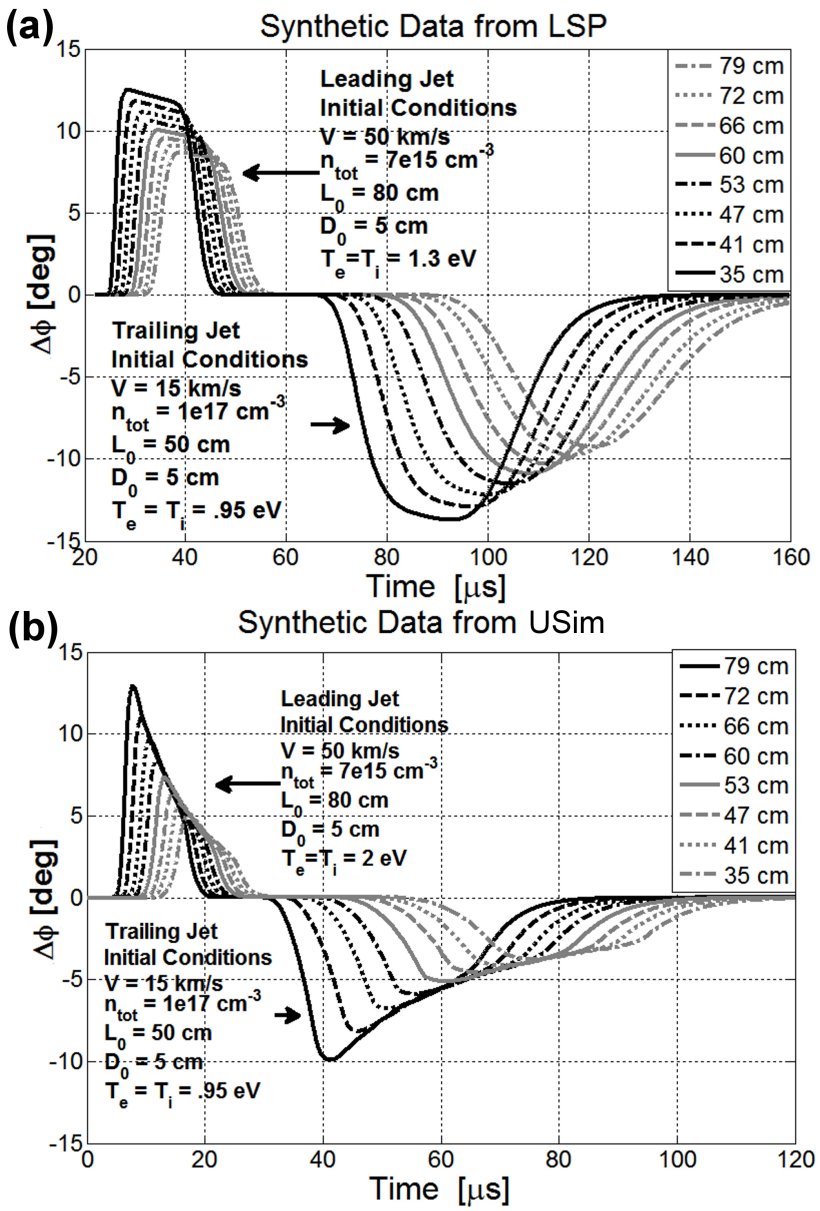

Figure 4.11: Synthetic interferometer phase-shift data from (left) LSP two-fluid and (right) USim single-fluid jet simulations. Initial conditions used in the simulations are indicated in the plots. Synthetic chord positions relative to the plasma gun are given in the legends.

The 1D LSP simulation assumes that the radius of both jets expands thermally for its path length calculation, to mimic 3D expansion. In both simulations, the trailing jet requires a lower initial temperature and corresponding f to generate a negative instead of positive phase shift. For these simulations we required that both the negative and positive signals have roughly equal amplitudes of $\Delta\phi \approx 10°$–$15°$, corresponding to early experimental values of $\Delta\phi$ averaged over 25 shots (between shots 358–448) with $I_{peak} = 260 \pm 5$ kA and a chamber pressure rise of $P = 0.4 \pm 0.1$ mtorr. The non-LTE EOS model used bounds the trailing jet temperature at $T_e < 1$ eV required for a negative phase shift, $f < 0.07 \ll 1$. The edges of the leading-jet synthetic phase-shift data also show a steep slope consistent with the experimental data. Overall the USim results are more consistent with the qualitative shape of the axial jet profile, since the synthetic profile possesses the distinctively non-linear decrease in $\Delta\phi_{peak}$ displayed in Fig. 4.16 (discussed in Sec. 4.5.2). These simulations, which have produced synthetic data in good agreement with the experimental data, can be used to both interpret and better understand the physics of single-jet propagation and increase the accuracy of future liner simulations.

4.5 Jet Radial Profile Measurements

Now that we have characterized the axial profile of the jet, we investigate the jet radial profile. Experiments to measure the jet's radial characteristics were conducted in two parts. The jet radial expansion can be inferred from measurements of $\Delta\phi_{peak}(t)$ and $L(t)$ from the same interferometer setup as the axial measurements (Fig. 4.2). Jet profile measurements required reconfiguration of the chord positions, from positioning the chords on the jet propagation axis to positioning the chords at different radial distances from the axis (Fig. 4.3).

Figure 4.12 shows the $\Delta\phi$ vs. time plots for a typical shot with the interferometer

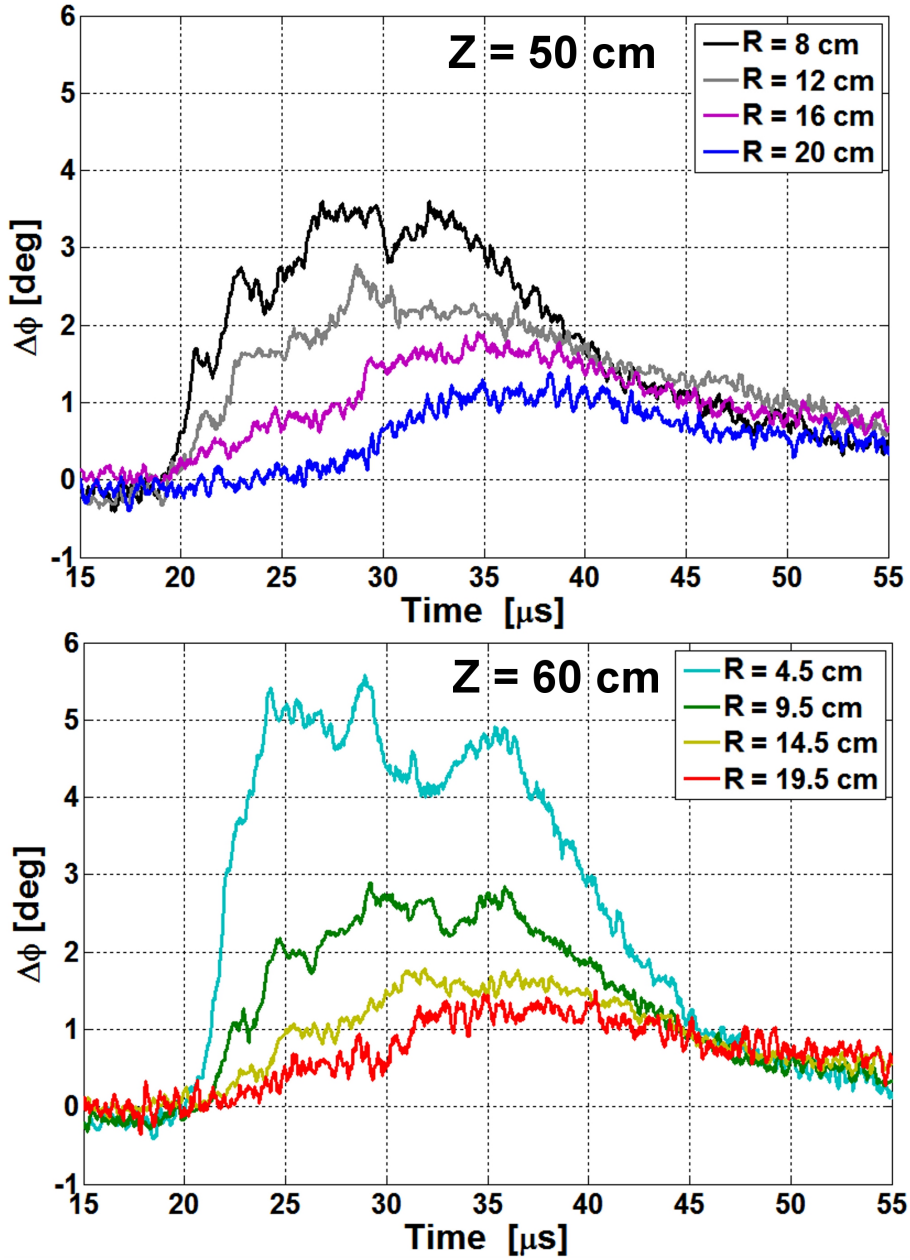

Figure 4.12: Plot of $\Delta\phi$ vs. time for shot 1106 with the interferometer chords positioned at $Z = 50, 60$ cm and radial distances from $R = 3.5$–20 cm, as shown in Fig. 4.3.

chords in the $Z = 50, 60$ cm configuration. Comparison of the $\Delta\phi$ magnitudes between chords shows a gradient in $\Delta\phi$ where the magnitude of $\Delta\phi$ decreases for increasing radial chord position R. This is consistent with the expectation that the jet possesses a non-constant radial density profile, with higher densities at the jet center.

4.5.1 Abel Inversion

The phase-shift formula for a singly-ionized argon plasma,

$$\Delta\phi_{tot} = C \int [f - f_0] n_{tot} dl, \tag{4.11}$$

relates the measurement from a single interferometer chord to the line-integrated plasma density. To extract the density profile information from phase-shift measurements, we use the Abel inversion technique.[30] The inversion technique is based on the Abel integral transform. For this transform, assume an axially-symmetric two-dimensional system with a radial function $g(r)$ inside the boundary, or circle $r = a$. A line-of-sight measurement of $g(r)$ along a chord of the circle at a distance y from the center is defined as the function $F(y)$, which is:[30]

$$F(y) = \int_{+\sqrt{a^2-y^2}}^{-\sqrt{a^2-y^2}} g(r) dl = 2 \int_y^a g(r) \frac{r dr}{\sqrt{r^2 - y^2}}. \tag{4.12}$$

To recover the function $g(r)$ from a known $F(y)$, the Abel transform is:[30]

$$g(r) = \frac{-1}{\pi} \int_r^a \frac{dF(y)}{dy} \frac{dy}{\sqrt{y^2 - r^2}}. \tag{4.13}$$

If we assume both the plasma density and ionization fraction are axially symmetric, or that at any position Z that $n_{tot} \equiv n_{tot}(r)$ and $f \equiv f(r)$, then in our system

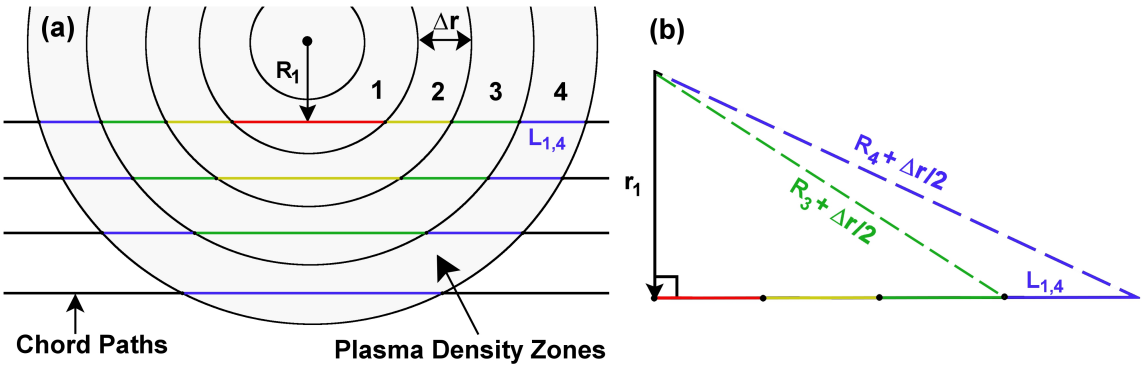

Figure 4.13: (a) Model of a radial cross-section of the plasma assuming the plasma is axially symmetric and divided into discreet zones. Each zone has an assumed width of Δr and a radial distance to the center of the zone R, where R is the minimum distance to the interferometer chord. (b) Geometric setup for calculating the length of the interferometer chord inside zone 4.

$g(r) = [f(r) - f_0]n_{tot}(r)$. The line-of-sight measurement is the phase shift at chord position R is $F(y) = \Delta\phi(R)$. The Abel transform would give us

$$[f(r) - f_0]n_{tot}(r) = \frac{-1}{\pi C}\int_r^a \frac{d\Delta\phi(R)}{dR}\frac{dR}{\sqrt{R^2 - r^2}}. \tag{4.14}$$

If we had continuous $\Delta\phi$ measurements in R, such as found in interferometric imaging, we could use this transform directly to find our $n_{tot}(r)$ and $f(r)$ profile. However, our system only has $\Delta\phi$ measurements at the discreet R of the chord positions. Thus, instead of using the integral transform for a continuous function, we use the matrix inversion form of the Abel transform for discrete systems.[10]

Since this a discrete system, we partition the plasma into radial zones of constant n_{tot} and f centered at the jet axis of propagation, as shown in Fig. 4.13(a). In our system we have four effective radial zones corresponding to the four radial chord positions R at a given Z position. We define each zone to have a width $\Delta r = d$, where d is the distance between interferometer chords. The distance to the center of each zone is defined as the distance R from the jet axis to the interferometer chord.

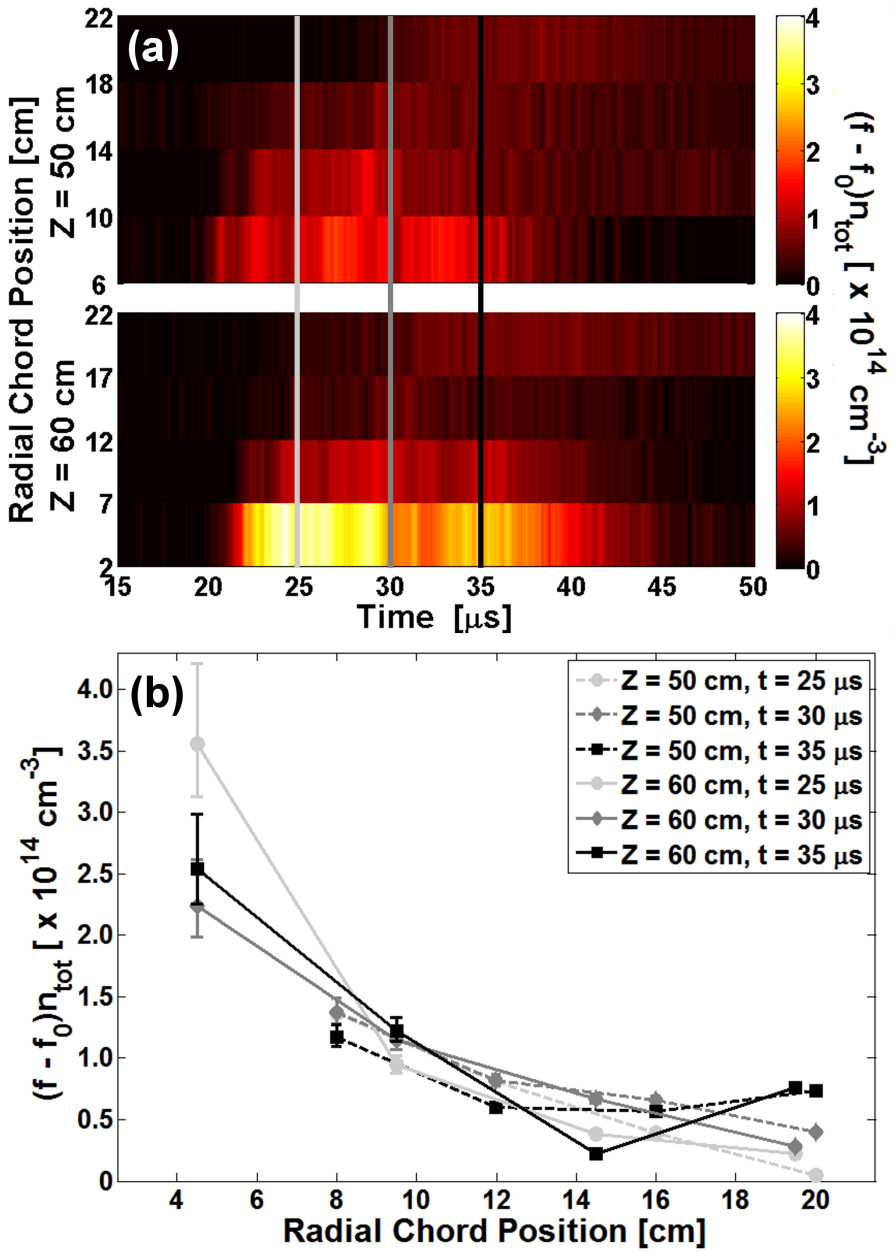

Figure 4.14: (a) Intensity plot of $[f - f_0]n_{tot}$ vs time and radial chord positions $R = 8$–20 cm with $\Delta r = 4$ cm at $Z = 50$ cm and $R = 4.5$–19.5 cm with $\Delta r = 5$ cm at $Z = 60$ cm. (b) Line-outs of (a) at $t = 25, 30, 35$ μs for both $Z = 50$ cm and 60 cm, as marked by vertical lines in (a).

Thus, for any $\Delta\phi$ measurement along a sightline 'i', the phase shift is given by

$$\Delta\phi_i = C\sum_{j=1}^{4} 2\mathbb{L}_{ij} g_j(f, n_{tot}) = 2C\sum_{j=1}^{4} \mathbb{L}_{ij}[f_j - f_0]n_{tot,j}, \tag{4.15}$$

where $\mathbb{L}_{ij}$ is the matrix of chord path lengths in one quadrant of the plasma, where L_{ij} is the path length through zone 'j' for a sightline 'i', represented as colored line segments in Fig. 4.13(a). Since $\mathbb{L}_{ij}$ is for only one quadrant, we multiply it by two to get the total chord distance in the plasma. The Abel inversion for this system is just a matrix inversion such that

$$[f_j - f_0]n_{tot,j} = \frac{1}{2C}\sum_{i=1}^{4} \mathbb{L}_{ji}^{-1}\Delta\phi_i. \tag{4.16}$$

This is equivalent to the integral form with $\mathbb{L}_{ji}^{-1}$ and $\Delta\phi_i$ corresponding to the $dR/\sqrt{R^2 - r^2}$ and $d\Delta\phi/dR$ terms in Eqn. 4.14 respectively.

The length matrix of the system can be determined from geometric principles. Figure 4.13(b) shows the geometric setup for calculating $L_{1,4}$, the chord length in zone 4 along sightline 1. Using the Pythagorean Theorem, then

$$L_{1,4} = [(R_4 + \Delta r/2)^2 - R_1^2]^{1/2} - [(R_3 + \Delta r/2)^2 - R_1^2]^{1/2}. \tag{4.17}$$

This generalizes to a length matrix of the form

$$\begin{aligned} L_{ij} &= [(R_{(n+1)-j} + \frac{\Delta r}{2})^2 - R_{(n+1)-i}^2]^{1/2} - [(R_{n-j} + \frac{\Delta r}{2})^2 - R_{(n+1)-i}^2]^{1/2} \text{ for } j < i \\ L_{ij} &= [(R_{(n+1)-j} + \frac{\Delta r}{2})^2 - R_{(n+1)-i}^2]^{1/2} \text{ for } j = i \text{ and} \\ L_{ij} &= 0 \text{ for } j > i, \end{aligned} \tag{4.18}$$

where n is the number of chords in the system, and $L_{ij} = 0$ for $j > i$ corresponds to chord paths outside the plasma. Each Z position $Z = 50$ cm and 60 cm has $n = 4$ chords.

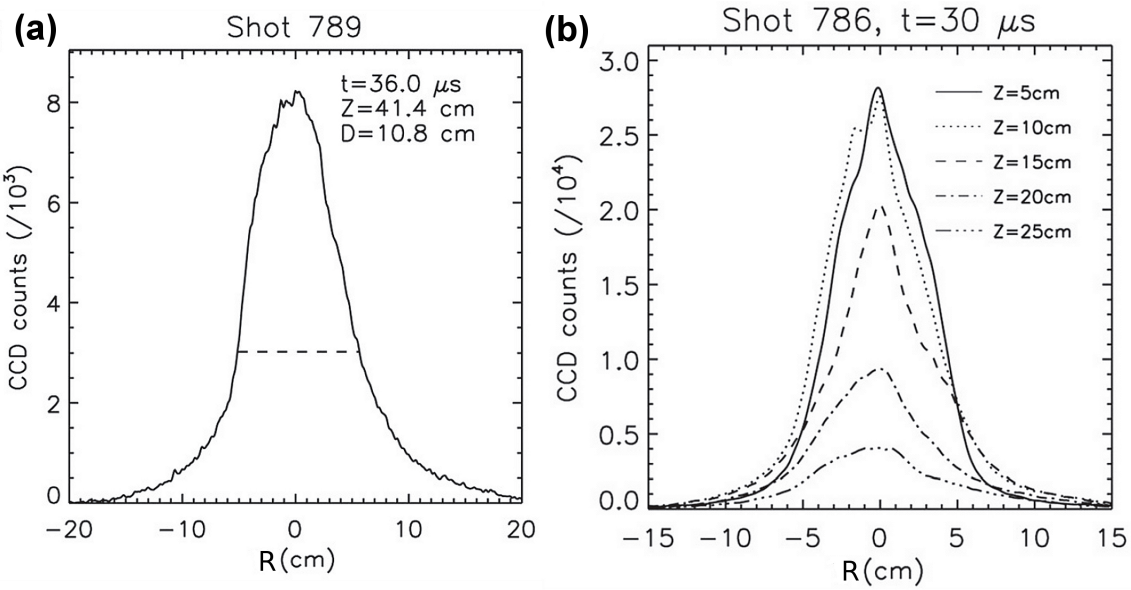

Figure 4.15: (a) CCD image line-out versus R, for frame $t = 36$ μs from Fig. 4.1 and $Z = 41.4$ cm corresponding to an interferometer chord, and the jet diameter D at a full-width (FW) of 1/e (dashed line).[26] (b) CCD line-outs at different Z positions from a single shot, with FW at 1/e jet diameters of 8.2, 8.5, 8.5, 9.1, 10.6 cm for the increasing Z values, respectively. Excerpted from [26].

Figure 4.14(a) is an intensity plot of the Abel inversion results for $[f - f_0]n_{tot}$ vs R and t for shot 1106. The chord positions of the interferometer are $R = 8$–20 cm with $\Delta r = 4$ cm at $Z = 50$ cm and $R = 4.5$–19.5 cm with $\Delta r = 5$ cm at $Z = 60$ cm. The intensity plot shows $[f - f_0]n_{tot}$ is larger at R positions closest to the jet axis, with the highest $[f - f_0]n_{tot}$ at the chord position with minimum R, $(Z, R) = (60 \text{ cm}, 4.5 \text{ cm})$. Line-outs of $[f - f_0]n_{tot}$ at $t = 25, 30, 35$ μs (Fig. 4.14(b)) show that the $[f - f_0]n_{tot}$ is peaked at chords close to the jet axis and decays non-linearly as R increases. A $\Delta R = \pm 1.5$ cm and 1.75 cm error, for $Z = 50$ cm and 60 cm respectively, is included to account for uncertainty in the chord positions due to variation in the alignment system, specifically error in the positioning of the alignment targets. Estimates using $1/e$ of peak $[f - f_0]n_{tot}$ at $R = 4.5$ cm place the jet's radius between chords $R = 9.5$ cm

and 12 cm. Thus the jet diameter is $D \approx 19$–24 cm between $Z = 50$–60 cm. So even after ~ 60 cm of propagation the jet profile is still concentrated along the jet axis.

CCD images show a similarly-shaped emission profile. Line-outs of the CCD images (Figure 4.15) show an emission profile with the peak on the jet propagation axis and a steep emission decrease with increasing R. The diameter of the emission profile at $Z = 41.4$ cm and a FW of $1/e$ is $D = 10.8$ cm.[26] So the diameter of the emission profile is roughly a factor of two smaller than the $[f - f_0]n_{tot}$ profile diameter for a similar Z range. This is consistent with the fact that emission depends strongly on density and temperature, but further detailed study is needed to make a more quantitative comparison of emission vs. density profile diameters. Figure 4.15(b) shows an initial emission diameter at $Z = 5$ cm of $D \approx 8.2$ cm, which is close to the 5 cm diameter of the railgun nozzle. The emission profile also shows a decrease in peak emission as well as radial expansion with greater propagation distances, from $D = 8.2$–10.6 cm for $Z = 5$–25 cm. Thus, from the CCD line-outs we can estimate the radial expansion of the emitting plasma. However, the $Z = 50, 60$ cm interferometer configuration does not provide significant radial expansion data for the $[f - f_0]n_{tot}$ profile. For radial $[f - f_0]n_{tot}$ expansion estimates we must use a different method.

4.5.2 Radial Expansion

The radial expansion of the jet can be estimated from axial $\Delta\phi$ measurements by assuming conservation of mass in the plasma jet. Conservation of mass tells us the total number of nuclei in the plasma, $n_{tot} = n_n + n_i$, is constant and

$$n_{tot}(t) \times V(t) = C_1, \tag{4.19}$$

where V is the volume of the plasma and C_1 is the initial number of particles in the plasma. The interferometer can measure the total number of particles in the

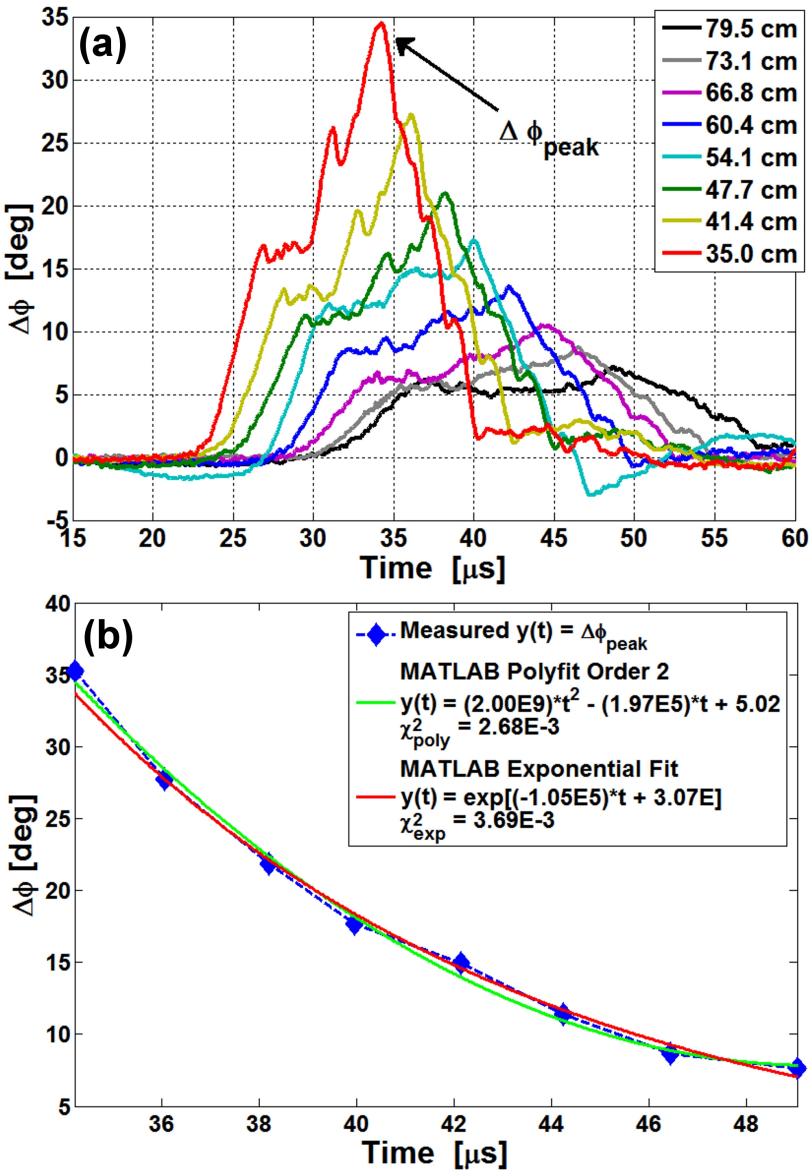

Figure 4.16: (a) Leading-jet interferometer $\Delta\phi$ profile vs time for shot 744. (b) Plot of $\Delta\phi_{peak}$ vs time, for the experimental values $\Delta\phi_{peak}$ at each chord for shot 744, and both polynomial and exponential fits to the experimental data as well as χ^2 fit-test values for both approximations. The time t for any experimental $\Delta\phi_{peak}$ value is the corresponding measured peak arrival time, $t = t(\Delta\phi_{peak})$.

plasma, $n_{tot} = n_i + n_n$, which, unlike n_e, is a quantity independent of recombination. Recombination converts ions to neutral particles but leaves n_{tot} unchanged. For the axial chord positions (Fig. 2.6) the chord path length is the jet diameter and we can approximate $\int n_{tot} dL \approx n_{tot} D$. Thus, assuming a conical jet, the conservation law gives

$$\begin{aligned} n_{tot}(t) \times D(t)^2 \times L(t) &\propto C_i \\ (n_{tot}D)(t) \times D(t) \times L(t) &\propto C_i, \end{aligned} \tag{4.20}$$

where $L(t)$ is the axial jet length and $D(t)$ is the jet diameter. The function of the jet diameter is then

$$D(t) \propto \frac{1}{(n_{tot}D)(t) \times L(t)}. \tag{4.21}$$

We determined the axial jet length $L(t)$ in Sec. 4.3.2 but still need to determine the form of $(n_{tot}D)(t)$. As we did for the velocity measurements, we use $\Delta\phi_{peak}$ as the basis of our measurement since the axial profile peak is an easily distinguishable structure at most chord positions. Thus, we approximate $(n_{tot}D)(t) \approx \Delta\phi_{peak}(t)/(f(t) - f_0)$. Spectroscopy measurements show negligible change in the ionization fraction f with jet propagation, with $f = 0.96$ decreasing to 0.94 between $Z = 0$ cm and 41.4 cm. If we assume $f(t)$ is constant over the jet propagation from $Z = 35.0$–79.5 cm, then $(n_{tot}D)(t) \propto \Delta\phi_{peak}(t)$ and the jet diameter,

$$D(t) \propto \frac{1}{\Delta\phi_{peak}(t) \times L(t)}, \tag{4.22}$$

is a function of measurable parameters from the axial $\Delta\phi$ profile. For shot 744 $\Delta\phi_{peak}$ is distinguishable at all interferometer chords (Figure 4.16(a)). Figure 4.16(b) is a plot of $\Delta\phi_{peak}(t)$ vs. time for shot 744, showing a non-linear decay in $\Delta\phi_{peak}$ with increasing time. A comparison of polynomial and exponential fits for $\Delta\phi(t)$, using

the χ^2 fit test, show the polynomial fit is a more precise match to the experimental data with $\chi^2_{polynomial} < \chi^2_{exponential}$.

To finish characterizing the $D(t)$ profile we also require a proportionality constant, D_0, such that

$$D(t) = \frac{D_0}{\Delta\phi_{peak}(t) \times L(t)}. \tag{4.23}$$

Radial profile phase-shift measurements from the $Z = 50, 60$ cm interferometer arrangement yield $D(Z = 60 \text{ cm}) \approx 21.5 \pm 2.5$ cm. The $\Delta\phi_{peak}$ arrival time at chord $Z = 60.4$ cm is $t \approx 42$ μs, thus $D(42\ \mu\text{s}) = 21.5$ cm provides a condition for calculating D_0. Similarly, we can use a CCD line-out measurement for the diameter of the emitting plasma as a condition for calculating D_0. This allows us to more directly compare the expansion as measured by the interferometer and CCD camera. CCD line-outs estimate the jet diameter as $D(36\ \mu\text{s}) = 10.8$ cm (Fig. 4.15(a)), corresponding to the peak arrival time at chord $Z = 41.4$ cm. Figure 4.17(a) shows the $D(t)$ evolution as calculated with scaling constants from both the interferometer and the CCD line-out for both the experimental values and fits of $\Delta\phi_{peak}(t)$ and $L(t)$ (Figs. 4.9 & 4.16 and shot 744). Figure 4.17(b) shows $D(t)$ measured using CCD line-outs at $Z = 41.4$ cm at various times. Both estimates suggest non-linear radial expansion between at least $t = 35$–45 μs with qualitatively similar growth curves. However, even using the CCD scaling constant, $D(t)$ estimates using Eqn. 4.23 still tend to overestimate the jet diameter compared to direct CCD measurements. Equation 4.23 with the CCD scaling constant estimates $D(44\ \mu\text{s}) \approx 20$ cm, while direct CCD measurements show $D(44\ \mu\text{s})_{CCD} \approx 15$ cm. Using the interferometer value of the scaling constant and Eqn. 4.23 we estimate the interferometer jet diameter to be larger than the CCD measurements by roughly $D(t) = 1.5 \times D_{CCD}(t)$. Between

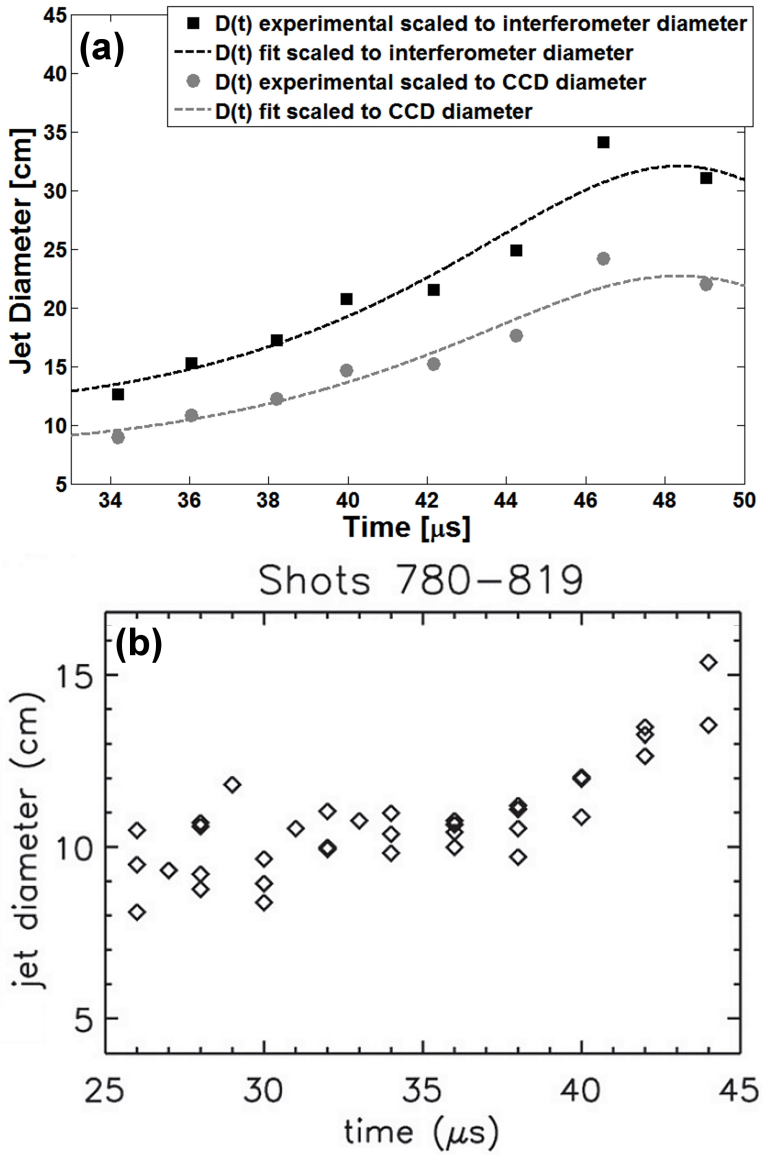

Figure 4.17: (a) Plot of jet diameter $D(t)$ vs. time as calculated using Eqn. 4.23 for experimental values and fits for $\Delta\phi_{peak}(t)$ and $L(t)$ from Figs. 4.9 & 4.16 for shot 744. Includes $D(t)$ calculated using both $D(42\ \mu s) = 21.5$ cm from interferometer measurements and $D(36\ \mu s) = 10.8$ cm from CCD measurements. (b) D versus time at $Z = 41.4$ cm from CCD line-outs (shots 780-819). Figure excerpted from [26].

$t = 35$–45 μs the interferometer estimate of $D(t)$ for shot 744 also gives

$$\begin{aligned} \dot{D}_{avg}/2 &= 0.63 \pm 0.41 \text{ cm}/\mu\text{s} \\ \dot{D}_{int}/2 &= 0.71 \text{ cm}/\mu\text{s}, \end{aligned} \tag{4.24}$$

where $\dot{D}_{int}/2$ is the radial expansion calculated between chord $Z = 35.0$ cm and 54.1 cm (similar to $\dot{L}_{int}$), and $\dot{D}_{avg}/2$ is the radial expansion averaged over the expansions calculated between subsequent chords (similar to v_{avg}) given by

$$\dot{D}_{avg}/2 = \frac{1}{2(n-1)} \sum_{1}^{n-1} \frac{(D_{i+1} - D_i)}{(t_{i+1} - t_i)}, \tag{4.25}$$

where t is the peak arrival time. Thus the radial expansion rate for shot 744 is within the range of the axial expansion $\dot{L}_{int}/2 = 0.88 \pm 0.47$ cm/μs, as calculated in Sec. 4.3.2, which we found was consistent with hydrodynamic expansion estimates.

4.6 Jet Total Density and Volume Expansion

Since we have estimates of the jet diameter, we can convert the line-integrated density measurements, $\int n_{tot} dl$, into actual density measurements n_{tot}. Earlier we approximated $\int n_{tot} dl \approx n_{tot} D$. Thus, the peak line-averaged total density is

$$n_{tot}(t) = \frac{(n_{tot} D)(t)}{D(t)} = \frac{\Delta\phi_{peak}(t)}{C(f - f_0) \times D(t)} \tag{4.26}$$

if we can measure $D(t)$ directly (from CCD line-outs), or

$$\begin{aligned} n_{tot}(t) &= \frac{(n_{tot} D)(t)}{D(t)} = \frac{\Delta\phi_{peak}(t)}{C(f - f_0)} \times \frac{\Delta\phi_{peak}(t) \times L(t)}{D_0} \\ &= \frac{\Delta\phi^2_{peak}(t) \times L(t)}{D_0 C(f - f_0)}, \end{aligned} \tag{4.27}$$

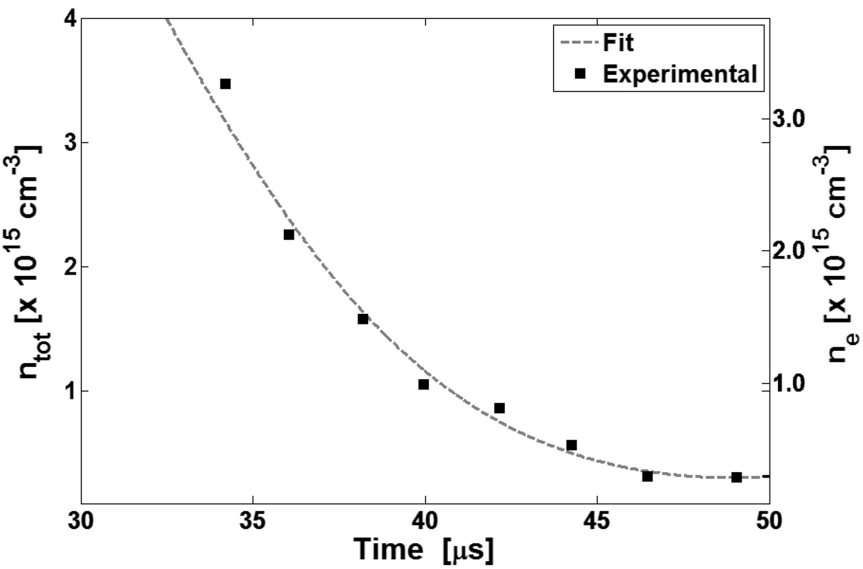

Figure 4.18: (a) Interferometer n_{tot} (left-hand axis) and $n_e = f \times n_{tot}$ (right-hand axis) vs. time for shot 744, using Eqn. 4.27 with $f = 0.94$ and $D(42\ \mu s) = 21.5$ cm, from spectroscopy and interferometer estimates respectively, and experimental and fitted estimates of $\Delta\phi_{peak}(t)$ and $L(t)$ from Figs. 4.9 & 4.16.

if we must estimate $D(t)$ using Eqn. 4.23 (from interferometer data only). Estimates of n_{tot} using Eqn. 4.27, $f = 0.94$ from spectroscopy and $D(42\ \mu s) = 21.5$ cm for shot 744 put $n_{tot} = 3.5 \times 10^{15}$ cm^{-3} decreasing to 2.9×10^{14} cm^{-3} for jet propagation between $Z = 35.0$ cm and 79.5 cm (left-hand axis of Fig. 4.18). We know both n_{tot} and f so we can also estimate n_e for a singly-ionized plasma, $n_e = n_i = f \times n_{tot}$ (right-hand axis of Fig. 4.18). Since $f \approx 1$ then $n_{tot} \approx n_e$.

As originally introduced in Sec. 4.3.1, the ionization fraction of the plasma $f = 0.94$ is a PrismSPECT estimate assuming a pure argon plasma with $T_e = 1.4$ eV and $n_e = 2 \times 10^{15}$ cm^{-3}. The iteration method for estimating the ionization fraction of the plasma from both spectroscopy and interferometer data is discussed in Sec. 2.3. Spectroscopy measurements were taken to correspond to $\Delta\phi$ measurements at chord $Z = 41.4$ cm, giving a joint estimate of $(f, n_e) \approx (0.94, 2 \times 10^{15}$ cm$^{-3})$ at this

position at the $\Delta\phi$ peak arrival time of $t \approx 36$ μs. Figure 4.19 shows a comparison of n_e from Stark broadening and n_e from interferometer estimates at $Z = 41.4$ cm, where interferometry estimates use $\Delta\phi$ averaged over shots 775-819, discrete $D(t)$ estimates from CCD line-outs at $Z = 41.4$ cm (Fig. 4.17(b)) and $f = 0.94$. Errors bars on the interferometer n_e estimates mark a lower bound for n_e to account for the difference in diameter estimates between the CCD line-outs and the interferometer profiles. This error assumes $D_{int}(t) \approx 2 \times D_{CCD}(t)$ corresponding to the upper bound on the jet diameter used to estimate D_0, $D(Z = 60 \text{ cm}) = 24$ cm. Overall, these interferometer and Stark broadening measurements of n_e agree within a factor of ≈ 2.

Stark broadening is also used to estimate $n_e \approx 2 \times 10^{16}$ cm^{-3} from spectroscopy at the gun nozzle, which is approximately a factor of 10 larger than $n_e \approx 2 \times 10^{15}$ cm^{-3} at the $Z = 41.4$ cm chord position.[26] Spectroscopy estimates also find $f = 0.96$ at the gun nozzle, so $n_e \approx n_{tot}$. Thus, the jets experience a factor of 10 drop in n_{tot} over this propagation distance as well. Similarly, n_{tot} estimates over the ≈ 45 cm propagation range of the interferometer chords show a factor of ≈ 10 decrease in density, from $n_{tot} = 3.0 \times 10^{15}$ cm^{-3} decreasing to 2.6×10^{14} cm^{-3} for values averaged over shots 775-819.

Hydrodynamic theory yields nearly a factor of twenty uncertainty for the predicted jet expansion, and a corresponding density drop. Hydrodynamics, assuming a constant jet velocity v and Mach number M, allows the radial and axial expansion rates to be approximated as between C_s, for the jet bulk, and $2C_s/(\gamma - 1)$.[37] For a propagation distance of $\Delta Z \approx 50$ cm with $v \approx 30$ km/s, the jet expands over the transit time $\Delta t \approx 16.7$ μs. For an argon plasma with $T_e = 1.4$ eV and $\gamma = 1.4$, the expansion rates are $C_s \approx 2.2$ km/s and $2C_s/(\gamma - 1) \approx 11$ km/s. Thus, the jet radius would increase by $\Delta r = C_s \Delta t$–$(2C_s/(\gamma - 1))\Delta t = 3.7$–$16.7$ cm. Assuming an initial jet radius of $r_0 = 2.5$ cm (gun nozzle radius), then the jet radius would

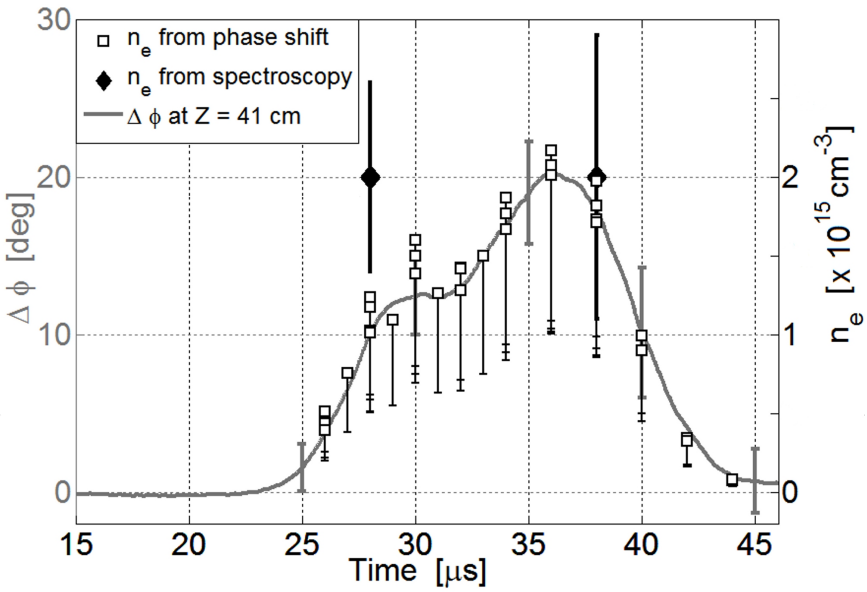

Figure 4.19: Interferometer phase shift $\Delta\phi$ averaged over shots 775-819 for the $Z = 41.4$ cm chord (left hand axis) and n_e (right hand axis) vs. time. The square data points are derived from Eqn. 4.26 using $f = 0.94$, and the jet diameter $D_{CCD}(t)$ obtained from CCD line-outs at $Z = 41.4$ cm (Fig. 4.17(b)), with error bars representing a lower limit due to the factor of two difference between CCD and interferometer diameter estimates, $D_{int}(t) \approx 2 \times D_{CCD}(t)$. The two diamond data points are from Stark broadening analysis of the H_β line from spectroscopy (shots 785 and 790). Each discrete data point corresponds to a separate shot.[26]

increase by a factor of $r/r_0 = 2.48$–7.68. Similarly, the jet length would increase by $\Delta L = 7.4$–33.4 cm, which would be a factor of $L/L_0 = 1.37$–2.67 assuming an initial jet length of $L_0 \approx 20$ cm from photodiode measurements. Overall, the jet volume could increase by a factor of $V/V_0 = 8.4$–157.5. Fortunately, experimental measurements place the volume expansion at the low end of this range, with $V/V_0 \approx 10$ corresponding to the measured decrease in n_e and n_{tot}. The measured expansion is most consistent with plasma bulk expansion (C_s), as might be expected from the persistence of a strongly-peaked axial and radial profile (cohesive jet bulk) during the investigated jet propagation range.

4.7 Conclusions

	$Z \approx 2$ cm	$Z \approx 50$ cm
$n_e \approx n_{tot}$	10^{16} cm^{-3}	10^{15} cm^{-3}
v	30 km/s	30 km/s
M	14	14
L	20 cm	50 cm
D	5 cm	10 cm (PD) - 20 cm (Int)

Table 4.1: Summary of both initial and downstream single-jet parameters.

Even operating at reduced gun currents, $I < 300$ kA, the overall plasma jet performance was very promising for future liner formation experiments. With a gun current of $I \approx 280$ kA, the jet had initial $n_e \approx n_{tot} \sim 10^{16}$ cm^{-3} and a velocity of $v \approx 30$ km/s, which are only a factor 10 and 2 respectively lower than the desired jet parameter achieved at HyperV Technologies. The jets have strongly peaked axial and radial profiles showing that the majority of the jet mass is confined at the jet center. These peaked profiles persist for the entire propagation distance of ≈ 60 cm, the radius the jets are expect to merge at in full liner experiments. The plasma jet profile not only stays cohesive, but shows only a factor of ≈ 10 drop in density (volume expansion) over this propagation distance. This density drop is near the lower limit of the 8.4–157.5 drop range predicted by hydrodynamics. An estimated jet temperature of $T_e \approx 1.4$ eV and velocity of $v \approx 30$ km/s at $Z \approx 40$ cm shows that the jet stays strongly supersonic during its propagation, with $M \approx 14$. Since the density drop is minimal but the jet maintains its initial velocity, the loss of jet kinetic energy during propagation is also minimal. This is promising for full liner experiments, since the greater the jet kinetic energy, the higher the peak pressures the plasma liner can achieve. Overall, the single-jet results indicated a readiness for PLX to proceed to jet-merging experiments.

Chapter 5

Two-Jet Oblique Merging Experiments

The second stage of experiments for PLX was designed to assess the suitability of plasma jet merging for formation of plasma liners. The first phase of this stage was to study two obliquely merging jets. Two railguns were mounted on adjacent chamber ports, as shown in Fig. 5.1(a), to mimic part of the preferred railgun placement for full liner experiments. For this positioning, the half-angle between the two jet axes of propagation is $\theta \approx 12^o$, with a nozzle separation of ≈ 46 cm (Fig 5.1(c)). Figure 5.2 shows CCD images of the time evolution of jet-merging. Formation of a stagnation layer along the jet-merge plane and a double-peaked emission profile transverse (R direction) to the layer are clearly visible. Our merging experiments focus on the experimental identification and characterization of the emergent stagnation layer, and the demonstration that our observations are consistent with hydrodynamic oblique shock theory. [37, 48] We made measurements for the cases of top-only, bottom-only, and both jets firing. This ensures the most direct comparison of single- to merged-jet measurements using the new diagnostic positions.

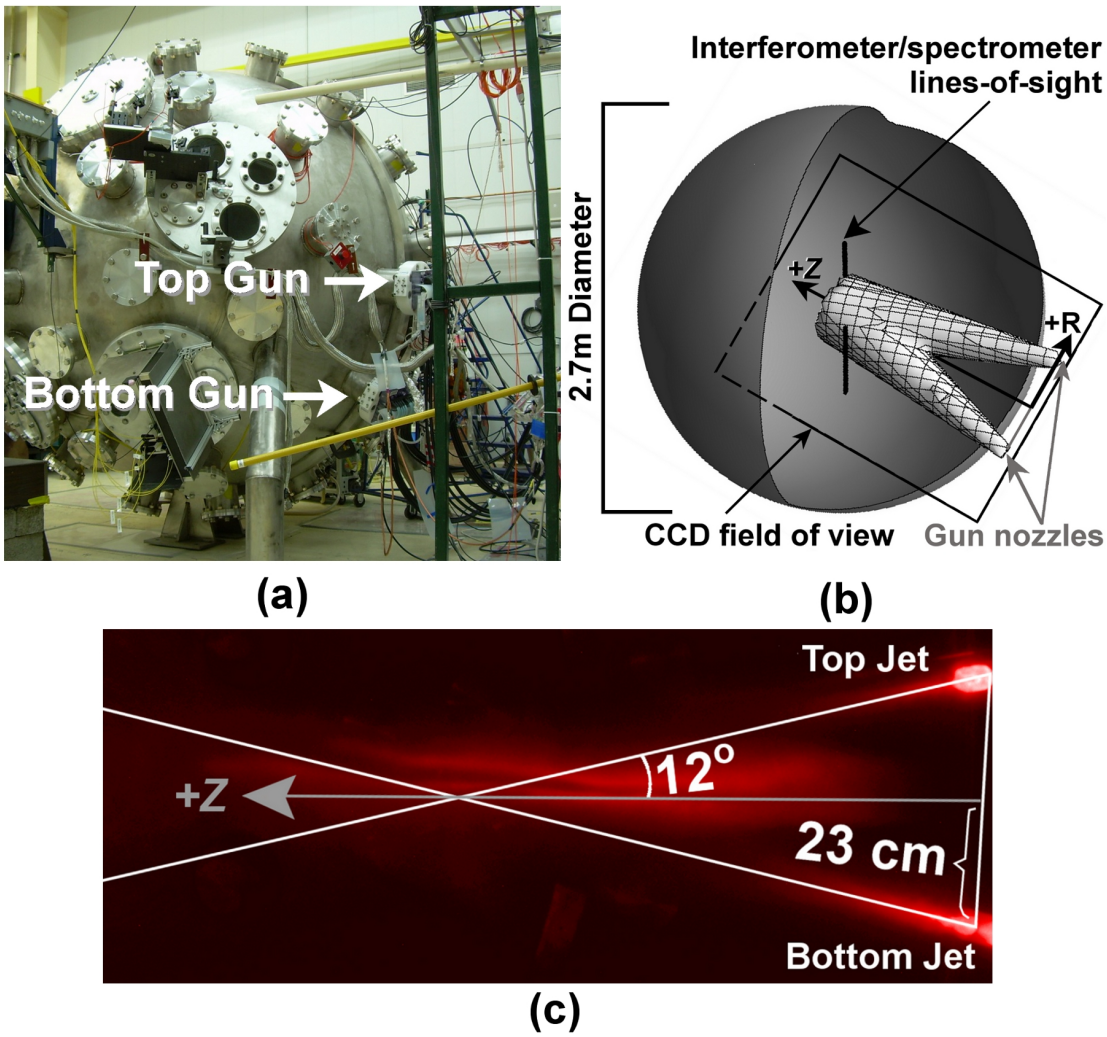

Figure 5.1: (a) Image of the experiment with two railguns installed on adjacent ports. (b) Schematic of the experiment showing the spherical vacuum chamber, location of railgun nozzles mounted 24° apart, two merging plasma jets, (R,Z) coordinates used in the paper, one set of approximate interferometer/spectrometer lines-of-sight ($Z \approx 84$ cm), and CCD camera field-of-view. (c) CCD image of two jets inside the chamber. The Z axis and individual jet axes of propagation are marked. Each railgun nozzle is approximately $R = 23$ cm from the midplane, and the half-angle between the jet axes of propagation is 12^o.

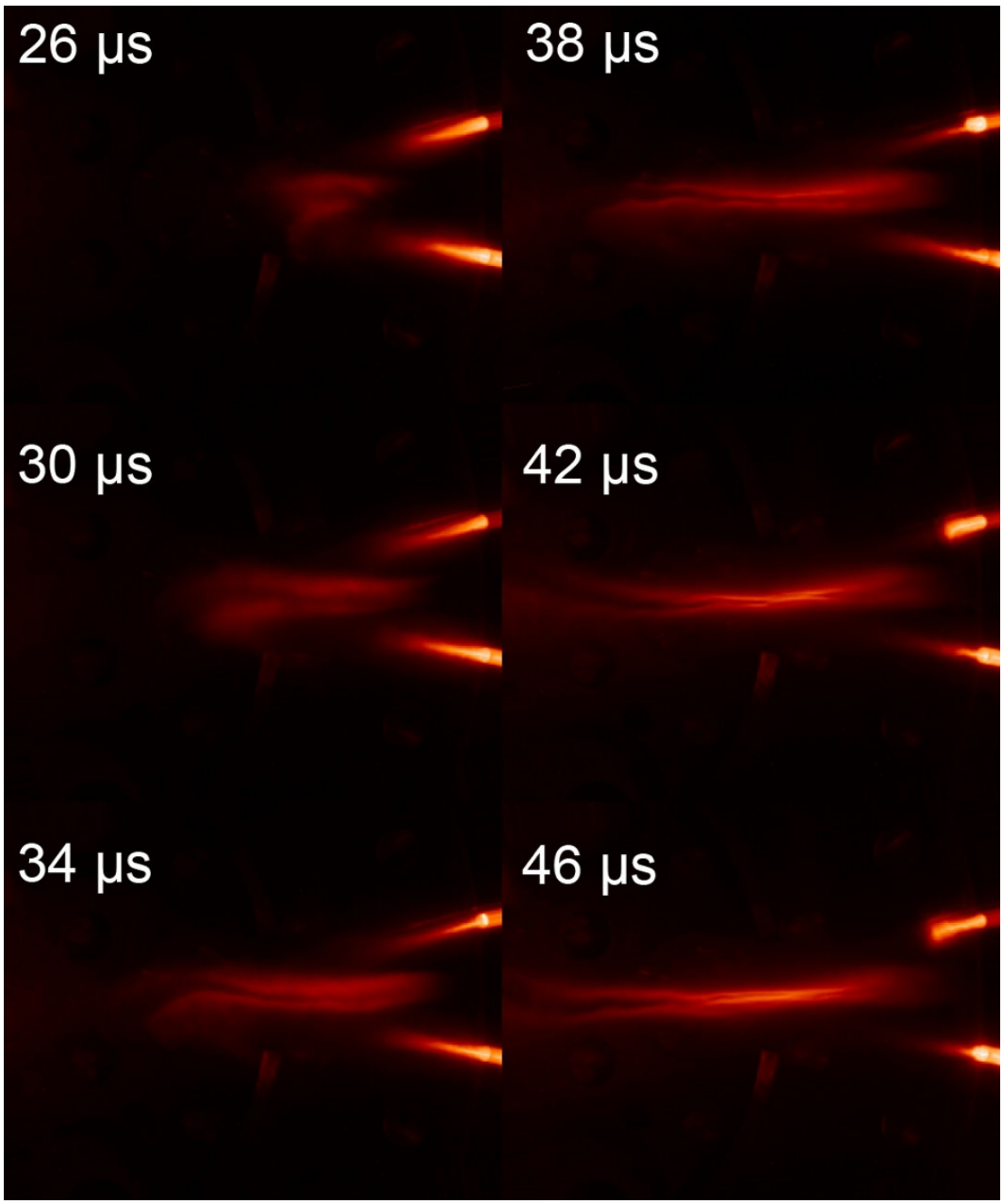

Figure 5.2: False-color CCD images (log intensity, 20 ns exposure) of oblique jet-merging (shots 1130, 1128, 1125, 1120, 1134, 1138). The two railgun nozzles ($\approx$ 46 cm apart) are visible on the right-hand-side of each image.

5.1 Diagnostic Suite Setup

During single-jet propagation experiments, diagnostics were situated about the axis of propagation of that jet. During oblique merging experiments, most of the physics of interest occurs along the merging plane of the two jets instead. The spectrometer, interferometer and CCD camera were repositioned to focus on several different areas along the merging plane.

Emission from a single jet decayed to a negligible level within the previous CCD view of $Z \approx 70$ cm. During jet merging, the merged-jet emission was observed out to much greater distances. Accordingly a wide-angle lens was added to the CCD camera to extend its field of view from $Z \approx 70$ cm to $Z \approx 150$ cm to encompass the entire length of the emitting plasma, as shown in Fig. 5.1(b).

The interferometer and spectrometer positions were reconfigured twice, once to focus on jet merging near the predicted initial jet interaction point, at $Z \approx 50, 60$ cm, and a second time to focus on the upstream merged-jet, at $Z \approx 85$ cm, as shown in Fig. 5.3. The initial point of jet interaction was predicted by assuming a jet adiabatic radial expansion speed of $2C_s/(\gamma - 1)$.[37] The expansion angle θ_{exp} is given by $\tan\theta_{exp} = [C_s/(\gamma - 1)]/v = 1/[M(\gamma - 1)]$. For a $M = 14$ jet with $\gamma = 1.4$, this gives a $\theta_{exp} \approx 10^o$. The merging geometry also includes a merging half-angle between the jet axes of $\theta_m = 12^o$. The predicted point of jet interaction is then:

$$Z = \frac{23 \text{ cm}}{\tan^{-1}(\theta_m + \theta_{exp})} = \frac{23 \text{ cm}}{\tan^{-1}(12^o + 10^o)} \approx 57 \text{ cm}. \tag{5.1}$$

The interferometer chords were placed on either side of the predicted interaction point in hope of measuring any potential shock boundary formation. This interferometer configuration placed four chords at $Z \approx 50$ cm with inter-chord spacing of $d = 4$ cm, and four chords at $Z \approx 60$ cm with inter-chord spacing of $d = 5$ cm. Both lines of chords were approximately perpendicular to the midplane. For this configuration

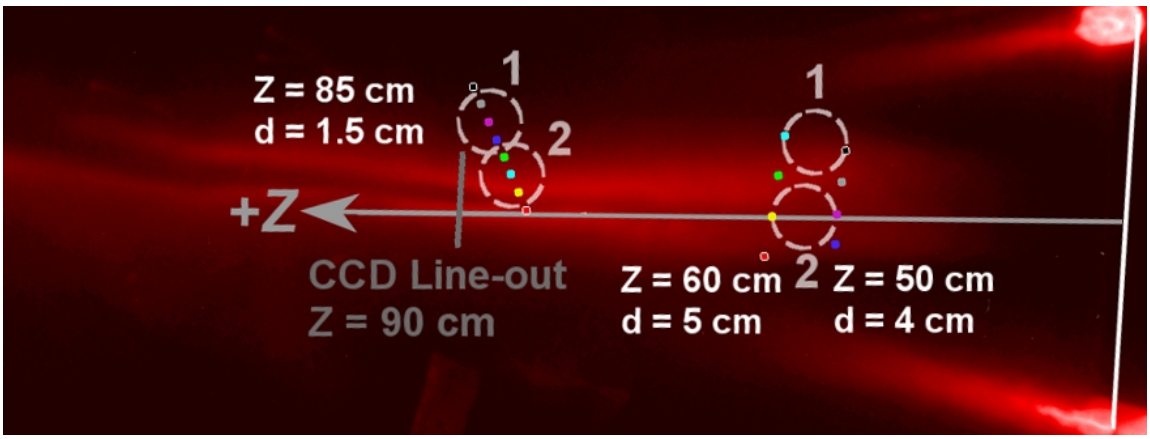

Figure 5.3: Interferometer chord and spectroscopy view positions for two different configurations during merging experiments. Each configuration has eight interferometer chords, marked as colored dots, and two spectroscopy areas of view, marked by dashed circles. The CCD line-out position at $Z = 90$ cm is represented as a dark gray line.

the spectrometer had two possible viewing areas at $Z \approx 55$ cm with one off axis at $R \approx 12$ cm (Position 1) and one on the midplane (Position 2). The spectrometer field of view had diameter ≈ 7 cm.

For the second diagnostic configuration the spectrometer and interferometer were moved to $Z \approx 85$ cm. The interferometer chords were arranged roughly perpendicular to the midplane, with inter-chord spacing of $d = 1.5$ cm, starting at $R = 0.75$ cm. The spectrometer was centered on the chords at $R = 8.25$ cm and $R = 3.75$ cm, labeled Position 1 and Position 2 respectively.

5.1.1 Impurity Considerations

Unlike the single-jet studies, the plasma impurity percentage rose to non-negligible levels during jet merging experiments. We measured the difference in the chamber pressure rise between argon gas-injection only and gas-injection with the railgun

discharge in order to estimate the upper limit on the impurity percentage of the plasma jet. From the difference in chamber pressure rise we estimated that the plasma jets are, in the worst case, approximately 30% argon with 70% impurities. Identification of bright Al and O spectral lines in our data (Fig. 5.4) suggest that impurities are from the zirconium-toughened alumina (0.15 ZrO_2 and 0.85 Al_2O_3) of the railgun insulators, which showed notable damage when inspected after the experiments. Due to lack of Zr lines, we limit our assumption of impurity species to just Al and O. Since we do not know precisely the impurity fraction or mixture ratios of impurities, we perform our data analysis by considering two extreme cases of (i) 100% argon and (ii) 30% argon with 70% impurities. Including non-argon species in our analysis also requires the use of the bounding function, Err, in the interferometer density calculations (Sec. 3.1.6–3.1.7) given by:

$$\int n_{tot} dl = \frac{\Delta\phi}{C_e[Z_{\text{eff}} - Err]}. \tag{5.2}$$

Thus, for case (ii), we approximate the plasma jet to be 43% O and 24% Al, from the Al and O ratios in the alumina, and assume that $Err_{max} = Err_{\text{Al I}} = 0.082$. The extreme cases of 30% Ar/70% Al and 30% Ar/70% O were also considered for use as limiting cases, but the PrismSPECT predictions for these mixtures provided was contradictory or incomplete when compared to experimental spectra.

Plasma composition directly affects jet Mach number, since Mach number is dependent on ion mass $\mu = m_i/m_p$, where m_p is the proton mass:[4]

$$M = \frac{v}{C_s} = \frac{v}{9.79 \times 10^3}\sqrt{\frac{\mu}{\gamma Z_{\text{eff}} T_e}}. \tag{5.3}$$

During single-jet experiments, we determined $M = 14$ for a single jet assuming the jet was 100% argon, $v = 30$ km/s, $T_e = 1.4$ eV and $f = Z_{\text{eff}} = 0.94$ (both from spectroscopy at $Z = 41$ cm), and $\gamma = 1.4$. Plasma composition also affects spectroscopy estimates of Z_{eff}. Assuming the 30%/70% mixture composition, $T_e =$

1.4 eV and $n_{tot} = 5 \times 10^{14} cm^{-3}$ (from Sec. 5.3.1) then $Z_{\text{eff}} = 0.92$, which is relatively unchanged compared to the previous case. For the 30%/70% mixture, $\mu = 0.30 \times \mu_{Ar} + 0.24 \times \mu_{Al} + 0.43 \times \mu_O = 25$ and $M \approx 11$ (for $v = 30$ km/s, $\gamma = 1.4$, $T_e = 1.4$ eV and $Z_{\text{eff}} = 0.92$). However, the 24% Al/43% O ratio is an assumption rather than a measured quantity. If we assume $\mu = \mu_O$, since O is the lightest element in the mix $\mu_O < \mu_{Al} < \mu_{Ar}$, this places a more stringent lower bound on the jet Mach number than the 24% Al/43% O estimate. For the same mixture parameters, $\mu = \mu_O$ yields $M = 9$. Thus the jet Mach number is estimated to be in the range $9 < M < 14$; still highly supersonic irrespective of impurity composition.

5.2 Merged-Jet Emission Envelope

During jet merging an emission structure forms about the jet interaction plane (Fig. 5.2) that is not present during single jet experiments. We postulate that the emission structure corresponds to shock formation, since the jet interaction forces a turn in a supersonic flow. Then the emission layers are post-shocked plasma, consistent with expected plasma density and/or temperature increases post-shock, and their edges (at larger $|R|$) correspond to the shock boundaries. Since we have already established that magnetic field is negligible by the time of jet-merging, $t > 20$ μs, we begin our treatment of shock formation with a comparison to one-dimensional hydrodynamic shock analysis.

5.2.1 1D Hydrodynamic Shock Theory

Qualitatively, the merging geometry for an individual jet resembles that of a supersonic flow past a wedge or compression corner.[37, 48] Figure 5.5(a) shows a simple schematic of the jet flows as they interact and Fig. 5.5(b) shows a similar structure

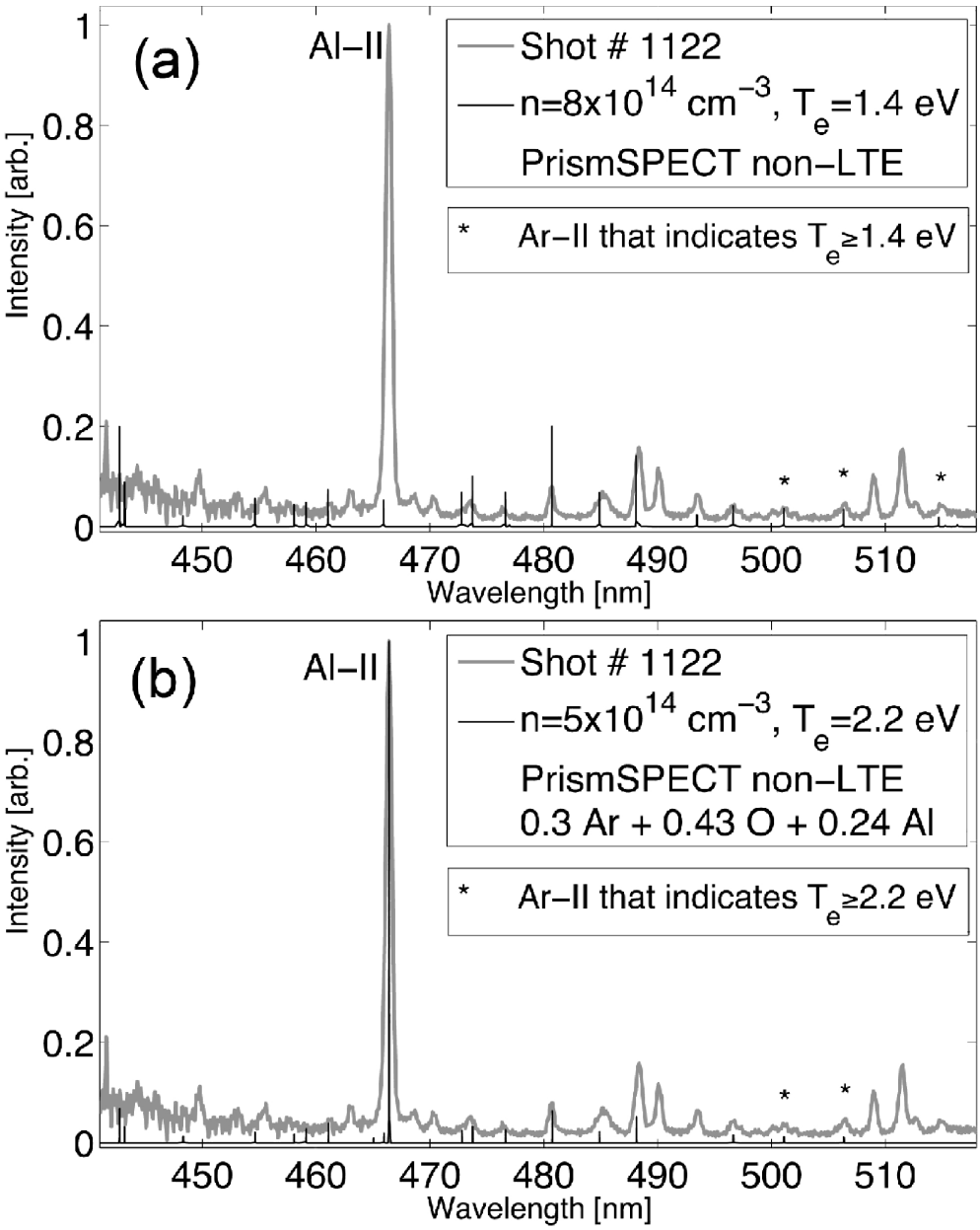

Figure 5.4: Spectral data (gray) and non-LTE PrismSPECT calculations (black) for the merged-jet stagnation layer ($Z \approx 84$ cm, $t = 36$ μs). The PrismSPECT calculations are for (a) 100% argon and (b) 30%/70% mixture. Lower bounds on peak T_e are inferred based on the presence of the Ar II lines indicated by asterisks.

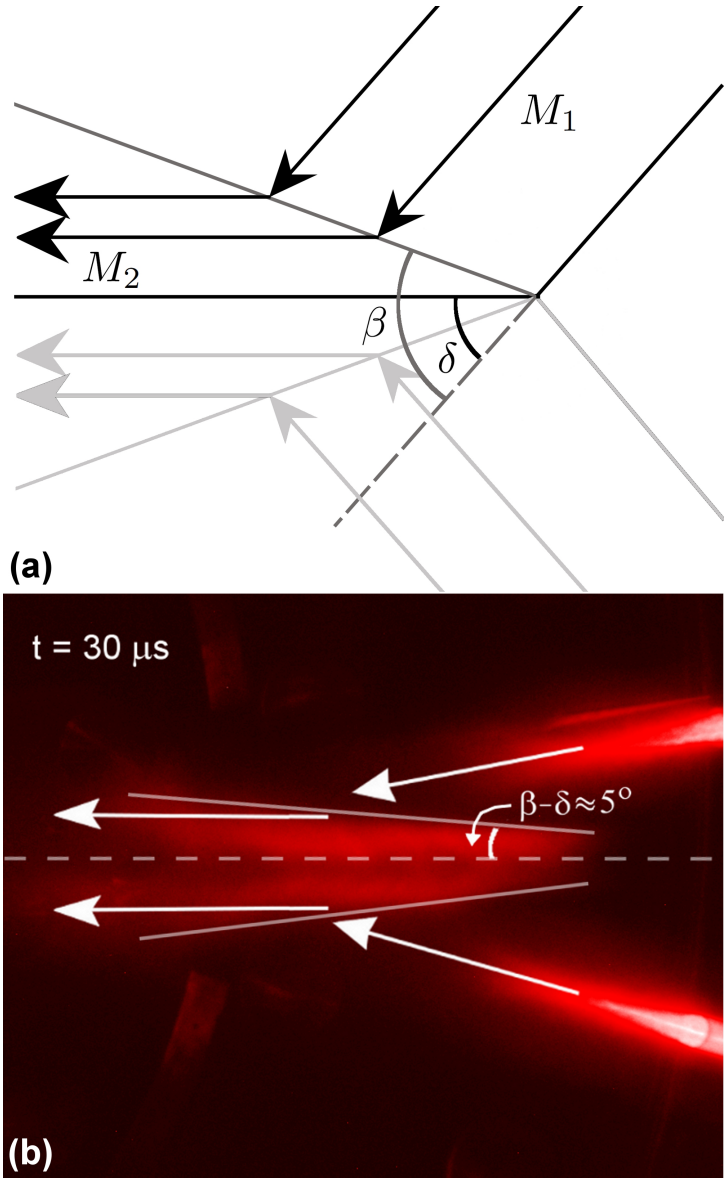

Figure 5.5: (a) Simple schematic of the interaction of two obliquely interacting supersonic flows with initial Mach numbers M_1. Flow intersect the midplane at an angle δ. A shock boundary forms at an angle β from the original flow direction. Post-shock flows have Mach number M_2 and flow direction parallel to the interaction plane. (b) CCD image (shot 1089, $t = 30$ μs) with postulated shock boundaries (solid white lines) and observed shock angle $\beta - \delta \approx 5^\circ$ relative to the midplane.

in a merged-jet CCD image at $t = 30$ μs. In the schematic, an individual jet flows toward the midplane with some initial (upstream) Mach number M_1, where the flow direction is at an angle δ to the midplane. In a compressible, neutral fluid model, the transverse components of the flow velocities have equal magnitude but opposing direction, $\vec{v}_{R,top} = -\vec{v}_{R,bottom}$. Thus, the net transverse flow at the midplane is zero and the plane approximates a boundary through which no fluid can pass. In a compression corner model, the boundary is the surface of the compression corner. Forcing a supersonic flow to turn causes the formation of an oblique shock boundary at an angle β to the original flow direction, as given by:[48, 21]

$$\tan\delta = 2\cot\beta\left[\frac{M_1^2\sin^2\beta - 1}{M_1^2(\gamma + \cos 2\beta) + 2}\right]. \tag{5.4}$$

The flow downstream (post-shock) of the shock is parallel to the midplane and has a new Mach number M_2, where $M_2 < M_1$.

The shock boundary is modeled as a discontinuity surface through which the fluid passes, separating the flow into pre-shock and post-shock regions. The pre-shock fluid parameters remain unaltered; the fluid passes through the shock boundary at a greater speed ($M_1 > 1$) than information about changes in the flow can propagate upstream ($M = 1$). For an oblique shock, only the flow components normal to the shock boundary contribute to shock formation. Assigning subscripts of '1' to pre-shock (and '2' to post-shock) values, the pre-shock normal flow components are given by

$$(M_{1n}, v_{1n}) = (M_1, v_1)\sin\beta. \tag{5.5}$$

The post-shock fluid parameters are determined by the jump conditions, which are derived from the conservation laws for mass, momentum, and energy. For a polytropic gas the jump conditions for an oblique shock in the reference frame of the

shock are:[48, 21]

$$\rho_1 v_1 \sin\beta = \rho_2 v_{n2} \tag{5.6}$$

$$\rho_1 (v_1 \sin\beta)^2 + p_1 = \rho_2 v_{n2}^2 + p_2 \tag{5.7}$$

$$\rho_1 v_1 \sin\beta (\frac{\gamma}{\gamma-1}\frac{p_1}{\rho_1} + \frac{v_1^2}{2}) = \rho_2 v_{n2} (\frac{\gamma}{\gamma-1}\frac{p_2}{\rho_2} + \frac{v_2^2}{2}). \tag{5.8}$$

Once we determine β, we can use the jump conditions to compare predicted and measured post-shock parameters to assess the consistency of the experiment with collisional shock formation.

5.2.2 Jet Envelope Formation

We can examine the merged-jet emission envelope in terms of the shock variables we just defined. In the experiments, the turning angle δ is a function of the distance from the guns at which the jets merge. We define $\tan\delta = (23\text{ cm})/Z_i$, where Z_i is the point at which jets first interact, estimated from CCD images as the minimum Z for which merged-jet emission is observed. Once we know Z_i, we can determine the shock boundary β from

$$(23\text{ cm})/Z_i = 2\cot\beta \left[\frac{M_1^2 \sin^2\beta - 1}{M_1^2(\gamma + \cos 2\beta) + 2}\right], \tag{5.9}$$

as long as we know M_1. We plot δ vs Z (Fig. 5.6(b)) for a range of possible Z, as well as the shock angle relative to the midplane $\beta - \delta$, for $M = 9$ and $M = 14$. For both $M = 9$ and $M = 14$ the $\beta - \delta$ solutions are very similar, as expected since $M \gtrsim 10$ approaches the $M \to \infty$ shock limit. One-dimensional oblique shock theory also predicts a maximum turning angle, $\delta < \delta_{max}$, for any given M, for which an oblique shock will form. At $M = 9$–14 the $\delta_{max} \approx 45°$ with a corresponding $Z_i \approx 25$ cm, shown as a cutoff for $\beta - \delta$ in Fig. 5.6(a). Thus for $Z_i \gtrapprox 25$ cm, we expect the merged-jet envelope to still resemble the wedge structures shown in Fig. 5.5.

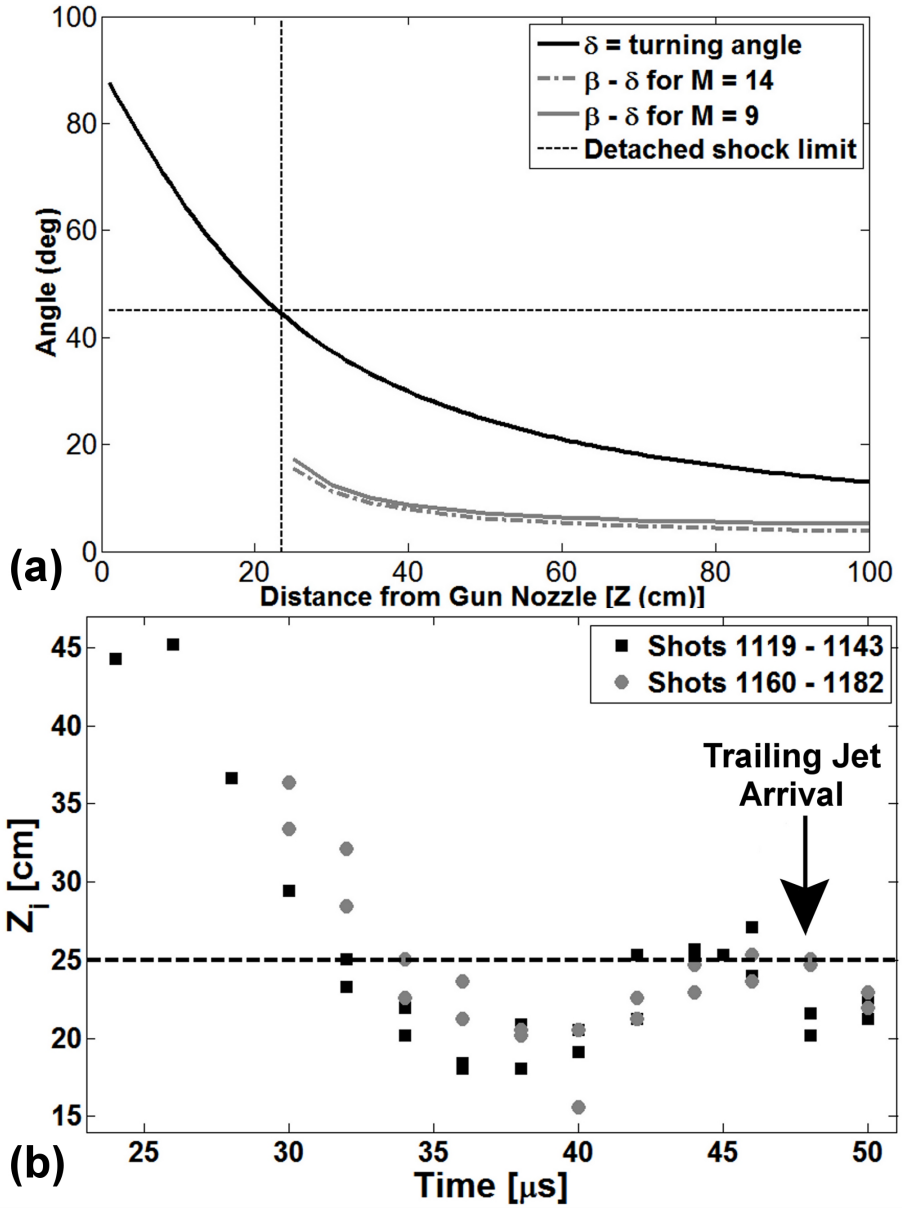

Figure 5.6: (a) Plot δ and $\beta - \delta$, for both $M = 9$ and $M = 14$, vs. Z. The predicted threshold turning angle, $\delta = \delta_{max} = 45°$, and corresponding $Z_i(\delta_{max}) \approx 25$ cm are marked with dashed lines. (b) Plot of Z_i vs. time for data sets shots 1119–1143 and shots 1160–1182. Theoretical cutoff for oblique shock formation, $Z_i \approx 25$ cm, is marked by a dashed line. Approximate trailing jet arrival time indicated.

For $t \simeq 24$–32 μs, the merged jet does have the same qualitative wedge-shaped boundary that is consistent with a simple oblique shock (Fig. 5.2). Figure 5.5(b) shows the CCD image for shot 1089, at $t = 30$ μs and $Z_i \approx 30$ cm, with marked postulated shock boundaries. In this case, the measured $\beta - \delta \approx 5°$. For $M = 9$–14, the predicted $\beta - \delta \approx 9°$–$10°$, which is within a factor of two of the measured value. This is reasonable given that the one-dimensional prediction does not include three-dimensional nor equation-of-state [46] effects. So for these times, the merged-jet envelope is consistent with our oblique shock expectations. From Fig. 5.2 we can see that Z_i varies in time during jet merging. Plotting Z_i vs t (Fig. 5.6(b)), for shots 1119–1143 and shots 1160–1182, shows that Z_i varies from $Z_i \approx 45$ cm at $t = 26$ μs to $Z_i \approx 18$ cm at $t = 36$ μs. We observe that Z_i initially decreases as time increases, $t \simeq 24$–40 μs, during jet merging. Z_i begins to increases at $t > 40$ μs, as the bulks of the leading jets finish merging, only to decrease again at $t \gtrsim 45$ μs, as the trailing jets begins to interact. Consistent with our hypothesis that the wedge-shaped merged jet observed at $t \simeq 24$–32 μs is an oblique shock, $Z_i \gtrapprox 25$ cm ($\delta < \delta_{max}$) for $t \gtrsim 32$ μs.

However, at later times, $t \gtrsim 32$ μs, we measure $Z_i \lessapprox 25$ cm ($\delta > \delta_{max}$). At these times the merged-jet also evolves from a wedge-like structure to a thinner layer concentrated along the midplane (Fig. 5.2). Hydrodynamic theory says that for $\delta > \delta_{max}$ a normal shock, or detached shock, will form instead of an oblique shock. To understand this we look back to the structure of an oblique shock. For a supersonic flow past a wedge with $\delta < \delta_{max}$, an oblique shock forms with the shock boundaries attached to the point of deflection, the tip of the wedge (Fig 5.7(a)). In an oblique shock, only the normal component of the flow changes at the flow boundary, becoming subsonic, while the tangential component remains unchanged. Thus the post-shock flow of an oblique shock is still usually supersonic; in some systems there are some limited combinations of M and δ where subsonic flow behind an oblique shock is possible. For a normal shock $\beta \approx 90°$ and the total flow velocity is normal to the shock boundary. So the post-shock velocity is completely subsonic. When a

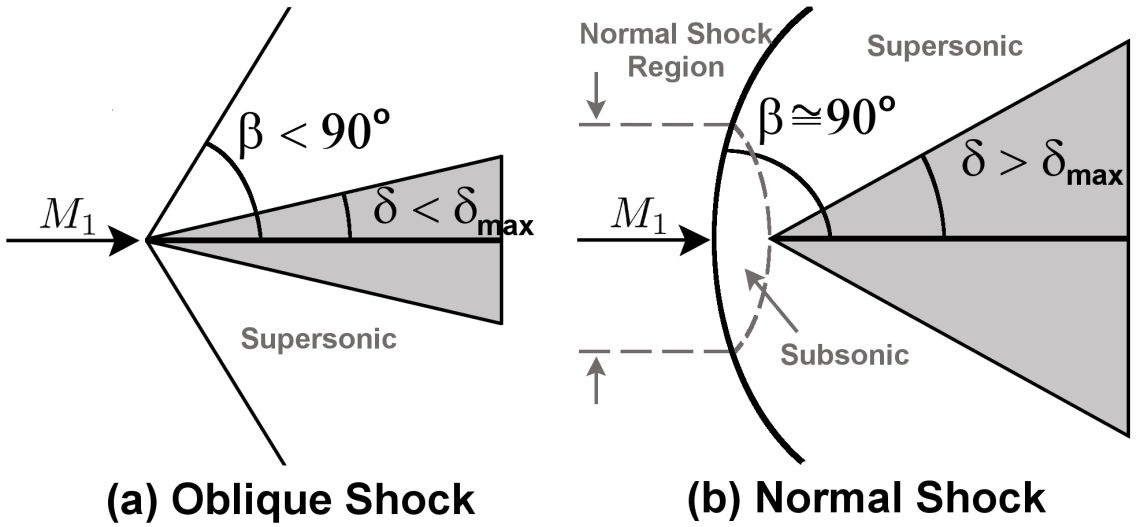

Figure 5.7: (a) Oblique shock formation from a wedge with $\delta < \delta_{max}$ and thus $\beta < 90°$. The shock boundary is attached to the wedge at the point of flow deflection. (b) Normal shock formation, $\beta \simeq 90°$, from a wedge with $\delta \geq \delta_{max}$. The shock boundary is detached, or forming at some distance, from the wedge.

supersonic flow is incident on a wedge with $\delta \geq \delta_{max}$, a normal shock forms upstream of the tip of the wedge (Fig. 5.7(b)). This leads to a region of subsonic flow in the area post-normal-shock, causing the shock boundary to be located at some distance from the wedge. Since the shock boundary is no longer attached to the wedge, this is known as a detached shock.

One possible explanation for the exact shape of the normal emission structure is that merging of the jets at this times more closely resembles a two-dimensional, instead of a one-dimensional, problem. Figure 5.8(a) demonstrates that for a jet with extended length of material along the midplane, we can postulate that each section of the jet has a different effective turning angle depending on its position Z. This is qualitatively equivalent to a flow past a curved surface or a surface with a continuously variable angle relative to the flow (Fig. 5.8(b)). Since this is a two-dimensional problem, a numerical simulation is required to predict the exact

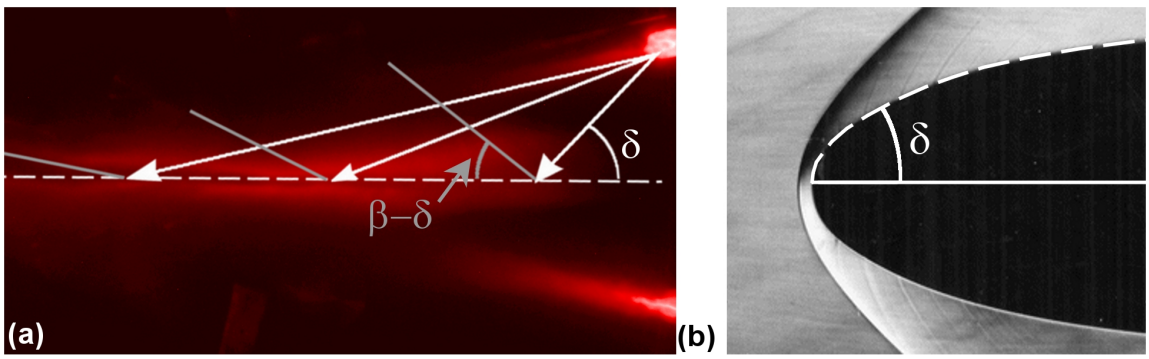

Figure 5.8: (a) Schematic of discrete jet flow directions, turning angles, and associated shock boundaries overlaid on a CCD image (shot 1170, $t = 38$ μs). Not to scale. (b) Schlieren photograph of supersonic flow past a curved object (Avco Everett Research Laboratory, Inc.). Shock boundary is curved and detached from object.

shock-boundary structure. This is left as future work.

5.3 Merged-Jet Density Analysis

If the merged-jet emission layers are post-shock plasma, as we postulated before, then the shock jump conditions can predict the density change of the plasma across the shock boundary. For an oblique shock, the ratio of the post-shock to pre-shock densities is given by

$$\frac{n_2}{n_1} = \frac{(M_1 \sin\beta)^2(\gamma+1)}{(M_1 \sin\beta)^2(\gamma-1)+2}, \tag{5.10}$$

which reduces to

$$\frac{n_2}{n_1} = \frac{M_1^2(\gamma+1)}{M_1^2(\gamma-1)+2} \tag{5.11}$$

in the case of a normal shock. To predict the density change in our system, we must carefully consider the possible ranges for both M and β. First, the Mach number is

bounded as $M_1 = M = 9$–14, due to impurities. Second, β is dependent on M as well as Z_i. For $Z_i < 25$ cm we've shown that theory predicts a normal shock $\beta \approx 90°$, for both $M = 9$ and $M = 14$. To bound β for an oblique shock we consider first $M = 9$, which yields $\beta = 35°$–$64°$ for measured $Z_i = 45$–25 cm. Thus the density change range is $n_2/n_1 = 5.1$–5.5. Similarly, for $M = 14$ we find $\beta = 58°$–$34°$ and $n_2/n_1 = 5.6$–5.8. For the normal shock we find $n_2/n_1 = 5.7$–5.9 for $M = 9$–14. Thus, the total predicted density change across the shock boundary is

$$\frac{n_2}{n_1} = 5.1 - 5.9. \tag{5.12}$$

Recall that we modified the interferometer and spectrometer positions to focus on the merged-jet dynamics at several positions along the midplane. In this section we will compare our experimental density changes during jet-merging to those predicted by the one-dimensional shock theory.

5.3.1 Density Enhancement at Z = 85 cm

As noted before, we made measurements for the cases of top-only, bottom-only, and both jets firing to collect data for the most direct comparison between merged- and single-jet data. At $Z = 85$ cm, top-jet-only shots show the jet has approximately uniform phase traces at all chords from $R = 0.75$–11.25. Figures 5.9(a)&(b) show typical top-jet $\Delta\phi$ vs. times and $\Delta\phi$ vs. R traces, for shot 1265. The variation in $\Delta\phi$ between chords is small, with standard deviation $\Delta\phi_{std} < 0.55°$. At $R = 2.25$ cm the average single-jet peak-phase shift is $\Delta\phi = 4.3 \pm 0.3°$ for top-jet only shots 1265–1267 (Fig. 5.10(b)). As expected, all other chord positions have similar $\Delta\phi \approx 4°$. Bottom-jet-only shots result in similar peak-phase shifts. Using the phase shift analysis accounting for multiple ionization states and the presence of impurities, we can calculate the single-jet density range. From the previously discussed single-jet spectroscopy at $Z = 41$ cm we estimate $Z_{\text{eff}} = 0.94$ and a jet diameter of 22

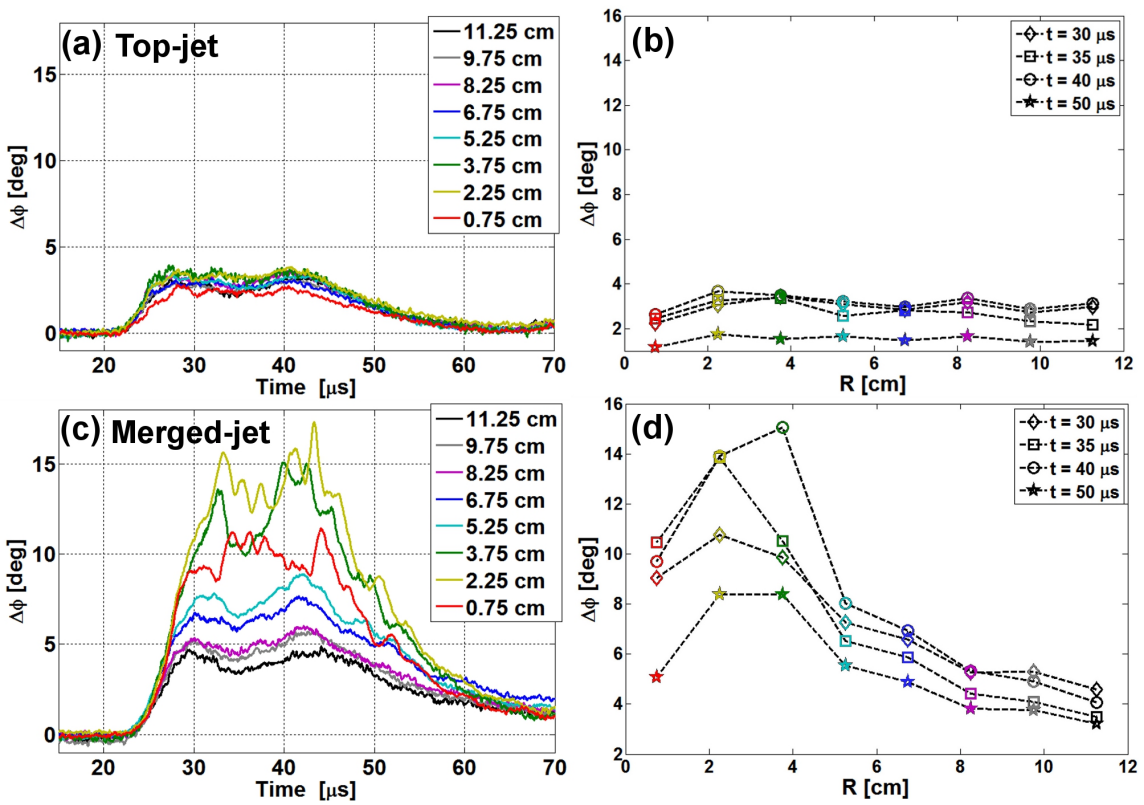

Figure 5.9: (a) Interferometer phase shift vs. time for a top-jet case (shot 1265), at chord positions at $Z = 85$ cm detailed in Fig.5.3. (b) Phase shift vs. chord position for a top-jet case (shot 1265) at several times. (c) Phase shift vs. time for a merged-jet case (shot 1120), at chord positions at $Z = 85$ cm detailed in Fig.5.3. (d) Phase shift vs. chord position for a jet-merging case (shot 1120) at several times.

cm. Spectroscopy estimates at $Z = 85$ cm for both positions for a single-jet are unavailable due to negligible jet emission. Thus, the single-jet density range is $n_{tot} = n_{single} = 2.1\text{–}2.3 \times 10^{14}$ cm^{-3}. The latter result changes by only a few percent for the 30%/70% mixture where the inferred mean charge is $Z_{\text{eff}} = 0.92$.

Merged-jet phase traces show significant differences from the single-jet case. Figures 5.9(c)&(d) show $\Delta\phi$ vs. time and $\Delta\phi$ vs. R for a typical merged-jet shot (shot 1120). Unlike the single-jet case, the merged-jet cases shows peak $\Delta\phi_{merged-jet} \approx$

$3.5 \times \Delta\phi_{single-jet}$ and the formation of a high $\Delta\phi$ layer near the midplane. Chords close to the midplane, $R \leq 6.75$ cm for shot 1120, show the highest phase shifts, with $\Delta\phi$ decreasing as R increases. At chords farther from the midplane, $R > 6.75$ cm for shot 1120, $\Delta\phi$ magnitudes are similar to those of the single-jet case. To investigate whether or not the increase in $\Delta\phi$ for the merged-jet is consistent with interpenetration of the top- and bottom-jet (i.e superposition of the two jet densities), we compare the phase shift of the merged jet to the expected sum of the phase shifts of the individual jets:

$$\Delta\psi = \Delta\phi_{merge} - (\Delta\phi_{top} + \Delta\phi_{bottom}). \tag{5.13}$$

Merged-jet measurements over the considered data set (merged jet, shots 1117-1196: bottom jet, shots 1277-1278: top jet, shots 1265-1267) show that, at $R < 5.25$ cm, $\Delta\psi > 0$ (Fig. 5.10(a)), implying that simple jet interpenetration cannot account for the observed $\Delta\phi$ of the merged-jet stagnation layer. However at large $R \geq 6.75$ cm, $\Delta\psi \approx 0$ which is consistent with jet interpenetration.

Phase enhancement greater than the sum of the two single-jet cases implies a density or ionization increase of the merged-jet. By iterating with our interferometry estimates for merged-jet density (shown later) and comparing our spectroscopy data with non-LTE spectral calculations using PrismSPECT [42], we infer Z_{eff} and T_e of the merged jet at $Z \approx 85$ cm and spectrometer position 2. PrismSPECT results for Z_{eff} and T_e are sensitive to the specific plasma mixture used. Based on the presence of certain Ar II lines in the data and by comparing to PrismSPECT results, we bound estimates of Z_{eff} and T_e using the 100% argon and 30%/70% mixture cases. For the former (Fig. 5.4(a)), we infer that peak $T_e \geq 1.4$ eV and $Z_{\text{eff}} = 0.94$. For the latter (Fig. 5.4(b)), we infer that 2.2 eV$\leq$ peak $T_e < 2.3$ eV and $Z_{\text{eff}} = 1.3$–1.4, with the upper bounds determined by the absence of an Al III line in the data. Thus, for the 100% argon case, we see approximately no change in plasma ionization from

Mixture	100% Ar	30%/70%
T_e	$\geq$ 1.4 eV	2.2 eV$\leq T_e <$2.3 eV
$Z_{\text{eff,single}}$	0.94	0.92
$Z_{\text{eff,merged}}$	0.94	1.4
n_{single}	2.1–2.3$\times 10^{14}$ cm^{-3}	2.2–2.4$\times 10^{14}$ cm^{-3}
n_{merged}	7.5–8.2$\times 10^{14}$ cm^{-3}	5.0–5.3$\times 10^{14}$ cm^{-3}
n_{single}/n_{merged}	3.2–3.8	2.1–2.5

Table 5.1: Summary of the experimental jet density enhancement for the two mixture cases, 100% Ar and 30% Ar / 70% Impurities. Single-jet and merged-jet densities are calculates assuming $\Delta\phi = 4^\circ$ and $\Delta\phi - 14^\circ$ respectively, as well as jet diameter of 22 cm and $Err = 0.082$.

the single-jet measurements, but the 30%/70% mixture case predicts an increase in plasma ionization during jet merging. In the 30%/70% mixture case this increased ionization accounts for some of the observed phase enhancement.

With estimates of the stagnation layer Z_{eff} in hand, we estimate the merged-jet density and compare it with the single-jet density. At $R = 2.25$ cm, the average peak $\Delta\phi = 14.3 \pm 2.4^\circ$ (Fig. 5.10(b)) (shots 1117–1196). Using $\Delta\phi = 14^\circ$, chord path length of 22 cm, and $Z_{\text{eff}} = 0.94$ (100% argon case), $n_{tot} = n_{merged} = 7.5$–$8.2\times 10^{14}$ cm^{-3}. In this case the density increase (Sec. 3.1.7) $n_{merged}/n_{single} = 3.2$–3.8. For $Z_{\text{eff}} = 1.4$ (30%/70% mixture case), the merged-jet density is $n_{tot} = n_{merged} = 5.0$–$5.3\times 10^{14}$ cm^{-3}, and the density increase is $n_{merged}/n_{single} = 2.1$–2.5. The smaller density increase for the 30%/70% mixture case is consistent with some of the phase enhancement being due to increased ionization. Still, the observed range of

$$\frac{n_{merged}}{n_{single}} = 2.1 - 3.8, \tag{5.14}$$

exceeds the factor of two expected for jet interpenetration, though it is smaller than the predicted $n_{shock}/n_{unshocked} = 5.1$–5.9. The difference between the measured and predicted density jumps could again be due to three-dimensional (e.g., pressure-relief in the out-of-page dimension) and/or equation-of-state (e.g., ionization [46]) effects

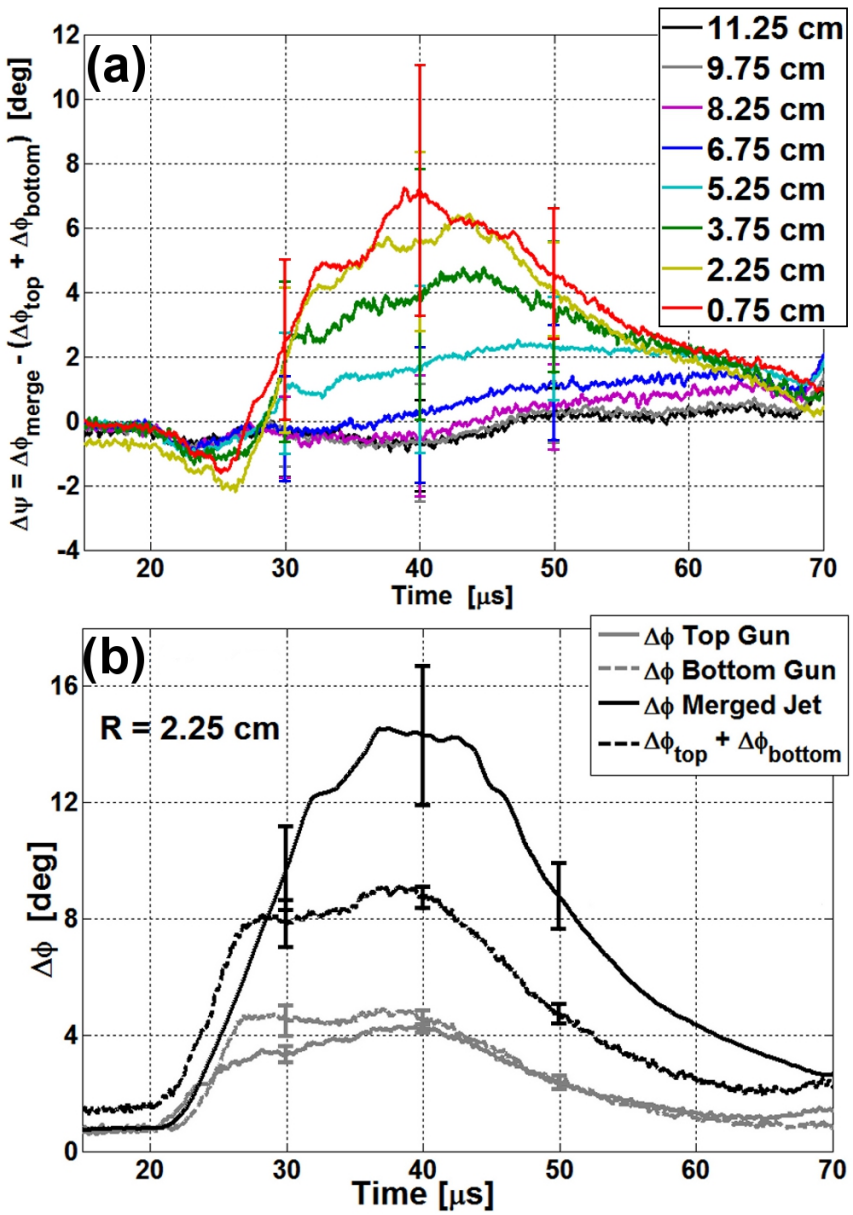

Figure 5.10: (a) Difference between merged-jet and single jet phase shifts, $\Delta\psi = \Delta\phi_{merge} - (\Delta\phi_{top} + \Delta\phi_{bottom})$, vs. time for data averaged over the shots sets shots 1117–1196 (merged-jet), shots 1277–1278 (bottom-jet) and shots 1265–1267 (top-jet). (b) Multi-shot (same data set) averaged interferometer phase shift vs. time at $R = 2.25$ cm, for top, bottom, and merged-jet cases.

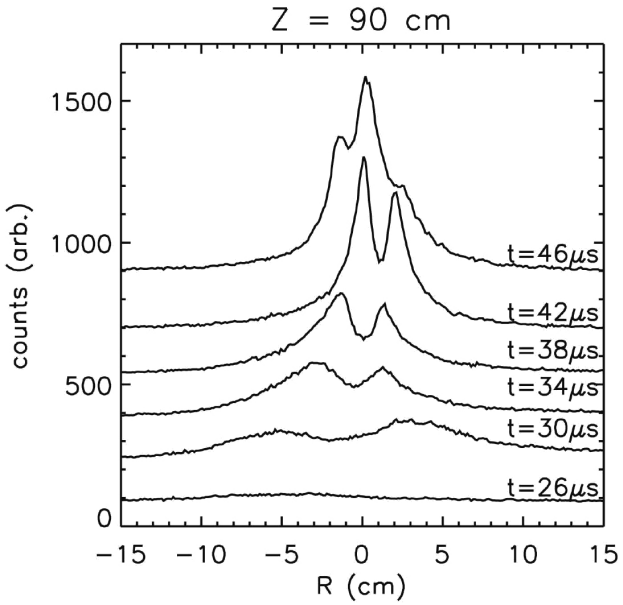

Figure 5.11: CCD image line-outs versus R (transverse to stagnation layer) at $Z =$ 90 cm (horizontal pixel # 654 out of 1024), corresponding to the images of Fig. 5.2. Progressive times are shown with increasing count offsets to avoid trace overlap.

not modeled by the one-dimensional hydrodynamic theory.

5.3.2 Density Layer Width

Density increases greater than interpenetration imply that the $\Delta\phi$ (Fig. 5.9(d)) structure near the midplane is indicative of a density layer. The CCD images (Fig. 5.2) also show an emission-layer formation about the midplane. CCD line-outs at $Z = 90$ cm (Fig. 5.11) show that the thicknesses of the observed merged-jet emission layer is similar to the $\Delta\phi$ vs. R profiles. Both the emission and $\Delta\phi$ peaks are of the same length scale (a few cm), and the $\Delta\phi$ dip at $R = 0.75$ cm and peak at $R = 2.24$–4 cm are well-aligned with the emission dip and peak, respectively.

In a collisional plasma, the density layer thickness is expected [55] to be on the

order of the counter-streaming ion-ion mean free path (mfp),[46]

$$\lambda_{ii'} \sim v_{rel}/4\nu_{ii'}, \tag{5.15}$$

where v_{rel} is the relative transverse velocity between obliquely-merging jets. The slowing-down rate in the fast approximation ($v_{rel} \gg v_{ti}$) is:[4]

$$\nu_{ii'} \approx 9.0 \times 10^{-8} \left(\frac{1}{\mu} + \frac{1}{\mu'}\right) \frac{\mu^{1/2}}{\epsilon^{3/2}} n_{i'} (Z_{\text{eff}} Z'_{\text{eff}})^2 \ln \Lambda_{ii'}, \tag{5.16}$$

where $\epsilon = m_i v_{rel}^2/2$ is the jet relative kinetic energy, and $\ln \Lambda$ is the Coulomb logarithm. For mixed ion-ion collisions, such as those due to impurities, the Coulomb logarithm is:[4]

$$\ln \Lambda_{ii'} = \ln \Lambda_{i'i} = 23 - \ln \left[\frac{Z_{\text{eff}} Z'_{\text{eff}} (\mu + \mu')}{\mu T_{i'} + \mu' T_i} \left(\frac{n_i Z_{\text{eff}}^2}{T_i} + \frac{n_{i'} Z'^2_{\text{eff}}}{T_{i'}} \right) \right]. \tag{5.17}$$

We estimate $\lambda_{ii'}$ by considering jets of 100% argon and the 30%/70% mixture previously discussed, in all cases using $v_{rel} = 20$ km/s. For Ar-Ar stopping $\lambda_{ii'} = 3.47$ cm, for parameters of $n_i = 8 \times 10^{14}$ cm^{-3} from interferometry, and $T_e = 1.4$ eV and $Z_{\text{eff}} = 0.94$ from spectroscopy. Pure Al-Al and O-O stopping yield $\lambda_{ii'} = 0.16$ cm and 0.62 cm, respectively, for $n_i = 5 \times 10^{14}$ cm^{-3}, $T_e = 2.2$ eV, $Z_{\text{eff,Al}} = 2.0$, and $Z_{\text{eff,O}} = 1.0$. For inter-species collisions in a mixed-species jet, using the 30% Ar, 43% O and 24% Al mixture given in Fig. 5.4(b) and $n_i = (\%\text{ ion species}) \times n_{tot}$, $\lambda_{ii'} \approx 0.57$–$6.18$ cm.

We can also estimate the inter-jet mfp due to Ar^+-Ar charge exchange and momentum transfer. Assuming $v_{rel} = 20$ km/s gives a kinetic energy of $KE \approx 80$ eV, corresponding to a charge exchange cross-sectional area of $\sigma_{CT} \approx 0.7 \times 10^{-18}$ m^2 and a momentum transfer cross-sectional area of $\sigma_m \approx 0.3 \times 10^{-18}$ m^2.[54] The total mfp for Ar^+-Ar interaction is $\lambda_{mfp} = 1/[\sigma_{tot} \times n_n] = 1/[(\sigma_{CT} + \sigma_m) \times n_n]$, where $n_n = (1 - Z_{\text{eff}}) \times n_{tot}$ is the neutral density in the plasma. For merged-jet parameters

		100% Ar	30%/70%
$\lambda_{ii'}$	Ar-Ar	3.47 cm	2.03 cm
	Al-Al		0.16 cm
	O-O		0.62 cm
	Interspecies		0.57–6.18 cm
λ_{ie}	Ar	3.1 cm	6.8 cm
	Al		1.1 cm
	O		4.5 cm

Table 5.2: Summary of collisional mean-free-paths for particles in the plasma, for both the 100% Ar and 30%/70% mixture cases.

of $Z_{\text{eff}} = 0.94$ and $n_{tot} = 8 \times 10^{20}$ m^{-3} for 100% argon, then $\lambda_{mfp} \approx 2$ cm. Thus, the collisional mfp for Ar^+-Ar interactions is $\sim \lambda_{ii'}$.

Note that in our parameter regime, the inter-jet ion-electron mfp is also $\lambda_{ie} \gtrsim \lambda_{ii'}$. In the ion-electron case we still have $\lambda_{ie} \sim v_{rel}/4\nu_{ie}$, but we must use the slow approximation ($v_{rel} \ll v_{te}$) for the slowing-down rate:[4]

$$\nu_{ie} \approx 1.6 \times 10^{-9} \mu^{-1} T^{-3/2} n_e Z_{\text{eff}}^2 \ln \Lambda_{ie}, \tag{5.18}$$

where $\ln \Lambda_{ie} = 23 - \ln(n_e^{1/2} Z_{\text{eff}} T_e^{-3/2} 0$ since $T_e < 2.3$ eV. Assuming $n_e = Z_{\text{eff}} n_{tot}$, for the 100% argon case of the merged-jet, $Z_{\text{eff}} = 0.94$, $T_e = 1.4$ eV and $n_{tot} = 8 \times 10^{14}$ cm^{-3}, then $\lambda_{ie} = 3.1$ cm. For the 30%/70% mixture, with $n_{tot} = 5 \times 10^{14}$ cm^{-3}, $T_e = 2.2$ eV, $Z_{\text{eff,Ar}} = 1.2$, $Z_{\text{eff,Al}} = 2.0$, and $Z_{\text{eff,O}} = 1.0$, then $\lambda_{ie} = 6.8$, 1.1, and 4.5 cm for Ar, Al, and O respectively.

All these estimates imply that our inter-jet merging is in a collisional regime, which is consistent with a more detailed treatment of inter-jet ion-ion stopping including jet profile effects.[46]

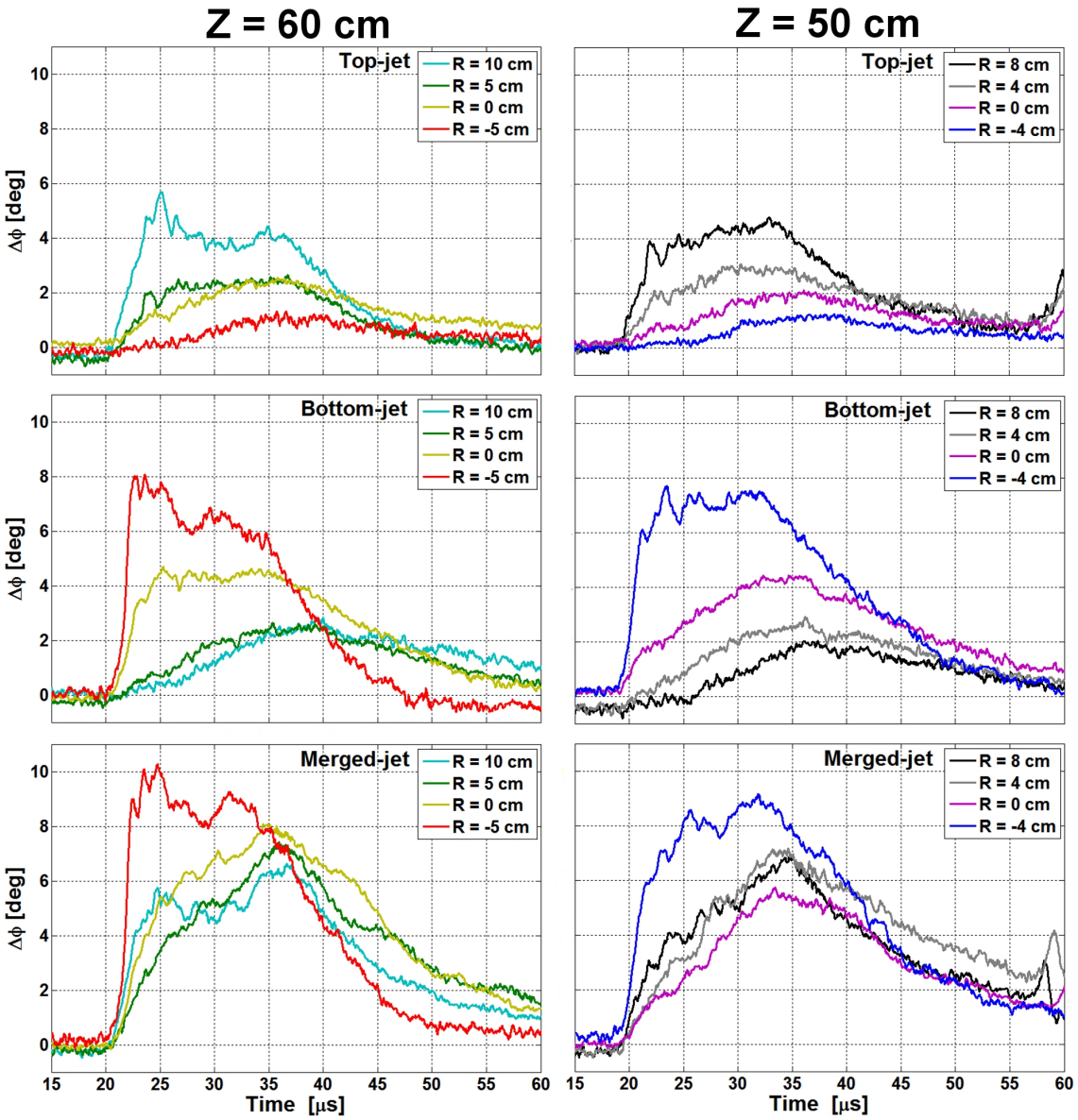

Figure 5.12: (a) Phase shift vs. time for a top-jet case (shot 1105), bottom-jet case (shot 1110), and merged-jet case (shot 1103) at chord positions at $Z = 50, 60$ cm detailed in Fig.5.3.

5.3.3 Density results at Z = 50, 60 cm

Experiments with diagnostics at $Z = 50, 60$ cm and experiments with diagnostics at $Z = 85$ cm have all the same experimental parameters except for the diagnostic

positions. However, interferometer results at $Z = 50, 60$ cm show greater consistency with simple jet interpenetration, instead of consistency with shock formation as seen in the results at $Z = 85$ cm.

Figure 5.12 shows typical $\Delta\phi$ vs. times results at $Z = 50, 60$ cm for a top-jet case (shot 1105), a bottom-jet case (shot 1110), and a merged-jet case (shot 1103). Unlike the top-jet case at $Z = 85$ cm, single-jet $\Delta\phi$ profiles at $Z = 50, 60$ cm are not of uniform magnitude, but instead show a $\Delta\phi$ gradient. As expected for top-jet shots, the magnitude of $\Delta\phi$ increases as R increases, or for R positions closer to the top-jet propagation axis. Similarly, for bottom-jet shots, the magnitude of $\Delta\phi$ increases as R decreases, or for R positions closer to the bottom-jet axis. Thus there may be profile effects during jet-merging at this position not accounted for in our simple one-dimensional uniform flow analysis. Also, bottom-jet shots have higher magnitude peak $\Delta\phi$ than top-jet shots at equal distances from the individual gun axes. This may be indicative of a performance imbalance between the two guns, also seen in the tendency of the merged-jet to appear slightly higher than the midplane in the CCD images. The imbalance between railgun performance is most likely due to the greater age and degradation of the top gun compared to the bottom gun. The imbalance is also present in experiments done with diagnostics at $Z = 85$ cm, so it does not account for the difference in phase enhancement between the diagnostic positions. However, future experiments should strive for balanced railgun performance to eliminate any uncertainty this may introduce into the system.

The merged-jet $\Delta\phi$ profiles at $Z = 50, 60$ cm show little variation from the top- and bottom-jet $\Delta\phi$ profiles, unlike the merged-jet profile at the $Z = 85$ cm position which showed the emergence of a distinct phase layer. Merged-jet profiles at $(Z, R) = (50 \text{ cm}, -4 \text{ cm})$ and $(Z, R) = (60 \text{ cm}, -5 \text{ cm})$, the chords nearest the bottom jet axis, strongly resemble the bottom-jet profiles at those positions. All other chords do not preferentially resemble either top- or bottom-jet shots. The $\Delta\phi$

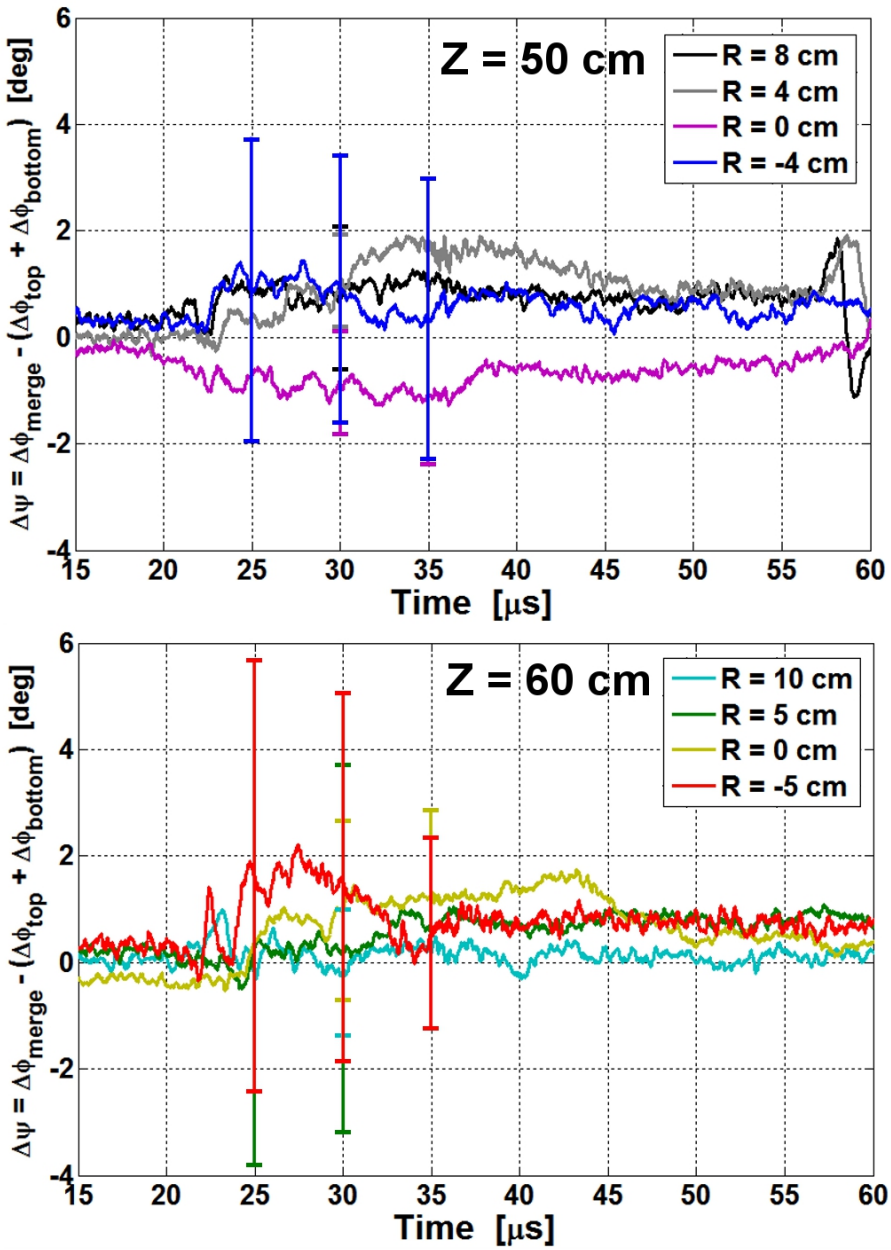

Figure 5.13: Difference between merged-jet and single-jet phase shifts, $\Delta\psi = \Delta\phi_{merge} - (\Delta\phi_{top} + \Delta\phi_{bottom})$, vs. time, at $Z = 50, 60$ cm, for data averaged over shots 1102–1104 (merged-jet), shots 1105–1108 (top-jet) and shots 1109–1112 (bottom-jet).

profiles at these positions are of similar magnitudes, and do not show a consistent phase gradient between the chord positions over the merging time interval. The merged-jet peak $\Delta\phi$ is also greater than either individual-jet peak $\Delta\phi$. However, $\Delta\psi \approx 0$ for all chords, as shown in Fig. 5.13. Assuming the mean charge for both individual jets is the same, $Z_{\text{eff}}^{single} = Z_{\text{eff}}^{top} = Z_{\text{eff}}^{bottom}$, then $\Delta\psi = 0$ implies:

$$[Z_{\text{eff}}^{merge} - Err] \int n_{tot}^{merge} dl^{merge} = [Z_{\text{eff}}^{single} - Err](\int n_{tot}^{top} dl^{top} + \int n_{tot}^{bottom} dl^{bottom}).$$

Assuming there is a density increase greater than interpenetration during merging,

$$\int n_{tot}^{merge} dl^{merge} > \int n_{tot}^{top} dl^{top} + \int n_{tot}^{bottom} dl^{bottom}, \tag{5.19}$$

requires that plasma ionization decreases during merging, $Z_{\text{eff}}^{merge} < Z_{\text{eff}}^{single}$. We chose a high-Z plasma to increase the chance of post-shock energy being distributed into increased plasma ionization instead of shock heating; Z_{eff} decreasing after merging seems improbable. Unfortunately, emission of a single jet at either spectrometer position at $Z = 50, 60$ cm is too low for reliable spectroscopy measurements, making a direct comparison of the pre- and post-merge Z_{eff} unavailable at this position.

The results seem more consistent with the assumption of

$$\int n_{tot}^{merge} dl^{merge} = \int n_{tot}^{top} dl^{top} + \int n_{tot}^{bottom} dl^{bottom}, \tag{5.20}$$

or simple jet interpenetration. Density enhancement measurements at $Z = 85$ cm imply that density enhancement should be present at $Z = 50, 60$ cm as well, since interferometer chords at both positions are within the merged-jet emission envelope. Also both positions are at $Z > Z_i$ for all times during merging, implying that measurements at both positions should measure post-shock plasma. The investigation of this discrepancy in the presence of merged-jet phase enhancement is left as future work.

5.4 Comparison to Simulation

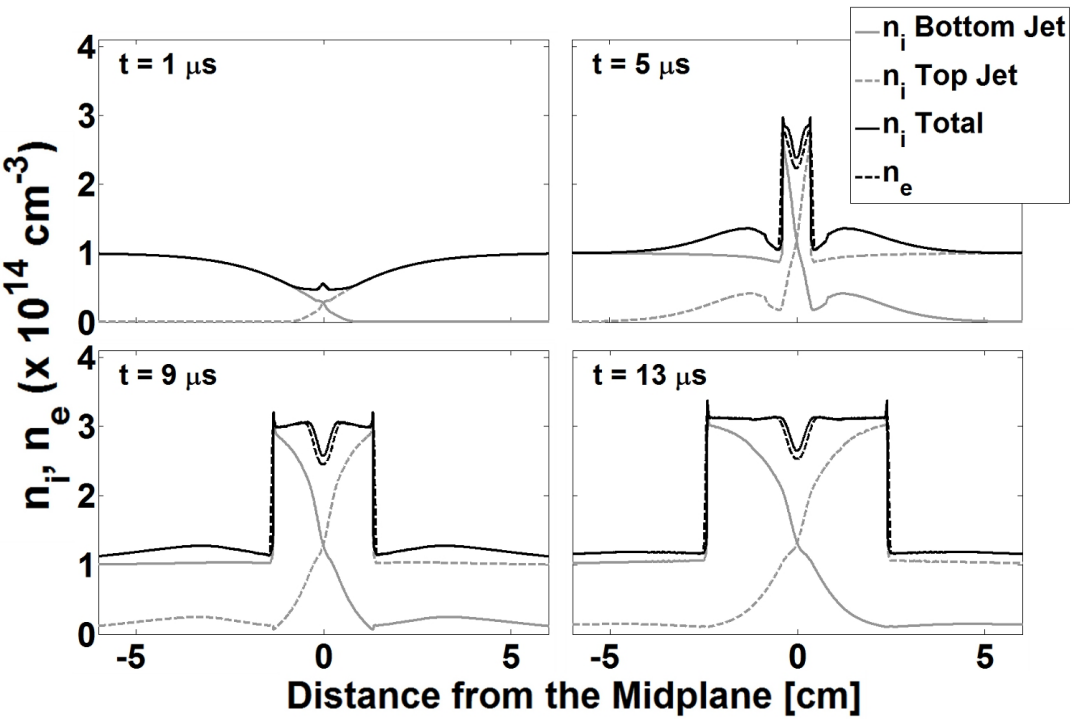

Figure 5.14: Density versus spatial dimension from a 1D multi-fluid collisional plasma simulation that models the transverse (R) dynamics of our experiments, illustrating the formation of reflected shocks.

To further evaluate the consistency of the experimental results with oblique shock theory,[37, 48] our collaborator, John Loverich at Tech-X Corp., ran one-dimensional multi-fluid simulations of merging jets. In these simulations the electrons were treated as one fluid and the ions of the top- and bottom-jets were treated as a second and third fluid. This models the transverse (R) dynamics of the oblique merging. Simulations were performed with the multi-fluid magnetohydrodynamics code USim, formerly known as Nautilus, which uses a semi-implicit numerical algorithm [36] and algorithms that have been verified against shock problems.[40] In the simulations, the jets are assumed to have approximately the measured single-jet parameters for

100% Ar II ($Z_{\text{eff}} = 1$): initial $n_e = n_i = 10^{14}$ cm^{-3}, $T_e = T_i = 1.4$ eV. The jet velocities are modeled as the lower limit of the transverse velocity $v = \pm 6.2$ km/s, with the transverse component of $v_{jet} \approx 30$ km/s at the merging half-angle of $\approx 12°$. We used a non-uniform density profile in the leading edge of the jet, as shown in the top left panel ($t = 1$ μs) of Fig. 5.14, in order to include some profile effects. The simulations assumed collisional interaction between all three fluids [55] for comparison to collisional shock theory. The simulations have resolution ~ 100 μm. The algorithm is shock capturing and able to step over plasma frequency so that electron fluid velocity and acoustic speed (rather than the electron plasma frequency) limit the simulation time step.

At 1 μs after merging begins, the simulations shows a small initial density buildup at the merging interface; the incoming electrons are very highly collisional and must pile up there. Within 5 μs, a density dip appears at the midplane, similar to the structure seen for tens of microseconds in the experiments (Fig. 5.2). The simulations indicate that this structure is a result of an initial charge separation at the midplane plane that generates reflected shocks. Jet interpenetration reaches ~ 1 cm (Fig. 5.14d), consistent with earlier estimates of λ_{ii}. These comparisons support the interpretation that our observations are consistent with collisional oblique shocks.

Since this is a one-dimensional simulation it inherently models only normal shock dynamics, and thus is most applicable for comparison to the merged-jet measurements for times $t > 32$ μs. Consistent with this restriction, the time range $t > 32$ μs is also when the double-peaked emission structure is most pronounced (Fig. 5.11). Investigations of the two- or three-dimensional aspects of the jet merging, such as the predicted oblique- to normal-shock transition are beyond the purview of this model. Experimental investigations of possible charge separation in the plasm as well as predicted reflected shocks are currently beyond the capabilities of the installed diagnostics, but could be an interesting future avenue of study.

5.5 Conclusions

We have completed the first steps to experimentally characterize the dynamics of two obliquely merging supersonic plasma jets. We observed the formation of a merged-jet emission structure that is consistent with predictions from one-dimensional hydrodynamic oblique shock theory for early times, and estimates for detached shock formation at later times. This emission envelope possesses a double-peaked emission profile transverse to the layer and centered about the midplane of the jets. The central dip and peak positions are consistent with the density layer structure observed in the interferometer data at $Z = 85$ cm. The layer thickness is of the same order of magnitude as the counter-streaming ion-ion mean free path, $\lambda_{ii'}$, as is consistent with shock predictions for a collisional plasma. Furthermore, collisional 1D multi-fluid plasma simulations of the transverse dynamics of the oblique merging do show the formation and evolution of reflected shocks with a central density dip consistent with the observed merged-jet layers.

The layer does show density enhancement of $n_{merged}/n_{single} = 2.1 - 3.8$ at $Z = 85$ cm, which is greater than simple jet interpenetration. This density increase is consistent with oblique shock predictions, expecting the presence of potential three-dimensional and equation-of-state effects not included in the one-dimensional hydrodynamic theory. The density increase is also promising for liner formation results, since high density after merging is desirable. Results at $Z = 50, 60$ cm show a density increase that is consistent with only simple jet interpenetration, and does not show density layer formation like the $Z = 85$ cm results. Resolution of this discrepancy is left for future work, since understanding the density dynamics is important for predicting full liner parameters. Overall, both the observed emission and density dynamics are consistent with collisional shock formation.

Chapter 6

Future Work

While we have made good progress towards assessing single-jet propagation and two-jet merging for liner formation, there is much more interesting work that can be done, including liner formation experiments themselves.

6.0.1 Experiments with a single jet

Throughout the reported experiments we have been operating under the assumption that the plasma jets are unmagnetized once they leave the gun nozzle. We make this assumption even though measurements from a set of magnetic probes inside the gun bore measure the jet magnetic field to be on the order of several tesla within the gun. Hsu *et al.* [26] has shown that for measured $T_e \approx 1.4$ eV, $n_e = 2 \times 10^{16}$ cm^{-3}, and $Z_{\text{eff}} = 1$ at the gun nozzle, the magnetic field will resistively decay to 0.05 of its originally value after 5.1 μs or 15.3 cm of jet propagation assuming $v = 30$ km/s. The propagation distances of interest, those at which jet merging occurs, are far enough from the gun nozzle, $Z > 15$ cm, that the magnetic field should be negligible. While no obvious magnetic effects appeared in our single-jet and jet-merging results, we should still verify that the magnetic field is negligible at the expected distance from

the gun nozzle. Efforts are underway at PLX to install and test a set of magnetic (B-dot) probe arrays[56] at the end of the gun nozzle and some distance downstream.

In addition to peak liner stagnation pressure P_{stag} scaling with n_i, v and M, simulations by Cassibry *et al.* [15] suggest that P_{stag} also scales inversely with liner thickness, $P_{\text{stag}} \sim 1/L$. In Sec. 4.2 we showed a correspondence between the period of the gun current ring and the generation of multiple plasma jets. Since the period of the gun current is related to jet creation/acceleration, it may be worth investigating whether varying the current profile can be used to control the initial jet length. Further work by Kagan *et al.* [33] proposed that tailoring the liner profile could be used to create a bounce-free implosion on an MIF target and thereby increase the target dwell time and fusion energy gain by a factor of four. Investigating whether modification of the high-voltage pulse-forming circuit, and thus the current profile, can be used to change the liner density profile may be beneficial for optimizing the performance of plasma liners.

6.0.2 Experiments in oblique two-jet merging

The first step for future jet-merging experiments is to reduce the impurity percentage in the jets by refurbishing the insulators in the railguns. Single-jet propagation experiments did have estimated plasma compositions of $\approx 80\%$ Ar. Reducing the impurity percentage would also reduce the uncertainty in the interferometry and spectroscopy analysis due to variation in T_e and Z_{eff} predictions for the different plasma compositions (100% Ar and 70%/30% Impurities/Ar). It may be worth repeating the previous two-jet merging experiments with purer Ar plasma jets to discern whether or not any of the previously observed results are due to the presence of multiple species in the jets, since the presence of multiple species during shock formation can cause species separation and shock layer broadening.[16, 58, 49, 50] Species separation may contribute to the formation of the double-peaked emission

structure observed along the jet-merging plane.

A second recommended improvement is to balance the performance of both (or all) railguns used in the jet-merging experiments. In our two-jet merging experiments the diagnostics were primarily focused on the top-jet performance. The photodiode array only measures the top-jet velocity, and the bottom-jet velocity was assumed to be approximately the same. This may require separate control systems for individual guns' high-voltage electronics, so that the voltage and trigger timing of the capacitor banks can be adjusted until the jets have similar velocities. To verify that the jets have similar velocities, photodiode arrays should be installed to measure the velocity of each jet.

If the jets have different velocities, that may introduce the conditions for streaming instabilities or other streaming effects at the jet-merging interface during merging experiments. This may be a particularly interesting field of study since the dynamics at the jet-merging interface are in a semi-collisional regime. During the two-jet merging experiments, interferometry results at $Z = 85$ cm show evidence of a phase structure with a transverse velocity, as shown in Fig. 6.1. The phase structure is a peak with a several degree magnitude and a width of ≈ 2 μs. Assuming a jet velocity of 30 km/s, the width of the structure is $d \approx 6$ cm. The appearance of the phase structure in the interferometer traces alternates between consecutive chords (for the three chords nearest the jet-merging plane); the rise in the phase peak on one chord corresponds to the fall in the peak on another chord. The structure alternates between chord traces at $\Delta t \approx 1.5$ μs intervals. Since the chords are 1.5 cm apart, the structure has a transverse velocity of $v \approx 15$ km/s. The underlying cause of this structure has not been investigated, but the first step to identifying if it is a streaming effect might be to see if it continues to appear even when the difference between the jet velocities is made small. Similarly, if the difference in jet velocities can be controlled, then jet-merging experiments may have applications to streaming

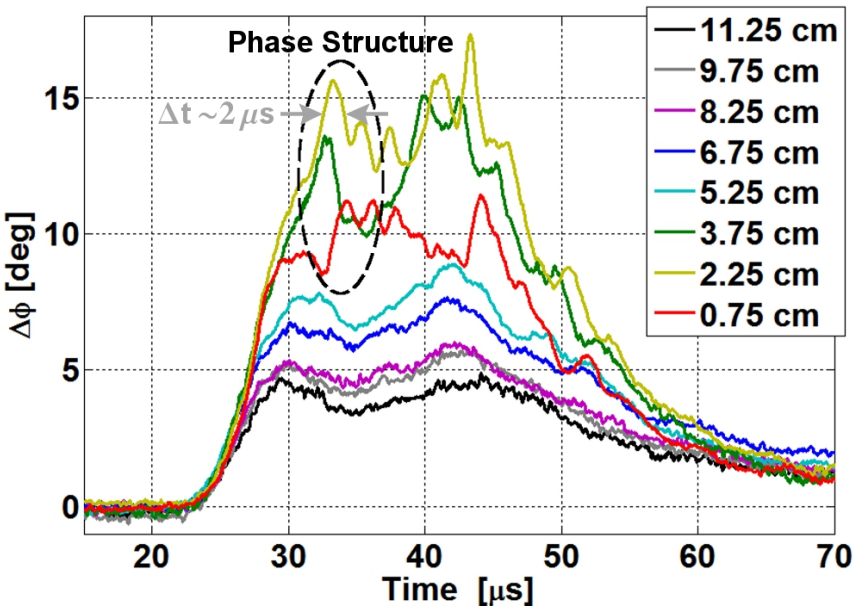

Figure 6.1: Phase shift vs. time for a merged-jet case (shot 1120) with multiple small phase peaks of amplitude $\sim 2.5°$ and width $\Delta t \sim 2$ μs. One such phase structure is highlighted by the dashed circle. Structure alternation between chords $R = 0.75$–3.75 cm indicates a transverse velocity of ≈ 15 km/s.

effect studies in the semi-collisional plasma regime.

In addition to equipment optimization there are several other oblique merging experiments that should be completed before proceeding on to full liner formation experiments. The spectroscopy data from the jet-merging experiments in Chap. 5 estimated T_e of the plasma post-merge. Even though T_e showed only a small potential increase during merging, from $T_e \approx 1.4$ eV to $T_e \approx 1.4$–2.3 eV, the ions in the plasma may have undergone more extreme heating. Unfortunately, PLX does not currently possess any T_i diagnostics. PLX is planning to upgrade from the 0.275 m and 0.152 nm/pixel resolution Acton SpectraPro[26] spectrometer to a 1 m and 0.008 nm SPEX 1802[45] spectrometer currently at the University of New Mexico. The spectrometer resolution may be high enough to measure T_i from Doppler

broadening, but further work is need to make that determination.

We also mentioned in Sec. 5.3.1 that the discrepancy between the measured and predicted density increase during jet merging may be due to three-dimensional (e.g., pressure-relief in the out-of-page dimension) and/or equation-of-state (e.g., ionization) effects not included in the one-dimensional hydrodynamic theory. While the USim simulations (Sec. 5.4) did extend the model to include multi-fluid and some kinetic effects, they were still a one-dimensional model. Further extension of the modeling effort to three-dimensional models or models with EOS effects may be able to resolve the density enhancement discrepancy.

The USim simulations predicted several collisionless phenomena that may be of interest for future study: ion interpenetration between the two jets and an initial charge separation at the merging interface that gave rise to the reflected shocks. We may be able to measure jet interpenetration by doping the jets with impurities that possess prominent emission lines in the visible spectrum and then adding filters to the fast imaging camera to isolate those emission frequencies. If each jet has an impurity with a different emission frequency, then adding the appropriate filter to the camera would produce an image of the emission, and thus approximate spatial extent, of an individual jet. Measurement of charge separation near the merging plane may be possible with a Langmuir probe or probe array.

6.1 Collisionless shock experiments

Currently PLX has changed its focus from experiments in support of plasma liner formation to an investigation of collisionless shocks for application to astrophysical phenomena.[47] PLX will attempt to generate collisionless shocks by colliding two hydrogen plasma jets head-on. The plasma jets will have densities of $\sim 10^{14}$ cm^{-3} (at merge) and velocities of ~ 100 km/s and are generated and accelerated by the

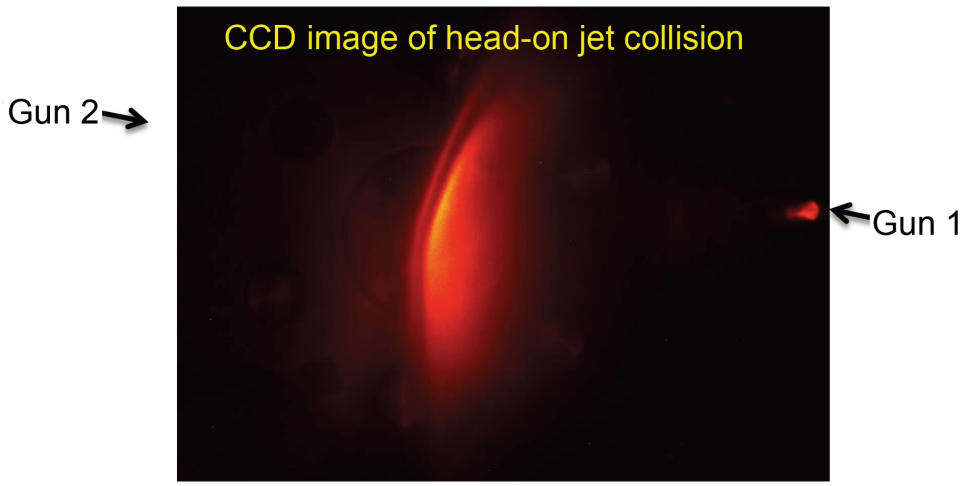

Figure 6.2: Image of head-on collision experiments with argon plasma jets from [28].

same HyperV railguns used in previous experiments. In addition to the B-dot probe array, a triple Langmuir probe [32] and a Schlieren imaging system [5] have been developed for PLX and are currently in the process of being tested. Head-on collision experiments have already been conducted with Ar jets with the same parameters as used in the oblique merging experiments, which were not expected to produce collisional instead of collisionless shocks. These experiments were done to test the new equipment configuration. The head-on merging shows a double-peaked emission structure (Fig. 6.2) similar to that observed for $t > 32$ μs in the oblique merging case. This may support further our previous assertion that, for late times during oblique merging, the merged-jet emission envelope is consistent with normal shock formation. Further comparison of head-on and oblique merging results with similar jets may lead to more insights into the two- and three-dimensional nature of the oblique jet-merging dynamics.

Appendix A

Interferometer Alignment Procedure

This appendix outlines the procedure for constructing and aligning the interferometer. It includes information about constructing the interferometer optical setup from scratch, guidelines for simpler maintenance alignment, and advice for rearranging the chord positioning in the chamber.

A.1 Aligning the interferometer from scratch

In this section we outline guidelines for aligning or repositioning optics in the interferometer after major modifications or repairs have occurred. We also detail some tips for aligning a laser beam into both types of fiber collimators in the system. This section also contains information about how to position the interferometer chords in the chamber itself.

A.1.1 Turning on the Laser

The laser and laser power supply are located inside a Hoffman box. Before turning the laser on, make sure that the physical shutter on the end of the laser is closed. Do not open this until you are ready to begin working with the laser. The cooling fan on the laser has a separate power cord than the power supply; make sure this is connected. The Hoffman box also has a set of cooling fans designed to circulate hot air out of the enclosure; make sure these are also on. The laser power supply has four requirements in order for the laser to be turned on:

1. The interlock circuit must be closed; when the laser is exposed (table-top enclosure open) the laser curtain must be closed with interlock cable connected at both the top and bottom, and both the "warning" (orange) and "danger" (red) lights must be on.

2. The laser must be turned on. The light on the power supply will be red at this stage.

3. The power supply key must be in the keyslot. The initial key position is the "off" position.

4. Once all other requirements have been met, turn the key to the "on" position to turn on the laser. The indicator light should begin flashing green. If the light remains red, then the interlock circuit is most likely not closed, and all interlock conditions should be re-checked. There are other possible reasons the laser won't turn on, such as overheating, but a problem with the interlock is the most common. Turn the key back to the initial "off" position while checking the system. Once the system has been checked, turn the key to the "on" position again. Repeat this procedure until the light begins flashing green.

The laser begins emitting light once the green light begins flashing. However, the laser light has not stabilized until the light stops flashing and becomes solid green. At this point the laser is ready to use, and the physical shutter can be opened. The laser does take about 5-10 minutes to stabilized, so the shutter should be used for any short term stops in laser operation. When not dealing directly with the laser, the shutter should be closed to reduce the chance of accidental exposure. Finally, the Hoffman box containing the laser should be closed once the laser is on so as not to obstruct any of the rest of the alignment procedure.

A.1.2 Aligning the laser beam into the AOM

The AOM system consists of two parts: the AOM itself and the RF signal generator. The RF generator is located in the interferometer electronics' screen box. Before turning on the RF generator make sure the RF power dial is turned to 0. Turn on the RF generator (the switch is on the back). To turn on the AOM, turn up the RF power dial to 10 (full power). We turn to RF generator to full power during experimental operation to maintain performance consistency since the RF power dial was not gradated for high accuracy. The AOM can be turned on before or after the laser because they are independent systems. However, we recommend turning on the RF generator before beginning work with the interferometer since the RF generator can have a long warm-up if the room is cold.

The beam exits the laser and enters the AOM. The entire beam should pass through the AOM aperture, taking care not to clip the beam on any of the aperture edges. Multiple beams exit the AOM. These beams consist of various frequency shifted modes of the original laser beam. The zero, or non-frequency-shifted, mode passes through the AOM without any deflection. The higher order modes are deflected to either side of the zero mode beam. The amount of power coupled into any higher order mode depends on the initial laser beam's entrance angle into the AOM.

Aligning the laser with the AOM consists of coupling as much power as possible into the first order mode directly to the left of the unaltered (zero mode) beam. At the point that the maximum power is coupled into one first order mode, minimal power will be coupled into any other higher order modes. The first order mode will be bright and the higher order modes will be dim in comparison but will not disappear completely.

Since the mode coupling depends on the entrance angle of the laser beam, the AOM has been mounted on a rotating pan/tilt platform. Hold an alignment card on the exit beam side of the AOM at a distance of between 1 and 2 ft. The higher order mode beams do not becomes perceivably separated from the zero mode beam until a couple feet away from the AOM. Since the laser has a visible wavelength, an alignment card can consist of any plain paper, as shown in Fig. A.1. Business or index cards are useful because of their size and availability but larger/taller alignment cards can also be made from stiff paper stock. Adjust the platform rotation and pan/tilt until the first order beam is as bright as possible.

The higher order beams all experience some beam distortion from the AOM while the zero order beam does not. Beam distortion decreases the efficiency of coupling the beam into a fiber. The distorted beam is used as the reference beam, so that the distortion only affects one chord. The process of coupling into a fiber discards the beam distortion; the beam exiting the fiber is not longer distorted. Instead, the shape of the beam exiting the fiber is dependent on the optics at that end of the fiber.

A.1.3 Initial establishment of the chords

The first order (reference) beam leaves the AOM and passes to a turning mirror. The beam reflects off of a set of three turning mirrors before passing through a neutral

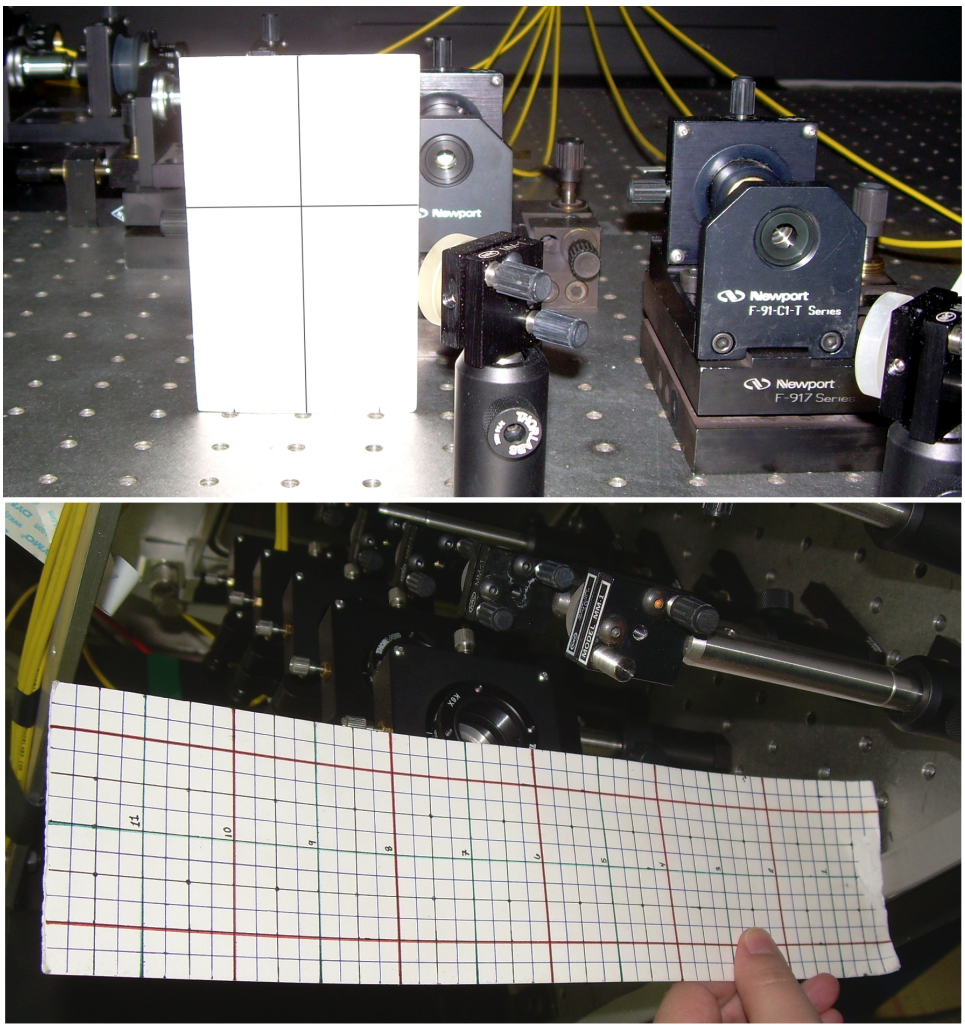

Figure A.1: (Top) Alignment card made from a 3" X 5" index card, marked with crossed lines intersecting at a 3" height from the bottom of the card. This alignment card was designed to align probe beams into Newport fiber couplers, which have an aperture center at a 3" height from the table. (Bottom) Grided alignment card designed for aligning the probe beams into the Thorlabs fiber couplers located on the vacuum chamber.

density ND filter. There are several ND filters that can be installed at this point to decrease the reference beam power to 10–15 mW. After the filter, the reference beam passes to a fiber coupler, similar to the the probe beam setup.

After the main (zero order) beam exits the AOM, it passes to a turning mirror. The mirror turns the beam roughly 90° to create a large enough physical separation between the main beam and the reference beam to accommodate the rest of the optics. After the turning mirror, the beam passes through a ND filter to decrease the beam power to approximately 80 mW and ensure that each probe beam is ≤ 10 mW once they reach the fiber couplers. The main beam enters a series of seven beam splitters arranged to split the initial beam into 8 beams of approximately equal power. Each beam splitter has one input beam and two output beams, and a beam blocker blocks the stray light on the final side. Each beam splitter is mounted on horizontal mount capable of a rough pan and tilt. After the final beam splitter, each probe beam is reflected off a turning mirror into the fiber coupler. The turning mirror is used to get the beam entrance into the fiber coupler as straight as possible. The smaller the entrance angle into the fiber coupler, the higher the coupling efficiency.

Since the coupling efficiency depends on a small entrance angle into the fiber coupler, it is often useful to align the beams along the rows of holes in the air table. All fiber couplers in the system are mounted, or manufactured, such that their light collection optics tend to be centered on these rows. The optics do not have to mounted so that this is the case, but it is helpful to do so. Aligning the beams along the hole rows is primarily accomplished using an alignment card with some version of a grid marked on it. The grid gives and easy reference for both the X and Y positions of the beam. Hold the card at multiple points along the row of holes the beam should correspond with and adjust the turning mirrors until the beam is at roughly the same X and Y positions at all positions. For this comparison, it is useful to the positions closest to and farthest from the turning mirror or beam splitter; the greater the distance between the comparison points the more efficient the coupling into the fiber should be in the end.

When adjusting the beam splitters to align the beams, it is important to remem-

ber that every probe beam passes through multiple beam splitters. Thus, *adjusting a single beam splitter may affects the positions of multiple beams.* Beams that pass straight through a beam splitter are not deflected by the beam splitter and adjusting the beam splitter does not change their position. Beams that are split off at 90° by a beam splitter are affected by adjusting the beam splitter and beam splitter can be used to change their position. Thus, adjusting the first beam splitter in the series, right after the ND filter, will change the positions of beams '1', '2', '5' and '6' (as labeled on the fiber chords). Beam '8' is the only probe beam that passes straight through all incident beam splitters. To adjust beam '8's position, use the turning mirror before the beam splitters. This does affect every probe beams position, so *align beam '8' first.*

Aligning a laser beam into a fiber optic cable with a Newport F-91-C1 fiber coupler

A fiber coupler consists of a focusing lens and a fiber held in a 5 axis stage, which can be adjusted for X, Y, Z (where Z is the axis along the fiber length), pan and tilt. Newport F-91-C1 fiber coupler uses a microscope objective to focus the laser into a single-mode fiber held in a fiber chuck. For these couplers the removal/replacement of the fiber/fiber chuck assembly is not high precision, so the alignment of the beam into the fiber must be done with the actual 20 m fiber mounted in the coupler. Other coupler designs may allow for the use of a shorter fiber patch cable for convenience.

All of the Newport fiber couplers are located on the large optical table, in the initial beam establishment stage of the interferometer. All beams at this stage are 3b beams and thus laser goggles must be worn at all times. During alignment, a laser power meter is placed after the launch optics on the other end of the fibers. Thus, for alignment of a single chord, for a given fiber coupler at the optical table the power meter should be secured to the corresponding fiber collimator on the

chamber. Since the power meter doesn't have a long enough chord to reach back to the laser enclosure, we have set up a video camera/tv system instead. We point the video camera at the power meter (at the chamber) and a BNC cable carries the video signal to the TV located in the laser enclosure. Make sure the BNC cable is connected to the video camera during alignment, but disconnected when the pulsed power system is in use.

The basic strategy for alignment is to adjust the fiber position until the power readout is at maximum. On average the coupling efficiency and attenuation from the fiber will drop the power at the other end of the fiber down to 35-50 percent of the input power. Since laser goggles must be worn at all times, the alignment relies solely on the power meter reading. If you have to align the chord from scratch (no signal), then a good technique for this type of alignment is to start by placing the fiber as close to the focusing optic (microscope objective) as the coupling stage will allow. Do this by rotating the fiber chuck holder. If the beam is entering the focusing optic at normal incidence, and at the lens center, then placing the fiber near along the center axis of the lens should collect enough light to produce a noticeable signal at the power meter. Once a signal is seen, adjust the X and Y axes (knobs on the chuck holder) until the signal is at maximum. Then, move the fiber away from the lens in Z (rotate the chuck mount). This should produce an increase in signal. Readjust the X and Y positions until the signal is at maximum again. Move the fiber another increment in Z. Repeat this procedure until the fiber positioned at the focus point of the beam. As the fiber position nears the beam focus, the fluctuations in the power signal become greater with smaller position adjustment. As the fiber nears alignment, Pan and Tilt adjustment (knobs on the coupler base) can be added to the X and Y adjustments. Also, as the fiber nears alignment, or the signal fluctuations become greater, the incremental steps in Z should be as small as possible, in order to not overshoot the focus point.

Aligning a laser beam into a fiber optic cable with a Thorlabs PAF-X-18-PC-A fiber coupler

Unlike the fiber couplers for the probe chords during the initial beam establishment stage, the reference chord uses a Thorlabs PAF-X-18-PC-A fiber coupler mounted on a Thorlabs K6X kinematic optic mount. The Thorblabs fiber coupler assembly does have a steeper learning curve and more sensitive adjustment screws than the Newport assembly, but the Thorlabs coupler also has the major advantage that the fiber can be removed and replaced without significantly affecting the light coupling into the fiber. The ability to switch out the fiber is due to the fiber screwing directly into the back of the coupler, instead into a fiber chuck that is separately inserted into the coupler assembly. Thus, instead of attaching the power meter to the end of the reference fiber in the recombination section and having to deal with complications arising from restricted access to the optics, we can instead use a short (1–2 m) fiber patch cable with a collimator attached directly to the portable power meter. The parts for this patch cable assembly are shown in Fig. A.2, while a photo of the entire assembly in use with a Thorlabs fiber coupler is shown in Fig. A.3.

The method for aligning a Thorlabs fiber coupler is essentially the same as a Newport coupler, with the major difference being in how the fiber position along each axis is adjusted. Start by placing the fiber as close to the focusing optic (front lens) as the coupling stage will allow. Do this by turning each of the three set screws in the back of the mount an equal amount until they are as far in as possible. These sets screws require a hex wrench to adjust. Once a signal is seen, adjust the X and Y axes (set screws on the sides of the mount, also requiring a hex wrench) until the signal is at maximum. Then, move the fiber away from the lens in Z, by again adjust the three set screws in the back of the mount equally. Readjust the X and Y positions until the signal is at maximum again. Move the fiber another increment in Z. As the fiber nears alignment, Pan and Tilt adjustment (knobs on the K6X coupler) can be

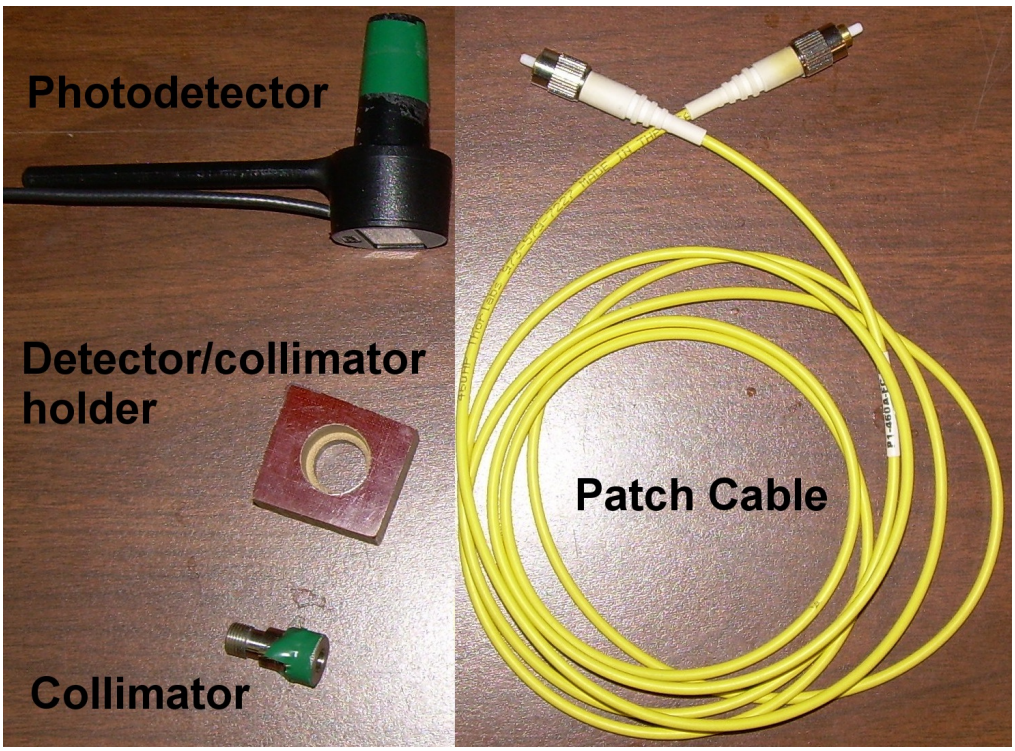

Figure A.2: Parts for the patch cable assembly consist of a 1 m Thorlabs 460HP single-mode fiber, a Thorlabs CFC-11X-A adjustable focal-length collimator, a Coherent Inc. OP-2 VIS photodetector (which is used with a Coherent Inc. FieldMaxII-TO power meter), and a homemade detector/collimator holder.

added to the X and Y adjustments. Repeat this procedure until the fiber positioned at the focus point of the beam.

A second advantage of the Thorlabs coupler is that the Z position is not affected by removing the fiber, so once the the Z position corresponding the the fiber focus is set the coupler's Z position should not have to be adjusted again unless a major change is made to the incoming beam. Instead, since the fiber slides into the holder before being screwed into place, we can adjust the fiber's position in the holder instead of adjusting the mount directly. Thus, to vary the Z position of the fiber during a maintenance alignment, place the fiber in the holder a pull it out slowly

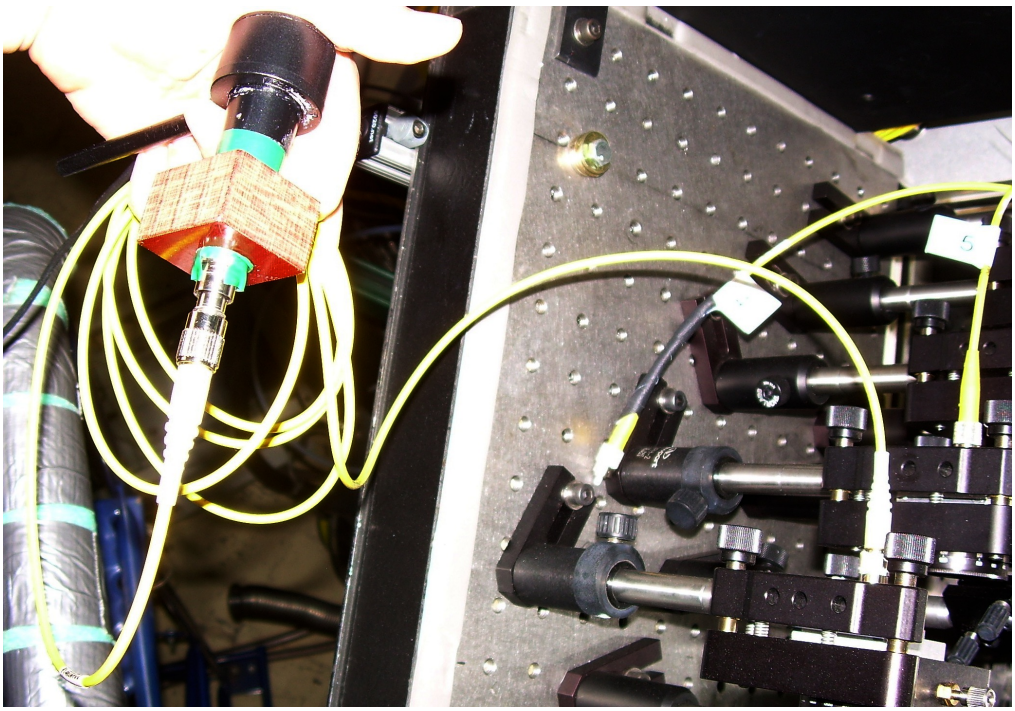

Figure A.3: Photo of the assemble patch cable assembly in use with a Thorlabs fiber coupler.

until it is as far as it can go before falling out of the holder. Adjust the Z position by gently pushing the fiber into the holder in as small increments as possible between each X and Y adjustment.

The fiber couplers on the chamber are also Thorlabs couplers. This is where the patch cable technique is especially beneficial, since the alternative requires use of a video camera and TV setup to align the system. The beams on the chamber are 3R, instead of 3b, so laser goggles are not required; this allows the introduction of some new techniques to the basic class 3b alignment technique. One technique is to remove the fiber from the coupler and hold an alignment card right next to the exit of the fiber holder. If the card is placed in the beam or waved repeated through it, one can see if the beam is coming out of the lens at normal incidence or not,

and adjust it so that it is centered. Another technique is to leave the fiber cable connected; the cable glows slightly when the beam is focused onto the fiber face. The glow will increase close to the focus point when the fiber is not aligned in Z. Once the fiber position is close to the focus point in Z as well, then the glow will decrease as the alignment improves, since more of the light will be coupled into the fiber core instead of dispersed along the fiber cladding. Both of these techniques are most useful for finding the beam, not precisely aligning it onto the fiber core. For example, if the fiber is positioned close to the focus point, but the fiber coupler gets bumped, or otherwise perturbed, then these techniques can help reposition the beam near the fiber core enough for a distinguishable signal without completely beginning alignment procedure again for that fiber coupler. Once a distinguishable signal is found, the previously outlined technique to fine tune the beam position.

A.2 Positioning the probe beam in the chamber

The probe beam travel from the initial fiber coupler to the chamber optics. Then they pass through a collimation optic, which consists of a holder for the fiber end and a collimation lens. The collimation optic allows the distance between the fiber and lens to be changed, in order to collimate, or even focus the laser light. For initial tests, collimation of the light works best.

To collimate the beam, place two alignment cards about 10 m apart (to simulate the collimator-to-coupler distance of the optics on the chamber). Compare the beam diameter at each card against the desired diameter and adjust the collimator until the diameter is the same at both alignment cards. Again, alignment cards with a grid or some other form of gradation will be required. As a precaution, run a card along the length of the beam to ensure that the diameter is approximately the same at all positions, and that the beam does not have an unintentional focus point.

After the beam leaves the collimator, it may be reflected off a turning mirror (depending on the chord arrangement), then propagates across the chamber, and finally reflects off a turning mirror or mirrors into the fiber coupler. The turning mirrors can be used to adjust for discrepancies in height or relative angle between the collimators on one side of the chamber and the fiber couplers on the other. The fiber couplers on the chamber are all Thorlabs fiber couplers, so once the beam is reflected into the fiber coupler use the procedure for coupling into these couplers as outline previously. Adjusting the initial collimator and turning mirror positions to place the beams at the desired positions in the chamber is covered in the next section.

Probe beam position alignment tools

It is useful to prepare a set of alignment tools outlining the desired probe beam positions before attempting to place any optics in the system. The three most convenient places to attach alignment tools to are the launch and receive windows, and along the propagation axis of one of the guns in the chamber. The suggested alignment tools for the windows are matching paper covers with grids that can be laid over the entire window. An example of a window alignment paper is shown in Figs. A.4 and B.15. The paper covers should also have some marking or indicator that lets you place the cover repeatedly in the approximately the same position on the window.

An alignment tool inside the chamber is optional in some cases, but makes for the highest accuracy in beam positioning. The tool should be able to be placed in the region of diagnostic interest, the probe beams should be visible at the tool, and the tool must be either partially transparent or easily removed such that you can see the beam positions at the receiving window. For previous positioning, we used a piece of wire or clothesline (as shown in Fig. A.5) a transparency (as shown in

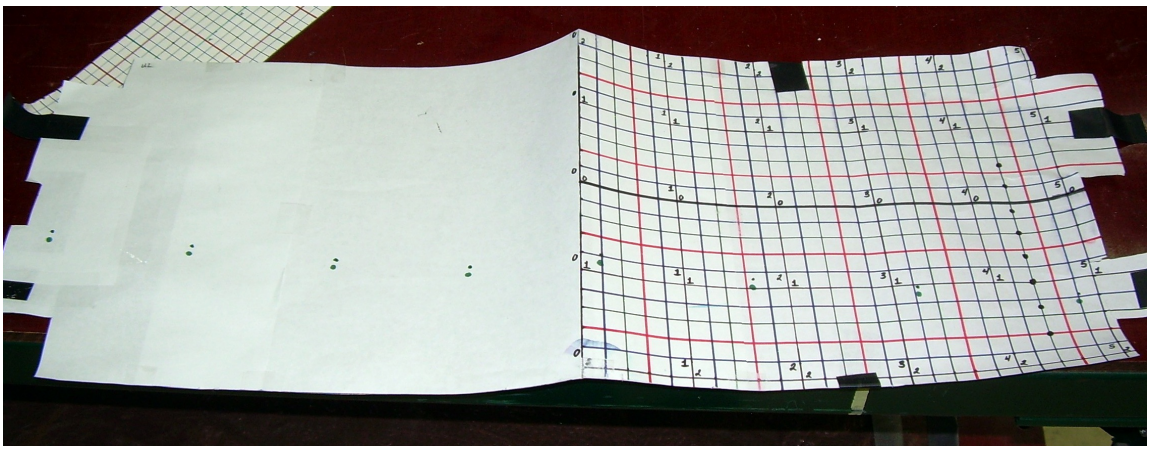

Figure A.4: Photo of a window alignment paper.

Figs. A.6&A.7), and a modified flange as our alignment tools. The wire was clipped to the end of the gun muzzle and run across the chamber to the modified flange, which had a hole in the center of the flange such that the wire could be run through the hole and secured on the outside of the flange. This way the wire approximated the axis of jet propagation from that gun. The transparency was marked with a grid (similar to size to the ones on the windows), a line approximating the jet axis, and the desired chord positions relative that jet axis. The transparency was taped to the wire at the desired distance from the gun such that the line approximating the jet axis lined up the wire.

Placing the launch optics

If it doesn't matter what angle the beam passes through the plasma at, then the goal is for each beam to pass through the desired spot (marked on the alignment tool) inside the chamber and still exit the receiving window. If it does matter what angle the beam passes through the plasma, then there should be two positions marked for each beam, one on the alignment tool in the chamber and one marked on the cover

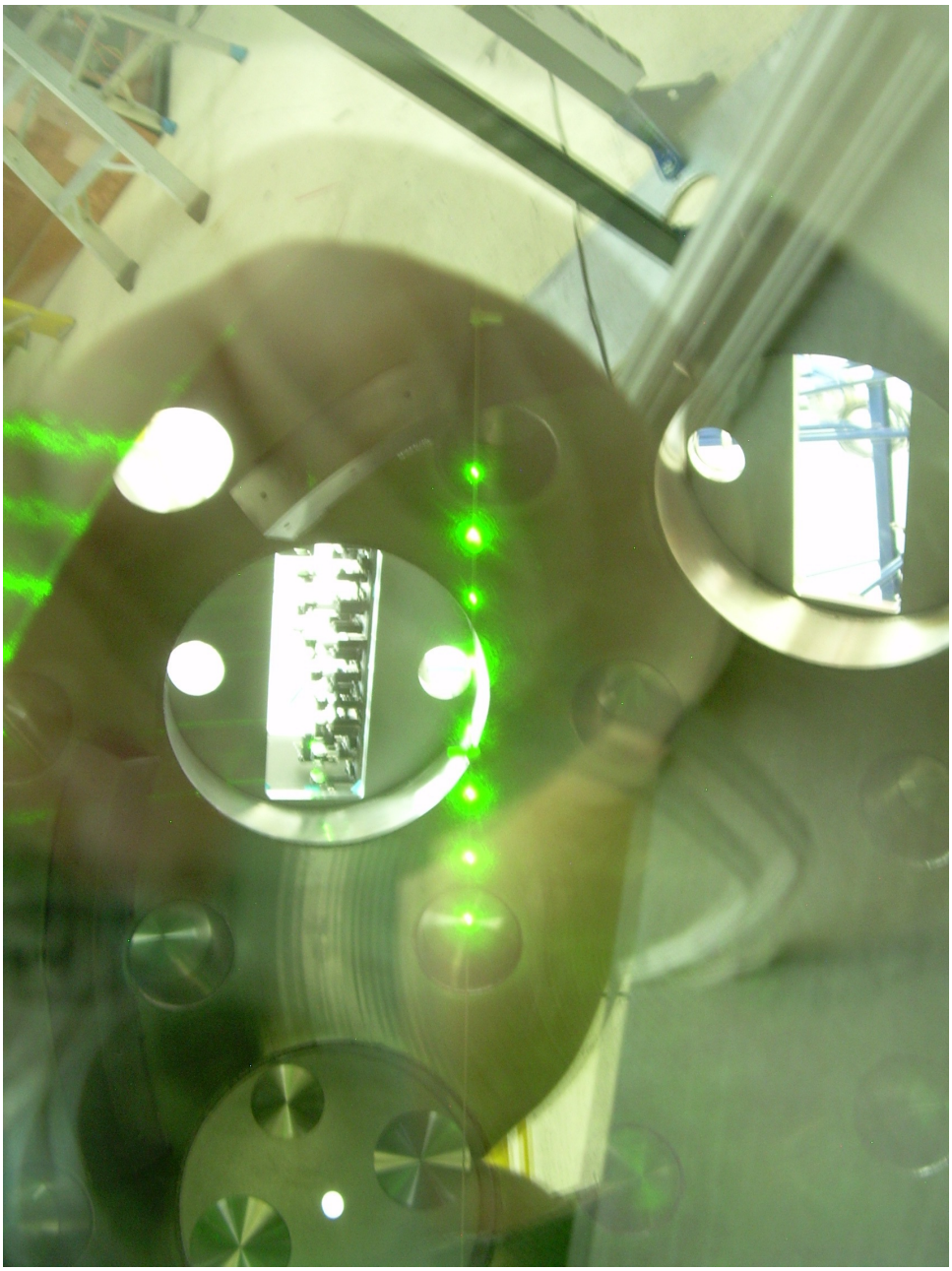

Figure A.5: Picture of the interferometer chords, for the single-jet axial experiments, along a clothesline strung between the railgun nozzle and the opposite port. Some reflections of the surrounding room off the window are also present.

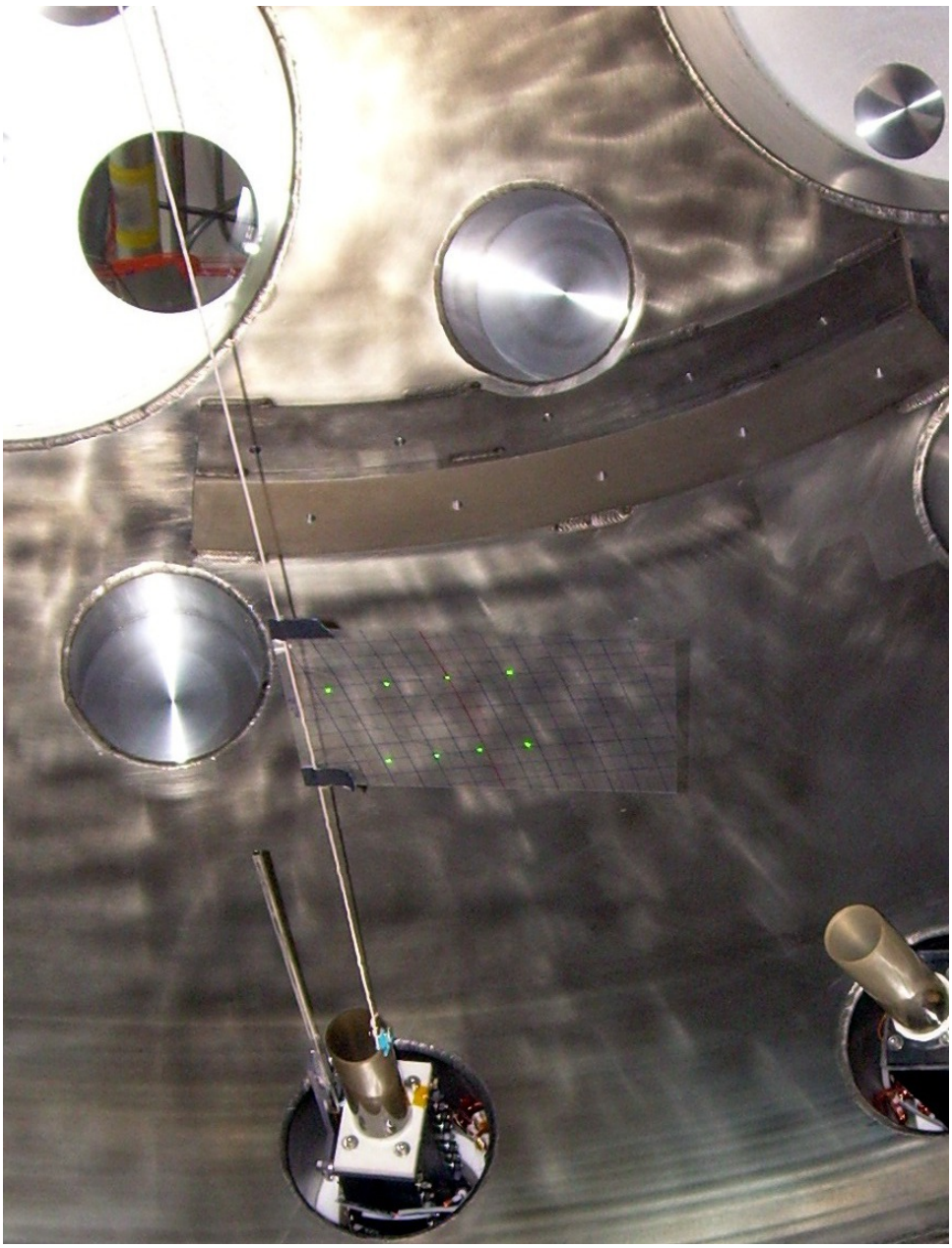

Figure A.6: Picture of a gridded transparency attached to a clothesline strung between the top railgun nozzle and the opposite port. Interferometer chords in the $Z = 50, 60$ cm configuration are present on the transparency.

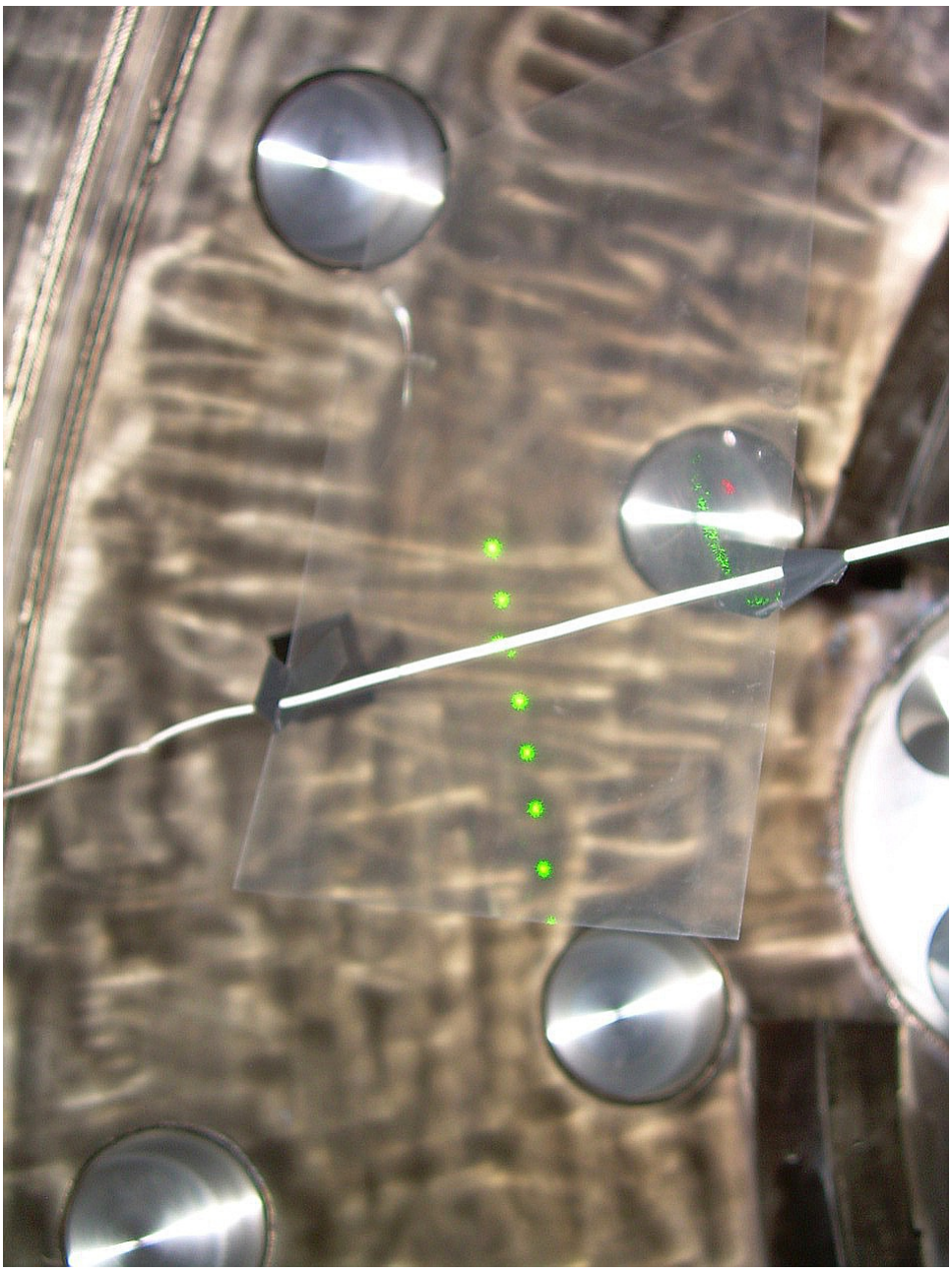

Figure A.7: Picture of a transparency attached to a clothesline strung between the top railgun nozzle and the opposite port. Interferometer chords in the $Z = 85$ cm configuration are present on the transparency.

for the receiving window.

Start with the optics for the chord that is closest to edge of the window, especially the edge of the window nearest to the breadboard. The width of the optic mounts will limit the minimum height of the beam off the breadboard. If the beam needs to be closer to the breadboard than the optics' width allows, then the breadboard can be mounted on the other side of the window and long posts can be used to span the height of the window.

If the beam positions are supposed to be at different heights relative to the breadboard, place the optics for the lowest beam positions first. This allows the higher beams to be directed over the hardware for the lower beams should space on the breadboard become limited.

Place the hardware for one beam at a time. Each beam should have a fiber launch collimator and mount as well as a post, a postholder and a base. The position of the post in the postholder can be used to make large adjustments to beam height and mount rotation. The position of the base can be used to make large adjustments of the horizontal beam position. Use these methods to get the beam close to the desired position. Once the beam is close, then use the pan/tilt adjustment screws on the mount to do fine adjustment.

Once the beam placement is done mark the final beam positions on both window covers. This way if the system gets disturbed, then the covers alone can be used to put the beams back in the correct positions. Also, if the chord positioning is done with the chamber at atmosphere the beams may experience a different deflection through the windows when the chamber is brought down to vacuum.

Before removing the in-chamber alignment tools check if the spectrometer needs to be moved to line up with any of the chord positions.

Placing the receive optics

The receive optics consist of a turning mirror or mirrors and a fiber coupler for each chord. The purpose of the turning mirror(s) is to direct the beam into the lens of the fiber coupler. The more centered and on axis the beam is when it enters the lens, the greater the amount of light that will actually be coupled into the fiber. The easiest way to do this is to use the turning mirror to make the beam parallel to the surface of the breadboard, as well as parallel to (not necessarily on) the grid lines of the breadboard.

Use a grided index/alignent card to determine the beam position on the grid with the card close to the mirror. Then move the card as far from the mirror as possible on the breadboard. Move the beam to the same position on the grid as before. For large adjustments rotate the mirror mount or base. For small adjustment use the pan/tilt screws on the mount. This will often take multiple passes since the beam grid position near the mirror will change with large adjustments.

Once the beam is in place, insert the coupler. It is easiest to line the post holder for the coupler up with the beam path first and then add the coupler itself (sans fiber) once the post holder is in place. Adjust the height of the post in the post holder to match the beam height. You can check this by holding a piece of paper near the output if the coupler. If the beam is on the lens, then the beam should appear on the paper. The beam will have multiple rings/fringes around the center spot due to diffraction from the collimator lens and windows. The fringes will help you center the beam on the lens. Use the post height, post holder position, and mount rotation to center the beam on the lens. The adjustment screws on the coupler mount are only useful for fine alignment of the beam into the fiber.

Once the coupler is in place, insert the fiber before adding another coupler. Since the fibers protrude from the back of coupler, their position must be taken into ac-

count when attempting to accommodate all the optics. The fibers can be bent, but sharp bends put strain on the fiber as well as effecting the beam polarization at the recombination stage. Make sure all fibers can be removed and re-inserted for fine alignment purposes.

A.2.1 Recombining the probe and reference beams

At this stage there are eight probe beams and one reference beam. All of these beams leave their fibers through the same type of collimation optic used to send the probe beams through the chamber. The eight probe beams have the collimation optics mounted in a rotating mount. The reference beam collimator is mounted in a standard mirror mount. Adjusted the collimator until the beam has the desired diameter along the pertinent length. The diameter of the probe beams should approximate the diameter of the reference beam to optimize the signal from recombination. For this purpose, collimating all the beams would be preferable; this should lead to the most consistent beam diameters, even if the propagation distances vary.

The reference beam is split into eight reference beams, all of approximately the same power, through a series of beam splitters. This setup mirrors the beam splitter and beam blocker arrangement originally used to divided the initial probe beam into eight beams. Each of the reference beams is aimed into another beam splitter, which is used to recombine the reference beam with one of the probe beams.

Each of the probe beams leave the their collimation optics and are reflected off a turning mirror into a recombination beam splitter. The turning mirror is necessary for alignment, since the rotation mount for the probe beams lack a Pan or Tilt control. The probe and reference beams should enter the beam splitter at the same height and near the center of the beam splitter face. An alignment card can be held close to the beam splitter face without an input or the recombined beam; both

reference and probe beams should be present on the card. The beam blocker on the beam splitter mount can serve the same purpose since the beams can be seen on it.

To optimize the interference signal, the polarizations of the probe and reference beams, as they enter the final fiber coupler, should be the same. A temporary polarizer is placed after the recombination beam splitter but before the fiber coupler. Hold an alignment card behind this. Cover or block the probe beam while the polarization of the reference beam is found. Once only the reference beam is present at the polarizer, adjust the polarizer such that the reference beam intensity is minimized at the alignment card. Next, unblock the probe beam and block the reference beam. Adjust the rotation mount holding the probe collimator, not the polarizer, such that the probe beam intensity is minimized at the alignment card. Unfortunately, rotating the collimation optics affects the probe beam position, so the final, careful alignment of the probe and reference beams should be left until after polarization is matched.

Adjust the reference and probe turning mirrors until both beams present on the card overlap. Finally, the reference and probe beams should overlap for the entire distance from the beam splitter to the fiber coupler. If the two beams overlap in the beam splitter, then adjustments to the beam splitter mount should be enough to create the beam overlap over the distance to the fiber coupler.

Once the probe and reference beams have been recombined, they will be coupled into a final multi-mode fiber, which will take them to the RF electronics. The alignment of the recombined beam into the fiber follows the same procedure as before, only using an oscilloscope readout from the bandpass filter or photo detector instead of a power meter readout. An inference pattern between the probe and reference beams generates a sinusoidal signal at 110 MHz, the frequency of the RF generator. To optimize the interference signal, set the oscilloscope to an AC readout and adjust the system turning mirror and recombination beam splitter to increase

the amplitude of the wave form. Polarization and beam overlap tend to be the most important aspects of the alignment affecting the wave form amplitude.

A.3 Quick alignment

For maintenance purposes, and before a experimental run, a quick alignment is all that should be required. In the completed interferometer system a quick alignment mainly consists of making sure the maximum amount of power is coupled into the fibers at the fiber couplers in the beam establishment stage and on the chamber. The recombination stage should only have to be adjusted periodically, not before every experimental run.

If the interferometer is regularly maintained/aligned, then when the power meter is attached to the end of the fiber some signal should still be present on most of the interferometer chords. If a signal is still present then, instead of using the full coupling procedure outlined in Secs. A.1.3&A.1.3, simply adjusting the X, Y, Pan and Tilt knobs/set screws may be able to maximize the power coupling without requiring any adjustments in Z.

The fiber couplers on the chamber are most likely to have the lowest coupling efficiencies since the propagation distance between the launch and collection optics is large and those optics/breadboards are more likely to be bumped during the course of a normal day. Also, if the room temperature deviates greatly ($\sim 10^\circ$ F) it causes enough chamber expansion to misalign the probe beams. Before beginning alignment of these couplers, it is worth using the window alignment papers to verify that the beams are in the correct place.

Appendix B

Interferometer Optics Configurations

This appendix contains photos of the interferometer optics configurations for all three chord configurations used in Chap. 3 and 4, and has been included to provide a resource for reproducing these configurations. As mentioned in Chap. 2, the fiber-optic nature of the interferometer effectively decouples the optics that determine chord placement from the rest of the system. So the both the set of optics dividing the initial singular laser beam into probe and reference paths and the set of optics used to recombine the probe and reference beams remain unchanged for all chord configurations; only the optics on vacuum chamber vary. We provide both side and top-down views of the launch and collection optics on the chamber to demonstrate both the placement of the optics on their breadboards and their various heights from the breadboard surfaces.

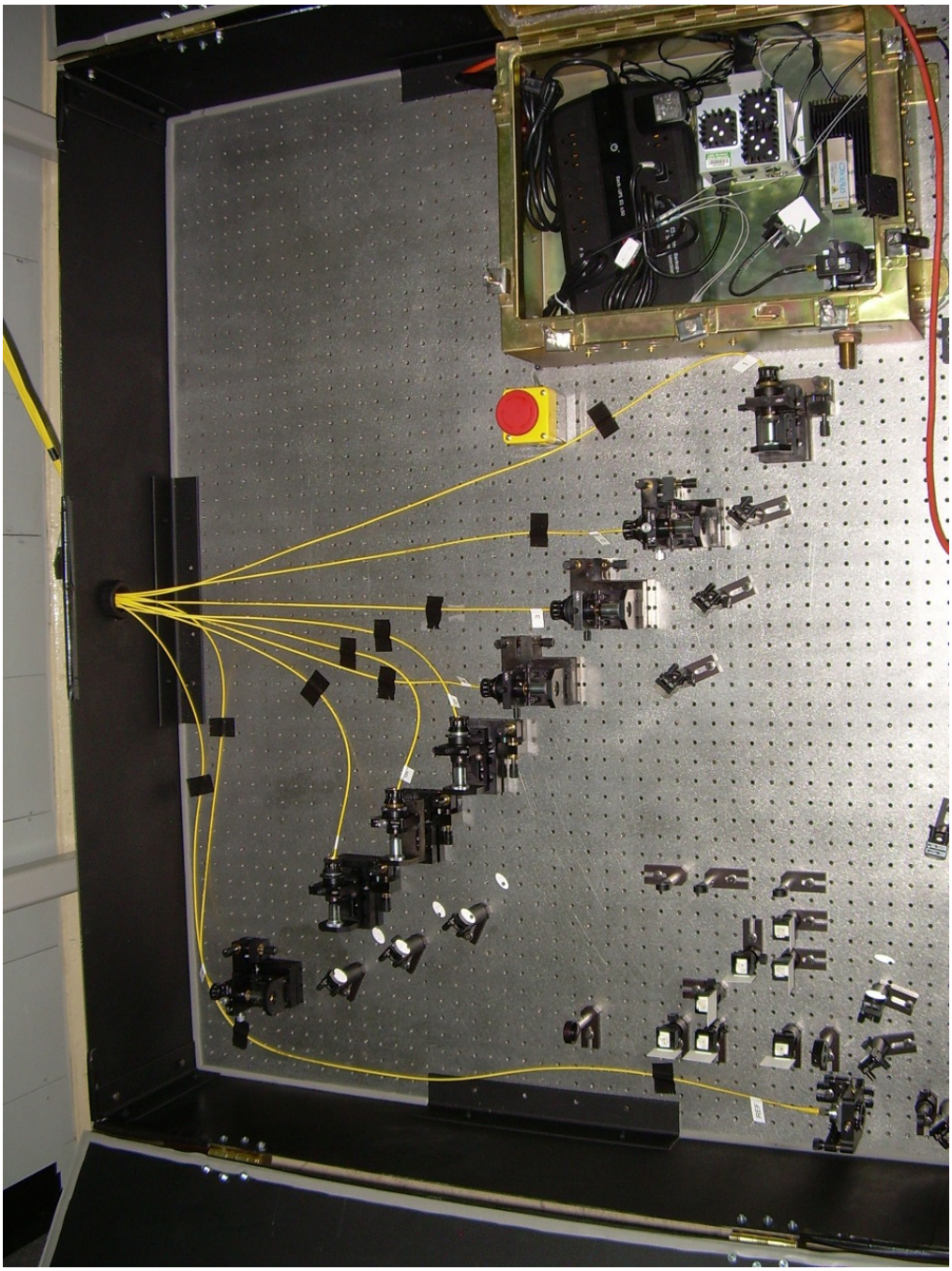

Figure B.1: Optics dividing the initial laser beam into eight probe beams and one reference beam, and coupling all beams into single-mode fiber leading to the vacuum chamber. The arrangement remains the same for all chord arrangements.

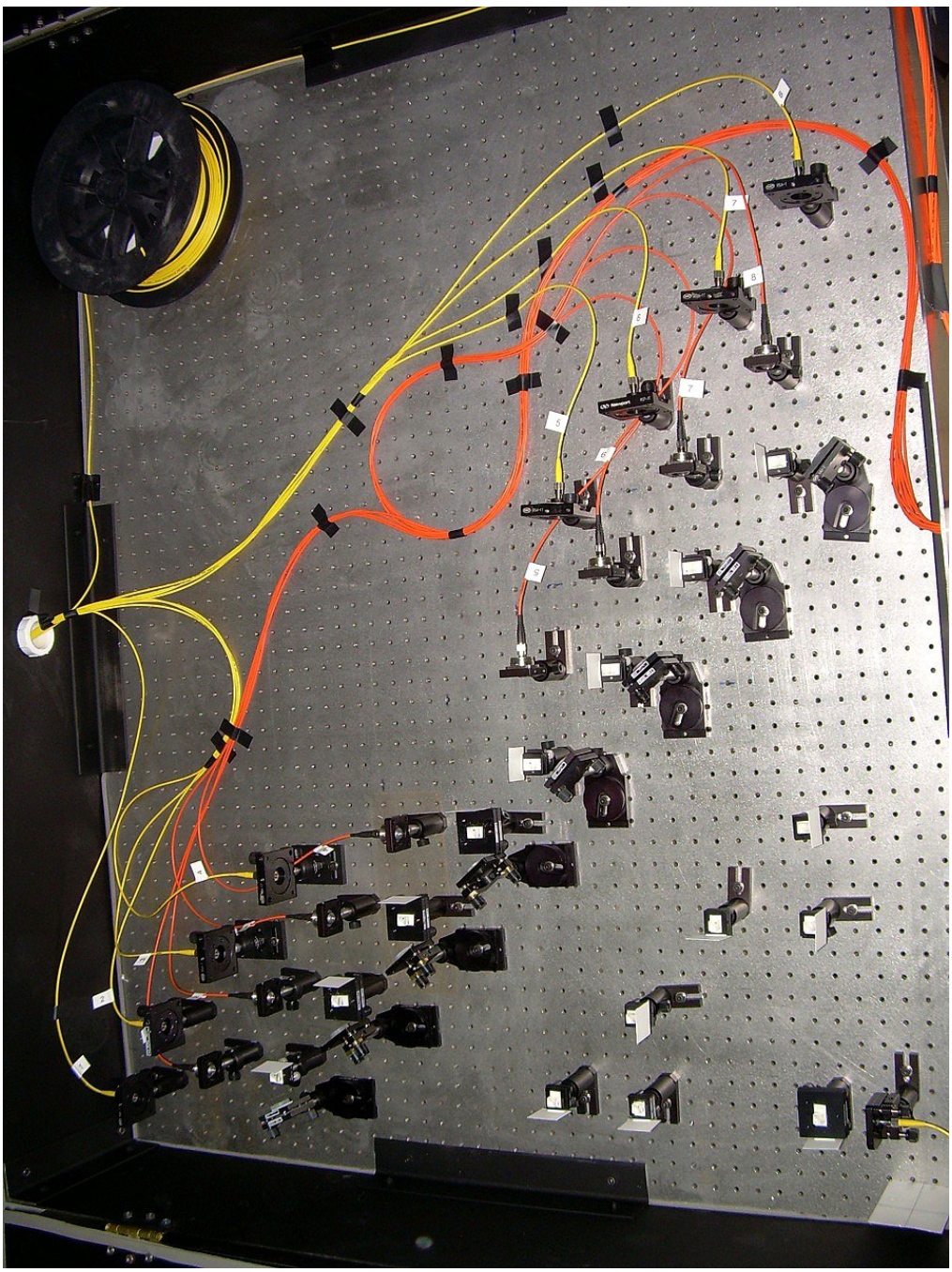

Figure B.2: Optics recombining the probe and reference beams to produce the interference signals. The arrangement remains the same for all chord arrangements.

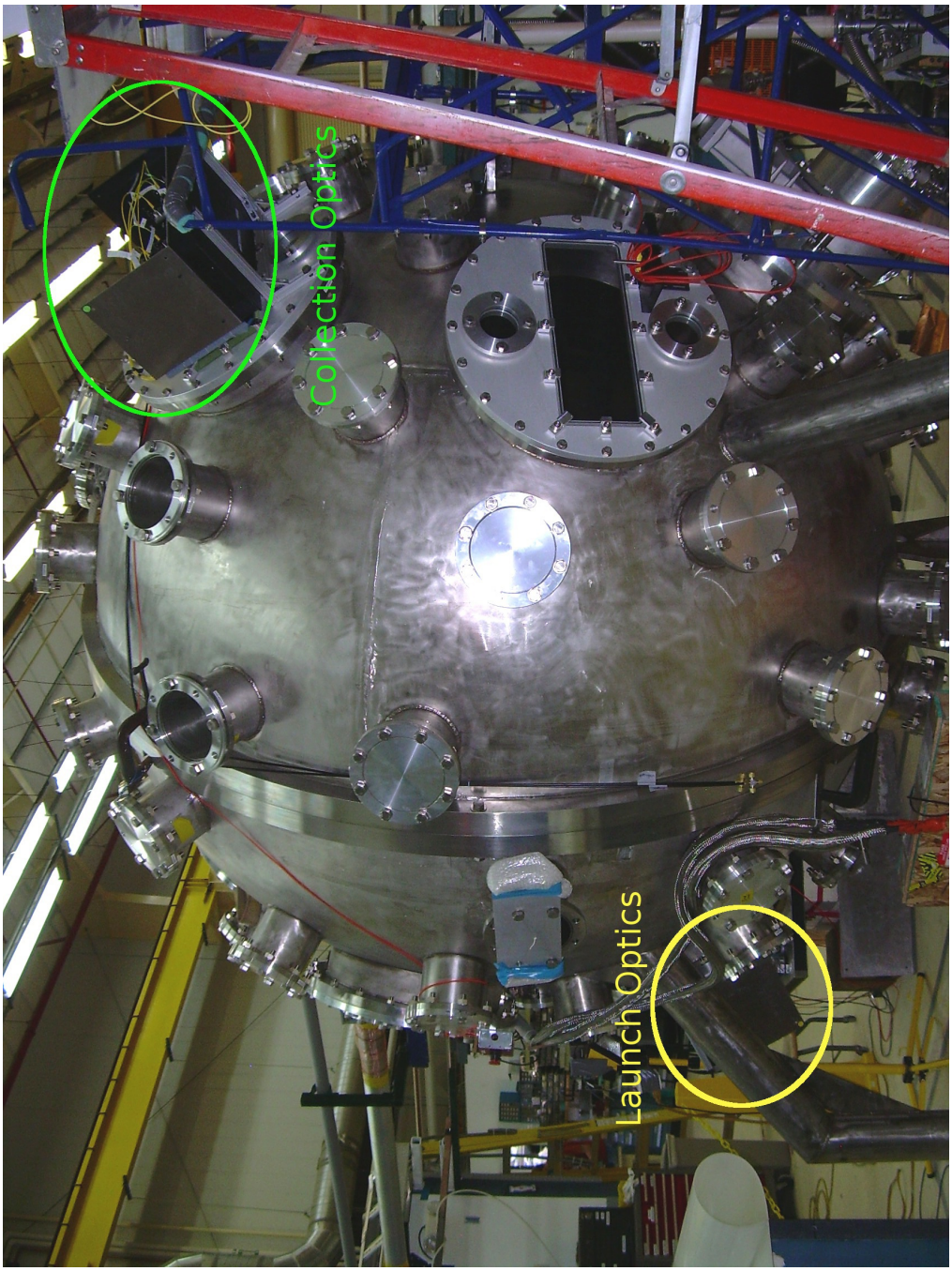

Figure B.3: Placement of the chord positioning optics, both launch and collection, on the vacuum chamber for the single-jet axial and $Z = 50, 60$ cm chord arrangements. Launch optics are on port $\theta 37\phi 216$ and collection optics are on port $\theta 143\phi 324$.

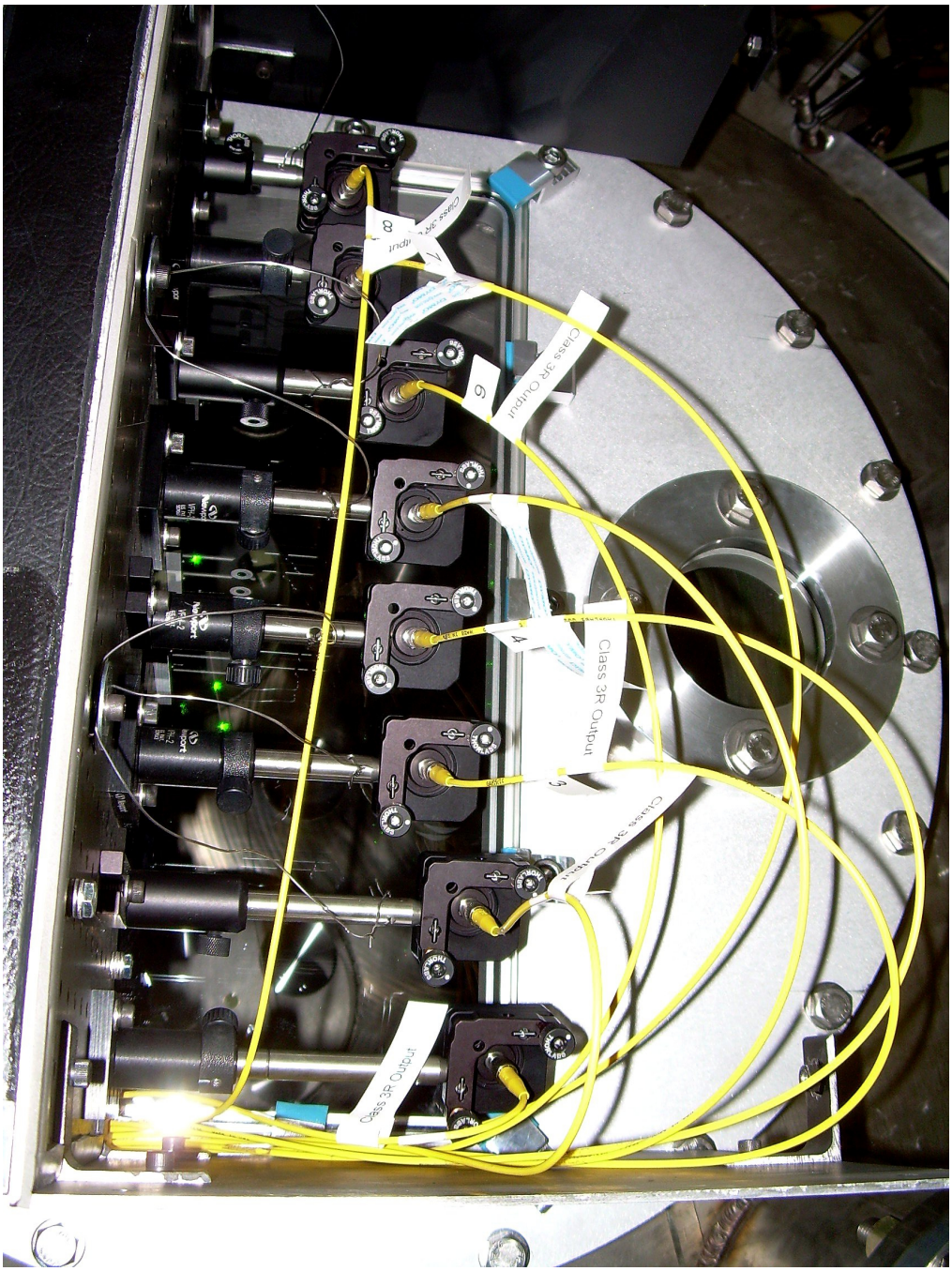

Figure B.4: Rear-view of the launch optics for single-jet axial measurements. The breadboard is mounted on port $\theta 37\phi 216$ and is pointing towards the ceiling with the optics hanging underneath.

Figure B.5: Top-view of the launch optics for single-jet axial measurements. The breadboard is no longer mounted on the chamber. The extra post-holders are for the spectrometer mount and mesh screen filters.

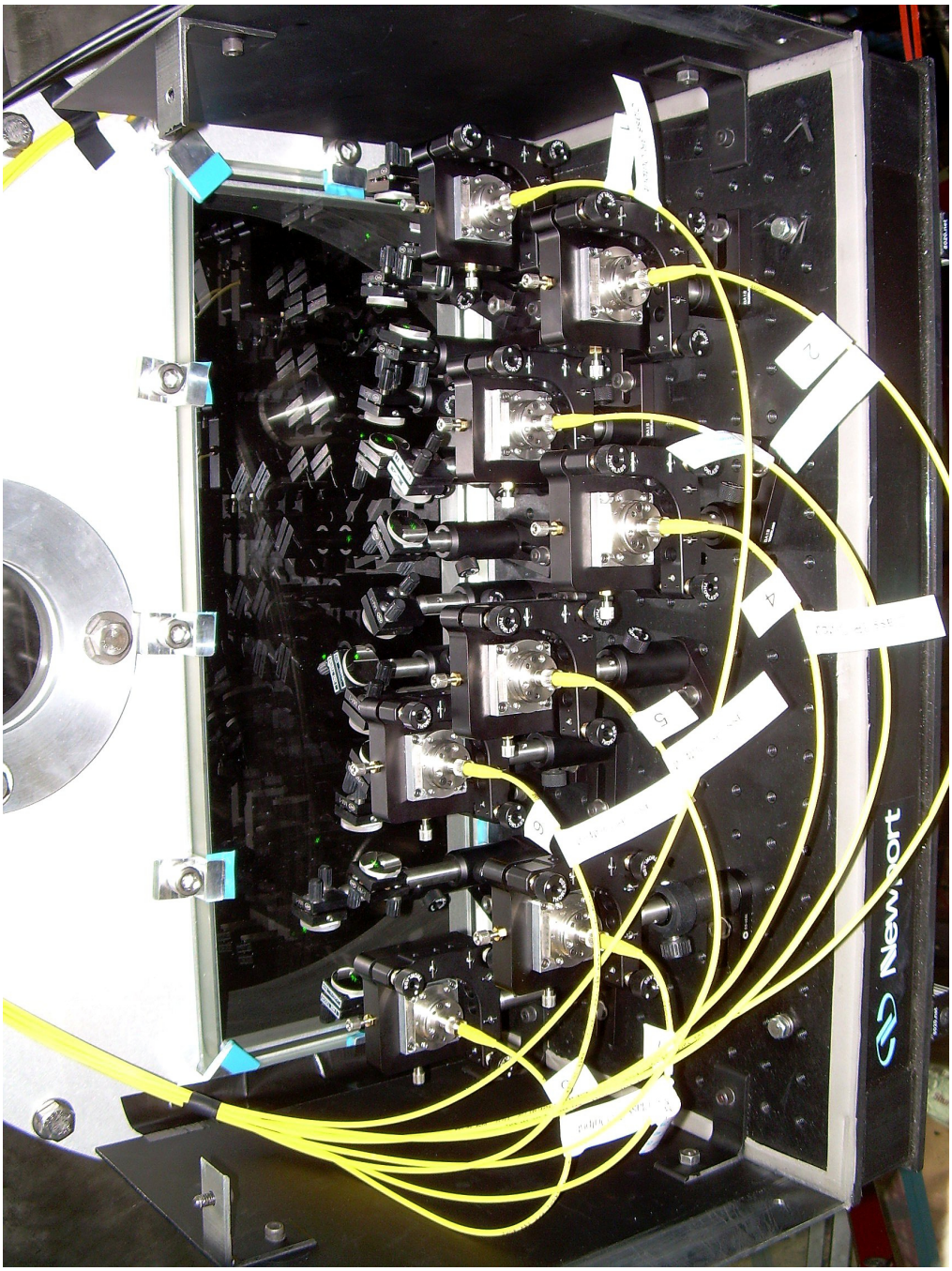

Figure B.6: Rear-view of the collection optics for single-jet axial measurements. The breadboard is mounted on port $\theta 143\phi 324$ and is pointing towards the floor with the optics mounted on top.

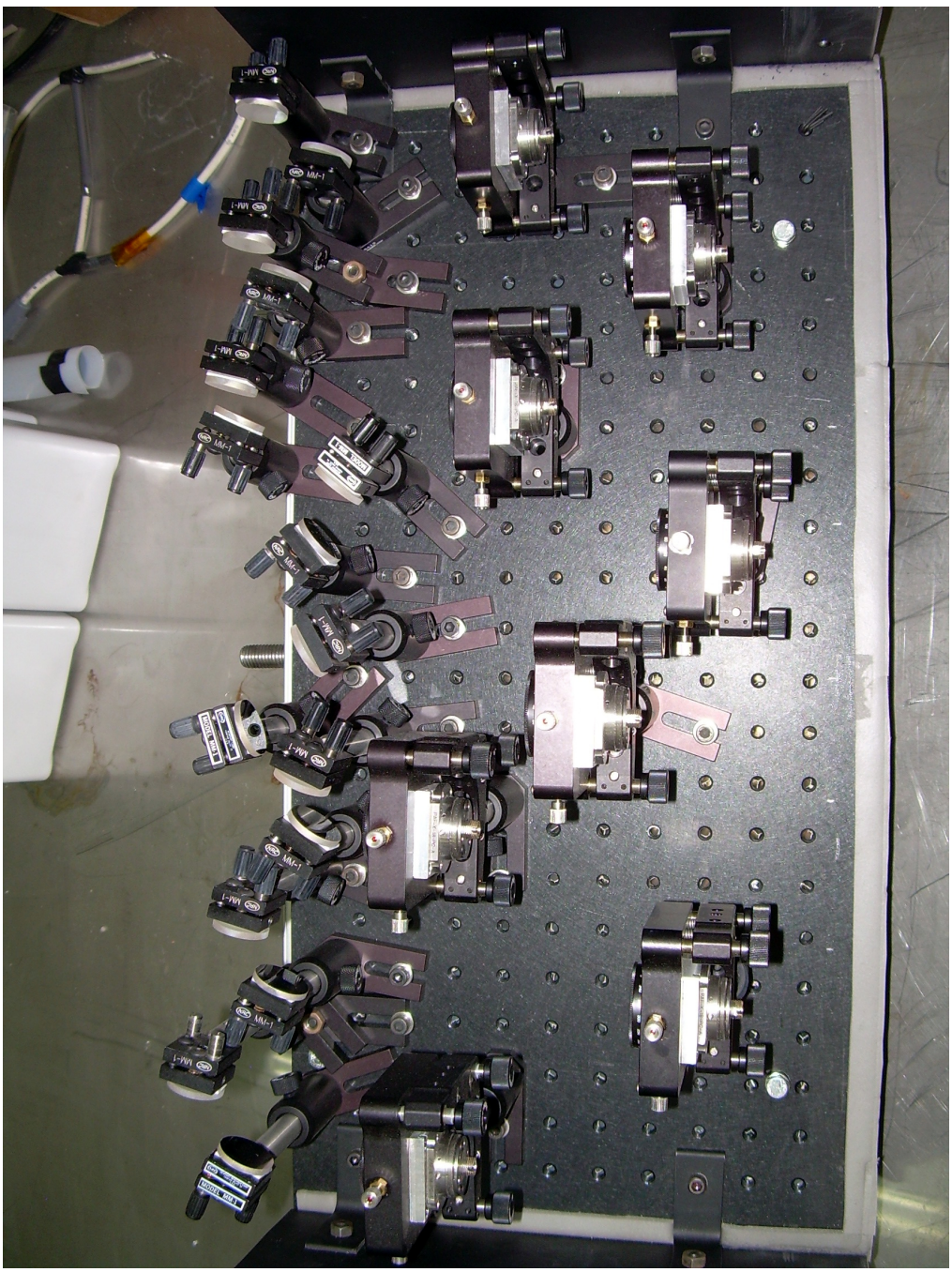

Figure B.7: Top-view of the collection optics for single-jet axial measurements. The breadboard is no longer mounted on the chamber.

Figure B.8: Orientation of the launch optics breadboard mounting on the vacuum chamber for the $Z = 50, 60$ cm chord arrangement. Breadboard is mounted on port $\theta 37 \phi 216$.

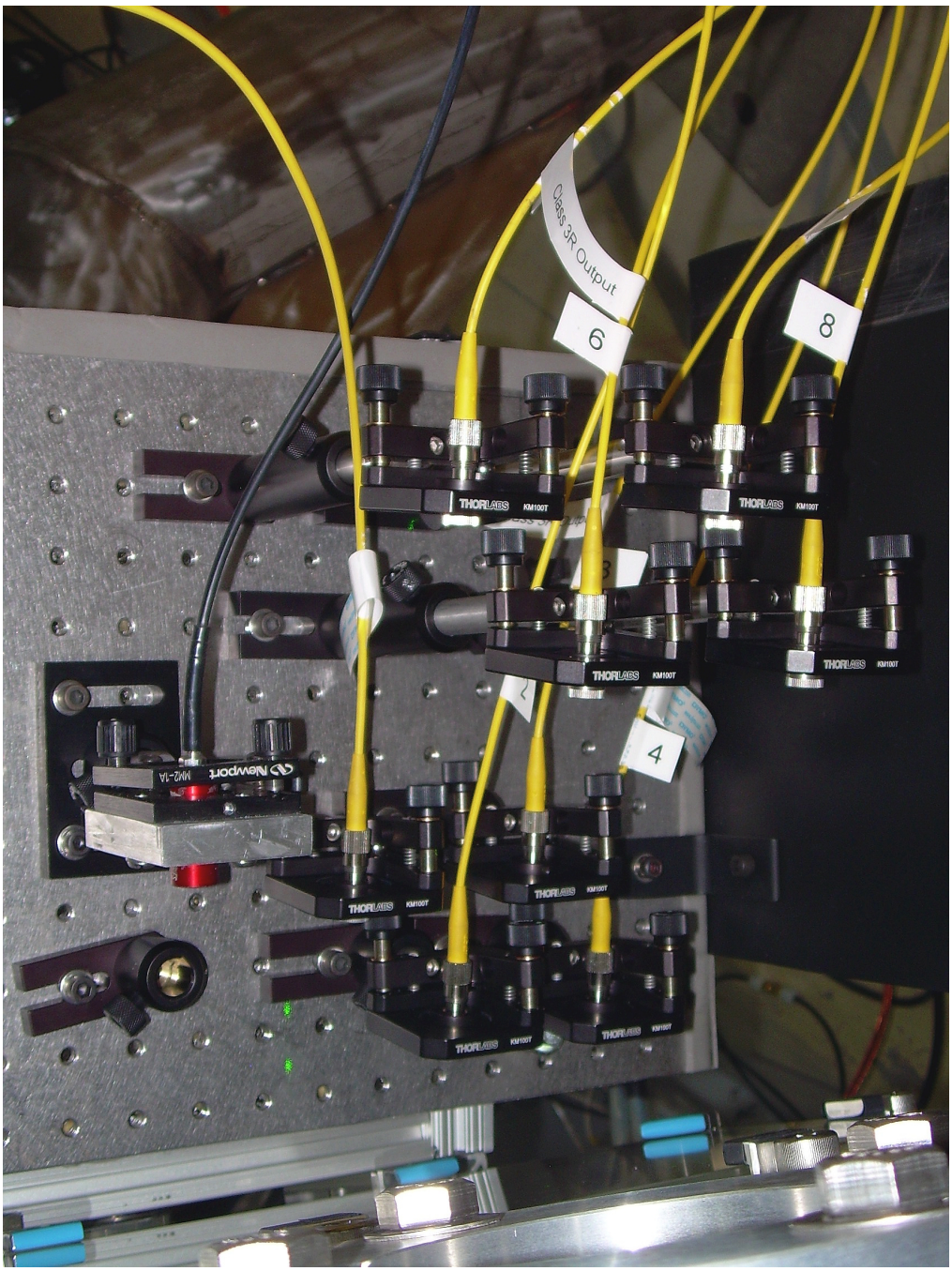

Figure B.9: Side-view of the launch optics for the $Z = 50, 60$ cm chord arrangement while the breadboard is mounted on port $\theta 37\phi 216$. The red fiber collimator is the spectrometer collection optic and the empty post-holder is for mounting mesh filters to reduce the light to the spectrometer.

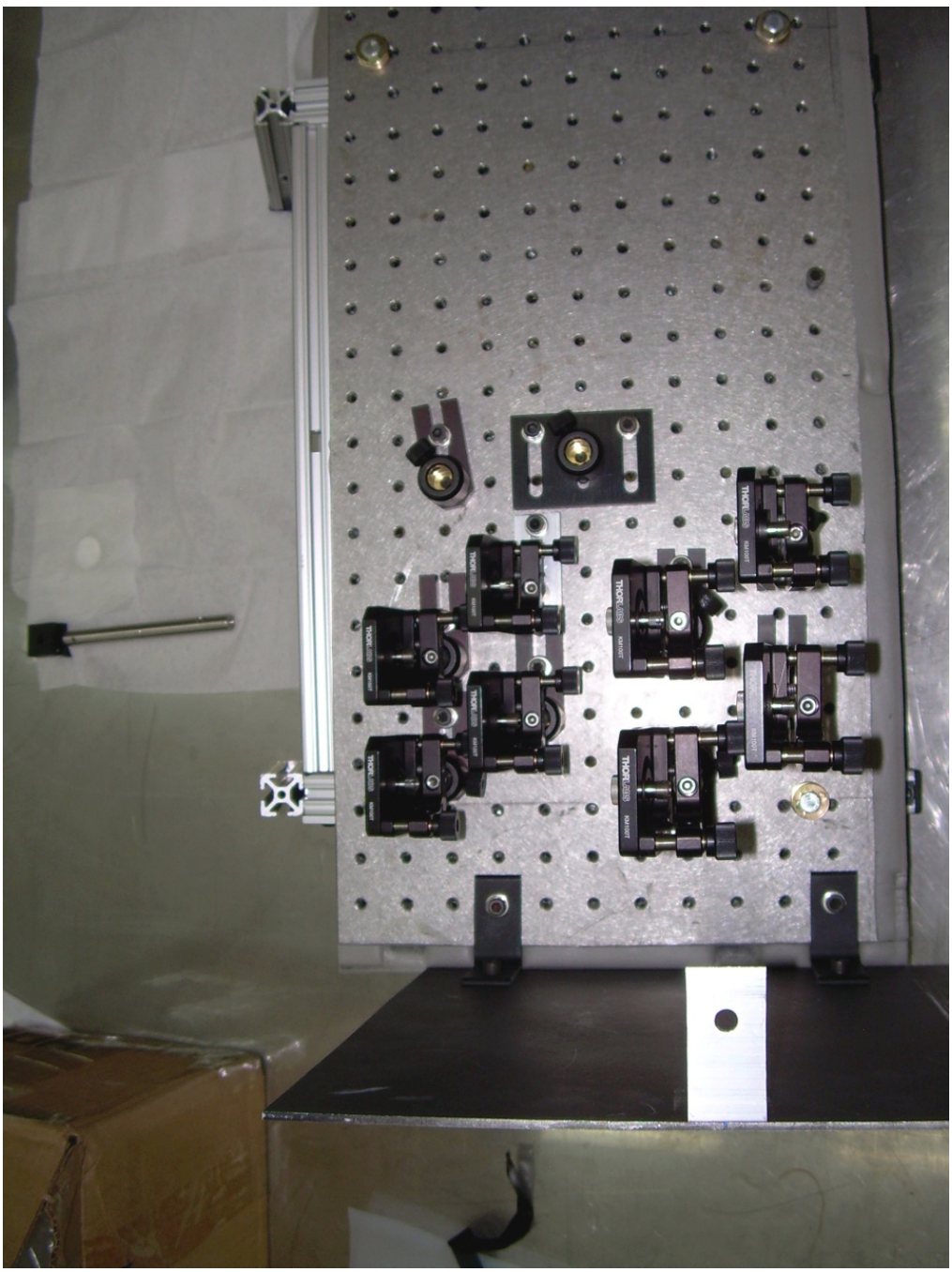

Figure B.10: Top-view of the launch optics for the $Z = 50, 60$ cm chord arrangement. The breadboard is no longer mounted on the chamber.

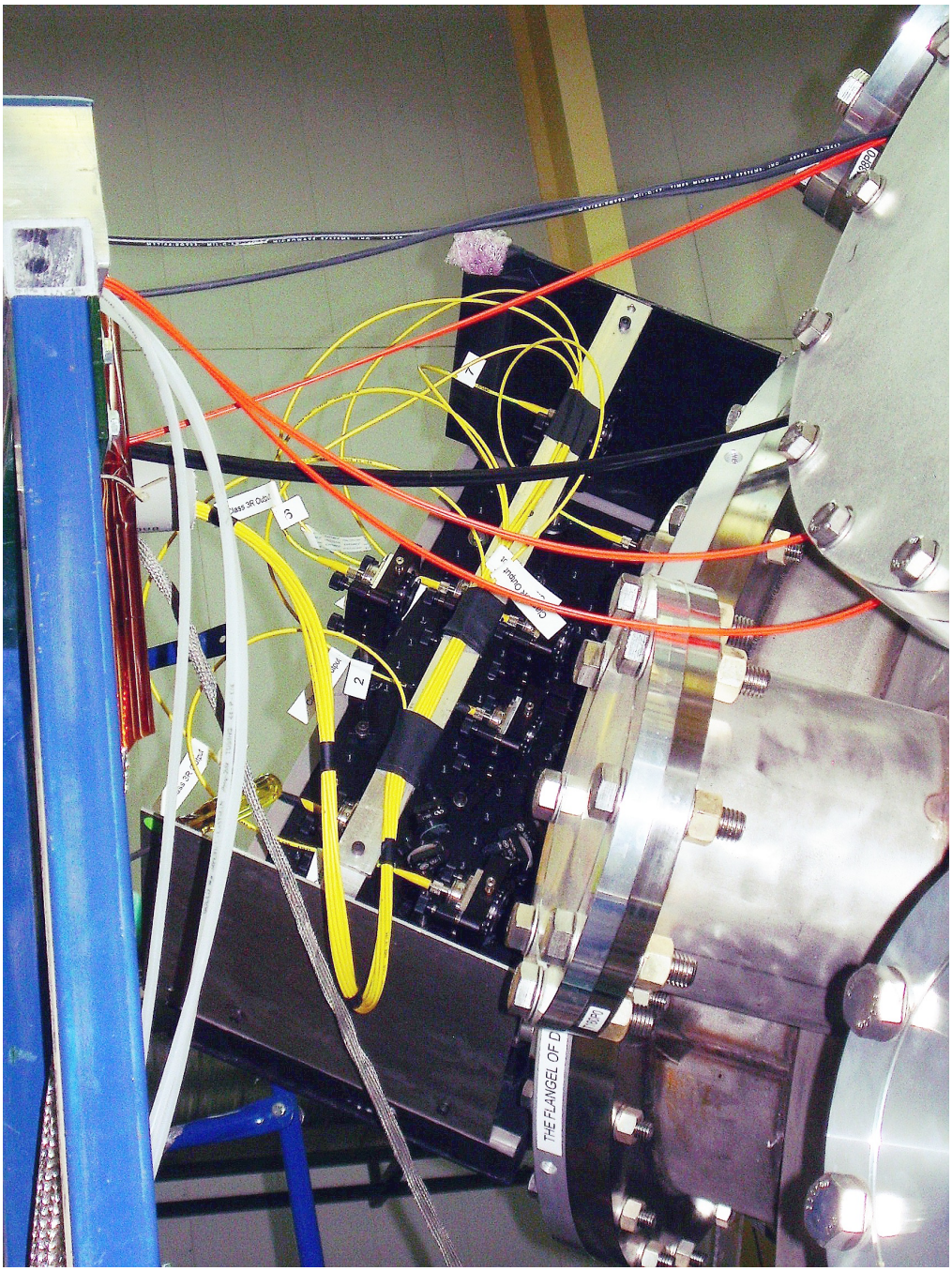

Figure B.11: Orientation of the collection optics breadboard mounting on the vacuum chamber for the $Z = 50, 60$ cm chord arrangement. Breadboard is mounted on port $\theta 143 \phi 324$.

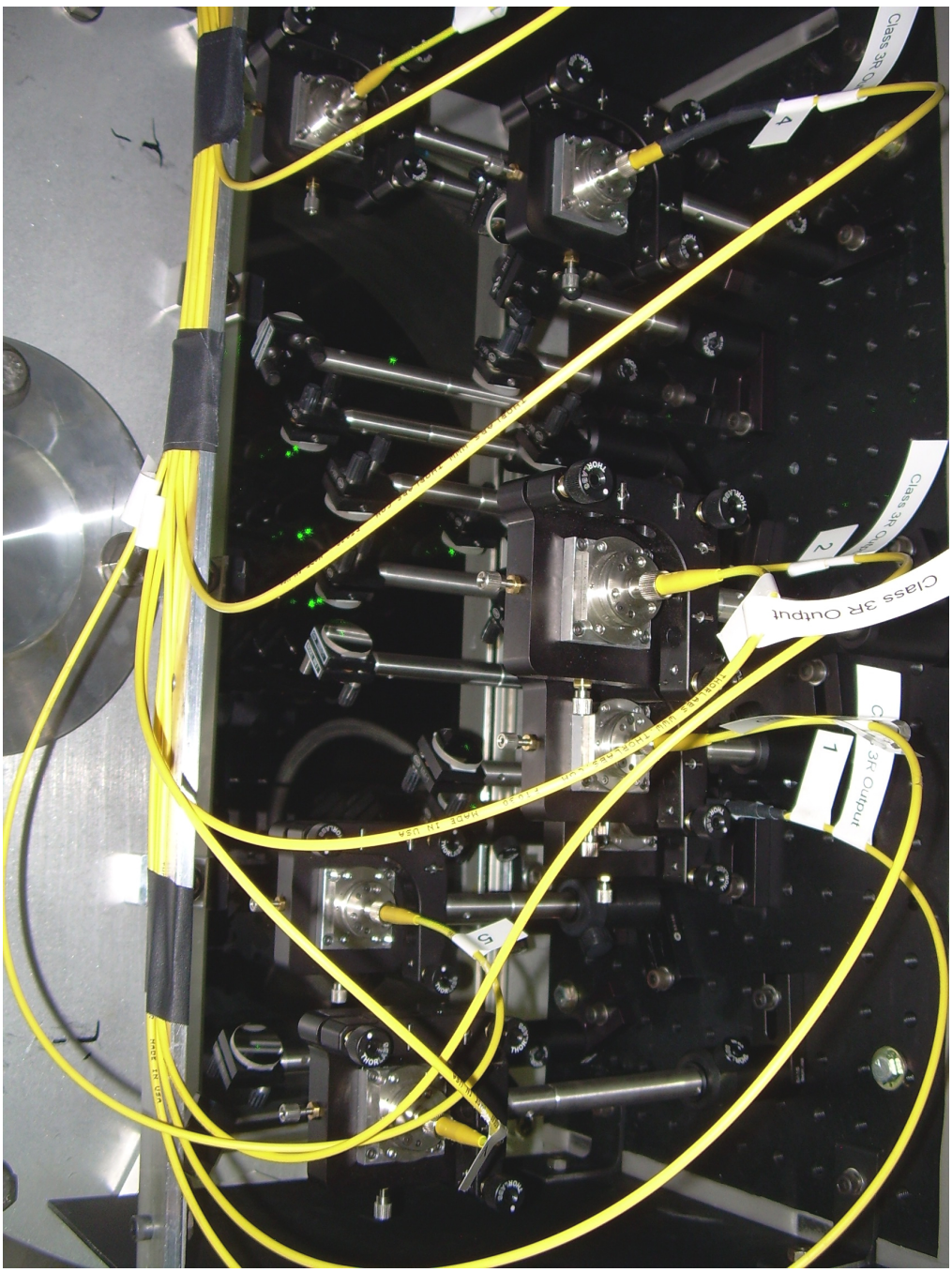

Figure B.12: Rear-view of the collection optics for the $Z = 50, 60$ cm chord arrangement. The breadboard is mounted on port $\theta 143\phi 324$.

Figure B.13: Top-view of the collection optics for the $Z = 50, 60$ cm chord arrangement. The breadboard is no longer mounted on the chamber.

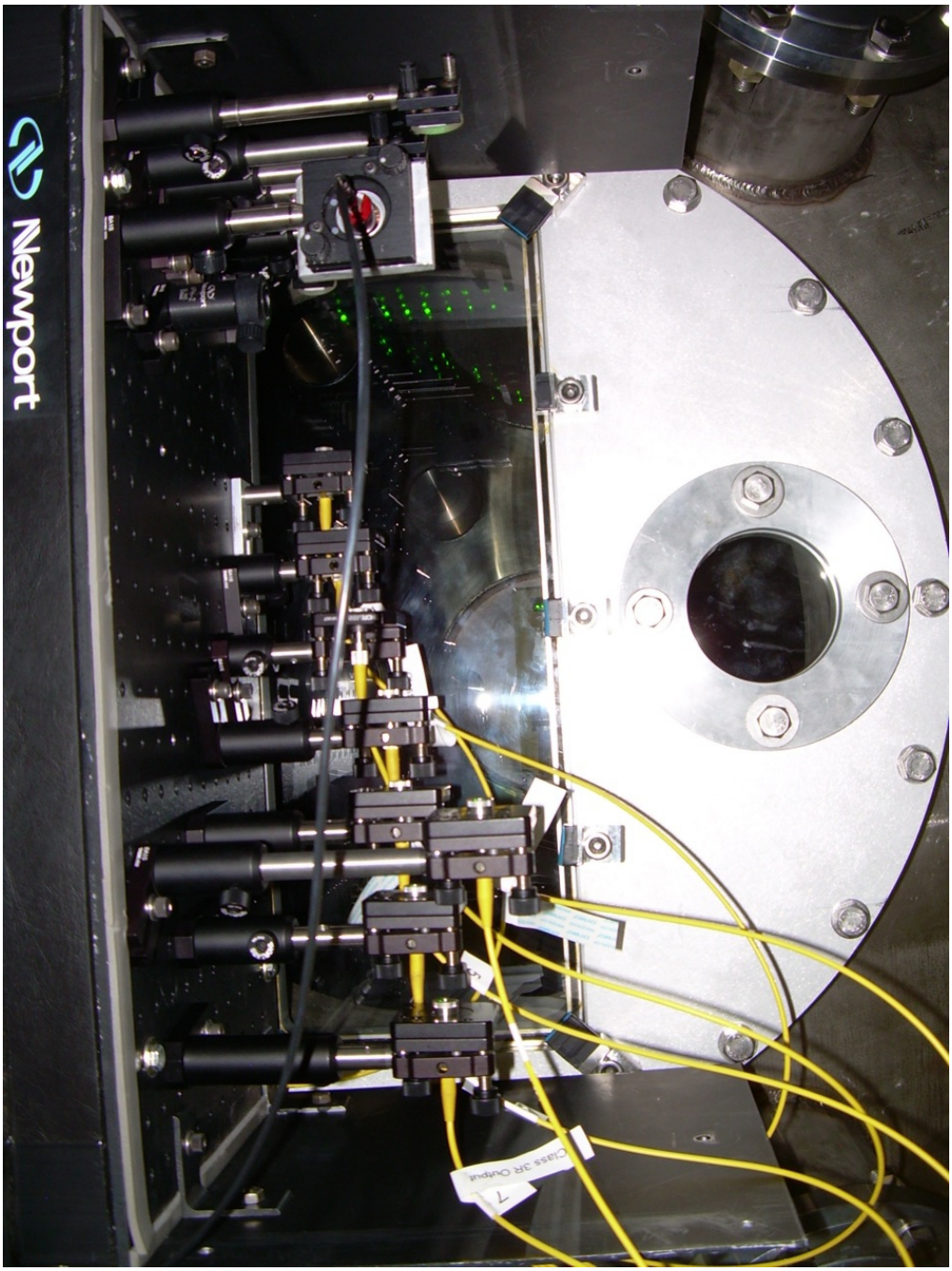

Figure B.14: Rear-view of the launch optics for the $Z = 85$ cm chord positions. The breadboard is mounted on port $\theta 37\phi 216$ and is pointing towards the ceiling with the optics hanging underneath.

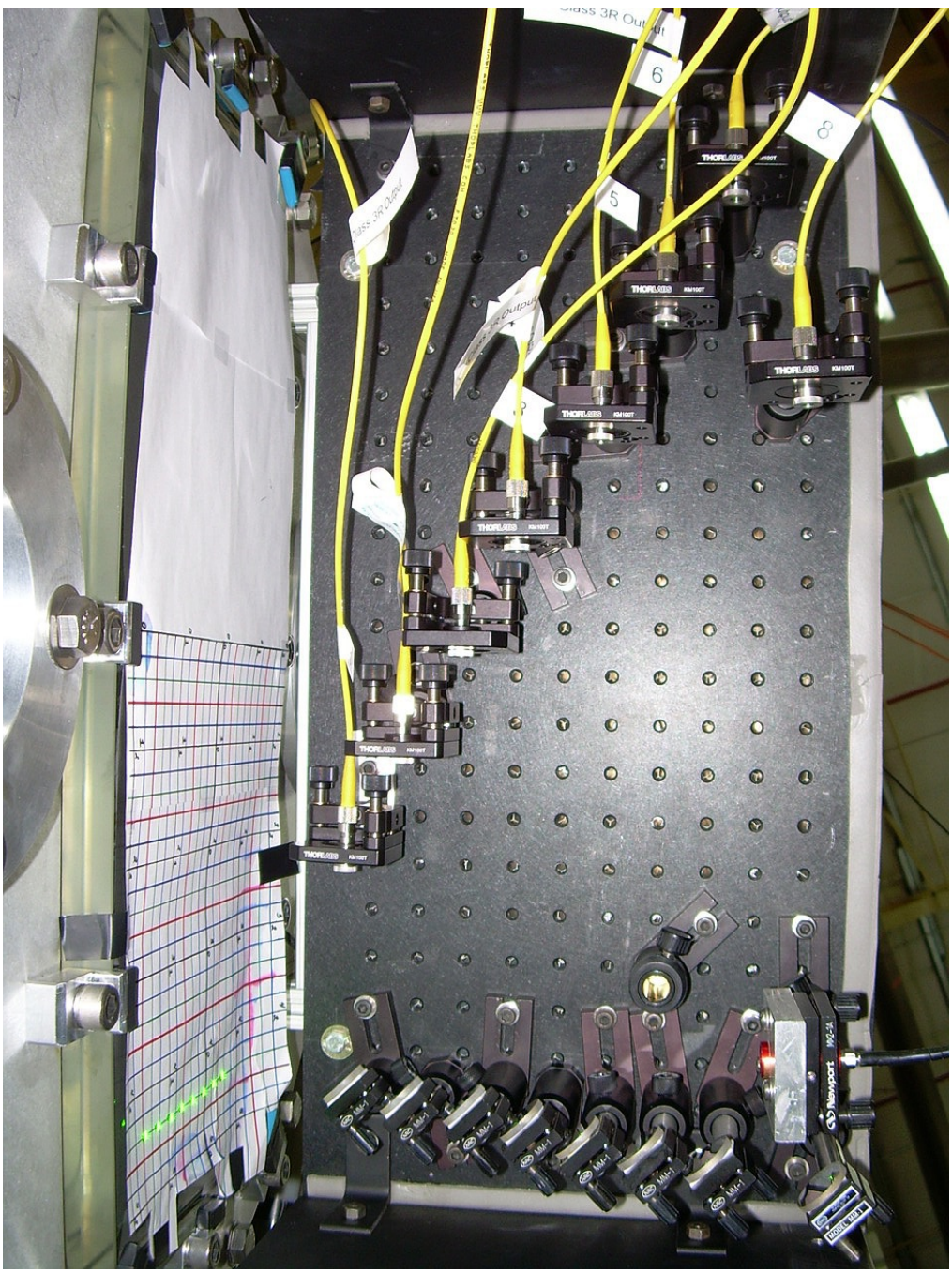

Figure B.15: Bottom-view (taken from the floor pointing up) of the launch optics for the $Z = 85$ cm chord positions. The breadboard is mounted on port $\theta 37\phi 216$ and is pointing towards the ceiling with the optics hanging underneath. Spectrometer optics and window alignment paper can also be seen.

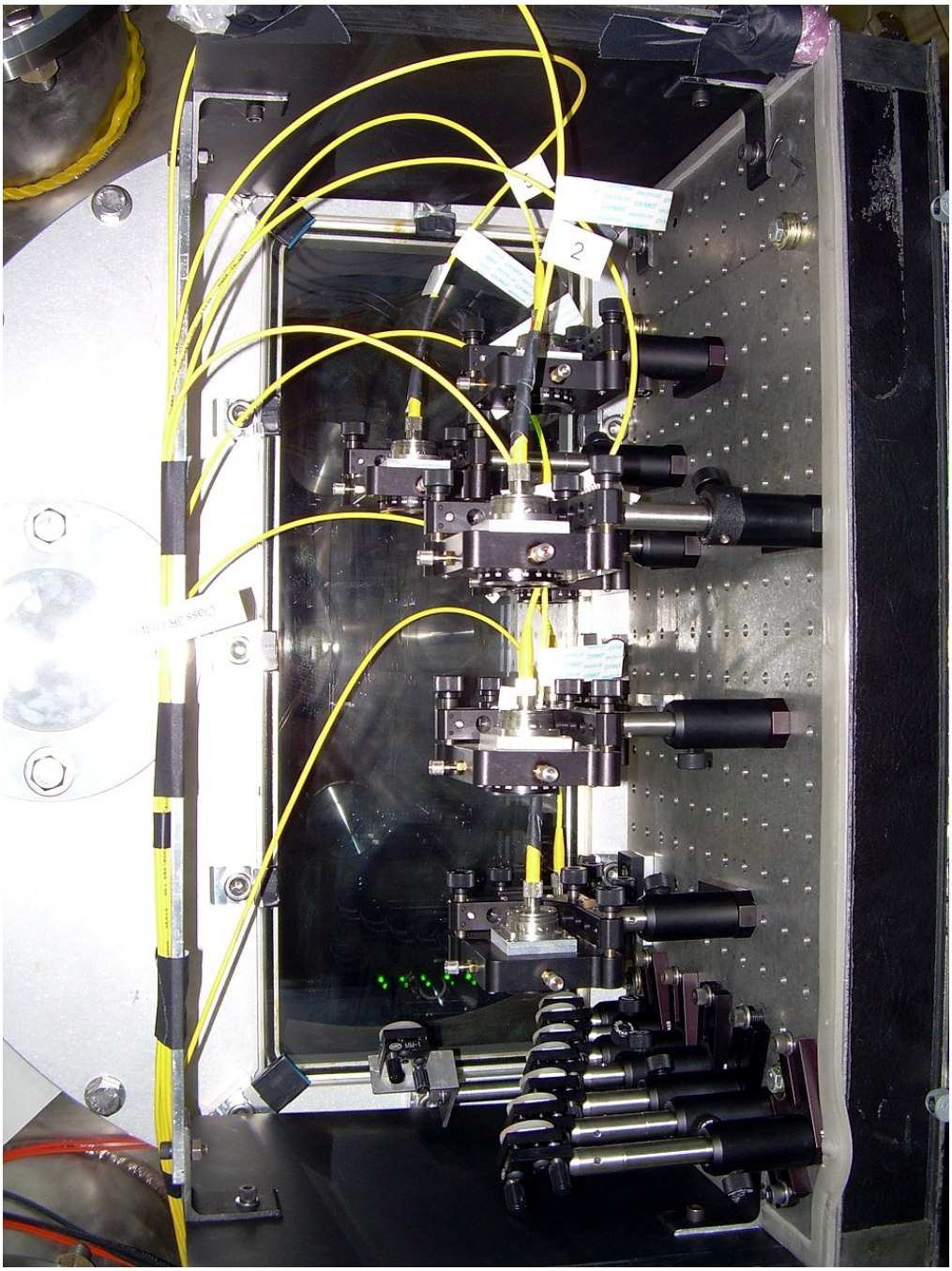

Figure B.16: Rear-view of the collection optics for the $Z = 85$ cm chord arrangement. The breadboard is mounted on port $\theta 143\phi 36$ and is pointing towards the floor with the optics mounted on top. Spectrometer optics can also be seen.

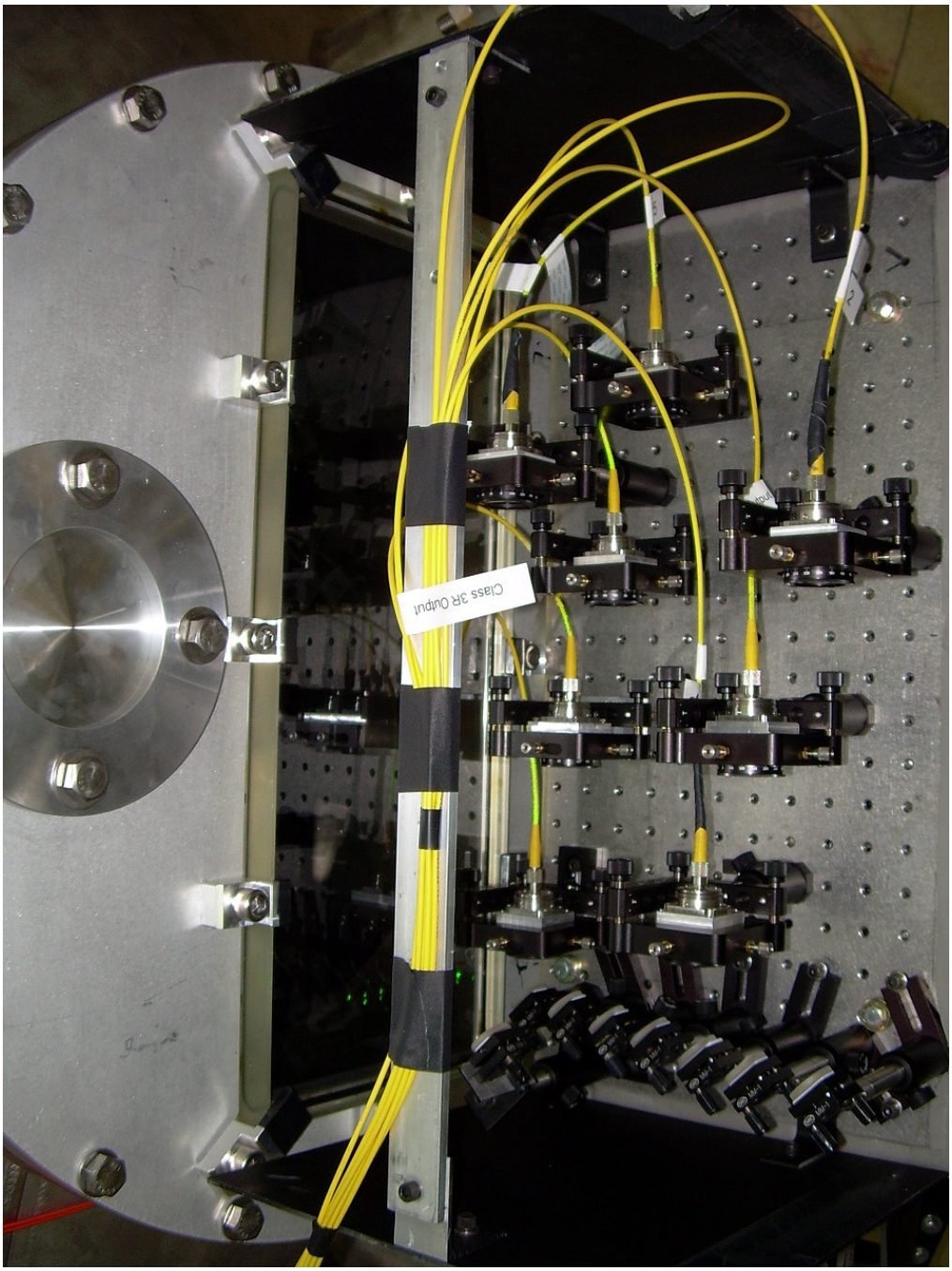

Figure B.17: Top-view of the collection optics for the $Z = 85$ cm chord arrangement. The breadboard is mounted on port $\theta 143\phi 36$ and is pointing towards the floor with the optics mounted on top. Spectrometer optics can also be seen.

Appendix C

MATLAB Phase Analysis Program

C.1 Single-jet axial chord configuration code

```
% Computes phi, the phase shift angle of the each interferometer
probe beam relative to its reference beam, based on the in-phase
& quadrature data from the I&Q demodulator outputs for each chord.
The demodulator output data has been smoothed using boxcar averaging.

clear
close all

%%%%%%%%%% Setting up global constants and parameters %%%%%%%%
shot_num = 744; % specify the shot of interest

% General Physical constants and parameters.
c=2.9979E8;                 % Speed of light [m/s].
e=1.6022E-19;               % Electronic charge [C].
```

```
m_e=9.1094E-31;             % Electron mass [kg].
mu0=4*pi*1E-7;              % Permeability of free space [H/m].
epsilon0=1/(mu0*c^2);       % Permittivity of free space [F/m].
lambda0=561.3E-9;           % Laser wavelength in free space [m]
micro_const = 10^6 ;        % Conversion from [sec] to [microsec]

% Physical constants for the gas species
n_stp = 1.000281;       % Index of refraction of neutral gas at STP
dn_stp = n_stp - 1;     % Index of refraction deviation from vacuum
num_den_stp = 2.683E25; % Number density of neutral gas at STP [m^-3]
ion_scale = .67;        % Scaling factor: ion const/neutral const
A = lambda0*(e^2)/(4*pi*epsilon0*m_e*(c^2));
B = (2*pi*dn_stp)/(lambda0*num_den_stp);
const1 = (A + (1-ion_scale)*B);
f0 = B/const1;

% Noise subtraction variables for each shot
p_order=4;
fit_interval= 1;

% Gives fraction of peak density at which to look for an edge value
euler = 2.71828;
peak_fraction = 1/euler; %value for FWHM

% Define the time interval of interest for the plasma signal
begintime =950;
endtime = 12000;
pickpoint = begintime;  %pickpoint eliminates ring from data limits
```

```
% Fitting constants for data analysis
exp_fit_chrd = 8;
vel_fit_int = 1;        %Initial chord for velocity calculations

%%%% Starting Loop for calculating phi & ne for each chord %%%%
mdsconnect('127.0.0.1:8000')
mdsopen('plx',shot_num)

%%%%%%%%%% Getting the signal from the tree %%%%%%%%%%

% Get the photodiode information from Z = 2.7 cm and Z = 52.7 cm
photodiode=mdsvalue('devices:screen_box:camac_1:jrg_tr_4:input_15');
time_diode=mdsvalue('dim_of(...
    devices:screen_box:camac_1:jrg_tr_4:input_15)');
photonozzle=mdsvalue('devices:screen_box:camac_1:jrg_tr_4:input_00');
time_nozzle=mdsvalue('dim_of(...
    devices:screen_box:camac_1:jrg_tr_4:input_00)');

% Get the chamber pressure
chamber_p = mdsvalue('shot_data:press_ch_af')*10^3 %[mTorr]

% Get/calcuate the gun current
ig = mdsvalue('devices:screen_box:camac_1:jrg_tr_3:...
    input_01')*86*10; %in [kA]
tig = mdsvalue('dim_of(...
    devices:screen_box:camac_1:jrg_tr_3:input_01)'); %in [sec]
ig = ig - mean(ig(1:100));
```

```
igs = smooth(smooth(smooth(smooth(smooth(smooth(ig,5),5),5),5),5),5);
igs_plot = igs;
ig_hold = find(tig <0);
[ig_hold2, ig_index] = max(ig_hold);
igs(1:ig_index) = 0;
[gun_I,tigmax] = max(igs)

%Get/calcuate the magnetic field in the gun bore
ibdot = mdsvalue('devices:screen_box:camac_1:jrg_tr_3:...
    input_03')*218; %in [kA]
tibdot = mdsvalue('dim_of(...
    devices:screen_box:camac_1:jrg_tr_3:input_03)'); %in [sec]
ibdot = ibdot - mean(ibdot(1:100));
ibdots = smooth(smooth(smooth(smooth(smooth(smooth(ibdot,...
    5),5),5),5),5),5);
ibdots_plot = ibdots;
ibdot_hold = find(tibdot <0);
[ibdot_hold2, ibdot_index] = max(ibdot_hold);
ibdots(1:ibdot_index) = 0;
[bdot_I,tibdotmax] = max(ibdots)

%Begin the interferometer analysis loop
for m = 1:8
chrdnum = m;

if m==1;
interf_A = mdsvalue('devices:screen_box:camac_1:jrg_tr_1:input_00');
interf_B = mdsvalue('devices:screen_box:camac_1:jrg_tr_1:input_01');
```

```
time = mdsvalue('dim_of(devices:screen_box:camac_1:jrg_tr_1:...
    input_00)');

elseif m==2;
interf_A = mdsvalue('devices:screen_box:camac_1:jrg_tr_1:input_02');
interf_B = mdsvalue('devices:screen_box:camac_1:jrg_tr_1:input_03');
time = mdsvalue('dim_of(devices:screen_box:camac_1:jrg_tr_1:...
    input_02)');

elseif m==3;
interf_A = mdsvalue('devices:screen_box:camac_1:jrg_tr_1:input_04');
interf_B = mdsvalue('devices:screen_box:camac_1:jrg_tr_1:input_05');
time = mdsvalue('dim_of(devices:screen_box:camac_1:jrg_tr_1:...
    input_04)');

elseif m==4;
interf_A = mdsvalue('devices:screen_box:camac_1:jrg_tr_2:input_00');
interf_B = mdsvalue('devices:screen_box:camac_1:jrg_tr_2:input_01');
time = mdsvalue('dim_of(devices:screen_box:camac_1:jrg_tr_2:...
    input_00)');

% Signal location for shots 79 - ~700
%interf_A = mdsvalue('devices:screen_box:camac_1:jrg_tr_2:input_06');
%interf_B = mdsvalue('devices:screen_box:camac_1:jrg_tr_2:input_07');
%time = mdsvalue('dim_of(devices:screen_box:camac_1:jrg_tr_2:...
 input_06)');

% Signal locations shots 31-68
```

```
%interf_A = -mdsvalue('devices:screen_box:camac_1:jrg_tr_1:...
    input_06');
%interf_B = mdsvalue('devices:screen_box:camac_1:jrg_tr_1:input_07');
%time = mdsvalue('dim_of(devices:screen_box:camac_1:jrg_tr_1:...
    input_06)');

elseif m==5;
interf_A = mdsvalue('devices:screen_box:camac_1:jrg_tr_2:input_08');
interf_B = mdsvalue('devices:screen_box:camac_1:jrg_tr_2:input_09');
time = mdsvalue('dim_of(devices:screen_box:camac_1:jrg_tr_2:...
    input_08)');

% Signal locations shots 31-68
%interf_A = mdsvalue('devices:screen_box:camac_1:jrg_tr_1:input_08');
%interf_B = mdsvalue('devices:screen_box:camac_1:jrg_tr_1:input_09');
%time = mdsvalue('dim_of(devices:screen_box:camac_1:jrg_tr_1:...
    input_08)');

elseif m==6;
interf_A = mdsvalue('devices:screen_box:camac_1:jrg_tr_1:input_10');
interf_B = mdsvalue('devices:screen_box:camac_1:jrg_tr_1:input_11');
time = mdsvalue('dim_of(devices:screen_box:camac_1:jrg_tr_1:...
    input_10)');

elseif m==7;
interf_A = mdsvalue('devices:screen_box:camac_1:jrg_tr_1:input_12');
interf_B = mdsvalue('devices:screen_box:camac_1:jrg_tr_1:input_13');
time = mdsvalue('dim_of(devices:screen_box:camac_1:jrg_tr_1:...
```

```
    input_12)');

elseif m==8;
interf_A = mdsvalue('devices:screen_box:camac_1:jrg_tr_1:input_14');
interf_B = mdsvalue('devices:screen_box:camac_1:jrg_tr_1:input_15');
time = mdsvalue('dim_of(devices:screen_box:camac_1:jrg_tr_1:...
    input_14)');
end

%%%%%%%%%%%%%% Setting up the arrays %%%%%%%%%%%%%%%%%%%
t=time;                          % Time vector [seconds].
V_demod_data=[time interf_A interf_B];
N_pts=length(time);          % Number of time points recorded.
N_IQ=2;                      % Number of "I"&"Q" demodulator outputs.
NIQ=1:N_IQ;                  % Vector of "I"&"Q" demodulator...
                               output indices.
V_demod=V_demod_data(:,2:3); % Demodulator raw data matrix with...
                               time vector removed [V].
t_start=t(1);                % Time value to start data processing...
                               to avoid trigger noise.
N_start=find(t >= t_start);  % Find indices t_micro>=t_start.
N_start=N_start(1);          % Index that corresponds to start time.
Ntime=N_start:N_pts;         % Vector of time indices
t=t(Ntime);                  % Time vector for data processing [sec].
V_demod=V_demod(Ntime,:);

tstart = t(begintime);
tstop = t(endtime);
```

```
%% Smooth raw data by doing moving average using FILTER function. %%
% This may be necessary to avoid phase shift order..
% changes due to noise.
N_smooth=5; % Number of points over which smoothing occurs
a=1;                              % Parameter for smoothing operation.
b=(1/N_smooth)*ones(1,N_smooth); % Parameter for smoothing operation.
V_demod_smoothed=filter(b,a,V_demod(Ntime,NIQ));
for n=NIQ
    V_demod_smoothed(1:N_smooth-1,n)=V_demod_smoothed(N_smooth,n);
end

% Define "I" & "Q" demodulator output data matrices for...
% each chord using smoothed data [V].
V_demod_I=V_demod_smoothed(:,1);
V_demod_Q=V_demod_smoothed(:,2);
V_demod_I=V_demod_I(:,1);
V_demod_Q=V_demod_Q(:,1);
V_demod=[V_demod_I V_demod_Q];
V_demod_proc=[t V_demod];

% Compute phase shift angle phi for each chord using...
% four-quadrant inverse tangent function.
% The phase shift is calculated assuming that
%       V_demod_I = A*cos(phi)
%       V_demod_Q = A*sin(phi)
phase(:,1)=atan2(V_demod_Q,V_demod_I);
phi=phase(:,1);
```

```
% Determine order of phase shift angle and make...
% it a continuous function.
order=zeros(N_pts,1);
for nt=1:N_pts-1
    if phi(nt+1)-phi(nt) < -pi
        Delta_order=floor(abs(phi(nt+1)-phi(nt))/pi);
        order((nt+1):N_pts)=order(nt)+Delta_order;
    elseif phi(nt+1)-phi(nt) > pi
        Delta_order=floor(abs(phi(nt+1)-phi(nt))/pi);
        order((nt+1):N_pts)=order(nt)-Delta_order;
    end
end
for nt=1:N_pts
    phi(nt)=phi(nt)+2*pi*order(nt);
end

% Create phase shift angle data matrix.
phi_data=[t phi phi];

% Establish data vectors to be used for fitting...
% data to a polynomial.
if endtime <= length(time)-1;

endfit = endtime + fit_interval*(endtime-begintime);
t_p=t(1:endfit);
y1=phi(1:endfit);
```

```
% Nullify data range of interest in order to exclude...
% it from baseline data to be fitted.
t_p(begintime:endtime) = [];
y1(begintime:endtime) = [];

% Fit polynomials to shifting baseline data and subtract...
% them from total signals for all chords to obtain final...
% line-integrated electron density data.
p=polyfit(t_p,y1,p_order);
y2=polyval(p,t);

if m==8
    phi_8_raw = phi(1:endfit);
    fit_curve = y2(1:endfit);
    t_fit = t(1:endfit);
end
% Subtract shifting baseline from data to obtain line-integrated...
% electron density with a corrected baseline.
phi_new = phi - y2;

elseif endtime==length(time);
phi_new=phi;
end

%%% Computing the quantities needed for velocities, peak density %%%
%%% and jet length calculations for axial chord configuration %%%%%%
clear begin_pt end_pt length_interval half_pt half_pt_fall
```

```
% Compute the peak phase shift of the jet
[peak_ne_ref, peak_time_index] = max(phi_new(pickpoint:endtime));
peak_time_ref = peak_time_index + pickpoint;
peak_ne2(chrdnum) = peak_ne_ref;
peak_time2(chrdnum) = t(peak_time_ref);

% Shifting the peak n_e values and peak n_e times so that...
% peak_time(8) = peak_ne(8) = 0 (orgin) for better fitting
peak_ne(9-chrdnum) = peak_ne_ref;
peak_time(9-chrdnum) = t(peak_time_ref);

% Select a point on the initial rising edge of the profile:...
% ne~frac*peak_ne to velocity time reference
pts_above = find(phi_new(pickpoint:peak_time_ref) >...
    peak_fraction*peak_ne_ref);

% Continuous indices are in the same interval: look for any...
% pts of discontinuity
half_pt(1) = pts_above(1);
ref = 0;
for k = 1:(length(pts_above)-5);
    if pts_above(k+1) ~= pts_above(k) + 1;
        if pts_above(k+5) ~= pts_above(k) + 5;
            ref = ref+1;
            half_pt(ref+1) = pts_above(k+1);
        end
    end
end
```

```
[t_halfmax, index] = max(half_pt);
time_halfmax(chrdnum) = t(t_halfmax + pickpoint);

% Select a point on the falling edge of the profile:...
% ne~frac3*peak_ne to velocity time reference
pts_above_fall = find(phi_new(peak_time_ref:endtime) >...
    peak_fraction*peak_ne_ref);

% Continuous indices are in the same interval:...
% look for any pts of discontinuity
half_pt_fall(1) = pts_above_fall(1);
ref = 0;
for k = 1:(length(pts_above_fall)-5);
    if pts_above_fall(k+1) ~= pts_above_fall(k) + 1;
        if pts_above_fall(k+5) ~= pts_above_fall(k) + 5;
            ref = ref+1;
            half_pt_fall(ref+1) = pts_above_fall(k+1);
        end
    end
end

if length(half_pt_fall)==1
    [half_pt_fall(1), index] = max(pts_above_fall);
end

[t_halfmax_fall, index] = max(half_pt_fall);
time_halfmax_fall(chrdnum) = t(t_halfmax_fall + peak_time_ref);
```

```
jet_length_index(chrdnum) = time_halfmax_fall(chrdnum)-...
    time_halfmax(chrdnum);

%%%%%% Saving data from the loop for comparison %%%%%%%%
t_save= t(begintime:endtime);
if m==1;
phi_raw_save_1 = phi(begintime:endtime);
phi_save_1 = phi_new(begintime:endtime);

elseif m==2;
phi_raw_save_2 = phi(begintime:endtime);
phi_save_2 = phi_new(begintime:endtime);

elseif m==3;
phi_raw_save_3 = phi(begintime:endtime);
phi_save_3 = phi_new(begintime:endtime);

elseif m==4;
phi_raw_save_4 = phi(begintime:endtime);
phi_save_4 = phi_new(begintime:endtime);

elseif m==5;
phi_raw_save_5 = phi(begintime:endtime);
phi_save_5 = phi_new(begintime:endtime);

elseif m==6;
phi_raw_save_6 = phi(begintime:endtime);
phi_save_6 = phi_new(begintime:endtime);
```

```
elseif m==7;
phi_raw_save_7 = phi(begintime:endtime);
phi_save_7 = phi_new(begintime:endtime);

elseif m==8;
phi_raw_save_8 = phi(begintime:endtime);
phi_save_8 = phi_new(begintime:endtime);

y2_save = y2(begintime:endtime);

end
end

%%%%%%%% Calculating Velocities %%%%%%%%%%%%%

% Compute the velocities of jet propagation between...
% chords using distance=6.35 cm
dist_btw_chords = 6.35*10^(-2); %units in m

% Compute the average velocity for the peaks
avg_vel_peak_ref = 0;
for k = (vel_fit_int + 1):8;
    delta_time_peak = abs(peak_time(k) - peak_time(k-1));
    vel_jet_peak(k-1) = dist_btw_chords/delta_time_peak; %[m/s]
    avg_vel_peak_ref = avg_vel_peak_ref + vel_jet_peak(k-1);
end
timecheck_peak = peak_time
```

```
velocities_peak = vel_jet_peak;
avg_vel_peak = avg_vel_peak_ref/(8-vel_fit_int)

%%%%%%%% Calculating Jet Length %%%%%%%%%%%%%
%Analysis of the jet length change with time
jet_length_time = jet_length_index
jet_length_distance = jet_length_time*avg_vel_peak;  %[m]
jet_length_distance = jet_length_distance*100;       %[cm]
jet_length_approx = polyfit(peak_time2, jet_length_distance,1)
jet_length_fit = polyval(jet_length_approx, t_save);

%%%%%%%%% Peak Decay Analysis %%%%%%%%%%%%%

% Fitting a polynomial using MATLAB's polynomial routine
fit_peaks_para = polyfit(peak_time, peak_ne, 2)
para_fit = polyval(fit_peaks_para, t_save);

% Fitting an exponential by taking the log of...
% peak n_e and fitting a line
m_sum = 0;
b_sum = 0;
for n = 2:8;
    delta_y = log10(peak_ne(n)) - log10(peak_ne(n-1));
    delta_x = peak_time(n) - peak_time(n-1);
    m_sum = m_sum + delta_y/delta_x;
    intercept = log10(peak_ne(n)) - delta_y*peak_time(n)/delta_x;
    b_sum = b_sum + intercept;
end
```

```
m_avg = m_sum/7;
b_avg = b_sum/7;
log_fit_analytic= m_avg*t_save + b_avg;

for n = 1:exp_fit_chrd
    log_hold(n) = log10(peak_ne(n));
    time_hold(n) = peak_time(n);
end
fit_peaks_log = polyfit(time_hold, log_hold, 1)
log_fit = polyval(fit_peaks_log, t_save);

conv_const = 1/log10(2.71828183);
fit_peaks_ln = conv_const*fit_peaks_log

% Fitting a parabola by finding the fitting...
% parameter a with the endpoints
a_avg =(peak_ne(1)-peak_ne(8))/(peak_time(1)-peak_time(8))^2;
fit_para_analytic =a_avg*(t_save-peak_time(8)).*...
    (t_save-peak_time(8)) + peak_ne(8);

%%%%%%%% Calculating chi^2 for each fit %%%%%%%%%
chi_para = 0;
chi_poly = 0;
chi_exp = 0;

for j = 1:exp_fit_chrd;
    chi_para_n(j) = (peak_ne2(j)-a_avg*peak_time2(j)^2)^2...
        /peak_ne2(j);
```

```
    chi_poly_n(j) = (peak_ne(j)-(fit_peaks_para(1)*peak_time(j)^2...
         + fit_peaks_para(2)*peak_time(j) + fit_peaks_para(3)))^2...
         /peak_ne(j);
    chi_exp_n(j) = (peak_ne(j)-exp(conv_const*(fit_peaks_log(1)*...
        peak_time(j) + fit_peaks_log(2))))^2/peak_ne(j);
end

for j = 1:exp_fit_chrd;
    chi_para = chi_para + chi_para_n(j);
    chi_poly = chi_poly + chi_poly_n(j);
    chi_exp = chi_exp + chi_exp_n(j);
end
chi_sqr_para = chi_para;
chi_sqr_poly = chi_poly
chi_sqr_exp = chi_exp

%%%%%%%%% Diameter Analysis and 3D expansion %%%%%%%%%%
% Calculate n_tot expansion using individual data pts
% Flip the jet length vector indices to correspond...
% with the peak_ne vector
clear one_hold one_hold_long diam_fit

d60 = 24; % cm
dnozz = 5; %
dccd = 10.8 % cm

fit_peaks_para2 = polyfit(peak_time2, peak_ne2, 2)
para_fit2 = polyval(fit_peaks_para2, t_save);
```

```
ind1 = find(t_save <= 42*10^(-6),1,'last');
tnozz = find(t_save <= 22*10^(-6),1,'last');

d_scale = d60*peak_ne2(4)*jet_length_distance(4);
d_scale_ccd = dccd*peak_ne2(7)*jet_length_distance(7);
d_scale_long = d60*para_fit2(ind1)*jet_length_fit(ind1);
d_scale_nozz = dnozz*para_fit2(tnozz)*jet_length_fit(tnozz)
inv_diam = para_fit2.*jet_length_fit;

%Calculate the jet diameter w/ scaling constant st chord 60 cm
diam_scaled = d_scale./(peak_ne2.*jet_length_distance);
diam_fit = d_scale./inv_diam;

diam_scaled_ccd = d_scale_ccd./(peak_ne2.*jet_length_distance);
diam_fit_ccd = d_scale_ccd./inv_diam;

%Calculate the diameter with a scaling constant from the nozzle
diam_nozz = d_scale_nozz./inv_diam;

%Compute the average radial expansion velocity
exp_lim = 3
rad_exp_ref = 0;
for k = (exp_lim + 1):8;
    delta_time_diam = abs(peak_time2(k) - peak_time2(k-1));
    diam_dist = abs(diam_scaled(k) - diam_scaled(k-1));
    exp_vel(k-1) = diam_dist/delta_time_diam;    %units in m/s
    rad_exp_ref = rad_exp_ref + exp_vel(k-1);
```

```
end

std_rad_exp = std(exp_vel)
avg_exp_vel = rad_exp_ref/(8-exp_lim)
chords_exp = (diam_scaled(5) - diam_scaled(8))/(peak_time2(5) -...
     peak_time2(8))

fspec = 0.94;
ntot_est = peak_ne2.*peak_ne2.*jet_length_distance./(const1*...
    d_scale*(fspec-f0));
ntot_est_fit =  para_fit2.*inv_diam./(const1*d_scale*(fspec-f0));

%%

for j = 1:8;
    jet_length_dist(j) = jet_length_distance(9-j);
end

n_e_data = peak_ne.*peak_ne.*jet_length_dist;
n_e_data_norm = peak_ne.*peak_ne.*jet_length_dist/n_e_data(1);

%Calculate n_e expansion using fitted values
n_int_pred =  exp(conv_const*log_fit);         %units of cm^-2
diam_pred =  1/(jet_length_fit.*n_int_pred);
n_e_pred = n_int_pred.*jet_length_fit.*n_int_pred;
n_e_pred_norm = n_int_pred.*jet_length_fit.*n_int_pred/n_e_data(1);

%Calculate an exponential fit for the experimental pts
```

```
for n= 1:4;
    ln_full_ne = log(n_e_data_norm);
end
fit_ne_ln = polyfit(peak_time, ln_full_ne, 1);
ne_full_ln = polyval(fit_ne_ln, t_save);
ne_fit_norm = exp(ne_full_ln);

%Fit a polynomial to the experimental pts
ntot_full_fit = polyfit(peak_time, n_e_data_norm, 5)
ntot_full_poly = polyval(ntot_full_fit, t_save);

%Find the chi^2 deviation
chi_poly_ntot = 0;
chi_exp_ntot = 0;

for j = 1:exp_fit_chrd;
    chi_poly_n_ntot(j) = (n_e_data_norm(j) - (ntot_full_fit(1)...
        *peak_time(j)^5 + ntot_full_fit(2)*peak_time(j)^4 +...
        ntot_full_fit(3)*peak_time(j)^3 + ntot_full_fit(4)*...
        peak_time(j)^2 + ntot_full_fit(5)*peak_time(j) + ...
        ntot_full_fit(6)))^2/n_e_data_norm(j);
    chi_exp_n_ntot(j) = (n_e_data_norm(j) - exp(conv_const*...
        (fit_ne_ln(1)*peak_time(j) + fit_ne_ln(2))))^2/...
        n_e_data_norm(j);
end

for j = 1:exp_fit_chrd;
    chi_poly_ntot = chi_poly_ntot + chi_poly_n_ntot(j);
```

```
    chi_exp_ntot = chi_exp_ntot + chi_exp_n_ntot(j);
end

chi_sqr_poly_ntot = chi_poly_ntot
chi_sqr_exp_ntot = chi_exp_ntot

%%%%% Converting Values to Strings for Plot Labels %%%%%%
shot_num = num2str(shot_num);
velocity = sprintf('%e',avg_vel);

log_fit_1 = sprintf('%e',fit_peaks_log(1));
log_fit_2 = sprintf('%e',fit_peaks_log(2));

ln_fit_1 = sprintf('%e', fit_peaks_ln(1));
ln_fit_2 = sprintf('%e', fit_peaks_ln(2));

fit_para_1 = sprintf('%e',fit_peaks_para(1));
fit_para_2 = sprintf('%e',fit_peaks_para(2));
fit_para_3 = sprintf('%e',fit_peaks_para(3));

chi_sqr_poly = sprintf('%e',chi_poly);
chi_sqr_exp =  sprintf('%e',chi_exp);

jet_fit_1 = sprintf('%e',jet_length_approx(1));
jet_fit_2 = sprintf('%e',jet_length_approx(2));

%%%%%%%%%%%%%% Plotting %%%%%%%%%%%%%%%
% Plot the phase shift vs time for all chords
```

```
figure
plot(t_save*micro_const, phi_save_1*360/(2*pi),'Color',...
    [0 0 0], 'LineWidth',2.5)
line(t_save*micro_const, phi_save_2*360/(2*pi),'Color',...
    [0.502 0.502 0.502],'LineWidth',2.5)
line(t_save*micro_const, phi_save_3*360/(2*pi),'Color',...
    [0.749 0 0.749],'LineWidth',2.5)
line(t_save*micro_const, phi_save_4*360/(2*pi),'Color',...
    [0 0 1],'LineWidth',2.5)
line(t_save*micro_const, phi_save_5*360/(2*pi),'Color',...
    [0 0.749 0.749],'LineWidth',2.5)
line(t_save*micro_const, phi_save_6*360/(2*pi),'Color',...
    [0 0.498 0],'LineWidth',2.5)
line(t_save*micro_const, phi_save_7*360/(2*pi),'Color',...
    [0.749 0.749 0],'LineWidth',2.5)
line(t_save*micro_const, phi_save_8*360/(2*pi),'Color',...
    [1 0 0],'LineWidth',2.5)
grid
axis([20 160 -Inf Inf])
axis autoy
legend('79.5 cm', '73.1 cm', '66.8 cm', '60.4 cm', '54.1 cm',...
    '47.7 cm', '41.4 cm', '35.0 cm')
xlabel('Time  [\mus]','FontSize', 24)
ylabel('\Delta\phi [deg]','FontSize', 24)
%title(['Phase Shift vs Time for Shot #' shot_num ], 'Fontsize', 20)
set(gca,'FontSize', 20)

% Plot ntot vs time for all chords
```

```
f = 0.95;
figure
plot(t_save*micro_const, phi_save_1*(10^(-6))/(const1*(f-f0)),...
    'Color',[0 0 0], 'LineWidth',2)
line(t_save*micro_const, phi_save_2*(10^(-6))/(const1*(f-f0)),...
    'Color',[0.502 0.502 0.502],'LineWidth',2)
line(t_save*micro_const, phi_save_3*(10^(-6))/(const1*(f-f0)),...
    'Color',[0.749 0 0.749],'LineWidth',2)
line(t_save*micro_const, phi_save_4*(10^(-6))/(const1*(f-f0)),...
    'Color',[0 0 1],'LineWidth',2)
line(t_save*micro_const, phi_save_5*(10^(-6))/(const1*(f-f0)),...
    'Color',[0 0.749 0.749],'LineWidth',2)
line(t_save*micro_const, phi_save_6*(10^(-6))/(const1*(f-f0)),...
    'Color',[0 0.498 0],'LineWidth',2)
line(t_save*micro_const, phi_save_7*(10^(-6))/(const1*(f-f0)),...
    'Color',[0.749 0.749 0],'LineWidth',2)
line(t_save*micro_const, phi_save_8*(10^(-6))/(const1*(f-f0)),...
    'Color',[1 0 0],'LineWidth',2)
grid
axis([tstart*micro_const tstop*micro_const -Inf Inf])
axis autoy
legend('79.5 cm', '73.1 cm', '66.8 cm', '60.4 cm', '54.1 cm',...
    '47.7 cm', '41.4 cm', '35.0 cm')
xlabel('Time  [\mus]','FontSize', 16)
ylabel('\int n_{tot} dl [*10^{14} cm^{-3}]','FontSize', 16)
%title(['Phase Shift vs Time for Shot #' shot_num ], 'Fontsize', 16)
set(gca,'FontSize', 14)
```

```
% Plot the radial expansion of the jet with multiple possible fits
figure
plot(peak_time*micro_const, peak_ne*360/(2*pi), '--db',...
    t_save*micro_const, para_fit*360/(2*pi),'-g',...
    t_save*micro_const, exp(conv_const*log_fit)*360/(2*pi),...
    '-r', 'LineWidth',2, 'MarkerSize', 10, 'MarkerFaceColor', 'b')
axis([peak_time(1)*micro_const peak_time(8)*micro_const -Inf Inf])
axis autoy
legend(['Measured' ,sprintf('\n'), 'y(t) = [\int n_e dL]_{peak}'],...
    ['MATLAB Polyfit Order 2', sprintf('\n'), 'y(t) =...
    (' fit_para_1 ')*t^2 + (' fit_para_2 ')*t + (' fit_para_3 ')'...
    ,sprintf('\n'), '\chi^2_{poly} = ' chi_sqr_poly], ['MATLAB...
    Exponential Fit' ,sprintf('\n'), 'y(t) = exp[(' ln_fit_1 ')*t...
    + ('ln_fit_2')]' ,sprintf('\n'), '\chi^2_{exp} = 'chi_sqr_exp])
xlabel('Time  [\mus]','FontSize', 16)
ylabel('\Delta\phi_{peak} [deg]','FontSize', 16);
title(['Peak Line-Integrated Electron Density vs Time for Shot...
    #' shot_num],'FontSize', 16)
set(gca,'FontSize', 14)

% Plot the Axial expansion of the jet
figure
plot(peak_time2*micro_const, jet_length_distance, '--db',...
    t_save*micro_const, jet_length_fit, '-r', 'LineWidth',2,...
    'MarkerSize', 10, 'MarkerFaceColor', 'b')
axis([peak_time2(8)*micro_const peak_time2(1)*micro_const -Inf Inf])
axis autoy
legend('Measured', ['Linear Fit' ,sprintf('\n'), 'y(t) =...
```

```
    (' jet_fit_1 ')*t + (' jet_fit_2 ')']);
xlabel('Time  [\mus]','FontSize', 16)
ylabel('Jet Length [cm]','FontSize', 16)
title(['Jet Length vs Time for Shot #' shot_num],'FontSize', 16)
set(gca,'FontSize', 14)

% Plot the predicted density curve ntot and ne
figure
[axx,hh1,hh2] = plotyy(peak_time2*micro_const, ntot_est*10^(-4),...
    t_save*micro_const, ntot_est_fit*fspec*10^(-4), 'plot');
xlim(axx(2),[30 50]);
xlim(axx(1),[30 50]);
ylim(axx(1),[1*10^(14) 4*10^(15)])
ylim(axx(2),[fspec*1*10^(14) fspec*4*10^(15)])
xlabel('Time  [\mus]','FontSize', 20)
ylabel(axx(1),'n_{tot} [cm^{-3}]','FontSize', 20);
ylabel(axx(2),'n_e [cm^{-3}]','FontSize', 20);

% Plot Chords 5 and 6 against the photodiode signal
figure
[ax, h1, h2]=plotyy(t_save(:,1)*micro_const, phi_save_6(:,1)...
    *360/(2*pi),time_diode*micro_const, photodiode,'plot');
line(t_save*micro_const, phi_save_5*360/(2*pi), 'LineWidth',...
     2, 'Color', 'r');
xlim(ax(1),[10 150]);
xlim(ax(2),[10 150]);
ylim(ax(1),[-15 30])
ylim(ax(2),[-.5 1])
```

```
set(h1,'LineWidth',2)
set(h2,'LineWidth',2)
xlabel('Time  [\mus]','FontSize', 16)
ylabel(ax(1),'\Delta \phi_{tot} [deg]','FontSize', 16);
ylabel(ax(2),'A.U.','FontSize', 16);
legend('Interferometer Chord at 47.7 cm','Interferometer Chord at...
     54.1 cm','PhotoDiode Signal at ')
title(['A Comparison of the Photodiode and Interferometer Signals...
     for Shot #' shot_num],'FontSize', 16)

%Some plots for noise analysis
figure
plot(t_fit*micro_const,phi_8_raw*360/(2*pi),t_fit*micro_const,...
    fit_curve*360/(2*pi))
grid
axis([0 t(endfit)*micro_const -Inf Inf])
axis autoy
xlabel('Time  [\mus]','FontSize', 16)
ylabel('{ \Delta \it \phi}  [deg]','FontSize', 16)
title(['Phase Shift vs Time for Shot #' shot_num ], 'Fontsize', 16)
set(gca,'FontSize', 14)

% Plotting the diameter fit for the data w/ scaling constant
figure
plot(peak_time2*micro_const, diam_scaled, t_save*micro_const,...
    diam_fit, peak_time2*micro_const, diam_scaled_ccd,...
    t_save*micro_const, diam_fit_ccd)
axis([33 50 -Inf Inf])
```

```
axis autoy
xlabel('Time [\mus]','FontSize', 16)
ylabel('Jet Diameter [cm]','FontSize', 16);
set(gca,'FontSize', 14)

%Writing plots back to the tree
mdsput('interferom:phase1','BUILD_SIGNAL($1,,$2)',...
    phi_save_1*360/(2*pi),t_save*micro_const);
mdsput('interferom:phase2','BUILD_SIGNAL($1,,$2)',...
    phi_save_2*360/(2*pi),t_save*micro_const);
mdsput('interferom:phase3','BUILD_SIGNAL($1,,$2)',...
    phi_save_3*360/(2*pi),t_save*micro_const);
mdsput('interferom:phase4','BUILD_SIGNAL($1,,$2)',...
    phi_save_4*360/(2*pi),t_save*micro_const);
mdsput('interferom:phase5','BUILD_SIGNAL($1,,$2)',...
    phi_save_5*360/(2*pi),t_save*micro_const);
mdsput('interferom:phase6','BUILD_SIGNAL($1,,$2)',...
    phi_save_6*360/(2*pi),t_save*micro_const);
mdsput('interferom:phase7','BUILD_SIGNAL($1,,$2)',...
    phi_save_7*360/(2*pi),t_save*micro_const);
mdsput('interferom:phase8','BUILD_SIGNAL($1,,$2)',...
    phi_save_8*360/(2*pi),t_save*micro_const);

mdsdisconnect;
```

C.2 Code for performing an Able inversion

```
%%%% Creating a length matrix for the abel inversion %%%
imax = 4;
jmax = 4;
dr50 = .04; % units [m]
r0_50 = .05 + .03;  % units [m]
dr = dr50;
r0 = r0_50;
offset = .03/2;

%Creating the radii matrix at Z = 50 cm
for k = 1:4
    r50(k) = r0 + (k-1)*dr;             % approximate chord radius
    r50_EU(k) = r0 + (k-1)*dr + offset; % radius for upper error bar
    r50_EL(k) = r0 + (k-1)*dr - offset; % radius for lower error bar
end

%Creating the length matrix for Z = 50 cm
for i = 1:imax
    for j = 1:jmax;
        if j < i;
            L50(i,j)=((r50(jmax+1-j)+dr/2)^2 -r50(imax+1-i)^2)...
                ^(1/2)-((r50(jmax-j)+dr/2)^2 -r50(imax+1-i)^2)^(1/2);
            L50_EU(i,j)=((r50_EU(jmax+1-j)+dr/2)^2 -...
                r50_EU(imax+1-i)^2)^(1/2)-((r50_EU(jmax-j)+dr/2)^2...
                - r50_EU(imax+1-i)^2)^(1/2);
            L50_EL(i,j)=((r50_EL(jmax+1-j)+dr/2)^2 -...
```

```
                r50_EL(imax+1-i)^2)^(1/2)-((r50_EL(jmax-j)+dr/2)^2...
                - r50_EL(imax+1-i)^2)^(1/2);
        elseif j == i;
            L50(i,j) =((r50(jmax+1-j)+dr/2)^2-r50(imax+1-i)^2)^(1/2);
            L50_EU(i,j) = ((r50_EU(jmax+1-j)+dr/2)^2 -...
                r50_EU(imax+1-i)^2)^(1/2);
            L50_EL(i,j) = ((r50_EL(jmax+1-j)+dr/2)^2 -...
                r50_EL(imax+1-i)^2)^(1/2);
        elseif j > i;
            L50(i,j) = 0;
            L50_EU(i,j) = 0;
            L50_EL(i,j) = 0;
        end
    end
end

%%
dr60 = .05;    % units [m]
r0_60 = .01 + .035;     % units [m]

dr = dr60;
r0 = r0_60;
offset = .035/2;

%Creating the radii matrix at Z = 60 cm
for k = 1:4
    r60(k) = r0 + (k-1)*dr              % approximate chord radius
    r60_EU(k) = r0 + (k-1)*dr + offset; % radius for upper error bar
```

```
    r60_EL(k) = r0 + (k-1)*dr - offset; % radius for lower error bar
end

%Creating the length matrix for Z = 60 cm
for i = 1:imax
    for j = 1:jmax;
        if j < i;
            L60(i,j)=((r60(jmax+1-j)+dr/2)^2 -r60(imax+1-i)^2)...
                ^(1/2)-((r60(jmax-j)+dr/2)^2 -r60(imax+1-i)^2)^(1/2);
            L60_EU(i,j)=((r60_EU(jmax+1-j)+dr/2)^2 -...
                r60_EU(imax+1-i)^2)^(1/2)-((r60_EU(jmax-j)+dr/2)^2...
                - r60_EU(imax+1-i)^2)^(1/2);
            L60_EL(i,j)=((r60_EL(jmax+1-j)+dr/2)^2 -...
                r60_EL(imax+1-i)^2)^(1/2)-((r60_EL(jmax-j)+dr/2)^2...
                - r60_EL(imax+1-i)^2)^(1/2);
        elseif j == i;
            L60(i,j) =((r60(jmax+1-j)+dr/2)^2-r60(imax+1-i)^2)^(1/2);
            L60_EU(i,j) = ((r60_EU(jmax+1-j)+dr/2)^2 -...
                r60_EU(imax+1-i)^2)^(1/2);
            L60_EL(i,j) = ((r60_EL(jmax+1-j)+dr/2)^2 -...
                r60_EL(imax+1-i)^2)^(1/2);
        elseif j > i;
            L60(i,j) = 0;
            L60_EU(i,j) = 0;
            L60_EL(i,j) = 0;
        end
    end
end
```

```
% Multiply the length matrices by 2 to convert radii to diameters
L50 = 2*L50;
L60 = 2*L60;

L50_EU = 2*L50_EU;
L60_EU = 2*L60_EU;

L50_EL = 2*L50_EL;
L60_EL = 2*L60_EL;

%%%%%%% Creating the time dependent phase matrix %%%%%%%%%

for k = 1:(endtime-begintime)+1
    PHI = [phi_save_4(k); phi_save_3(k); phi_save_2(k);...
         phi_save_1(k)];
    M = (1E-6/const1)*inv(L50)*PHI;
    M_EU = (1E-6/const1)*inv(L50_EU)*PHI;
    M_EL = (1E-6/const1)*inv(L50_EL)*PHI;

    ntotf_4(k) = M(1);
    ntotf_3(k) = M(2);
    ntotf_2(k) = M(3);
    ntotf_1(k) = M(4);

    ntotf_4_EU(k) = M_EU(1);
    ntotf_3_EU(k) = M_EU(2);
    ntotf_2_EU(k) = M_EU(3);
```

```
    ntotf_1_EU(k) = M_EU(4);

    ntotf_4_EL(k) = M_EL(1);
    ntotf_3_EL(k) = M_EL(2);
    ntotf_2_EL(k) = M_EL(3);
    ntotf_1_EL(k) = M_EL(4);
end

for k = 1:(endtime-begintime)+1
    PHI = [phi_save_8(k); phi_save_7(k); phi_save_6(k);...
         phi_save_5(k)];
    M = (1E-6/const1)*inv(L60)*PHI;
    M_EU = (1E-6/const1)*inv(L60_EU)*PHI;
    M_EL = (1E-6/const1)*inv(L60_EL)*PHI;

    ntotf_8(k) = M(1);
    ntotf_7(k) = M(2);
    ntotf_6(k) = M(3);
    ntotf_5(k) = M(4);

    ntotf_8_EU(k) = M_EU(1);
    ntotf_7_EU(k) = M_EU(2);
    ntotf_6_EU(k) = M_EU(3);
    ntotf_5_EU(k) = M_EU(4);

    ntotf_8_EL(k) = M_EL(1);
    ntotf_7_EL(k) = M_EL(2);
    ntotf_6_EL(k) = M_EL(3);
```

```
    ntotf_5_EL(k) = M_EL(4);
end

%%%%%%%%%% Plotting the radial functions %%%%%%%%%%
shot_num = num2str(shot_num);

%Plot an intensity plot of all the signals vs time

P50 = (r0_50-dr50/2):dr50:(r0_50 + 3.5*dr50)
holder = zeros(endtime-begintime + 1, 1);
S50 = [ntotf_1' ntotf_2' ntotf_3' ntotf_4' holder];

figure
subplot(2,1,1)
pcolor(t_save*micro_const, P50, S50');
shading flat
axis([15 50 (r0_50-dr50/2) (r0_50 + 3.5*dr50)])
set(gca,'YTick',P50,'YTickLabel',P50*100)
colorbar
%xlabel('Time  [\mus]','FontSize', 16)
ylabel(['Radial Chord Position [cm] for Shot...
     #' shot_num],'FontSize', 20)

P60 = (r0_60-dr60/2):dr60:(r0_60 + 3.5*dr60)
S60 = [ntotf_5' ntotf_6' ntotf_7' ntotf_8' holder];

subplot(2,1,2)
pcolor(t_save*micro_const, P60, S60');
```

```
shading flat
axis([15 50 (r0_60-dr60/2) (r0_60 + 3.5*dr60)])
set(gca,'YTick',P60,'YTickLabel',P60*100)
colorbar
xlabel('Time  [\mus]','FontSize', 20)
%ylabel('Chord Position Relative to the Midplane of...
     the Gun Axes [cm]','FontSize', 16)
```

References

[1] http://www.prism-cs.com.

[2] J. K. Ziemer, "A Review of Gas-Fed Pulsed Plasma Thruster Research over the Last Half-Century," Electric Propulsion and Plasma Dynamics Lab report (unpublished), Princeton University (2000); available at http://alfven.princeton.edu/papers/GFPPTReview.pdf.

[3] J.T. Cassibry, University of Alabama in Huntsville, Huntsville, AL, private communication, 2010.

[4] J. D. Huba, *NRL Plasma Formulary*, 2009.

[5] C.S. Adams, A.G. Lynn, M.A. Gilmore, E.C. Merritt, A.L Moser, and S.C. Hsu, *Schlieren imaging diagnostic for a collisionless shock experiment*, Bull. Amer. Phys. Soc **57** (2012), 12.

[6] Ralph A. Alpher and Donald R. White, Phys. Fluids **2** (1959), 153–161.

[7] ———, Phys. Fluids **2** (1959), 162–169.

[8] Thomas J Awe, Colin S Adams, Josh S Davis, David S Hanna, Scott C Hsu, and Jason T Cassibry, *One-dimensional radiation-hydrodynamic scaling studies of imploding spherical plasma liners*, Phys. Plasmas **18** (2011), 072705.

[9] M.M. Basko, A.J. Kemp, and J. Meyer ter Vehn, *Ignition conditions for magnetized target fusion in cylindrical geometry*, Nucl. Fusion **40** (2000), 59.

[10] Ronald E. Bell, *An inversion technique to obtain full polodial velocity profiles in a tokamak plasma*, Rev. Sci. Instrum. **68** (1997), 1273.

[11] Max Born and Emil Wolf, *Principles of optics*, 4th ed., Pergamon Press, 1970.

[12] A. Case, S. Messer, R. Bomgardner, and F.D. Witherspoon, *Interferometer density measurements of a high-velocity plasmoid*, Phys. Plasmas **17** (2010), 053503.

[13] J. T. Cassibry, R. J. Cortez, S. C. Hsu, and F. D. Witherspoon, *Estimates of confinement time and energy gain for plasma liner driven magnetoinertial fusion using an analytic self-similar converging shock model*, Phys. Plasmas **16** (2009), 112707.

[14] J. T. Cassibry, M. Stanic, S. C. Hsu, F. D. Witherspoon, and S. I. Abarzhi, *Tendency of spherically imploding plasma liners formed by merging plasma jets to evolve toward spherical symmetry*, Phys. Plasmas **19** (2012), 052702.

[15] J.T. Cassibry, M. Stanic, and S.C. Hsu, *Scaling relations for a stagnated imploding spherical plasma liner formed by an array of merging plasma jets*, Phys. Plasmas **20** (2013), 032706.

[16] R.E. Center, *Measurement of shock-wave structure in helium-argon mixture*, Phys. Fluids **10** (1967), 1777–1784.

[17] Francis F. Chen, *Introduction to plasma physics and controlled fusion, volume 1: Plasma physics*, 2nd ed., Springer, 2006.

[18] M.E. Cuneo, M.C. Herrmann, D.B. Sinars, S.A. Slutz, W.A. Stygar, R.A. Vesey, A.B. Sefkow, G.A. Chandler, J.E. Bailey, J.L. Porter, R.D. McBride, D.C. Rovang, M.G. Mazarakis, E.P. Yu, D.C. Lamppa, K.J. Peterson, C. Nakhleh, S.B. Hansen, A.J. Lopez, M.E. Savage, C.A. Jennings, M.R. Martin, R.W. Lemke, B.W. Atherton, I.C. Smith, P.K. Rambo, M. Jones, M.R. Lopez, P.J. Christenson, M.A. Sweeney, B. Jones, L.A. McPherson, E. Harding, M.R. Gomez, P.F. Knapp, T.J. Awe, R.J. Leeper, C.L. Ruiz, G.W. Cooper, K.D. Hahn, J. McKenney, A.C. Owen, G.R. McKee, G.T. Leifeste, D.J. Ampleford, E.M. Waisman, A. Harvey-Thompson, R.J. Kaye, M.H. Hess, S.E. Rosenthal, and M.K. Matzen, *Magnetically driven implosions for inertial confinement fusion at sandia national laboratories*, IEEE Trans. Plasma Sci. **40** (2012), 3222–3245.

[19] J. S. Davis, S. C. Hsu, I. E. Golovkin, J. J. MacFarlane, and J. T. Cassibry, *One-dimensional radiation-hydrodynamic simulations of imploding spherical plasma liners with detailed equation-of-state modeling*, Phys. Plasmas **19** (2012), 102701.

[20] James H. Degnan, William L. Baker, Maynard Cowan Jr., Jack D. Graham, Jed L. Holmes, Emmanuel A. Lopez, David W. Price, Dale Ralph, and Norman F. Roderick, *Operation of cylindrical array of plasma guns*, Fusion Technol. **35** (1999), 354–359.

[21] R.P. Drake, *High-energy-density-physics*, Springer-Verlag, Berlin, 2006.

[22] Eugene Hecht, *Optics*, 4th ed., Addison Wesley, 2002.

[23] M. Hohenberger, P.Y. Chang, G. Fiskel, J.P. Knauer, R. Betti, F.J. Marshall, D.D. Meyerhofer, F.H. Séguin, and R.D. Petrasso, *Inertial confinement fusion implosions with imposed magnetic field compression using the omega laser*, Phys. Plasmas **19** (2012), 056306.

[24] S. C. Hsu, *Technical summary of the first u.s. plasma jet workshop*, J. Fusion Energy **28** (2009), 246.

[25] S. C. Hsu, T. J. Awe, S. Brockington, A. Case, J. T. Cassibry, G. Kagan, S. J. Messer, M. Stanic, X. Tang, D. R. Welch, and F. D. Witherspoon, *Spherically imploding plasma liners as a standoff driver for magnetoinertial fusion*, IEEE Trans. Plasma Sci. **40** (2012), 1287.

[26] S. C. Hsu, E. C. Merritt, A. L. Moser, T. J. Awe, S. J. E. Brockington, and et al, *Experimental characterization of railgun-driven supersonic plasma jets motivated by high energy density physics applications*, Phys. Plasmas **19** (2012), 123514.

[27] S. C. Hsu, F. D. Witherspoon, J. T. Cassibry, and M. A. Gilmore, *Overview of the plasma liner experiment*, Bull. Amer. Phys. Soc. **56** (2011), 307.

[28] S.C. Hsu, A.L. Moser, J.S. Davis, J.P. Dunn, T.J. Awe, E.C. Merritt, C.S. Adams, A.G. Lynn, M.A. Gilmore, S. Brockington, A. Case, S.J. Messer, D. van Doren, F.D. Witherspoon, J.T. Cassibry, and M. Stanic, *Summary of plasma liner experiment (plx) research results*, Bull. Amer. Phys. Soc **57** (2012), 12.

[29] Richard H Huddlestone and Stanley L Leonard, *Plasma diagnostic techniques*, Academic Press Inc, New York, 1965.

[30] I.H. Hutchinson, *Principles of plasma diagnostics*, 2nd ed., Cambridge University Press, New York, 2002.

[31] T. Intrator, G.A. Wurden, P.E. Sieck, W.J. Waganaar, L. Dorf, M. Kostora, R.J. Cortez, J.H. Degnan, E.L. Ruden, M. Domonkos, P. Adamson, C. Grabowski, D.G. Gale, M. Kostora, W. Sommars, M. Frese, S. Frese, J.F. Camacho, P. Parks, R.E. Siemon, T. Awe, A.G. Lynn, and R. Gribble, *Field reversed configuration translation and the magnetized target fusion collaboration*, J. Fusion Energy **28** (2008), 165–169.

[32] H. Ji, H. Toyama, K. Yamagishi, S. Shinohara, A. Fujisawa, and K. Miyamoto, *Probe measurements in the repute-l reversed field pinch*, Rev. Sci. Instrum. **62** (1991), 10.

[33] G. Kagan, X. Tang, S. C. Hsu, and T. J. Awe, *Bounce-free spherical hydrodynamic implosion*, Phys. Plasmas **18** (2011), 120702.

[34] H. Kim, R. Samulyak, L. Zhang, and P. Parks, *Influence of atomic processes on the implosion of plasma liners*, Phys. Plasmas **19** (2012), 082711.

[35] Deepak Kumar, *Experimental investigations of magnetohydrodynamic plasma jets*, Ph.D. thesis, California Institute of Technology, 2009.

[36] H. Kumar and S. Mishra, *Entropy stable numerical schemes for two-fluid plasma equations*, J. Sci. Comput. **52** (2012), 401.

[37] L. D. Landau and E. M. Lifshitz, *Fluid mechanics 2nd ed.*, vol. 6, Butterworth-Heinmann, 2011.

[38] Wu Linchun, Mike Phillips, Sarah Messer, Andrew Case, and F. Douglas Witherspoon, *Numerical simulation of merging plasma jets using high-z gases*, IEEE Trans. Plasma Sci. **41** (2013), 4.

[39] I. R. Lindemuth and R. E. Siemon, *The fundamental parameter space of controlled thermonuclear fusion*, Amer. J. Phys. **77** (2009), 407.

[40] John Loverich and Ammar Hakim, *Two-dimensional modeling of ideal merging plasma jets*, J. Fusion Energy **29** (2010), 532–539.

[41] A. G. Lynn, E. Merritt, M. Gilmore, S. C. Hsu, F. D. Witherspoon, and J. T. Cassibry, *Diagnostics for the plasma liner experiment*, Rev. Sci. Instrum. **81** (2010), 10E115.

[42] J. J. MacFarlane et al., *Simulation of the ionization dynamics of aluminum irradiated by intense short-pulse lasers*, Inertial Fusion Sciences and Applications 2003 (B. A. Hammel, D. D. Meyerhofer, and J. Meyer-ter-Vehn, eds.), American Nuclear Society, 2004, p. 457.

[43] J. J. MacFarlane, I. E. Golovkin, and P. R. Woodruff, *Helios-cr – a 1-d radiation-magnetohydrodynamics code with inline atomic kinetics modeling*, J. Quant. Spect. Rad. Transfer **99** (2006), 381.

[44] I. R. McNab and F. C. Beach, *Naval railguns*, IEEE Trans. Magnetics **43** (2007), 463.

[45] Elizabeth C. Merritt, Mark A Gilmore, Alan G. Lynn, Bruno Bauer, F. Douglas Witherspoon, Jason Cassibry, and Scott C. Hsu, *Diagnostics for the plasma liner experiment (plx)*, Bull. Amer. Phys. Soc **55** (2010), 15.

[46] S. Messer et al., *Nonlinear compressions in merging plasma jets*, Phys. Plasmas **20** (2013), 032306.

[47] A.L. Moser, S.C. Hsu, J.P. Dunn, D.T. Martens, C.S. Adams, E.C. Merritt, A.G. Lynn, M.A. Gilmore, C. Thoma, and D.R. Welch, *Laboratory experiment to investigate collisionless shock production and dynamics*, Bull. Amer. Phys. Soc **57** (2012), 12.

[48] Robert H. Nunn, *Intermediate fluid dynamics*, Hemisphere Publishing, 1989.

[49] M.M. Oberai, *Kinetic-theory approach to problem of shock-wave structure in a binary mixture*, Phys. Fluids **8** (1965), 826.

[50] ———, *A mott-smith distribution to describe structure of a plane shock wave in a binary mixture*, Phys. Fluids **9** (1966), 1634.

[51] The Committee on High Energy Density Plasma Physics, *Frontiers in high energy density physics: The x-games of contemporary science*, National Academies Press, 2003.

[52] Oxxius SA, *Oxxius slim plug and play datasheet*, 2010.

[53] P. B. Parks, *On the efficacy of imploding plasma liners for magnetized fusion target compression*, Phys. Plasmas **15** (2008), 062506.

[54] A. V. Phelps, J. Phys. Chem. Ref. Data **20** (1990), 557.

[55] P. W. Rambo and J. Denavit, Phys. Plasmas **1** (1994), 4050.

[56] C.A. Romero-Talamás, P.M. Bellan, and S.C. Hsu, *Multielement magnetic probe using commercial chip inductors*, Rev. Sci. Instrum. **75** (2004), 8.

[57] Peter Shajenko, *Phenomenon of interference between two light beams propagating in optical fibers having a large path difference*, Applied Optics **22** (1983), no. 13.

[58] F.S. Sherman, *Shock-wave structure in binary mixtures of chemically inert perfect gases*, J. Fluid Mech. **8** (1960), 465.

[59] Y. C. F. Thio, C. E. Knapp, R. C. Kirkpatrick, R. E. Siemon, and P. J. Turchi, *A physics exploratory experiment on plasma liner formation*, J. Fusion Energy **20** (2001), 1.

[60] Cartsen Thoma, Dale R. Welch, Robert E. Clark, Nichelle Bruner, Joseph J. MacFarlane, and Igor E. Golovkin, *Two-fluid electromagnetic simulations of plasma-jet acceleration with detailed equation-of-state*, Phys. Plasmas **18** (2011), 103507.

[61] Seth Thompson and Jason Cassibry, *Modeling of formation and implosion of plasma liners by discrete jets*, Proc. 39th Plasmadynamics and Lasers Conference, 2008.

[62] F. Douglas Witherspoon, Richard Bomgardner II, Andrew Case, Sarah Messer, Samuel Brockington, L. Wu, Ramond Elton, Scott C. Hsu, and Mark Gilmore, *Overview of plasma guns for the plasma liner experiment (plx)*, Bull. Amer. Phys. Soc **55** (2010), 358.

[63] F. Douglas Witherspoon, Richard Bomgardner II, Andrew Case, Sarah J Messer, Samuel Brockington, L Wu, and Ramond Elton, *Minirailgun accelerator for plasma liner driven hedp and magneto-inertial fusion experiments*, 36th ICOPS Meeting (2009).

[64] F. Douglas Witherspoon, Samuel Brockington, Andrew Case, Sarah J Messer, L Wu, Ramond Elton, Scott C. Hsu, and Mark Gilmore, *Development of mini-railguns for the plasma liner experiment (plx)*, Bull. Amer. Phys. Soc **56** (2011), 311.

[65] F. Douglas Witherspoon, Andrew Case, Sarah J. Messer, Richard Bomgardner II, Michael W. Philips, Samuel Brockington, and Ramond Elton, Rev. Sci. Instrum. **80** (2009), no. 083506-1.